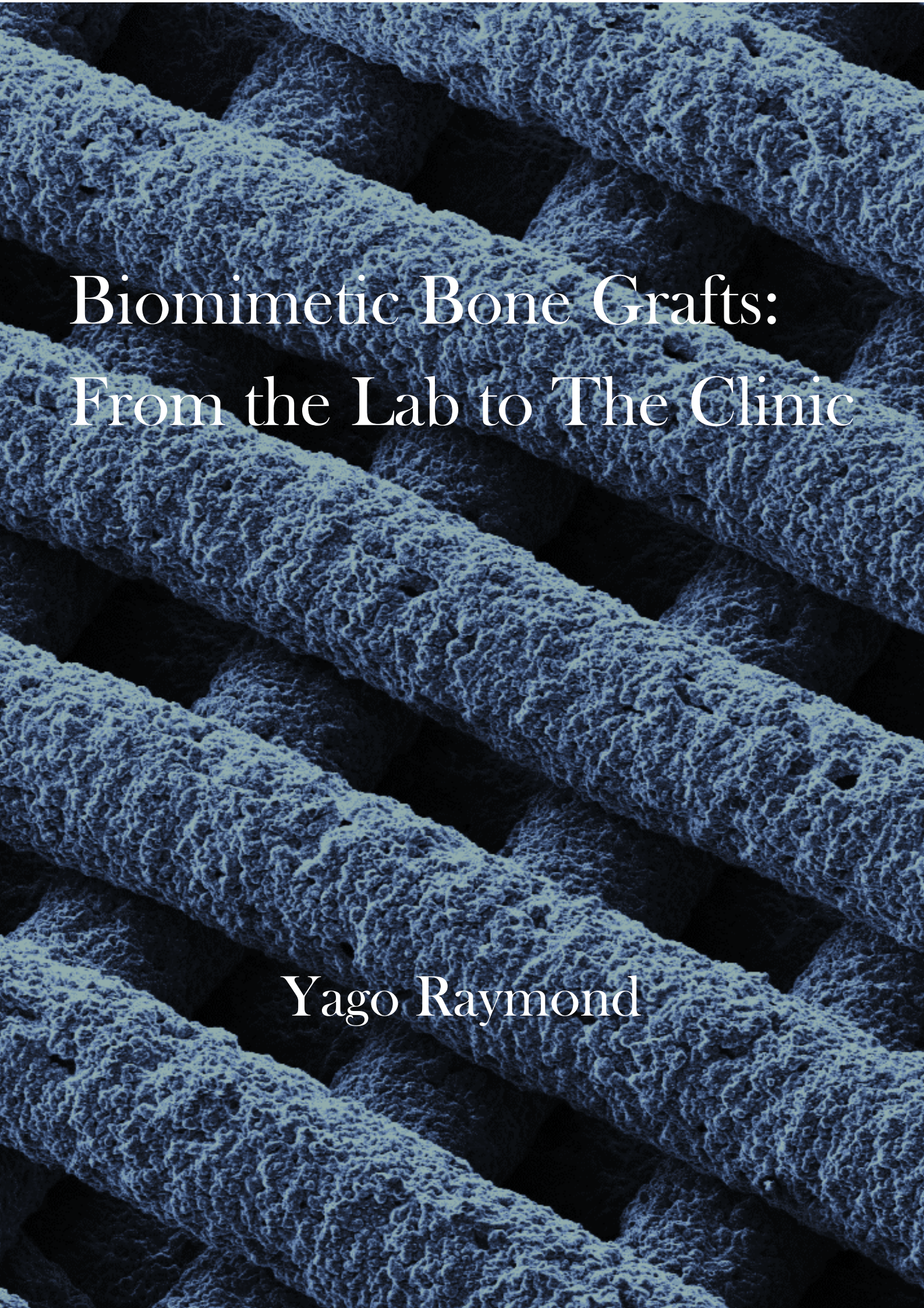

Biomimetic Bone Grafts: From the Lab to The Clinic

Yago Raymond

UNIVERSITAT POLITÈCNICA DE CATALUNYA BARCELONATECH

Biomimetic Bone Grafts: From the Lab to the Clinic

Yago Raymond

PhD Thesis

BIOMIMETIC BONE GRAFTS: FROM THE LAB TO THE CLINIC

Doctoral Program of Materials Science and Engineering

Yago Raymond Llorens

Supervisor:
Prof. Maria-Pau Ginebra Molins

Biomaterials, Biomechanics and Tissue Engineering Group
Department of Materials Science and Engineering
Universitat Politècnica de Catalunya

Barcelona, 2021

A les Mars

People tend to write inspiring cites.
However, I am usually more inspired by music:

Aphex Twin - Avril 14th / Flim

Brian Eno - An Ending (Ascent)

Nils Frahm - Says

Table of contents

Abstract

Bone grafting is a common medical practice in today's society, being bone the second most transplanted tissue worldwide after blood. Therefore, it represents a field of major interest for both biomedical research and the biomedical industry. Despite the ability of bone to self-heal, in some scenarios where defects are large or complex, bone grafts are essential for a successful regeneration. Although autografting is still today the gold standard in terms of biological performance, the limited availability and morbidity associated with this practice drive to search for alternatives. Synthetic grafts arise as a promising option due to their unlimited availability and the possibility to tune their structure and composition for optimal performance.

The present thesis explores biomimetic calcium-deficient hydroxyapatite (CDHA), a promising material for synthetic bone grafts, in a translational-oriented perspective. Two product presentations are studied: A more conventional granulated conformation and a 3D-printed personalised format.

Chapter 1 offers a brief overview of bone biology, as well as a state of the art of the currently available bone grafting strategies found in the literature. **Chapter 2** focuses on the validation of the *in vivo* performance of CDHA granules compared to a well-established bovine particulate xenograft in a dental indication in miniature swine. It is concluded that both biomaterials meet the requirements for bone grafting, (*i.e.* biocompatibility, osseointegration and osteoconduction). Moreover, it is revealed that granule morphology is a key factor to ensure the preservation of the grafted volume. In the following chapters, the focus is moved to the 3D-printed personalised CDHA bone grafts. **Chapter 3** investigates different approaches to accelerate the consolidation process of the 3D-printed grafts in order to make the technology more suitable for industrial applications, and develops a hydrothermal treatment that reduces the reaction time to 30 minutes instead of the 7 days needed in the biomimetic approach. Despite the slight differences in physicochemical properties associated to this approach (*e.g.* microstructure, crystalline phase, microporosity, specific surface area), the resulting scaffolds support adhesion and proliferation of rat mesenchymal stem cells, suggesting the potential as bone graft substitutes. In **Chapter 4** the hydrothermal route introduced in the previous chapter is compared to the long-established biomimetic treatment in terms of the *in vivo* performance of the 3D-printed scaffolds through orthotopic implantation in rabbit condyle monocortical defects. The samples treated with this new process, in addition to the excellent biocompatibility, osseointegrative and osteoconductive properties characteristic of biomimetic CDHA, exhibit a significantly higher amount of newly formed bone than the biomimetic counterpart. This enhanced performance is attributed to the higher permeability of the microstructure, as demonstrated with a protein adsorption test. **Chapter 5** explores a strategy to enhance the degree of concavity and specific surface area of 3D-printed structures obtained by microextrusion, by using nozzles with non-circular cross-sections. Besides achieving the intended purpose and characterising the 3D-printed structures, different technical constraints for the printing process associated to the use of non-circular nozzles are identified. In a further step, this developed technology is applied to the fabrication of 3D-printed bone grafts with concave filament surfaces and tested *in vivo* in a rabbit condyle orthotopic model in **Chapter 6**. It is found that using strands with star-shaped cross-sections helps to guide bone, enhancing the osteoconductive properties of the scaffolds. Finally, **Chapter 7** summarises all the

work carried out in this thesis to transfer the 3D printing technology of synthetic bone grafts to the market, turning it into a commercially available product.

Resum

L'ús d'empelts ossis és cada vegada més freqüent: l'os és el segon teixit més trasplantat del món, després de la sang. Per aquesta raó, aquesta pràctica atreu un gran interès tant a nivell de recerca acadèmica com per a la indústria biomèdica. Tot i la capacitat d'autoregeneració que tenen els ossos, en casos en què els defectes són massa grossos o complexos, l'ús d'empelts ossis és essencial per aconseguir-ne una bona regeneració. Malgrat que els autoempelts segueixen sent el tractament de primera elecció a causa de la seva eficàcia a nivell biològic, la seva disponibilitat limitada així com la morbiditat associada a aquest tipus de pràctiques fan necessari buscar altres solucions. Els empelts sintètics sorgeixen com una alternativa prometedora, donada la seva àmplia disponibilitat i la possibilitat de modificar-ne l'estructura i la composició per obtenir un rendiment òptim.

En aquesta tesi s'estudia la hidroxiapatita biomimètica deficient en calci (CDHA) com a material prometedor per a la fabricació d'empelts ossis sintètics, des d'una perspectiva orientada a la recerca translacional. S'estudien dues presentacions diferents del producte: una configuració en forma de grànuls, més convencional, i un format personalitzat obtingut per impressió 3D.

El **Capítol 1** recull una breu descripció general de la biologia de l'os, juntament amb l'estat de l'art de les diferents estratègies d'empelts ossis que es poden trobar a la literatura. El **Capítol 2** se centra en l'estudi de la resposta *in vivo* de grànuls de CDHA, en comparació amb el xenoempelt boví amb més reconeixement mèdic, en una indicació dental en porcs en miniatura. L'estudi conclou que ambdós biomaterials compleixen els requeriments d'un empelt ossi, és a dir, biocompatibilitat, osteointegració i osteoconducció. A més, es demostra que la morfologia dels grànuls és un factor clau per assegurar la preservació del volum empeltat. Els capítols següents es focalitzen en empelts ossis de CDHA personalitzats obtinguts per impressió 3D. En el **Capítol 3** s'investiguen diferents processos per accelerar la consolidació dels empelts impresos en 3D per tal d'aconseguir una tecnologia més adient per a aplicacions industrials, i es desenvolupa un tractament hidrotèrmic que redueix el temps de reacció dels 7 dies necessaris per mètodes biomimètics a només 30 minuts. Tot i que amb el nou tractament s'observen petites diferències en les propietats fisicoquímiques (per exemple, en la microestructura, en la fase cristal·lina, la microporositat o la superfície específica), els empelts obtinguts permeten l'adhesió i la proliferació de cèl·lules mare mesenquimals de rata, la qual cosa indica que són una solució viable com a substituts ossis. En el **Capítol 4** el procés hidrotèrmic introduït al capítol anterior es compara amb el tractament biomimètic, en termes del comportament *in vivo* dels empelts impresos, mitjançant la implantació ortotòpica en defectes monocorticals en còndils de conills. Les mostres tractades amb aquest nou procediment, a més de presentar l'excel·lent biocompatibilitat i les propietats osteointegratives i osteoconductives pròpies de la CDHA biomimètica, també mostren una quantitat significativament més gran de teixit ossi neoformat que la seva contrapart. Aquestes diferències s'atribueixen a la major permeabilitat de la microestructura, tal com es demostra mitjançant un assaig d'absorció de proteïnes. En el **Capítol 5** s'estudia una estratègia per millorar tant el grau de concavitat com la superfície específica d'estructures impreses en 3D obtingudes per microextrusió. La tàctica consisteix a utilitzar broquets d'extrusió amb seccions transversals no circulars. A més d'aconseguir-ho i caracteritzar les propietats de les estructures impreses, s'identifiquen un conjunt de restriccions tècniques per al procés d'impressió

associades a l'ús de broquets no circulars. En un pas més, aquesta estratègia s'aplica a la fabricació d'empelts ossis amb superfícies de filament còncaves i, en el **Capítol 6**, s'assaja *in vivo* en un model ortotòpic de còndil de conill. S'observa que utilitzar filaments amb una secció transversal en forma d'estrella ajuda a guiar l'os i millora les propietats osteoconductives dels empelts. Finalment, el **Capítol 7** resumeix la feina duta a terme al llarg de la tesi per transferir al mercat la tecnologia d'impressió 3D i convertir-la en un producte comercial.

Acknowledgements

Moltes gràcies Pau per donar-me l'oportunitat d'embarcar-me en aquest projecte, per creure i confiar en mi del primer moment fins a l'últim. Estic molt agraït de tot el que he après al teu costat. La teva visió crítica, la perseverança i l'incorformisme han sigut vitals per tirar endavant aquesta tesi i per fer-me millor científic. Ara que veig la tesi acabada m'adono de tot el temps que m'has dedicat, de la bona feina que hem fet junts i no m'imagino una millor tutora que tu. Gràcies.

Muchas gracias Ana, David y Yassine por el apoyo que me habéis dado durante el transcurso de esta tesis. Habéis hecho que me sienta muy valorado en la empresa. Gracias a vosotros los logros de esta tesis tienen más sentido y aportan una utilidad tangible en la sociedad. Ana, muchas gracias especialmente a ti por el soporte, la paciencia y por entenderme siempre.

No vull oblidar-me de la Marta i el Romain, que van descobrir-me el món dels biomaterials a nivell pràctic. Moltes gràcies per donar-me llibertat i confiança absoluta, i despertar-me l'interès en la recerca. També agraeixo sincerament al ¨old-school¨ BBT (Anna Diez, Cédric, Joanna Sadowska, Judit i Giuseppe) i als de CIEFMA (Miquel Turon, Erica, Danielas…) tot allò que m'heu ensenyat i, sobretot, els bons moments que vam passar duran els meus inicis al BBT. També em sento afortunat d'haver coincidit amb el grup de doctorands i TFM a l'ETSEIB (Diego, Quim, Mar, Violeta), els molts moments compartits al chiringuito i els compartits dinant junts. Moltes gràcies a tot el staff del BBT pel suport i ajuda (Txell, Montse, Miquel, Marta, Carles, Cristina i Noelia). Sincerament, crec que sou un gran equip, a nivell tècnic però, sobretot, a nivell personal. Incloc també en els agraïments als que ja no són al grup però m'han ajudat o donat suport en algun moment: Mònica, Roman i Sergi. Agraeixo l'ajuda dels tècnics del departament i del multiescala, el bon rollo i tot el que he après gràcies a ells: Kim, Trifon i Araceli. Moltes gràcies a la Panxa team per tots els bons moments de comboi durant aquesta segona part del doctorat!!! Tot i no ser-ne membre oficial, m'heu adoptat com un més! Agradezco a todos los estudiantes de TFG y TFM que habéis participado en este proyecto: Joanna Konka, Cyril, Eilidth, Javi y Antonio. Muchas gracias también a los compañeros de despacho por vuestra compañía y amabilidad: Lluguís, Joanna, Ana, Inès, Mar, Sergio y Violeta.

Por otro lado, agradezco al equipo de Mimetis tanto los buenos momentos que me habéis dado como la ayuda prestada. Estoy muy orgulloso del compañerismo, el buen ambiente y la dinámica de equipo que hay en la empresa. Gracias David, Ana, Victor, Christian, Emilie, Margaux, Linh, Lamis y Anna. También muchas gracias a los que han seguido otros caminos pero en su momento estuvieron en el equipo: Andrea xurrriii, Yassine, Amarilys, Cristian, Vivianne, Marc, Thibault, Claudia y Biel.

Quiero agradecer también a la gente que ha contribuido y colaborado en este proyecto, mejorando la calidad de este trabajo y permitiendo que llegara donde ha llegado: Jordi Franch, Cristina Manzanares, Raúl Benítez, Juan Pou y Antonio Riveiro.

Finalment, vull agrair a la meva família i amics més íntims el suport incondicional i la comprensió durant aquests quasi 5 anys.

I, per últim, Mar, moltes gràcies per haver estat al meu costat durant tota aquesta etapa de la meva vida, compartint els bons i els mals moments. Per tots els moments feliços que hem viscut junts! Però, sobretot, gràcies per donar-me suport incondicional, animar-me i ajudar-me a relativitzar les coses quan tot se'm feia una

muntanya i no veia el final. Gràcies per entendre'm i escoltar-me. El millor que m'emporto de la tesi és haver-te conegut.

PD. Perdoneu si m'he deixat algú, ja sabeu que soc molt despistat...

Objective and Innovations

The aim of the present industrial Philosophy Doctor (PhD) thesis was to investigate, develop, validate and transfer to the market innovative bone grafting solutions based on biomimetic calcium deficient hydroxyapatite (CDHA).

Specifically, the following objectives were established and addressed in this thesis:

- Validate the *in vivo* performance of the product MimetikOss® Granules in a dental indication (**CHAPTER 2**).

- Reduce the consolidation time of self-setting 3D-printed calcium phosphate bone grafts to make the technology more suitable for its industrialisation (**CHAPTER 3**).

- Compare the biological performance of 3D-printed calcium phosphate scaffolds obtained by accelerated hardening routes to the traditional biomimetic routes (**CHAPTER 4**).

- Develop a method to introduce concavities and increase the surface area of the 3D-printed bone grafts (**CHAPTER 5**).

- Test the *in vivo* performance of the scaffolds with enhanced degree of concavity and surface area compared to the traditional structures (**CHAPTER 6**).

- Transform the technology into a commercial product: MimetikOss® 3D patient-specific bone grafts, the first personalised biomimetic bone graft in the market (**CHAPTER 7**).

Abbreviations

3D	Three-dimensional
3ITT	Three interval thixotropy test
α-TCP	Alpha-tricalcium phosphate
β-TCP	Beta-tricalcium phosphate
μ-CT	Micro-computed tomography
ALP	Alkaline phosphatase
AM	Additive manufacturing
ANOVA	Analysis of variance
AR	Aspect ratio
B	Biomimetic
BET	Theory by Brunauer, Emmett, and Teller for physical adsorption
BG	Bone graft
BMP-2	Bone morphogenetic protein 2
BS/TS	Bone surface over total surface
BSA	Bovine serum albumin
BSD	Backscattered electron detector
BV/TV	Bone volume over total volume
C3D4	4-node linear tetrahedral elements
C	Cylindrical
CAD	Computer-aided design
CAM	Computer-aided manufacturing
CaP	Calcium phosphate
CBQCA	3-(4-carboxybenxoyl) quinoline-2-carboxaldehyde
CDHA	Calcium-deficient hydroxyapatite
CI	Confidence intervals
CNC	Computer numerical control
COD	Crystallography open database
CPC	Calcium phosphate cement
CRO	Clinical research organisation
CT	Computed tomography
DICOM	Digital imaging and communications in medicine
DIW	Direct ink writing
DXF	Drawing exchange format file
ECM	Extracellular matrix
FDM	Fused deposition modelling
FEA	Finite element analysis
FP	Flow point
FTIR	Fourier-transform infrared spectroscopy
G'	Storage modulus
G"	Loss modulus
GLP	Good laboratory practices
GMM	Gaussian mixture model
H	Hydrothermal
HA	Hydroxyapatite
HC	Honeycomb printing pattern
HPMC	Hydroxypropyl methylcellulose
ICSD	Inorganic crystal structure database
IM	Administered intramuscularly
IV	Administered intravenous
LDH	Lactate dehydrogenase
LPL	Linearly polarised light
LVR	Linear viscoelastic region
MIP	Mercury intrusion porosimetry
MPC	Magnesium phosphate cement
M-PER	Mammalian protein extraction reagent
MS	Material surface
MSC's	Mesenchymal stem cells
MV	Material volume
NC	Non-cylindrical
O	Orthogonal printing pattern
OR	Orthogonal rotated printing pattern
PBS	Phosphate-buffered saline
PCL	Polycaprolactone
PCR	Perimeter concavity ratio
PEEK	Polyether ether ketone
PEG	Polyethylene glycol
PEN	Polyethylene naphthalate
PLGA	Poly(lactic-co-glycolic acid)
PLLA	Poly(L-lactic acid)
PMMA	Poly(methyl methacrylate)
PRP	Platelet-rich plasma
PVA	Polyvinyl alcohol
qPCR	Real-time polymerase chain reaction
rMSC	Rat mesenchymal stem cells
SCP	Surface concavity percentage
SEM	Scanning electron microscopy
SG	Synthetic graft
SLA	Stereolithography
SLS	Selective laser sintering
SM	Subtractive manufacturing
SOP	Standard operating procedure
SSA	Specific surface area
STL	Standard triangle language
SVF	Solid volume fraction
TGA	Thermogravimetric analysis

TGG Templated grain growth

UCS Ultimate compressive strength

UV Ultraviolet

VOI Volume of interest

WI Work instruction

XG Xenogenic graft

XRD X-ray diffraction

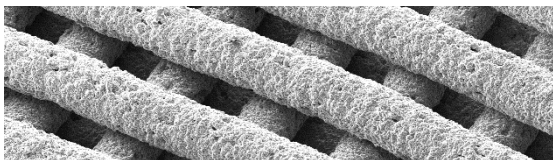

Chapter 1

Introduction

INTRODUCTION

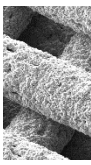

Bone is a complex organ with both mechanical and metabolic functions. After blood, bone is the second most transplanted tissue [1] with more than 500,000 grafting procedures taking place annually only in the US [2]. Moreover, this number has growing perspectives with the global ageing of the world's population and the consequent increasing number of age-associated pathologies such as osteoporosis [3,4]. The global bone grafts and substitutes market represented approximately 2.7 M$ by 2018 and it is previewed to generate 4.2 M$ by 2026 [5]. All these data evidence the academic and commercial interest in investigating and developing improved bone regeneration solutions.

The following sections show an overview of the main characteristics of bone focusing on its function, composition, structure and remodelling process. Subsequently, the different scenarios where bone regeneration is required are presented. Finally, the current strategies for bone regeneration are exposed focusing on the patient-specific bone grafts and the implications that this novel approach represents.

1.1 Bone Tissue

1.1.1 Function

Bone is a complex and dynamic organ whose functions are simultaneously biomechanical and metabolic. The biomechanical function includes the ensemble of bones that make up the skeleton serving as the structural support of the body [6]. Bones have the ability to change their shape and size to adapt their performance to varying mechanical stimuli. Furthermore, bones serve as protection for the internal organs and give mobility to the body together with the muscles and ligaments [7]. Moving on to the metabolic function, bone is responsible for detoxifying the heavy metals by collecting and cumulating them as well as maintaining the balance of calcium and phosphate ions in the body. This second action is realised by liberating calcium or phosphate ions from its mineral structure [8]. Additionally, bone has a hematopoietic function.

1.1.2 Composition

Bone is a composite material formed by a combination of an extracellular matrix (ECM), cells, and water. The ECM is composed by an organic phase and an inorganic phase. The inorganic phase constitutes the 70 wt.% and is composed of low-crystallinity calcium-deficient hydroxyapatite (CDHA) with numerous ionic substitutions (*e.g.* carbonate, sodium, magnesium, fluoride or citrate) [9]. The organic phase, usually referred to as osteoid, represents the remaining 30 wt.% and is composed of collagen, proteoglycans, glycoproteins, phospholipids and phosphoproteins. Whilst the inorganic phase provides the stiffness and strength, the organic phase is responsible for the flexibility and fracture toughness of the tissue [10].

1.1.3 Structure

The human skeleton is composed of 213 bones which can be classified into four families: long bones (*e.g.* femur, tibia, fibula, humerus, radius, and ulna), short bones

(*e.g.* metacarpals and phalanges), flat bones (*e.g.* parietal, scapula, ribs, sternum, and hips) and irregular bones (*e.g.* maxilla, mandible, and vertebrae).

Regardless of the bone family, a similar structure is found in all the bones. The external tissue is composed of a dense region known as compact or cortical bone which surrounds a marrow cavity containing a less dense bone structure named spongy, trabecular, or cancellous bone [8]. The proportions of these two regions vary depending on the bone family and function.

The cortical bone represents 80% of the total bone mass of an adult skeleton. This tissue presents a highly hierarchical structure and is responsible for providing mechanical properties. Cortical bone is highly compact with only 5 to 10% of porosity consisting of Haversian canals, Volkmann´s canals and resorption cavities [10].

Trabecular bone represents only the remaining 20% of the bone mass of the skeleton. This tissue presents a large porosity ranging from 75 to 95% [8]. Trabecular bone has the function to confine the bone marrow within a microporous trabeculae structure consisting of interconnected plates and rods with a thickness of around 200 μm.

The combination of an external compact tissue and an internal spongy tissue constitutes a composite sandwich structure that offers an optimised relation of mechanical properties in regard to the amount of material involved. This structure provides high resistance to compressive stresses and a considerable deformation before failure [8].

The bone tissue is structured in a hierarchical arrangement presenting seven successive levels [11]. At the basic level, we find the ECM, cells and water. The ECM is composed of plate-like apatite crystals located within the discrete spaces of the collagen fibrils. These crystals are oriented with the crystallographic c-axis aligned to the collagen fibres [12] and contain impurities of carbonate, HPO_4, Na, Mg, citrate and K. The collagen fibrils consist in mineralised aggrupation of collagen fibres distributed in orthogonal arrays. The aggrupation of fibrils form planar arrangements called lamellae which range from 3 to 7 μm in thickness [13]. Lamellae tend to arrange in different ways depending on the region of the bone with three possible tissue arrangements: (1) a compact and mature layered arrangement usually found in cortical bone. In this tissue, lamellae are distributed concentrically forming osteons: structures of 200-250 μm in diameter, perpendicular to the bone surface, surrounding a central Haversian canal [14]. These canals contain blood vessels and are interconnected through the Volkmann's canals (perpendicular to the Haversian canals) forming an elaborated system (*i.e.* Haversian system) responsible for the vascularisation of the tissue. (2) immature compact structures formed around a framework of collagen fibres with a more anisotropic distribution, which are found in woven bone. This tissue is eventually replaced by lamellar bone during the remodelling process creating osteon arrangements. (3) an interconnected framework of trabeculae, composed of concentrically oriented lamellae positioned along the lines of stress of the bone, typical of the cancellous bone. The diameter of the trabecular rods varies from 50 to 300 μm. Furthermore, the bone tissue structure is classified into cortical and trabecular regions and presents a last level of structure according to its external geometry.

1.1.4 Biology

Bone contains four main types of cells: osteoprogenitor cells, osteoblasts, osteocytes and osteoclasts. All of them play an important role in the bone remodelling process, where the tissue is progressively renewed by local resorption and regeneration.

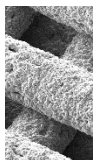

Osteoprogenitor cells are undifferentiated mesenchymal stem cells (MSCs) with the capacity to differentiate into osteoblasts, chondroblasts, fibroblasts or bone marrow stem cells depending on the bodily demands. These cells have the potential to persist in postnatal life as bone-lining cells and reactivate in adults to regenerate bone fractures. These cells are located in the periosteum, in the endosteum lining marrow cavities, and in the Haversian and Volkmann's canals.

Osteoblasts are large cells derived from osteoprogenitor cells, located along the bone surface. They represent 4 to 6% of the total resident bone cells. Their function is the synthesis and mineralisation of the ECM during the initial bone formation (growth) as well as during the later adult bone remodelling [15]. Osteoblasts are responsible for the production of the alkaline phosphatase and collagenase enzymes, growth factors, hormones such as osteocalcin and the collagenic part of the organic unmineralised phase of the bone known as osteoid. The synthesis of the bone matrix occurs in two main steps: First the deposition of an organic matrix consisting in the secretion of collagen type I proteins and then its subsequent mineralisation. When osteoblasts become trapped in their own bone matrix they become osteocytes [16].

Osteocytes are the most abundant cells in the bone, comprising between a 90 and a 95% of the total bone cells and the most long-lasting bone cells with a lifespan of up to 25 years [17]. Osteocytes are located within small chambers named lacunae, confined by a mineralised bone matrix. These cells derive from osteoblasts that become trapped surrounded by the substances secreted by themselves during the osteogenesis process. Although the osteocyte cell body is located inside the lacunae, more than 50 cytoplasmic processes per cell extend away from the lacunae through small tunnels named canaliculi. Osteocytes can exchange nutrients and waste products to maintain their viability. In addition, these canaliculi connect the cell with its neighbour osteocytes, creating a network known as osteocyte lacunocanalicular system [18]. The function of osteocytes in the bone tissue is to act as mechanosensors, guiding the osteoblasts and osteoclasts activity. From this, bone is remodelled according to the mechanical pressures and loads applied to each region, adapting its size and shape to the experienced mechanical stresses [19,20]. This phenomenon is called mechanotransduction. Moreover, osteocytes may have a role in the release of calcium ions when the calcium level of the body is too low.

Osteoclasts are large multinucleated cells, which originate from mononuclear cells in the hematopoietic stem cell lineage. They are responsible for the dissolution and absorption of bone either as a stage of the constant remodelling process that bone experiences, or motivated by a need of ion release to the body. During their resorptive activity, osteoclasts create small depressions on the bone's surface, called Howship lacunae. Osteoclasts tend to have between 5 and 20 nuclei, although there have been reported osteoclasts with as many as 200 nuclei. The mechanism to resorb bone is a multistep process: First, osteoclasts attach to the bone surface by polarising their membrane, forming what is known as ruffled membrane and creating a sealed active region. After, osteoclasts secrete a number of enzymes (*e.g.* acid phosphatase) and ions to acidify the active region (pH $\approx$ 4.5) and locally dissolve both the organic collagen and the inorganic calcium and phosphorus of bone. This process results in

the breaking of small fragments of mineralised bone which the osteoclast engulfs and digests within the cytoplasmic vacuoles. The product of this dissolution is calcium and phosphorous ions that are liberated to the blood flow [21].

Bone tissue is continuously forming and modifying during our lives. At an early stage, during childhood, these two processes allow the bone to grow and change in shape. Later, during adulthood, the skeleton is constantly renewed through a remodelling process. All the periods require a simultaneous and coordinated occurrence of both resorption and bone formation to be effective [8].

1.2 Bone Defects

Bone defects can have multiple origins, including fractures caused by traumatic accidents or metabolic disorders such as osteoporosis [22], morphological alterations such as osteotomies performed to remove bone tumours [23], bone resorption caused by a deficient mechanical stimulation (frequent in dental medicine after tooth extraction being alveolar ridge [24] and maxillary sinus floor [25] resorption two of the most common situations) or congenital diseases like cleft lip and cleft palate [26]. Additionally, bone defects can also be a consequence of a surgical procedure such as craniotomies performed to access the brain or the harvesting of the patients' bone to use it as autologous graft on another body region.

If the defect compromises the biomechanical functions of the bone, external stability must be provided. In the simplest cases, it is sufficient with guaranteeing an immobilisation of the region with an external cast or brace. However, in more complex situations a fixation of the bone fragments is required. Either external fixation devices or osteosynthesis plates (*i.e.* internal) can be used for this purpose [27].

Generally, bone has the capacity of self-regenerating the injuries suffered. Nonetheless, in some cases, when the defect exceeds a critical size, bone is not capable of regenerating spontaneously [28]. In these cases, there is a need for external help to achieve the desired regeneration and bone grafts are usually a crucial element in this process.

Bone regeneration is a healthcare relevant issue. In this PhD thesis bone grafting solutions will be developed and new approaches to improve bone regeneration will be studied.

1.3 Bone Grafts

Bone grafting is a surgical procedure to achieve a replacement or augmentation of bone in a defect. Bone grafts accelerate the bone formation process by enabling a volume regeneration instead of the layer-by-layer process occurring in the natural process of bone regeneration.

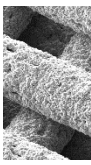

1.3.1 Performance

The following four properties are pursued in a bone substitute: osteoconduction, osteogenicity, osteoinduction and structural integrity [29]. Osteoconduction refers to the capacity of the graft to guide the bone ingrowth. Osteogenicity consists in the potential of the substitute to generate bone inside the grafted defect. Osteoinduction is described as the capacity of the bone substitute to induce new bone formation. Finally, structural integrity is related to the mechanical performance of the grafts, which can range from inconsistent incohesive structures (*e.g.* granulated bone substitutes), through grafts which maintain the post-operatory shape, to bone substitutes with load-bearing capabilities.

1.3.2 Porosity

The porosity in a bone graft is a key feature for achieving the desired performance. For the optimal behaviour of the bone graft, the porosity needs to be interconnected, cover a wide range of sizes and present some degree of concavity.

Firstly, interconnectivity is an essential feature that porosity must have to guarantee that the blood vessels can reach the whole graft volume [30,31]. Vascularisation is required to supply oxygen and nutrients, remove the metabolic waste, and provide easy access to cells and proteins [32]. Secondly, porosity must cover different size ranges, which can be understood as a combination of macroporosity (*i.e.* porosity in the macroscopic range, usually ranging from 100 to 300 μm) and nano-microporosity (*i.e.* porosity in the nano- and microscopic range), plays a double role: Whilst macroporosity guarantees tissue ingrowth, nano-microporosity (which is directly related to the structure's specific surface area) promotes the interaction of the bone graft with the host tissue [33] as well as protein adsorption and oxygen diffusion. The latter is essential for cell proliferation [30]. Finally, the shape of the pores is also an attribute that conditions the bone formation process. A conveniently designed pore structure can promote concave microenvironments which, in turn, will accelerate the bone formation process and, in the adequate configuration, will even be capable of inducing bone formation [34,35].

The present PhD thesis will study strategies to meet all the porosity requirements in a bone graft at once.

1.3.3 Origin

Different approaches have been used during the last decades to regenerate bone defects. Depending on the origin, bone grafts can be classified in autografts, allografts, xenografts and synthetic grafts.

Autografts are fragments of the patient's own bone [36]. They are considered the gold standard in bone regeneration as they are composed of living bone tissue of the same patient and, therefore, are fully biocompatible and bioactive [37]. However, this technique presents two main drawbacks: Firstly, the additional surgery required to retrieve the tissue, which involves a potential risk, adds morbidity for the patient and

prolongs the surgical times. In second place its limited availability. Hence, other strategies have been developed.

Allografts are bone fragments obtained from a generically unrelated donor of the same species. The most usual process entails the extraction of trabecular bone from cadaveric donors followed by multiple treatments that vary depending on the manufacturer (*e.g.* washing, sanitising, demineralising and sterilising processes). The performance of the final graft is highly influenced by these treatments [38]. Allografts provide a proper architecture for bone cells to regenerate as the porosity of the graft's trabeculae allow the bone to grow inside the cavities. Nevertheless, unlike autografts, they are neither osteoinductive nor osteogenic and although low, there is always a risk of transmission of diseases from the donor.

Based on the same principle as allografts, xenografts are derived from a donor of different animal species. Bovine is the most extended origin. However, porcine and equine species are also used [39]. These materials are denaturalised with either a chemical treatment or a high-temperature treatment to prevent the risk of rejection or cross-contamination with viral proteins, thus resulting in a material with a similar structure to the natural bone but without osteoinductive or osteogenic properties.

Both xenografts and allografts avoid the additional surgery required for autografts. Nonetheless, they may present a longer regeneration time as none of them offers osteogenic nor osteoinductive properties. In addition, besides the low but not negligible risk of disease transmission and immune response, its origin may rise ethical or cultural objections [39,40].

Synthetic grafts stand out as an alternative solution to bone harvesting. This approach consists in elaborating bone substitutes from the ground up based biocompatible raw materials. Although other synthetic materials such as bioactive glass, calcium silicates or magnesium phosphates have been used as bone grafts, calcium phosphates are the most studied compounds [41]. This is probably due to their similarity to the mineral phase found in the natural bone and the proper biological performance that they exhibit [42]. Moreover, these ceramics can be bioactive, osteointegrative, osteoconductive, resorbable and even osteoinductive depending on the specific compound, phase, and the conformation processes [43,44].

In this PhD thesis, synthetic bone grafts will be studied, harnessing the promising innovation possibilities that this solution offers.

1.3.4 Forms of presentation

Diverse grafting systems have been developed in order to cover different surgical needs. Grafts can be presented with multiple shapes to meet the desired specifications. The main ones are granules, putties, injectables, sponges and plugs, standard blocks, and personalised grafts.

Granules are the most extended bone graft presentation in the market. They are in particles ranging between 0.2 and 4 mm in diameter that are usually mixed with either saline solution, patients' blood or patients' PRP. This creates a mixture with higher consistency and cohesion that is then grafted in the defect with a spoon or spatula.

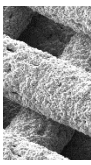

This technique is very extended in the dental field and is very effective in closed defects such as three- and four-wall bony defects. However, they lack structural integrity and this represents a considerable limitation in non-confined or large defects.

Putties and cements are mouldable products. They usually consist of a two-compound combination, and the cements are able to harden a few minutes after being mixed. They are designed to be mixed by the surgeon and placed instantaneously into the defect [45], and therefore have the advantages of perfectly fitting the defect and being structurally stable. They are osteoconductive and have osteointegrative properties [46]. However, they lack microporosity, which prevents vascularisation and bone tissue colonisation.

The injectable products are designed for minimally invasive applications. These are applications where no extra surgical procedures apart from bone grafting are required where, the surgeon only needs to perform a small incision in the soft tissue and inject the bone graft. Vertebroplasty and kyphoplasty are two typical examples [47,48]. Different formulations can be injected. Some of them consist of a mixture of bone graft particles similar to the granules and a hydrogel that acts as binder phase guaranteeing the injectability. Nonetheless, they lack structural integrity. Other injectables harden after being injected, achieving structural integrity but lacking the macroporosity required to allow bone colonisation throughout the material. Finally, some other products overcome this limitation by introducing an interconnected pore network through a foaming emulsion or leaching of sacrificial material.

Sponges and plugs are soft and malleable materials, designed to be press-fitted in confined bone defects. They are popular in the dental field commonly used for socket preservation [49] and in the orthopaedic field usually employed in lumbar spine fusions [50]. Sponges and plugs usually consist of a matrix of collagen loaded with ceramic particles (usually hydroxyapatite [50]). These materials can be impregnated with biologically active substances such as heparinised bone marrow or BMP-2. Its application is limited to confined defects due to their soft consistency.

Standard blocks are conceived for the regeneration of medium to large bone defects. These are structurally stable grafts with geometrically standard shapes (*e.g.* rectangular blocks and wedges) designed to be hand shaped and adapted to the defect's geometry by the clinician during the surgery. Whilst they allow to graft non-confined defects and perform vertical bone augmentations, the hand shaping process results in an inaccurate fit and a prolongation of the surgery's duration which entails an increase of the surgical morbidity and the operation cost. Additionally, the results are highly conditioned by the skills of the surgeon to shape the blocks.

Finally, with the democratisation of CAD/CAM technologies in the recent years, personalised bone grafts have emerged as a reality. This approach allows fabricating bone grafts with structural integrity that perfectly fit the defect's anatomy. The solution meets all the advantages of the standard blocks, and it moreover brings greater precision and speed to the surgical procedure.

Granules are the most popular bone graft presentation forms in the dental industry and represent a very polyvalent solution. Nonetheless, personalised bone grafts are the future of medicine especially in geometrically complex defects as each patient is anatomically different. In the present PhD both strategies will be studied.

1.4 Calcium Phosphates

1.4.1 Composition

Calcium phosphates are commonly used as synthetic bone substitutes due to their optimal performance in bone regeneration applications since they can present bioactivity [51], resorbability [52], osteoconductivity [53], and even osteoinductivity [44].

Specifically, calcium orthophosphates (CaPs) are salts of orthophosphoric acid composed of calcium and phosphate ions. Within the calcium orthophosphates family, there are eleven different compounds that can be synthesised through different routes by adjusting the calcium to phosphate (Ca/P) ionic ratio. The molar Ca/P ratio of these compounds ranges from 0.5 to 2; the compounds with lower Ca/P molar ratio are more acidic and water-soluble [7]. The less soluble a CaP is, the more stable the phase is and its resorption kinetics are slower. It should be noted that all the compounds with pH stability below 7.4 will degrade in physiological conditions.

Table 1.1. Calcium orthophosphates and their main properties. Adapted from [7].

Ca/P ionic ratio	Compound	Acronym	Chemical formula	Solubility* [g/L]	pH stability range*
0.50	Monocalcium phosphate monohydrate	MCPM	$Ca(H_2PO_4)_2 \cdot 2H_2O$	~18	0.0 – 2.0
0.50	Monocalcium phosphate anhydrous	MCPA	$Ca(H_2PO_4)_2$	~17	[c]
1.00	Dicalcium phosphate dehydrate (brushite)	DCPD	$CaHPO_4 \cdot 2H_2O$	~0.088	2.0 – 6.0
1.00	Dicalcium phosphate anhydrous (monetite)	DCPA	$CaHPO_4$	~0.048	[c]
1.33	Octacalcium phosphate	OCP	$Ca_8(HPO_4)_2 (PO_4)_4 \cdot 5H_2O$	~0.0081	5.5 – 7.0
1.50	α-Tricalcium phosphate	α-TCP	$\alpha\text{-}Ca_3(PO_4)_2$	~0.0025	[a]
1.50	β-Tricalcium phosphate	β-TCP	$\beta\text{-}Ca_3(PO_4)_2$	~0.0005	[a]
1.20-2.20	Amorphous calcium phosphate	ACP	$Ca_XH_Y(PO_4)_Z \cdot nH_2O$ n=3-4.5	[b]	~ 5 - 12[d]
1.50-1.67	Calcium-deficient hydroxyapatite	CDHA	$Ca_{10-X}(HPO_4)_X (PO_4)_{6-X}(OH)_{2-X}$	~0.0094	6.5 – 9.5
1.67	Hydroxyapatite	HA	$Ca_{10}(PO_4)_6(OH)_2$	~0.0003	9.5 - 12
2.00	Tetracalcium phosphate	TTCP	$Ca_4(PO_4)_2O$	~0.0007	[a]

* in aqueous solution at 25 ºC.

[a] These compounds cannot be precipitated from aqueous solutions.

[b] Cannot be measured precisely. However, the following values were found: 25.7 ± 0.1 (pH = 7.40), 29.9 ± 0.1 (pH = 6.00), 32.7 ± 0.1 (pH = 5.28).

[c] Stable at temperatures above 100 ºC.

[d] Always metastable.

1.4.2 Synthesis

Two main strategies exist for the synthesis of calcium orthophosphates: Solid-state reactions and precipitation processes.

Solid-state reactions take place at high temperature (*i.e.* >800 ºC). The calcium orthophosphates obtained with this processing technique are α-tricalcium phosphate (α-TCP), β-tricalcium phosphate (β-TCP), tetracalcium phosphate (TTCP) and stoichiometric hydroxyapatite (HA). Whilst α-TCP and TTCP are used as precursor materials for the synthesis of other calcium phosphates, β-TCP and HA are commonly used as final bone substitutes either individually or combined in biphasic calcium phosphates (BCP).

Some calcium orthophosphates can be obtained by precipitation routes in aqueous media and at low temperatures. The calcium orthophosphates that can be obtained through this route are monocalcium phosphate monohydrate (MCPM) and its anhydrous form (MCPA), dicalcium phosphate dihydrate (DCPD), dicalcium phosphate anhydrous (DCPA), octacalcium phosphate (OCP), amorphous calcium phosphate (ACP), calcium-deficient hydroxyapatite (CDHA) and stoichiometric hydroxyapatite (HA). Some of these low-temperature precipitation processes analogously occur in the natural bone mineralisation process.

1.4.3 Calcium Phosphate Cements

Calcium phosphate cements (CPCs) were first discovered by Legeros [54] and Chow [55] in the 1980s. They are based on the dissolution and precipitation reactions taking place in highly loaded hydraulic ceramic suspensions (*i.e.* ceramic pastes), which result in a progressive hardening of the paste to a solid body. These cements have found application in bone regeneration due some attractive properties, such as the ability to set in a physiological environment, the injectability compatible with minimally invasive applications and the similarity in composition and texture with the mineral phase of bone [56]. The mild setting reaction enables their combination with cells [57] and drugs [58]. Additionally, the nanostructure resulting from the cementitious reaction leads to high specific surface areas, enhancing bioactivity [59]. The physicochemical properties (*e.g.* microstructure, specific surface area, porosity, degradability) of CPSs can be tuned by controlling the processing parameters (*e.g.* powder size, liquid to powder ratio, liquid phase composition, and reaction environment and time).

CPCs are divided according to their final reaction products into apatitic and brushitic cements. Apatitic cements form hydroxyapatite as final product, which can be obtained either through the hydrolysis of α-TCP to CDHA or through an acid-base reaction, for instance, between TTCP and DCPD or DCP. In contrast, brushitic cements react to form brushite as the final compound. The setting mechanism consists in an acid-base reaction, for example, between β-TCP and MCPM or MCPA in aqueous solution.

Table 1.2. Different types of calcium phosphate cements and examples of starting reagents, reaction types and final compositions [58].

	Reactants	Reaction	Final product
Apatitic Cements	α-TCP + water	Hydrolysis	CDHA crystals
	TTCP + DCPD/DCPA + water	Acid-base	HA crystals
Brushitic Cements	β-TCP + MCPM/MCPA + water	Acid-base	Brushite crystals

The hardening mechanism in CPCs is based on a dissolution-precipitation process consisting of the dissolution of the reactants and the nucleation and crystal growth of a new phase [60]. During the process, the departure salts partially dissolve leading to a solution supersaturated in calcium and phosphate ions. Once the ionic concentration reaches a critical value, it nucleates into a new phase. The surface of the undissolved reactant particles acts as nucleation points. Afterwards, the new phase continues growing forming acicularly distributed crystals and the reagents continue their dissolution process. At some point, the crystals collide resulting in a mechanical interlocking cement that acts as the setting mechanism. **Fig. 1.1** describes the process for an α-TCP-based CPC reaction.

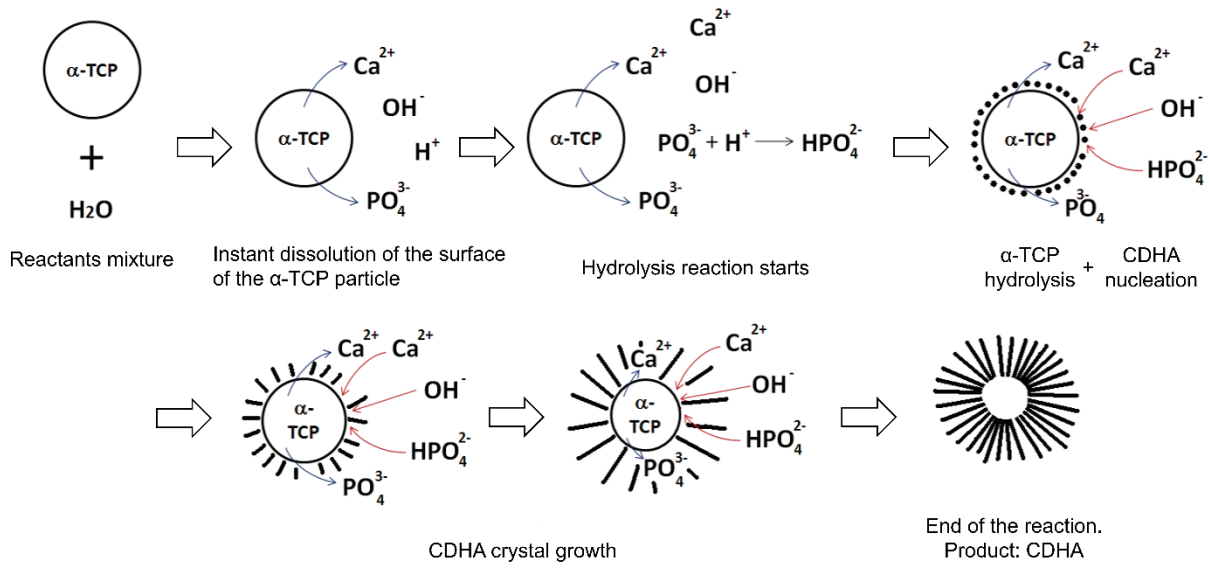

Fig. 1.1. Schema of the setting process of α-TCP-based calcium phosphate cements. Adapted from [61].

The cements setting mechanism has been denominated biomimetic as it is based on a dissolution and precipitation process from a supersaturated solution at body temperature, similarly to what happens *in vivo* during the mineralisation of the organic matrix secreted by osteoblasts during the natural bone formation process. In addition, the microstructure of CaP precipitated nanocrystals resemble the bone mineral phase morphology [62].

1.4.4 CDHA Cements

The CDHA obtained from apatitic cementitious reactions (**Equation 1.1**, [63]) is very similar in composition and structure to the mineral phase of natural bone as it is produced by a low-temperature precipitation process. Its microstructure consists of nanometric crystals which additionally present a low crystallinity and calcium vacancies (which in natural bone are substituted by doping ions). Unlike the acid-base reactions, the CDHA cementitious reaction departs from a single reagent which guarantees a stable non-stoichiometric Ca/P ratio of 1.5 [63,64].

$$3\alpha - Ca_3(PO_4)_2 + H_2O \rightarrow Ca_9(HPO_4)(PO_4)_5OH \qquad \textbf{Equation 1.1}$$

CDHA cements present a high intrinsic porosity in the nano- and micrometric range associated with the voids between precipitated crystals [59]. By controlling the processing conditions (*e.g.* L/P and reaction kinetics), the amount and size distribution of this porosity can be tailored. This porosity is crucial for the biological performance of the material as it entails a high surface interaction with the host tissue (*i.e.* specific surface area, SSA) allowing protein adsorption, cell adhesion and later bone tissue formation. Moreover, the nano/microporosity combined with the poor crystallinity enhance the tissue restorability. On the other hand, porosity is detrimental to the mechanical properties. Combining this with the weak nature of the consolidation process (consisting in a physical interlocking without a mechanical continuity in contrast to sintered ceramics) results in limited application of CPC bone substitutes to non-load-bearing applications.

However, CPCs lack intrinsic macroporosity. Bone grafts require a macroscopic interconnected porosity which guarantees the vascularisation needed to supply nutrients and oxygen to the colonising bone cells. To overcome this limitation, multiple strategies have been developed in recent years. The most popular ones are leaching or degradation of a second phase, foaming (either by using gas-forming chemical reactions or surface-active foaming agents), emulsions, freeze-drying, moulding and rapid prototyping [62]. An alternative to introducing porosity to the structure is the conformation of non-cohesive particles (granules) with interparticle interconnected macroporosity. This is a simple approach in the expense of sacrificing the structural integrity of the final graft.

In this PhD thesis we will focus on CDHA-based bone grafts with the aim of harnessing the benefits associated with its biomimetic character and seeking strategies to overcome the above-mentioned limitations.

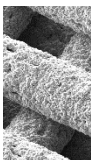

1.5 Patient-specific bone grafts

Computer-aided design and manufacturing (CAD/CAM) technologies open unprecedented possibilities for the new paradigm of personalised medicine. This new approach allows producing patient-specific grafts based on the 3D-medical images of the patient's bone defect [65-68]. However, personalised bone grafts are just one part of the puzzle. This technology involves a transformation of the whole surgery work-flow. Previous to the operation, the surgeons must perform a virtual surgery to establish the surgical approach using a 3D anatomic model based on computerised topographies (CT scans) of the patient. This allows studying each case in detail without the time constraints of the operating room. Hence, the decisions can be taken with more information, as the 3D reconstruction allows to observe all the relative positions of arteries, veins, soft tissues and surrounding bones. This strategic approach contributes to a higher precision of planning for the surgery. Then, the virtual design is translated to the real surgery with the CAM fabrication of custom-made elements: cutting guides, positioning guides, bone grafts, etc.

The usual manufacturing process of patient-specific bone grafts consists of the following stages [68,69]: First, the clinician acquires 3D scans of the patient. Then, the images are segmented to create a 3D anatomic model of the bone defect. Afterwards, the clinicians need to define the surgical inputs (*e.g.* surgical approach, volume to regenerate, if personalised cutting or positioning guides and osteosynthesis plates are also required, etc.). Subsequently, the graft is 3D modelled with CAD software based on the 3D anatomic model and the surgical inputs. Usually, the company commercialising the grafts performs the defect segmentation and graft design processes. The final graft design has to be approved by the clinician before moving on to the fabrication stage. Usually, the graft design and validation steps become an iterative process rather than a two-step linear procedure. After the clinician's validation, the graft is fabricated. This step can include multiple sub-processes. For instance, the elaboration of the graft, the quality control, the packaging and the sterilisation processes. In parallel to this step, the fabrication of the anatomic model, cutting guides, positioning guides and osteosynthesis plates is carried out, if required. Finally, the product is released, shipped to the clinician and implanted into the patient. The main steps of this process are schematised in **Fig. 1.2**.

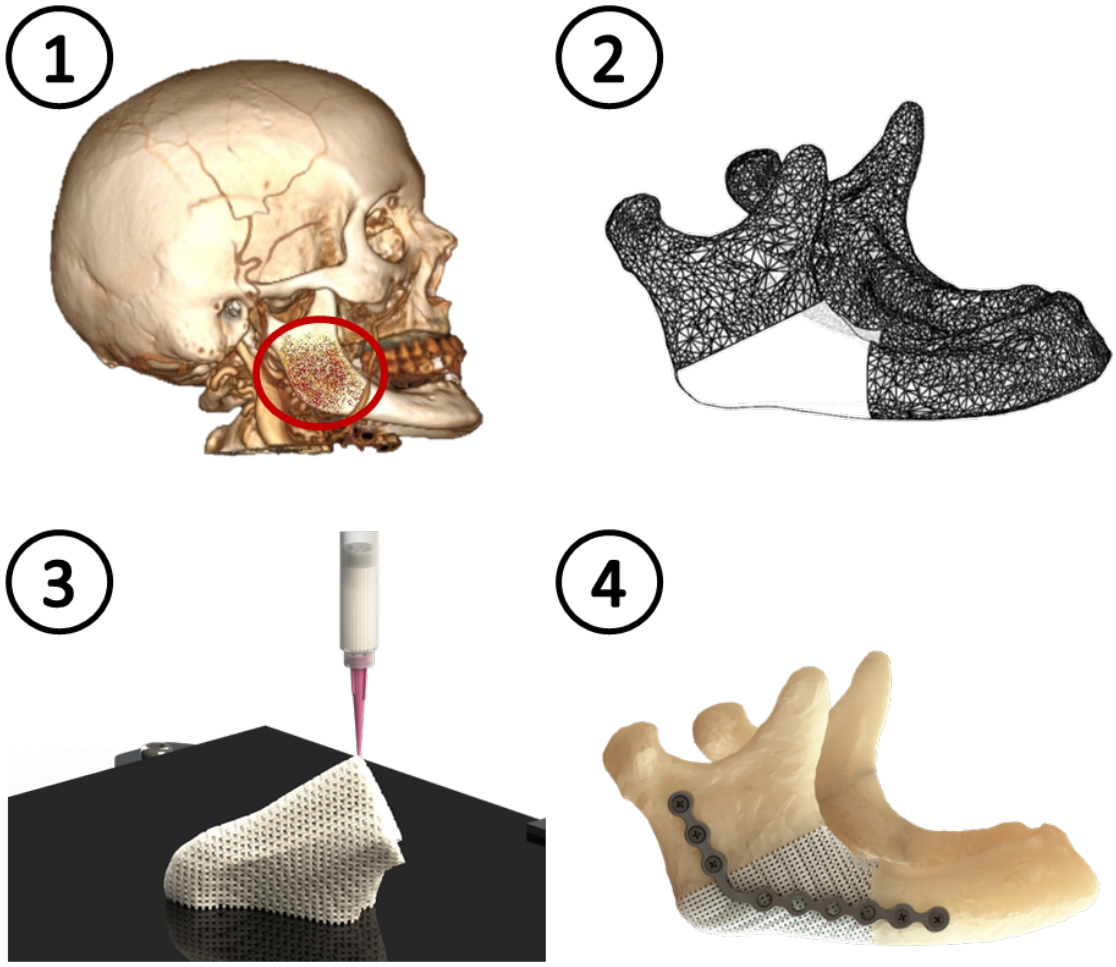

Fig. 1.2. Schematic representation of the patient-specific bone graft manufacturing process fork flow: **1** Anatomic model of the bone defect segmented from a CT scan, **2** Bone graft 3D modelling, **3** Bone graft computer-aided manufacturing (DIW in this example) and **4** Graft implantation.

Personalised bone grafts allow regenerating complex defects that require fine control of the geometry. Therefore, they are of special interest in maxillofacial applications where the aesthetics of the final result is crucial. Additionally, they are also relevant for large bone defects where the structural integrity of the graft is required, avoiding the use of autografts, which imply a second surgery (*e.g.* in the iliac crest, proximal tibia or fibula) and its associated morbidity.

Although being a promising technology, the implementation of personalised medical devices represents a considerable challenge. On one side, there is a lack of clear regulatory guidelines. On the other side, the flow of the industrial supply chain differs considerably from the traditional manufacturing processes. Since each product has to be specifically manufactured for a specific patient, mass production is not possible, nor is it possible to have a stock of final products. Moreover, such medical devices require a short lead time. Therefore, it is crucial to ensure a fast and agile manufacturing and distribution process. All these challenges represent a higher cost of the bone graft compared to standard approaches where the extra cost is only justified in applications which this technology represents a substantial improvement.

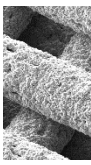

Regarding the computer-aided manufacturing (CAM) techniques that can be used to materialise a CAD design, there are two major strategies: subtractive manufacturing (SM) and additive manufacturing (AM). Subtractive manufacturing refers to all the controlled machining techniques based on the removal of material from an initial block (blank or workpiece) to achieve the desired geometry. Although there are other techniques grouped in this category, when one refers to SM, it is generally referring to computer numerical control (CNC) machining, which consists in guiding a cutting tool through a toolpath to generate the desired geometry. In this technology, blocks of allograft are commonly used as departure material [68]. In contrast to SM, additive manufacturing consists in adding successive layers of material to generate the desired geometry. Within this category, we find a multitude of approaches used for tissue engineering. These technologies depart from three classes of materials: Powders in selective laser sintering (SLS) [70-72] and binder jetting [73,74], liquids in stereolithography (SLA) [75,76] and material jetting [77], and pastes in direct ink writing (DIW) [78,79]. **Fig. 1.3** schematises the principle of each of the technologies. Whilst SM stands out for the freedom in the material choice but presents geometrical restrictions, AM techniques offer high geometrical freedom, even allowing fine control of the macropore structure. However, AM technology is restricted to specific materials. Moreover, the SM approach generates a considerable amount of waste material which represent an economical inconvenience as biomaterials are precious.

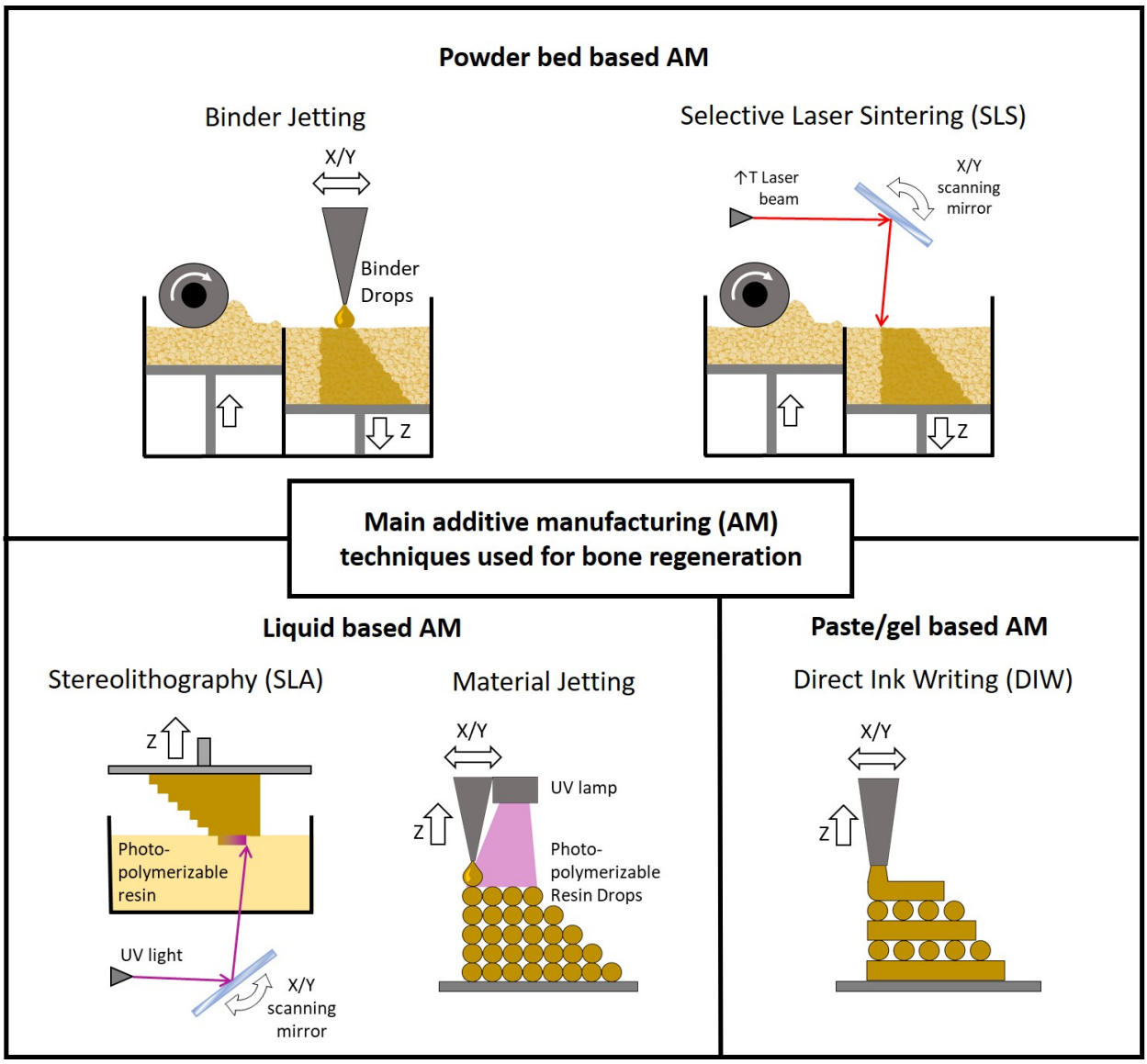

Fig. 1.3. Schematic representation of the most common additive manufacturing (AM) techniques used for the elaboration of bone substitutes classified by the principles in which are based.

Patient-specific bone grafts represent a cutting-edge technological advance in the paradigm of personalised medicine. The present PhD thesis will focus on studying the possibilities of the DIW additive manufacturing, with a view to transferring the optimal process to the market.

1.6 Direct Ink Writing

1.6.1. Technology

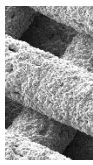

Direct ink writing is an additive manufacturing technique that employs a computer-controlled robot to position an ink deposition nozzle and generate three-dimensional objects with controlled architecture [80]. Within this fabrication technique, we distinguish two branches [81]: Droplet-based DIW, which relies on ink-jet printing of material in the form of droplets, and filamentary-based DIW consisting in the extrusion of an ink through a nozzle depositing a filamentary element. This second category includes multiple technologies such as robocasting, fused deposition fabrication and micro-pen writing.

Direct ink writing is a very versatile technique when it comes to composition, allowing the use of a multitude of materials. It represents one of the best options for the additive manufacturing of parts with high ceramic loads. Additionally, it is compatible with mild conformation processes. As a consequence, in the recent years, DIW has drawn an especial interest in tissue engineering applications for the 3D printing of bioinks (*i.e.* inks with living cells embedded) and inks with bioactive substances [82].

In contrast, this technique presents some inconveniences: Firstly, the design limitations on spanning, overhanging and floating geometries. A restriction which can be easily overcome by using sacrificial support material [83]. Another more limiting restriction of DIW is its resolution. In this technique, the resolution is directly conditioned by the nozzle diameter used. Although researchers have succeeded in printing with rod diameters as small as 500 nm, the lower limit of the nozzle diameter depends on the machine extrusion force and the viscosity of the ink [84]. Reducing the printing nozzle diameter represents an exponential increase of the processing time and the extrusion force required. For this reason, the common nozzle diameter where most applications find the balance of acceptable resolution and process requirements ranges between 500 and 50 μm. Therefore, the resolution achieved with this setup is far below the one obtained with other AM techniques.

1.6.2. Robocasting

This fabrication technique belongs to the DIW family and is based on the filamentary extrusion of ceramic suspensions, allowing to print dense ceramic-based inks. The design of the ink represents the most critical aspect of this technique. According to the literature [85], an adequate ink for robocasting requires a good homogeneity, a high enough ceramic charge to minimise shrinkage, a sufficiently low viscosity to be extruded and an adequate stiffness to guarantee the structural stability once deposited.

A common strategy for fulfilling the last two requirements at once is to develop inks with a shear-thinning (or pseudoplastic) rheological behaviour. This type of time-independent non-Newtonian behaviour guarantees a low viscosity upon the extrusion process. It is caused by the high shear forces of nozzle convergent flow, followed by a recovery of the initial ink viscosity as the ink is dispensed and the pressure drops [86]. Two main approaches exist to achieve such rheological behaviour: Colloidal suspensions and gel-embedded suspensions.

Colloidal suspensions consist of a slurry composed of a high ceramic load (typically 50-60 vol.%) combined with a liquid volatile solvent (commonly water) and a small

portion of organic additives (<1 vol.%). The ink guarantees the injectability through the use of a dispersant agent. Moreover, the use of an adequate liquid to powder ratio in the slurry confers to the ink a pseudoplastic behaviour (through interparticle interactions) that enables the extrusion process whilst guaranteeing structural integrity of the ink after deposition. This phenomenon is combined with the progressive partial drying of the layers to achieve a stable print [87]. Nevertheless, the inks obtained with this approach present reduced self-supporting capabilities, agglomerates that hinder the printing process with small nozzles and are no robust systems as the process success relies upon the evaporation rate of the ink, which is a parameter hard to control. More advanced setups additionally induce the coagulation of the slurry to promote a fluid-to-gel transition in the ink and overcome these limitations [81]. The most common coagulation methods consist on use coagulation agents (*e.g.* $Pb(NO_3)$ [88] and cellulose [85]) and the functionalisation of the particles' surface to tailor the interparticle interactions [89]. The main drawback of these solutions is that the fluid-to-gel transition is very sensitive to variations on the chemistry and pH of the environment turning it unstable and difficult to control.

Conversely, gel-embedded suspensions rely on a gel phase to achieve the desired rheological properties and disperse the particles instead of tuning the properties of the powder phase [90]. This results in more stable suspensions at expense of reducing the maximum powder fraction that the inks can handle. The gel used for this purpose must have a pseudoplastic rheological behaviour which is the most common behaviour of polymer melts and polymer solutions above a critical concentration [91]. Additionally, this gel requires a sufficient viscosity when sheared to guarantee the powder dispersion and prevent the phase separation upon the extrusion process [92,56]. Hydrogels are the most usual choice due to their easy manipulation, the low volatility of the water compared to other solvents and the possibility to use them in mild processes in biomedical applications, among them Pluronic® F127 [93], Tween 80 [94], gelatine [95], alginate [96], and polyvinyl alcohol (PVA) [97]. Although being less common, organogels (*i.e.* gels composed of a polymer dissolved in an organic solvent) are also explored in the literature [98][99]. Here the list of possibilities and combinations is endless. In general, solvents with low volatility are preferred and biopolymers are the most studied compounds (*e.g.* poly(L-lactic acid) (PLLA), poly(lactic-co-glycolic acid) PLGA, polyethylene glycol (PEG) and polycaprolactone (PCL)). As the approach used in gel-embedded suspensions is not based on the surface chemistry of the particles, the technique is potentially compatible with any material in the form of powder [90] as long as the powder presents the adequate properties.

Controlling the powder particle size, distribution and morphology is crucial for successfully developing an ink. Whilst a too small particle size (*i.e.* in the nano-scale range) will promote the interparticle interaction forces leading to undesirably high viscosities [100], an excessively large particle size will potentially clog the nozzle [101]. Even though the most frequent particle size distributions used in the literature are monomodal (probably because it is the simplest configuration), it has been demonstrated that by using a bimodal distribution the maximum packaging solid volume fraction (SVF_{max}) of the slurry can be increased. This improves the flowability of the ink and allows to increase its solid fraction. To achieve this effect, the small particles need to be sufficiently small to fill the interparticle gaps of the large particles without disrupting the packing structure. Moreover, the volume fraction of both populations need to be tailored to ensure that the amount of small particles is sufficient

but not excessive [92]. Finally, the particle size has also been reported to play a key role in the injectability of the paste with spherical particles presenting a better injectability than irregular ones [102].

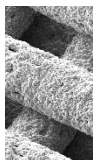

1.6.3. Consolidation Strategies

Once the ink has been deposited, the green printed parts need to undergo consolidation process to acquire the final mechanical properties. Although some strategies rely on the consolidation of the polymeric phase of the ink (usually by crosslinking [95,96], polymerisation [103] or solvent evaporation [99]), this section will be focused on the strategies to consolidate the ceramic phase of the ink. Two main strategies can be applied for hardening the printed ceramic structures obtained by DIW, namely sintering and cementitious reaction.

Sintering is the most traditional approach and consists in subjecting the green parts to a thermal treatment slightly below the melting temperature of the powder phase that promotes the interparticle solid-state atomic diffusion leading to a necking phenomenon and interparticle union [103]. As the diffusion process goes on, the interparticle necks grow, resulting in a reduction of the interparticle porosity with the consequent shrinkage, in a process known as densification [104]. In most cases, prior to the sintering treatment, the samples undergo a debinding step at a lower temperature that burns off the organic compounds found in the liquid phase [105]. The main drawback of the debinding and sintering processes is the shrinkage experienced as a consequence of the densification, which may lead to cracking and warping of the printed part. This phenomenon can be minimised by formulating inks with high solid loads, fine ceramic powders and minimal organic additives (always preserving the rheological properties) [105]. Another strategy consists in minimising the densification process to the detriment of the size of the sintering necks and final mechanical properties of the structure [106].

Cementitious reactions are reactions in which a powder phase and a liquid phase are combined leading to a hardening of the mixture known as setting process. They have been exploited for bone regeneration applications, for the design of injectables and putties [107]. The most popular formulations include calcium sulphate, calcium phosphate and magnesium phosphate cements. Calcium sulphate cements (also referred in the literature as Gypsum or plaster of Paris), with the first reported use to fill bone defects back in 1892 [108], are based on the hydrolysis reaction of $CaSO_4$ [109]. Calcium phosphate cements (CPCs) were discovered by LeGeros, Brown and Chow in 1982-1983 [42] and represented a revolution due to their similarity in composition to the natural bone and their bioactive properties [110]. More recently, magnesium phosphate cements (MPC) have been proposed for bone regeneration applications [111]. They involve the reaction between a magnesium oxide (MgO) and a phosphate salt [112,113]. These generally offer higher mechanical strengths than CPCs and fast degradation kinetics.

In recent years, some of these cement formulations have been adapted to the design of self-setting ceramic inks for DIW. Due to the similarity of requirements of the ink used in DIW with the injectable bone substitutes, the transfer results considerably straightforward. In the literature, we can find ink compositions consisting of magnesium phosphate cements [114], tricalcium silicate (Ca_3SiO_5) cements [115],

calcium sulphate hydrate cements ($CaSO_4 \cdot 0.5H_2O$) [116] and calcium phosphate cements [117,95] among others.

The inks based on cementitious reactions can be designed to be reactive or non-reactive. Whilst the reactive inks use a water based liquid phase (usually an hydrogel), the non-reactive inks use a non-aqueous liquid phase (*e.g.* oils and organogels). The first ones start reacting just after mixing (but can be further treated to finish the reaction after the printing process) [95,115,118], whereas the second ones start the cementitious reaction in a post-printing setting treatment [114,116,119,120] (usually by vapour saturation or immersion in a reactant solution). The non-reactive inks present the advantage of having a long shelf-life after being prepared, whilst reactive-inks need to be prepared just before printing or must be stored frozen to pause the setting reaction (*e.g.* at -80 ºC [121]). This makes non-reactive inks more suitable to be commercialised as ready to use end-product which can be distributed for research (*e.g.* Plotter-Paste-CPC, Innotere Biomaterials, Radebeul, Germany) or medical applications. In contrast, a drawback of the non-reactive inks is that the setting treatment process may be elapsed by the non-reactive binding agent which has to be progressively replaced by the reactive agent.

One of the advantages of the sintering consolidation strategy is that better mechanical properties of the final parts are achieved, due to the good densification and the continuity in the material through the interparticle bonding, reaching properties similar to the cortical bone [122] which cannot be achieved with the cementitious reactions due to the intrinsic porosity [123]. On the other hand, self-setting inks have the great advantage of exhibiting an extremely small shrinkage, which makes them very suitable for the fabrication of patient-specific bone grafts. Moreover, their mild processing is compatible with biomimetic approaches and makes them suitable for biological tethering (*e.g.* cell-laden inks, drug-releasing inks, functionalisation with proteins and peptides). This opens a wide range of perspectives and has raised a lot of interest in the scientific community in recent years [30].

In the present PhD thesis, we will work with self-setting calcium phosphate inks. Considering the importance of reducing the manufacturing time on patient-specific bone grafts, different consolidation strategies will be addressed to accelerate the fabrication process.

1.6.4. Self-setting α-TCP inks

Inks based on apatitic cementitious reactions stand out as one of the most promising for bone regeneration applications. This is probably due to the similarity in microstructure and composition of the resulting CDHA to the mineral phase of natural bone and their excellent biological performance. There are several ink formulations reported in the literature. For instance, introducing additional types of CaP in the ink's powder phase (*e.g.* HA particles acting as nucleating agents to accelerate the crystal precipitation reaction and calcium carbonate to enhance the bone regeneration process), using a wide range of binders (most of them based in hydrogel solutions), combining different solid fractions (ranging from ~60 to ~80 wt./wt.%) and applying a variety of setting treatments (based on bringing the printed parts in contact with the

setting medium through immersion or saturated atmospheres). **Table 1.3** summarises the main strategies found in the literature.

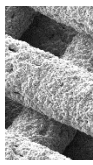

Table 1.3. Self-setting ink formulations based on α-TCP and hardening treatments reported in the literature.

Solid Phase [a]	Liquid/Gel Phase [b]	Solid Fraction	Reactive Ink	Setting Treatment [c]	Ref.
60 w% α-TCP, 26 w% DCPA, 10 w% $CaCO_3$, 4 w% pHA	Short-chain triglyceride (Miglyol 812), polysorbate 80 (Tween 80), phosphoric acid monohexadecyl ester (Amphisol A)	80 w/w %	No	Immersion in water, 37 ºC, 4 d	[119]
				Immersion in water, 37 ºC, 5 h	[117]
				Immersion in water, 37 ºC, 3 d	[94], [124]
				Set in a water-saturated atmosphere, 37 ºC, 3 d	[94]
				Set in a water-saturated atmosphere, 37 ºC, 15 min followed by immersion in cell culture medium up to 21 d	[125], [126]
				Wet steam autoclave sterilisation cycle (134 ºC, 3 abs. atm., 18 min)	[127]
α-TCP	Gelatine, water	61 w/v %	Yes	Immersion in EDC/NHS 2:1, 4 ºC, overnight (gelatine crosslinking) followed by immersion in water, R.T., 7 d (cement setting)	[95]
α-TCP	HPMC, ethanol	61- 65 w/w %	No	Immersion in PBS, 37 ºC, 0-24 h	[120]
α-TCP	Pluronic® F-127, water	61 w/w %	Yes	Immersion in water, 37 ºC, 10 d	[128]
α-TCP	Type-I collagen, TA (crosslinking), water	80 v/v %	Yes	Immersion in cell culture medium, 37 ºC, up to 14 d	[118]
α-TCP	-	-	-	-	[129], [130]
96 w% α-TCP, 4 w% nano-HA	P-CL-MA crosslinkable poloxamer derivate, PBS	70 w/w %	Yes	Immersion in TEMED solution in PBS, 37 ºC, 1 h	[131]
96 w% α-TCP, 4 w% nano-HA	P-CL-MA crosslinkable poloxamer derivate, PBS (APS supplemented)	60 w/v %	Yes	Set in a water-saturated atmosphere, 37 ºC, 3 d followed by immersion in TEMED aqueous solution, 37 ºC, 1 h	[132]
96 w% α-TCP, 4 w% nano-HA	Pluronic® F-127, PBS	60 w/v %	Yes	Set in a water-saturated atmosphere, 37 ºC, 3 d	[132]
α-TCP	Pluronic® F-127	67 w/w %	Yes	Set in a water-saturated atmosphere 100 ºC, 1 abs. atm., 10 min followed by immersion in water 121 ºC, 2 abs. atm., 30 min	[133], [134]
α-TCP	Glycerol, ammonium phosphate dibasic, polyoxyethylenesorbitan monooleate	60.5 w/w %	No	Immersion in cell culture medium, 37 ºC, up to 14 d	[135]

[a] α-TCP: α- tricalcium phosphate; DCPA: dicalcium phosphate anhydride; $CaCO_3$: calcium carbonate; pHA: precipitated hydroxyapatite; nano-HA: nano-hydroxyapatite particles; [b] HPMC: hydroxyl propyl methyl cellulose; TA: tannic acid; P-CL-MA: custom synthesised polymer consisting of a ε-caprolactone ester block and a methacrylate group onto both terminal hydroxyl groups of poloxamer 407; PBS: phosphate-buffered saline; APS: ammonium persulphate; [c] EDC: 1-ethyl-3-(3-dimethylaminopropyl; NHS: N-hydroxysuccinimide; R.T.: room temperature; TEMED: tetramethylethylenediamine.

1.5 References

[1] H. Shegarfi and O. Reikeras, “Review Article: Bone Transplantation and Immune Response” *J. Orthop. Surg.*, vol. 17, no. 2, pp. 206–211, Aug. 2009, doi: 10.1177/230949900901700218.

[2] “Healthcare Cost and Utilization Project (HCUP) | Agency for Health Research and Quality” https://www.ahrq.gov/data/hcup/index.html (accessed Nov. 25, 2020).

[3] T. Sözen, L. Özişik, N.Ç. Başaran, "An overview and management of osteoporosis. European journal of rheumatology", vol. 4, no. 1, pp. 46, 2017.

[4] L. J. Melton, E. J. Atkinson, M. K. O’Connor, W. M. O’Fallon, and B. L. Riggs, “Bone Density and Fracture Risk in Men” *J. Bone Miner. Res.*, vol. 13, no. 12, pp. 1915–1923, Dec. 1998, doi: 10.1359/jbmr.1998.13.12.1915.

[5] J. A. Kanis *et al.*, “Global Bone Grafts and Substitutes Market Will Reach USD 4,235 Million By 2026: Zion Market Research” *Zion Market Research*, Nov. 25, 2019.

[6] F. Bronner, M. C. Farach-Carson, and A. G. Mikos, *Engineering of functional skeletal tissues.* Springer-Verlag London Limited, 2007.

[7] S. Dorozhkin, “Calcium Orthophosphates in Nature, Biology and Medicine” *Materials*, vol. 2, no. 2, pp. 399–498, Apr. 2009, doi: 10.3390/ma2020399.

[8] J. S. Khurana, E. F. McCarthy, and P. J. Zhang, *Essentials in Bone and Soft-Tissue Pathology*. Boston, MA: Springer US, 2010.

[9] M. Vallet-Regí and J. Gonzalez-Calbet, “Calcium phosphates as substitution of bone tissues” *Prog. Solid State Chem.*, vol. 32, no. 1–2, pp. 1–31, 2004, doi: 10.1016/j.progsolidstchem.2004.07.001.

[10] X. Wang, J. S. Nyman, X. Dong, H. Leng, and M. Reyes, “Fundamental Biomechanics in Bone Tissue Engineering” *Synth. Lect. Tissue Eng.*, vol. 2, no. 1, pp. 1–225, Jan. 2010, doi: 10.2200/S00246ED1V01Y200912TIS004.

[11] J.-Y. Rho, L. Kuhn-Spearing, and P. Zioupos, “Mechanical properties and the hierarchical structure of bone” *Med. Eng. Phys.*, vol. 20, no. 2, pp. 92–102, Mar. 1998, doi: 10.1016/S1350-4533(98)00007-1.

[12] Kuhn-Spearing L, Rey C, Kim HM, Glimcher MJ, “Carbonated apatite nanocrystals of bone” in *Synthesis and Processing of Nanocrystalline Powder,* 1996, pp. 57–68.

[13] G. Marotti, “A new theory of bone lamellation” *Calcif. Tissue Int.*, vol. 53, no. S1, pp. S47–S56, Feb. 1993, doi: 10.1007/BF01673402.

[14] Bullough P., *Atlas of orthopaedic pathology*. Butterworth-Heinemann Ltd, 1985.

[15] M. Capulli, R. Paone, and N. Rucci, “Osteoblast and osteocyte: Games without frontiers” *Arch. Biochem. Biophys.*, vol. 561, no. May, pp. 3–12, Nov. 2014, doi: 10.1016/j.abb.2014.05.003.

[16] R. L. Jilka, R. S. Weinstein, T. Bellido, A. M. Parfitt, and S. C. Manolagas, “Osteoblast Programmed Cell Death (Apoptosis): Modulation by Growth Factors and Cytokines” *J. Bone Miner. Res.*, vol. 13, no. 5, pp. 793–802, May 1998, doi: 10.1359/jbmr.1998.13.5.793.

[17] T. A. Franz-Odendaal, B. K. Hall, and P. E. Witten, “Buried alive: How osteoblasts become osteocytes” *Dev. Dyn.*, vol. 235, no. 1, pp. 176–190, Jan. 2006, doi: 10.1002/dvdy.20603.

[18] S. C. Manolagas, “Choreography from the tomb: An emerging role of dying osteocytes in the purposeful, and perhaps not so purposeful, targeting of bone remodeling” *BoneKEy-Osteovision*, vol. 3, no. 1, pp. 5–14, Jan. 2006, doi: 10.1138/20060193.

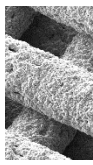

[19] L. F. Bonewald, “Osteocytes as Dynamic Multifunctional Cells” *Ann. N. Y. Acad. Sci.*, vol. 1116, no. 1, pp. 281–290, Nov. 2007, doi: 10.1196/annals.1402.018.

[20] S. L. Dallas, M. Prideaux, and L. F. Bonewald, “The Osteocyte: An Endocrine Cell … and More” *Endocr. Rev.*, vol. 34, no. 5, pp. 658–690, Oct. 2013, doi: 10.1210/er.2012-1026.

[21] R. Florencio-Silva, G. R. da S. Sasso, E. Sasso-Cerri, M. J. Simões, and P. S. Cerri, “Biology of Bone Tissue: Structure, Function, and Factors That Influence Bone Cells” *Biomed Res. Int.*, vol. 2015, pp. 1–17, 2015, doi: 10.1155/2015/421746.

[22] D. Dempster, R. Lindsay, Dempster, and Lindsay, “Pathogenesis of osteoporosis” *Lancet*, vol. 341, no. 8848, pp. 797–801, Mar. 1993, doi: 10.1016/0140-6736(93)90570-7.

[23] D. S. Geller and R. Gorlick, “Osteosarcoma: a review of diagnosis, management, and treatment strategies” *Clin. Adv. Hematol. Oncol.*, vol. 8, no. 10, pp. 705–18, Oct. 2010.

[24] J. Pietrokovski and M. Massler, “Alveolar ridge resorption following tooth extraction” *J. Prosthet. Dent.*, vol. 17, no. 1, pp. 21–27, Jan. 1967, doi: 10.1016/0022-3913(67)90046-7.

[25] P. K. Moy, S. Lundgren, and R. E. Holmes, “Maxillary sinus augmentation: Histomorphometric analysis of graft materials for maxillary sinus floor augmentation” *J. Oral Maxillofac. Surg.*, vol. 51, no. 8, pp. 857–862, Aug. 1993, doi: 10.1016/S0278-2391(10)80103-X.

[26] P. A. Mossey, J. Little, R. G. Munger, M. J. Dixon, and W. C. Shaw, “Cleft lip and palate” *Lancet*, vol. 374, no. 9703, pp. 1773–1785, Nov. 2009, doi: 10.1016/S0140-6736(09)60695-4.

[27] J. Sonderegger, K. R. Grob, and M. S. Kuster, “Dynamic plate osteosynthesis for fracture stabilization : how to do it” vol. 2, pp. 10–13, 2010, doi: 10.4081/or.2010.e4.

[28] Z. Gugala and S. Gogolewski, “Regeneration of Segmental Diaphyseal Defects in Sheep Tibiae Using Resorbable Polymeric Membranes: A Preliminary Study” *J. Orthop. Trauma*, vol. 13, no. 3, pp. 187–195, Mar. 1999, doi: 10.1097/00005131-199903000-00006.

[29] J. A. McAuliffe, “Bone graft substitutes” *J. Hand Ther.*, vol. 16, no. 2, pp. 180–187, Apr. 2003, doi: 10.1016/S0894-1130(03)80013-3.

[30] A. Kumar *et al.*, “Low temperature additive manufacturing of three dimensional scaffolds for bone-tissue engineering applications: Processing related challenges and property assessment” *Mater. Sci. Eng. R Reports*, vol. 103, pp. 1–39, May 2016, doi: 10.1016/j.mser.2016.01.001.

[31] V. P. Galván-Chacón and P. Habibovic, “Deconvoluting the Bioactivity of Calcium Phosphate-Based Bone Graft Substitutes: Strategies to Understand the Role of Individual Material Properties” *Adv. Healthc. Mater.*, vol. 6, no. 13, p. 1601478, Jul. 2017, doi: 10.1002/adhm.201601478.

[32] V. Karageorgiou and D. Kaplan, “Porosity of 3D biomaterial scaffolds and osteogenesis” *Biomaterials*, vol. 26, no. 27, pp. 5474–5491, Sep. 2005, doi: 10.1016/j.biomaterials.2005.02.002.

[33] O. Chan *et al.*, “The effects of microporosity on osteoinduction of calcium phosphate bone graft substitute biomaterials” *Acta Biomater.*, vol. 8, no. 7, pp. 2788–2794, Jul. 2012, doi: 10.1016/j.actbio.2012.03.038.

[34] P. Habibovic, H. Yuan, C. M. van der Valk, G. Meijer, C. a van Blitterswijk, and K. de Groot, “3D microenvironment as essential element for osteoinduction by biomaterials”

Biomaterials, vol. 26, no. 17, pp. 3565–3575, Jun. 2005, doi: 10.1016/j.biomaterials.2004.09.056.

[35] A. Barba *et al.*, “Osteoinduction by Foamed and 3D-Printed Calcium Phosphate Scaffolds: Effect of Nanostructure and Pore Architecture” *ACS Appl. Mater. Interfaces*, vol. 9, no. 48, pp. 41722–41736, Dec. 2017, doi: 10.1021/acsami.7b14175.

[36] A. M. Jakoi, J. A. Iorio, and P. J. Cahill, “Autologous bone graft harvesting: a review of grafts and surgical techniques” *Musculoskelet. Surg.*, vol. 99, no. 3, pp. 171–178, Dec. 2015, doi: 10.1007/s12306-015-0351-6.

[37] H. C. Pape, A. Evans, and P. Kobbe, “Autologous Bone Graft: Properties and Techniques” *J. Orthop. Trauma*, vol. 24, no. SUPPL. 1, pp. S36–S40, Mar. 2010, doi: 10.1097/BOT.0b013e3181cec4a1.

[38] T. Boyce, J. Edwards, and N. Scarborough, “Allograft bone. The influence of processing on safety and performance” *Orthop. Clin. North Am.*, vol. 30, no. 4, pp. 571–581, Oct. 1999, doi: 10.1016/S0030-5898(05)70110-3.

[39] H. J. Haugen, S. P. Lyngstadaas, F. Rossi, and G. Perale, “Bone grafts: which is the ideal biomaterial?” *J. Clin. Periodontol.*, vol. 46, no. 5, pp. 92–102, Jun. 2019, doi: 10.1111/jcpe.13058.

[40] C. J. Damien and J. R. Parsons, “Bone graft and bone graft substitutes: A review of current technology and applications” *J. Appl. Biomater.*, vol. 2, no. 3, pp. 187–208, 1991, doi: 10.1002/jab.770020307.

[41] W. R. Moore, S. E. Graves, and G. I. Bain, “Synthetic bone graft substitutes” *ANZ J. Surg.*, vol. 71, no. 6, pp. 354–361, Jun. 2001, doi: 10.1046/j.1440-1622.2001.02128.x.

[42] R. Z. Legeros, “Calcium Phosphate Materials in Restorative Dentistry: a Review” *Adv. Dent. Res.*, vol. 2, no. 1, pp. 164–180, Aug. 1988, doi: 10.1177/08959374880020011101.

[43] P. Habibovic and K. de Groot, “Osteoinductive biomaterials—properties and relevance in bone repair” *J. Tissue Eng. Regen. Med.*, vol. 1, no. 1, pp. 25–32, Jan. 2007, doi: 10.1002/term.5.

[44] H. Yuan *et al.*, “Osteoinductive ceramics as a synthetic alternative to autologous bone grafting” *Proc. Natl. Acad. Sci.*, vol. 107, no. 31, pp. 13614–13619, Aug. 2010, doi: 10.1073/pnas.1003600107.

[45] L. S. Pryor *et al.*, “Review of Bone Substitutes” *Craniomaxillofac. Trauma Reconstr.*, vol. 2, no. 3–4, pp. 151–160, Oct. 2009, doi: 10.1055/s-0029-1224777.

[46] J. E. Zins, A. Moreira-Gonzalez, A. Parikh, E. Arslan, T. Bauer, and M. Siemionow, “Biomechanical and Histologic Evaluation of the Norian Craniofacial Repair System and Norian Craniofacial Repair System Fast Set Putty in the Long-Term Reconstruction of Full-Thickness Skull Defects in a Sheep Model” *Plast. Reconstr. Surg.*, vol. 121, no. 5, pp. 271e-282e, May 2008, doi: 10.1097/PRS.0b013e31816a9fd1.

[47] L. C. Chow, “Next generation calcium phosphate-based biomaterials” *Dent. Mater. J.*, vol. 28, no. 1, pp. 1–10, Jan. 2009, doi: 10.4012/dmj.28.1.

[48] G. Lewis, “Injectable bone cements for use in vertebroplasty and kyphoplasty: State-of-the-art review” *J. Biomed. Mater. Res. - Part B Appl. Biomater.*, vol. 76, no. 2, pp. 456–468, 2006, doi: 10.1002/jbm.b.30398.

[49] G. Kotsakis, V. Chrepa, N. Marcou, H. Prasad, and J. Hinrichs, “Flapless Alveolar Ridge Preservation Utilizing the ‘Socket-Plug’ Technique: Clinical Technique and Review of the Literature” *J. Oral Implantol.*, vol. 40, no. 6, pp. 690–698, Dec. 2014, doi: 10.1563/AAID-JOI-D-12-00028.

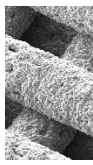

[50] C. Kraiwattanapong, S. D. Boden, J. Louis-Ugbo, E. Attallah, B. Barnes, and W. C. Hutton, “Comparison of Healos/Bone Marrow to INFUSE(rhBMP-2/ACS) With a Collagen-Ceramic Sponge Bulking Agent as Graft Substitutes for Lumbar Spine Fusion” *Spine*, vol. 30, no. 9, pp. 1001–1007, May 2005, doi: 10.1097/01.brs.0000160997.91502.3b.

[51] C. Rey, C. Combes, C. Drouet, and D. Grossin, “Bioactive Ceramics: Physical Chemistry” in *Comprehensive Biomaterials*, vol. 1, Elsevier, 2011, pp. 187–221.

[52] S. Yamada, “Osteoclastic resorption of calcium phosphate ceramics with different hydroxyapatite/β-tricalcium phosphate ratios” *Biomaterials*, vol. 18, no. 15, pp. 1037–1041, Aug. 1997, doi: 10.1016/S0142-9612(97)00036-7.

[53] N. Miño-Fariña *et al.*, “Quantitative analysis of the resorption and osteoconduction of a macroporous calcium phosphate bone cement for the repair of a critical size defect in the femoral condyle” *Vet. J.*, vol. 179, no. 2, pp. 264–272, Feb. 2009, doi: 10.1016/j.tvjl.2007.09.011.

[54] R. Z. LeGeros, A. Chohayeb, and A. Shulman, “Apatitic calcium phosphates: possible dental restorative materials” *J Dent Res*, vol. 61, p. 343, 1982.

[55] W. E. Brown and L. C. Chow, “A new calcium phosphate setting cement” *J Dent Res*, vol. 62, p. 672, 1983.

[56] Y. Maazouz, E. B. Montufar, J. Malbert, M. Espanol, and M.-P. Ginebra, “Self-hardening and thermoresponsive alpha tricalcium phosphate/pluronic pastes” *Acta Biomater.*, vol. 49, pp. 563–574, Feb. 2017, doi: 10.1016/j.actbio.2016.11.043.

[57] N. Raja and H. Yun, “A simultaneous 3D printing process for the fabrication of bioceramic and cell-laden hydrogel core/shell scaffolds with potential application in bone tissue regeneration” *J. Mater. Chem. B*, vol. 4, no. 27, pp. 4707–4716, 2016, doi: 10.1039/C6TB00849F.

[58] M.-P. Ginebra, C. Canal, M. Espanol, D. Pastorino, and E. B. Montufar, “Calcium phosphate cements as drug delivery materials” *Adv. Drug Deliv. Rev.*, vol. 64, no. 12, pp. 1090–1110, Sep. 2012, doi: 10.1016/j.addr.2012.01.008.

[59] M. Espanol, R. A. Perez, E. B. Montufar, C. Marichal, A. Sacco, and M. P. Ginebra, “Intrinsic porosity of calcium phosphate cements and its significance for drug delivery and tissue engineering applications” *Acta Biomater.*, vol. 5, no. 7, pp. 2752–2762, Sep. 2009, doi: 10.1016/j.actbio.2009.03.011.

[60] W.-C. Chen, J.-H. C. Lin, and C.-P. Ju, “Transmission electron microscopic study on setting mechanism of tetracalcium phosphate/dicalcium phosphate anhydrous-based calcium phosphate cement” *J. Biomed. Mater. Res.*, vol. 64A, no. 4, pp. 664–671, Mar. 2003, doi: 10.1002/jbm.a.10250.

[61] E. Montufar, “Espumas inyectables de hidroxiapatita obtenidas por el método de espumado de la fase líquida de un cemento de fosfato tricálcico alfa . Universidad Politécnica de Cataluña” UPC, 2010.

[62] M. P. Ginebra, M. Espanol, E. B. Montufar, R. A. Perez, and G. Mestres, “New processing approaches in calcium phosphate cements and their applications in regenerative medicine” *Acta Biomater.*, vol. 6, no. 8, pp. 2863–2873, Aug. 2010, doi: 10.1016/j.actbio.2010.01.036.

[63] M. P. Ginebra *et al.*, “Setting Reaction and Hardening of an Apatitic Calcium Phosphate Cement” *J. Dent. Res.*, vol. 76, no. 4, pp. 905–912, Apr. 1997, doi: 10.1177/00220345970760041201.

[64] M.-P. Ginebra, E. Fernández, F. C. M. Driessens, and J. A. Planell, “Modeling of the Hydrolysis of α-Tricalcium Phosphate” *J. Am. Ceram. Soc.*, vol. 82, no. 10, pp. 2808–

2812, Dec. 2004, doi: 10.1111/j.1151-2916.1999.tb02160.x.

[65] N. Ayoub *et al.*, “Evaluation of computer-assisted mandibular reconstruction with vascularized iliac crest bone graft compared to conventional surgery: a randomized prospective clinical trial” *Trials*, vol. 15, no. 1, p. 114, 2014, doi: 10.1186/1745-6215-15-114.

[66] M. Castilho *et al.*, “Application of a 3D printed customized implant for canine cruciate ligament treatment by tibial tuberosity advancement” *Biofabrication*, vol. 6, no. 2, p. 025005, Mar. 2014, doi: 10.1088/1758-5082/6/2/025005.

[67] H. Saijo *et al.*, “Maxillofacial reconstruction using custom-made artificial bones fabricated by inkjet printing technology” *J. Artif. Organs*, vol. 12, no. 3, pp. 200–205, Sep. 2009, doi: 10.1007/s10047-009-0462-7.

[68] J. C. Brune *et al.*, “CT lesion model-based structural allografts: Custom fabrication and clinical experience” *Transfus. Med. Hemotherapy*, vol. 39, no. 6, pp. 395–404, 2012, doi: 10.1159/000345269.

[69] S. Mok *et al.*, “From the printer: Potential of three-dimensional printing for orthopaedic applications” *J. Orthop. Transl.*, vol. 6, pp. 42–49, Jul. 2016, doi: 10.1016/j.jot.2016.04.003.

[70] F. E. Wiria, C. K. Chua, K. F. Leong, Z. Y. Quah, M. Chandrasekaran, and M. W. Lee, “Improved biocomposite development of poly(vinyl alcohol) and hydroxyapatite for tissue engineering scaffold fabrication using selective laser sintering” *J. Mater. Sci. Mater. Med.*, vol. 19, no. 3, pp. 989–996, Mar. 2008, doi: 10.1007/s10856-007-3176-5.

[71] S. Eosoly, D. Brabazon, S. Lohfeld, and L. Looney, “Selective laser sintering of hydroxyapatite/poly-ε-caprolactone scaffolds” *Acta Biomater.*, vol. 6, no. 7, pp. 2511–2517, Jul. 2010, doi: 10.1016/j.actbio.2009.07.018.

[72] Y. Xia *et al.*, “Selective laser sintering fabrication of nano-hydroxyapatite/poly-ε-caprolactone scaffolds for bone tissue engineering applications” *Int. J. Nanomedicine*, vol. 8, pp. 4197–213, Nov. 2013, doi: 10.2147/IJN.S50685.

[73] H. Seitz, W. Rieder, S. Irsen, B. Leukers, and C. Tille, “Three-dimensional printing of porous ceramic scaffolds for bone tissue engineering” *J. Biomed. Mater. Res. Part B Appl. Biomater.*, vol. 74B, no. 2, pp. 782–788, Aug. 2005, doi: 10.1002/jbm.b.30291.

[74] S. Tarafder, N. M. Davies, A. Bandyopadhyay, and S. Bose, “3D printed tricalcium phosphate bone tissue engineering scaffolds: effect of SrO and MgO doping on in vivo osteogenesis in a rat distal femoral defect model” *Biomater. Sci.*, vol. 1, no. 12, p. 1250, 2013, doi: 10.1039/c3bm60132c.

[75] J. W. Lee, K. S. Kang, S. H. Lee, J.-Y. Kim, B.-K. Lee, and D.-W. Cho, “Bone regeneration using a microstereolithography-produced customized poly(propylene fumarate)/diethyl fumarate photopolymer 3D scaffold incorporating BMP-2 loaded PLGA microspheres” *Biomaterials*, vol. 32, no. 3, pp. 744–752, Jan. 2011, doi: 10.1016/j.biomaterials.2010.09.035.

[76] R. Owen, C. Sherborne, T. Paterson, N. H. Green, G. C. Reilly, and F. Claeyssens, “Emulsion templated scaffolds with tunable mechanical properties for bone tissue engineering” *J. Mech. Behav. Biomed. Mater.*, vol. 54, pp. 159–172, Feb. 2016, doi: 10.1016/j.jmbbm.2015.09.019.

[77] J. H. Song, M. J. Edirisinghe, and J. R. G. Evans, “Formulation and Multilayer Jet Printing of Ceramic Inks” *J. Am. Ceram. Soc.*, vol. 82, no. 12, pp. 3374–3380, Dec. 2004, doi: 10.1111/j.1151-2916.1999.tb02253.x.

[78] X. Liu, M. N. Rahaman, G. E. Hilmas, and B. S. Bal, “Mechanical properties of

bioactive glass (13-93) scaffolds fabricated by robotic deposition for structural bone repair" *Acta Biomater.*, vol. 9, no. 6, pp. 7025–7034, Jun. 2013, doi: 10.1016/j.actbio.2013.02.026.

[79] P. Miranda, E. Saiz, K. Gryn, and A. P. Tomsia, "Sintering and robocasting of β-tricalcium phosphate scaffolds for orthopaedic applications" *Acta Biomater.*, vol. 2, no. 4, pp. 457–466, Jul. 2006, doi: 10.1016/j.actbio.2006.02.004.

[80] J. A. Lewis and G. M. Gratson, "Direct writing in three dimensions" *Mater. Today*, vol. 7, no. 7–8, pp. 32–39, Jul. 2004, doi: 10.1016/S1369-7021(04)00344-X.

[81] J. A. Lewis, J. E. Smay, J. Stuecker, and J. Cesarano, "Direct Ink Writing of Three-Dimensional Ceramic Structures" *J. Am. Ceram. Soc.*, vol. 89, no. 12, pp. 3599–3609, Dec. 2006, doi: 10.1111/j.1551-2916.2006.01382.x.

[82] M. Hospodiuk, M. Dey, D. Sosnoski, and I. T. Ozbolat, "The bioink: A comprehensive review on bioprintable materials" *Biotechnol. Adv.*, vol. 35, no. 2, pp. 217–239, Mar. 2017, doi: 10.1016/j.biotechadv.2016.12.006.

[83] E. Feilden, "Additive manufacturing of ceramics and ceramic composites via robocasting" Imperial College London, 2017.

[84] G. M. Gratson and J. A. Lewis, "Phase Behavior and Rheological Properties of Polyelectrolyte Inks for Direct-Write Assembly" *Langmuir*, vol. 21, no. 1, pp. 457–464, Jan. 2005, doi: 10.1021/la048228d.

[85] J. E. Smay, J. Cesarano, and J. a Lewis, "Colloidal Inks for Directed Assembly of 3-D Periodic Structures" *Langmuir*, vol. 18, no. 14, pp. 5429–5437, Jul. 2002, doi: 10.1021/la0257135.

[86] A. M'Barki, L. Bocquet, and A. Stevenson, "Linking Rheology and Printability for Dense and Strong Ceramics by Direct Ink Writing" *Sci. Rep.*, vol. 7, no. 1, p. 6017, Dec. 2017, doi: 10.1038/s41598-017-06115-0.

[87] J. Cesarano, "A Review of Robocasting Technology" *MRS Proc.*, vol. 542, p. 133, Feb. 1998, doi: 10.1557/PROC-542-133.

[88] B. A. Tuttle *et al.*, "Robocast Pb(Zr 0.95 Ti 0.05)O 3 Ceramic Monoliths and Composites" *J. Am. Ceram. Soc.*, vol. 84, no. 4, pp. 872–874, Apr. 2001, doi: 10.1111/j.1151-2916.2001.tb00756.x.

[89] Q. Li and J. A. Lewis, "Nanoparticle Inks for Directed Assembly of Three-Dimensional Periodic Structures" *Adv. Mater.*, vol. 15, no. 19, pp. 1639–1643, Oct. 2003, doi: 10.1002/adma.200305413.

[90] E. Munch, J. Franco, S. Deville, P. Hunger, E. Saiz, and A. P. Tomsia, "Porous ceramic scaffolds with complex architectures" *JOM*, vol. 60, no. 6, pp. 54–58, Jun. 2008, doi: 10.1007/s11837-008-0072-5.

[91] T. G. Mezger, *The Rheology Handbook*. Vincentz Network, 2012.

[92] R. O'Neill *et al.*, "Critical review: Injectability of calcium phosphate pastes and cements" *Acta Biomater.*, vol. 50, pp. 1–19, Mar. 2017, doi: 10.1016/j.actbio.2016.11.019.

[93] E. Feilden, E. G.-T. Blanca, F. Giuliani, E. Saiz, and L. Vandeperre, "Robocasting of structural ceramic parts with hydrogel inks" *J. Eur. Ceram. Soc.*, vol. 36, no. 10, pp. 2525–2533, Aug. 2016, doi: 10.1016/j.jeurceramsoc.2016.03.001.

[94] A. R. Akkineni, Y. Luo, M. Schumacher, B. Nies, A. Lode, and M. Gelinsky, "3D plotting of growth factor loaded calcium phosphate cement scaffolds" *Acta Biomater.*, vol. 27, pp. 264–274, Nov. 2015, doi: 10.1016/j.actbio.2015.08.036.

[95] Y. Maazouz *et al.*, "Robocasting of biomimetic hydroxyapatite scaffolds using self-

setting inks" *J. Mater. Chem. B*, vol. 2, no. 33, pp. 5378–5386, 2014, doi: 10.1039/C4TB00438H.

[96] Y. Luo, C. Wu, A. Lode, and M. Gelinsky, "Hierarchical mesoporous bioactive glass/alginate composite scaffolds fabricated by three-dimensional plotting for bone tissue engineering" *Biofabrication*, vol. 5, no. 1, p. 015005, Dec. 2012, doi: 10.1088/1758-5082/5/1/015005.

[97] C. Wu *et al.*, "3D-printing of highly uniform CaSiO3 ceramic scaffolds: preparation, characterization and in vivo osteogenesis" *J. Mater. Chem.*, vol. 22, no. 24, p. 12288, 2012, doi: 10.1039/c2jm30566f.

[98] B. Zhang, S. H. Chung, S. Barker, D. Craig, R. J. Narayan, and J. Huang, "Direct ink writing of polycaprolactone / polyethylene oxide based 3D constructs" *Prog. Nat. Sci. Mater. Int.*, Oct. 2020, doi: 10.1016/j.pnsc.2020.10.001.

[99] A. E. Jakus *et al.*, "Hyperelastic 'bone': A highly versatile, growth factor–free, osteoregenerative, scalable, and surgically friendly biomaterial" *Sci. Transl. Med.*, vol. 8, no. 358, pp. 358ra127, Sep. 2016, doi: 10.1126/scitranslmed.aaf7704.

[100] M. L. Fisher, M. Colic, M. P. Rao, and F. F. Lange, "Effect of Silica Nanoparticle Size on the Stability of Alumina/Silica Suspensions" *J. Am. Ceram. Soc.*, vol. 84, no. 4, pp. 713–718, Apr. 2001, doi: 10.1111/j.1151-2916.2001.tb00731.x.

[101] H. Barati, M. Wu, A. Kharicha, and A. Ludwig, "A transient model for nozzle clogging" *Powder Technol.*, vol. 329, pp. 181–198, Apr. 2018, doi: 10.1016/j.powtec.2018.01.053.

[102] I. Kunio, "Effects of Spherical Tetracalcium Phosphate on Injectability and Basic Properties of Apatitic Cement" *Key Eng. Mater.*, vol. 240–242, pp. 369–372, May 2003, doi: 10.4028/www.scientific.net/KEM.240-242.369.

[103] S.-J. L. Kang, *Sintering: Densification, Grain Growth and Microstructure*. Elsevier, 2005.

[104] F. Abdeljawad *et al.*, "Sintering processes in direct ink write additive manufacturing: A mesoscopic modeling approach" *Acta Mater.*, vol. 169, pp. 60–75, May 2019, doi: 10.1016/j.actamat.2019.01.011.

[105] E. Peng, D. Zhang, and J. Ding, "Ceramic Robocasting: Recent Achievements, Potential, and Future Developments" *Adv. Mater.*, vol. 30, no. 47, p. 1802404, Nov. 2018, doi: 10.1002/adma.201802404.

[106] X. Xu, P. Lu, and R. M. German, "Densification and strength evolution in solid-state sintering. Part II Strength model" *J. Mater. Sci.*, vol. 37, no. 3, pp. 117–126, 2002, doi: 10.1023/A:1013110328307.

[107] M. Bohner, "Design of ceramic-based cements and putties for bone graft substitution" *Eur. Cells Mater.*, vol. 20, pp. 1–12, Jul. 2010, doi: 10.22203/eCM.v020a01.

[108] L. F. Peltier, "The use of plaster of paris to fill large defects in bone" *Am. J. Surg.*, vol. 97, no. 3, pp. 311–315, Mar. 1959, doi: 10.1016/0002-9610(59)90305-8.

[109] W. S. Pietrzak and R. Ronk, "Calcium Sulfate Bone Void Filler: A Review and a Look Ahead" *J. Craniofac. Surg.*, vol. 11, no. 4, pp. 327–333, Jul. 2000, doi: 10.1097/00001665-200011040-00009.

[110] A. J. Ambard and L. Mueninghoff, "Calcium Phosphate Cement: Review of Mechanical and Biological Properties" *J. Prosthodont.*, vol. 15, no. 5, pp. 321–328, Sep. 2006, doi: 10.1111/j.1532-849X.2006.00129.x.

[111] N. Ostrowski, A. Roy, and P. N. Kumta, "Magnesium Phosphate Cement Systems for Hard Tissue Applications: A Review" *ACS Biomater. Sci. Eng.*, vol. 2, no. 7, pp. 1067–

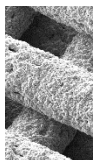

1083, Jul. 2016, doi: 10.1021/acsbiomaterials.6b00056.

[112] E. Soudée and J. Péra, “Mechanism of setting reaction in magnesia-phosphate cements” *Cem. Concr. Res.*, vol. 30, no. 2, pp. 315–321, 2000, doi: 10.1016/S0008-8846(99)00254-9.

[113] M. Nabiyouni, T. Brückner, H. Zhou, U. Gbureck, and S. B. Bhaduri, “Magnesium-based bioceramics in orthopedic applications” *Acta Biomater.*, vol. 66, pp. 23–43, Jan. 2018, doi: 10.1016/j.actbio.2017.11.033.

[114] M. M. Farag and H. Yun, “Effect of gelatin addition on fabrication of magnesium phosphate-based scaffolds prepared by additive manufacturing system” *Mater. Lett.*, vol. 132, pp. 111–115, Oct. 2014, doi: 10.1016/j.matlet.2014.06.055.

[115] C. Yang *et al.*, “3D-Printed Bioactive Ca 3 SiO 5 Bone Cement Scaffolds with Nano Surface Structure for Bone Regeneration” *ACS Appl. Mater. Interfaces*, vol. 9, no. 7, pp. 5757–5767, Feb. 2017, doi: 10.1021/acsami.6b14297.

[116] X. Qi *et al.*, “Three dimensional printing of calcium sulfate and mesoporous bioactive glass scaffolds for improving bone regeneration in vitro and in vivo” *Sci. Rep.*, vol. 7, no. 1, p. 42556, Mar. 2017, doi: 10.1038/srep42556.

[117] Y. Luo, A. Lode, F. Sonntag, B. Nies, and M. Gelinsky, “Well-ordered biphasic calcium phosphate–alginate scaffolds fabricated by multi-channel 3D plotting under mild conditions” *J. Mater. Chem. B*, vol. 1, no. 33, p. 4088, 2013, doi: 10.1039/c3tb20511h.

[118] W. J. Kim, H.-S. Yun, and G. H. Kim, “An innovative cell-laden α-TCP/collagen scaffold fabricated using a two-step printing process for potential application in regenerating hard tissues” *Sci. Rep.*, vol. 7, no. 1, p. 3181, Dec. 2017, doi: 10.1038/s41598-017-03455-9.

[119] A. Lode *et al.*, “Fabrication of porous scaffolds by three-dimensional plotting of a pasty calcium phosphate bone cement under mild conditions” *J. Tissue Eng. Regen. Med.*, vol. 8, no. 9, pp. 682–693, Sep. 2014, doi: 10.1002/term.1563.

[120] N. Raja, A. Sung, H. Park, and H. Yun, “Low-temperature fabrication of calcium deficient hydroxyapatite bone scaffold by optimization of 3D printing conditions” *Ceram. Int.*, vol. 47, no. 5, pp. 7005–7016, Mar. 2021, doi: 10.1016/j.ceramint.2020.11.051.

[121] L. M. Grover, M. P. Hofmann, U. Gbureck, B. Kumarasami, and J. E. Barralet, “Frozen delivery of brushite calcium phosphate cements” *Acta Biomater.*, vol. 4, no. 6, pp. 1916–1923, Nov. 2008, doi: 10.1016/j.actbio.2008.06.003.

[122] P. Miranda, A. Pajares, E. Saiz, A. P. Tomsia, and F. Guiberteau, “Mechanical properties of calcium phosphate scaffolds fabricated by robocasting” *J. Biomed. Mater. Res. Part A*, vol. 85A, no. 1, pp. 218–227, Apr. 2008, doi: 10.1002/jbm.a.31587.

[123] A. Kumar, A. R. Akkineni, B. Basu, and M. Gelinsky, “Three-dimensional plotted hydroxyapatite scaffolds with predefined architecture: comparison of stabilization by alginate cross-linking versus sintering” *J. Biomater. Appl.*, vol. 30, no. 8, pp. 1168–1181, Mar. 2016, doi: 10.1177/0885328215617058.

[124] T. Ahlfeld *et al.*, “Design and Fabrication of Complex Scaffolds for Bone Defect Healing: Combined 3D Plotting of a Calcium Phosphate Cement and a Growth Factor-Loaded Hydrogel” *Ann. Biomed. Eng.*, vol. 45, no. 1, pp. 224–236, Jan. 2017, doi: 10.1007/s10439-016-1685-4.

[125] T. Ahlfeld *et al.*, “Toward Biofabrication of Resorbable Implants Consisting of a Calcium Phosphate Cement and Fibrin—A Characterization In Vitro and In Vivo” *Int. J. Mol. Sci.*, vol. 22, no. 3, p. 1218, Jan. 2021, doi: 10.3390/ijms22031218.

[126] P. Korn *et al.*, “3D Printing of Bone Grafts for Cleft Alveolar Osteoplasty – In vivo Evaluation in a Preclinical Model” *Front. Bioeng. Biotechnol.*, vol. 8, no. March, pp. 1–16, Mar. 2020, doi: 10.3389/fbioe.2020.00217.

[127] R. Bagnol *et al.*, “Coaxial micro-extrusion of a calcium phosphate ink with aqueous solvents improves printing stability, structure fidelity and mechanical properties” *Acta Biomater.*, vol. 125, pp. 322–332, Apr. 2021, doi: 10.1016/j.actbio.2021.02.022.

[128] A. Barba *et al.*, “Osteogenesis by foamed and 3D-printed nanostructured calcium phosphate scaffolds: Effect of pore architecture” *Acta Biomater.*, vol. 79, no. 2, pp. 135–147, Oct. 2018, doi: 10.1016/j.actbio.2018.09.003.

[129] J.-P. Carrel, A. Wiskott, M. Moussa, P. Rieder, S. Scherrer, and S. Durual, “A 3D printed TCP/HA structure as a new osteoconductive scaffold for vertical bone augmentation” *Clin. Oral Implants Res.*, vol. 27, no. 1, pp. 55–62, Jan. 2016, doi: 10.1111/clr.12503.

[130] J.-P. Carrel, A. Wiskott, S. Scherrer, and S. Durual, “Large Bone Vertical Augmentation Using a Three-Dimensional Printed TCP/HA Bone Graft: A Pilot Study in Dog Mandible” *Clin. Implant Dent. Relat. Res.*, vol. 18, no. 6, pp. 1183–1192, Dec. 2016, doi: 10.1111/cid.12394.

[131] P. Diloksumpan *et al.*, “Orthotopic Bone Regeneration within 3D Printed Bioceramic Scaffolds with Region-Dependent Porosity Gradients in an Equine Model” *Adv. Healthc. Mater.*, vol. 1901807, pp. 1–11, 2020, doi: 10.1002/adhm.201901807.

[132] P. Diloksumpan *et al.*, “Combining multi-scale 3D printing technologies to engineer reinforced hydrogel-ceramic interfaces” *Biofabrication*, vol. 12, no. 2, p. 025014, Feb. 2020, doi: 10.1088/1758-5090/ab69d9.

[133] S. Raymond *et al.*, “Accelerated hardening of nanotextured 3D-plotted self-setting calcium phosphate inks” *Acta Biomater.*, vol. 75, pp. 451–462, Jul. 2018, doi: 10.1016/j.actbio.2018.05.042.

[134] L. Vidal *et al.*, “Regeneration of segmental defects in metatarsus of sheep with vascularized and customized 3D-printed calcium phosphate scaffolds” *Sci. Rep.*, vol. 10, no. 1, p. 7068, Dec. 2020, doi: 10.1038/s41598-020-63742-w.

[135] S. Romanazzo *et al.*, “Synthetic Bone-Like Structures Through Omnidirectional Ceramic Bioprinting in Cell Suspensions” *Adv. Funct. Mater.*, vol. 2008216, p. 2008216, 2021, doi: 10.1002/adfm.202008216.

Chapter 2

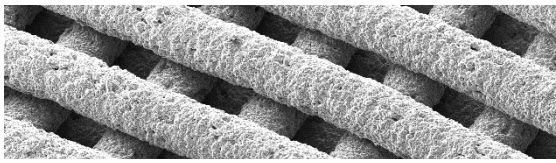

Computed Tomography and Histological Evaluation of Xenogenic and Biomimetic Bone Grafts in Three-Wall Alveolar Defects in Minipigs

COMPUTED TOMOGRAPHY AND HISTOLOGICAL EVALUATION OF XENOGENIC AND BIOMIMETIC BONE GRAFTS IN THREE-WALL ALVEOLAR DEFECTS IN MINIPIGS

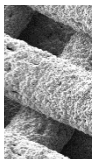

Abstract

Objectives: This study aimed to compare the performance of a xenograft (XG) and a biomimetic synthetic graft (SG) in three-wall alveolar defects in minipigs by means of 3D computerised tomography and histology.

Materials and methods: Eight minipigs were used. A total of eight defects were created in the jaw of each animal, three of which were grafted with XGs, three with SGs and two were left empty as a negative control. The allocation of the different grafts was randomised. Four animals were euthanised at 6 weeks and four at 12 weeks. The grafted volume was then measured by spiral computed tomography to assess volume preservation. Additionally, a histological analysis was performed in undecalcified samples by backscattered scanning electron microscopy and optical microscopy after Masson's trichrome staining.

Results: A linear mixed-effects model was applied considering four fixed factors (bone graft type, regeneration time, anatomic position, and maxilla/mandible) and one random factor (animal). The SG exhibited significantly larger grafted volume (19%) than the XG. The anterior sites preserved better the grafted volume than the posterior ones. Finally, regeneration time had a positive effect on the grafted volume. Histological observations revealed excellent osseointegration and osteoconductive properties for both biomaterials. Some concavities found in the spheroidal morphologies of SGs were associated with osteoclastic resorption.

Conclusions: Both biomaterials met the requirements for bone grafting, *i.e.* biocompatibility, osseointegration, and osteoconduction. Granule morphology was identified as an important factor to ensure a good volume preservation.

Clinical relevance: Whereas both biomaterials showed excellent osteoconduction, SGs resulted in better volume preservation.

2.1 Introduction

Bone loss continues to be a major clinical burden in the dental field, especially in cases where tooth extraction is not quickly followed by the placement of an implant. In this case, the lack of local mechanical stimulation leads to considerable bone resorption [1]. During this process, the bundle bone, *i.e.* the bone that surrounds the tooth and contains the periodontal ligament fibres binding the tooth to the bone, is no longer necessary and is progressively resorbed and replaced by woven bone [2]. This results in an accentuated vertical reduction of the buccal alveolar crest, which is exclusively composed of bundle bone. Simultaneously, there is a resorption of the outer surfaces of both the buccal and the lingual bone walls, which greatly reduces the amount of bone to successfully place an implant with lasting benefits [2]. In these situations, bone augmentation is a widely used solution [3].

Bone grafts (BGs) are used to fill bone defects and support bone regeneration in the grafted volume. The aim is often to achieve the volume required to place a stable dental implant. BGs are available in different shapes and delivery systems such as granules, blocks, or putties [4]. In the dental field, granules are the most common option for the treatment of walled bone defects [5]. BGs can be classified, based on their origin, as autografts, allografts, xenografts or synthetic grafts [6,7]. Since their introduction in the 1970s synthetic BGs have progressively evolved, and different strategies have been tried to improve their biological performance. One of the strategies that has recently been proposed is based on the development of biomimetic materials, which are synthesised using mild processing conditions instead of the traditional high-temperature ceramic methods. This results in a material that is considerably more similar to the mineral phase of bone, not only in terms of composition, but also in terms of microstructure and reactivity [8]. In previous studies it has been shown that biomimetic calcium phosphates have very interesting properties in terms of osteoimmunomodulation [9], *in vivo* osteoconductivity [10], and osteoinductivity [11]. However, there still exists a lack of information regarding the efficacy of these biomimetic materials compared to the xenogenic grafts in clinically relevant defects for dental applications in large animals.

The clinical success of a bone grafting procedure is linked to the preservation of the grafted volume. This is achieved by preventing a short-term volume loss [12,13] and promoting the long-term remodelling of the graft into the vascularised bone, without compromising the volume [14]. The regeneration process associated with a bone graft depends on numerous factors. Recent studies have demonstrated that it largely depends on the carefully coordinated interactions between various cell types, including immune, endothelial, and bone cells [15]. While a certain degree of inflammation has been shown to trigger the bone regeneration cascade, the benefits of early inflammation are to be contained, as excessive or prolonged inflammation may result in a suboptimal bone formation [16]. Moreover, a high vascularisation is required to guarantee the oxygen and nutrient supply to the highly metabolically active cells involved in tissue regeneration [17]. The features of bone grafts are known to play a crucial role in the modulation of all these biological processes [8]. Not only composition matters, but also textural properties are important. Achieving the adequate porosity is necessary to promote vascularisation and tissue colonisation, enhancing the interaction of the material with the host tissue [18,19]. Finally, the graft must have the appropriate mechanical properties to guarantee the preservation of the biomechanical functions of bone during the healing process, thus avoiding both weakening and stress shielding effects [20].

The present work focuses on the comparative evaluation of two bone substitutes with different origins: A synthetic biomimetic calcium phosphate (MimetikOss®, Mimetis Biomaterials, Spain) and a deproteinised bovine bone matrix (Bio-Oss®, Geistlich Biomaterials, Switzerland). For this purpose, the volume preservation and tissue regeneration processes were evaluated after 6 and 12 weeks of healing in three-wall bone defects created in the mandible and maxilla of minipigs grafted with the two different materials.

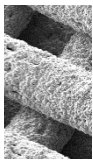

2.2 Materials and Methods

2.2.1 Bone Grafts

Two types of bone grafts (BGs) were used to fill the defects:

- a control group being a xenograft (XG) from bovine origin (Bio-Oss®, Geistlich Biomaterials, Switzerland) in granular form with sizes between 0.25 and 1 mm and;

- a test group being a synthetic biomimetic graft (SG) processed at low temperature and composed of 80% biomimetic calcium deficient hydroxyapatite and 20% β-tricalcium phosphate (MimetikOss®, Mimetis Biomaterials, Spain) in granular form with sizes between 0.2 and 1 mm.

Both biomaterials were commercially available in vials sealed into blisters, provided in sterile conditions, and used appropriately by following their instructions for use. The physicochemical properties of the two grafting materials are described in a previous study [21].

2.2.2 Animals

Eight landrace minipigs (6-months-old, mixed sexes and from 18 to 31 kg) were provided by a GLP clinical research organisation (CRO) (Specipig S.L., Barcelona, Spain). The animals were kept in presurgical housing for 1 week.

2.2.3 Study Design

The study was conducted complying with the EU Directives 2004/10/EU, 2010/63/EU and the Spanish law RD 1369/2000 regarding the protection of animals used for scientific purposes. The experiments were carried out at the GLP facilities of the CRO and werereviewed and approved by the Specipig Ethics Committee for Animal Experimentation. The surgical procedure was performed by I.G.

The indication chosen was the regeneration of a three-wall defect in the alveolar ridge, which is one of the most common surgical procedures in modern dentistry [22].

Eight defects were created per animal in the surgical sites indicated in **Fig. 2.1 a** and referenced accordingly. For each animal, three defects were filled with XGs, three with SGs and two were left empty. The distribution of the grafts and the empty defects was defined in a balanced manner (*i.e.* all together, each biomaterial was grafted the same number of times in each of the eight surgical sites), and randomly assigned to the animals. All defects were then covered with resorbable collagen membranes (Creos Xenoprotect, Nobel Biocare, Switzerland). Two time points were evaluated: 6 and 12

weeks. At each time point four animals were euthanised, which gave 12 replicates per material and time point.

Computerised tomography (CT) of each animal was performed postoperatively and at the time of euthanasia. Additionally, the grafted regions were explanted and processed for histological evaluation.

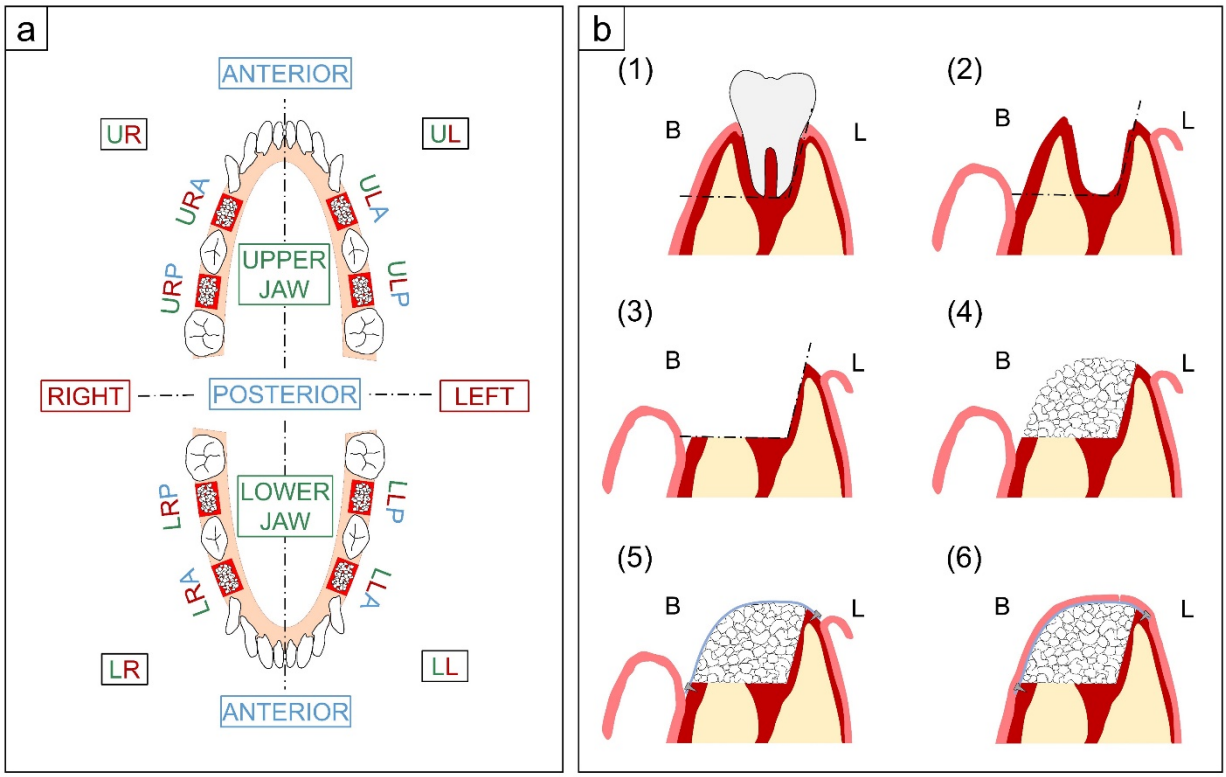

Fig. 2.1 a Scheme of the created defects and reference names. Coronal plane projection of the upper (U) and lower (L) jaw. L and R stand for left and right and M and D stand for mesial and distal anatomic sites, respectively. **b** Procedure to create the standardised three-wall bone defect, grafting and suturing: (1) Initial situation, (2) tooth extraction and rising of the flap, (3) creation of the three-wall bone defect by removing the buccal alveolar ridge, (4) grafting of the defect, (5) covering the graft with a collagen membrane and (6) stitching the gingiva. B and L stand for buccal and lingual sides, respectively.

2.2.4 Surgical Procedure

Anaesthesia and medication

A premedication of 0.04 mg kg^{-1} of atropine was administered intramuscularly (IM) in the neck. Using the same method, sedation was achieved with 0.020 to 0.035 mg kg^{-1} of dexmedetomidine and 0.08 to 0.30 mg kg^{-1} of midazolam combined with 0.15 to 0.30 mg kg^{-1} of butorphanol as an analgesic. After 15-20 min, an intravenous (IV) catheter was placed in order to continue with IV fluid therapy using ringer lactate serum combined with the medication. Animals were then pre-oxygenated with 100% oxygen for 3 min 1.5 to 5.0 mg kg^{-1} of propofol was administered through IV injection. Endotracheal intubation was performed using isoflurane with a minimum alveolar concentration of 1.2-2.4% and 2% oxygen. Immediately after surgery, a nonsteroidal anti-inflammatory (meloxicam 0.4 mg kg^{-1} IM in the neck muscles) and a general

antibiotic coverage (enrofloxacin from 2.5-5 mg kg^{-1} IM in the neck muscles) were administered.

Tooth extraction and creation of the defect

Right before starting the surgical procedure, the oral cavity was scrubbed with 10% iodine povidone. Additionally, the teeth to be removed were manually scaled and calculus was eliminated. Then, a full-thickness flap from the first premolar to the most distal molar was raised both buccally and lingually as seen in **Fig. 2.1 b-2**. Eight three-wall bone defects were shaped after tooth extraction by removing the buccal plate to half of its height as illustrated in **Fig. 2.1 b-3**. The removed teeth were the first and third premolars of the lower quadrants and the first premolar and first molar of the upper quadrants. A periodontal probe and a high-speed handpiece under copious irrigation were utilised to create the standard-sized alveolar defects. The size of the defects was 12 mm in depth and 10 mm in width.

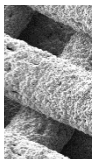

Grafting

BGs were first hydrated with Ringer's solution and then placed in the defects by gently packing to achieve the best volume filling (**Fig. 2.1 b-4**). Then, a collagen resorbable membrane was cut and adapted to the size of the defect. The wound was prepared for tension-free closure by releasing the periosteum underneath the flap. Primary closure was achieved in all cases with 4-0 Vicryl® degradable braided suture (polyglactin 910, Johnson & Johnson, USA). Horizontal mattress and single interrupted sutures were used to close the wound (**Figs. 2.1 b-5** and **b-6**).

Post-operative

After the surgery, butorphanol was administered IM 0.15-0.30 mg kg^{-1} every 12 h as an analgesic for 2 d. Anti-inflammatory treatment with meloxicam was administered IM 0.4 mg kg^{-1} every 24 h for 5 d. Antibiotic treatment with enrofloxacin was administered IM 2.5-5.0 mg kg^{-1} every 24 h for 5 d post-surgery. One week after the surgical procedure, animals were sedated and wounds were reviewed to look for any possible events that would compromise healing and overall results. No screaming nor altered behaviour was registered. No bleeding nor vocalisation was observed or heard during the 2 weeks following the surgeries.

Monitoring

The minipigs were maintained on a soft diet for 48 h after the surgery. Animal weight was tracked weekly. All the animals showed a proper evolution. In addition, the specimens were observed twice a day for any abnormality.

2.2.5 Computerised Tomography (CT)

An initial CT scan was registered for each animal one day after the surgery (Philips IQUON CT-SCAN, Royal Philips, the Netherlands). A second CT scan was performed before euthanasia at 6 or 12 weeks depending on the group. Stacks of images were

acquired with an isotropic pixel size of 500 µm. Slices were performed in the coronal plane and through the whole range of the mandible and maxilla (**Fig. 2.2**).

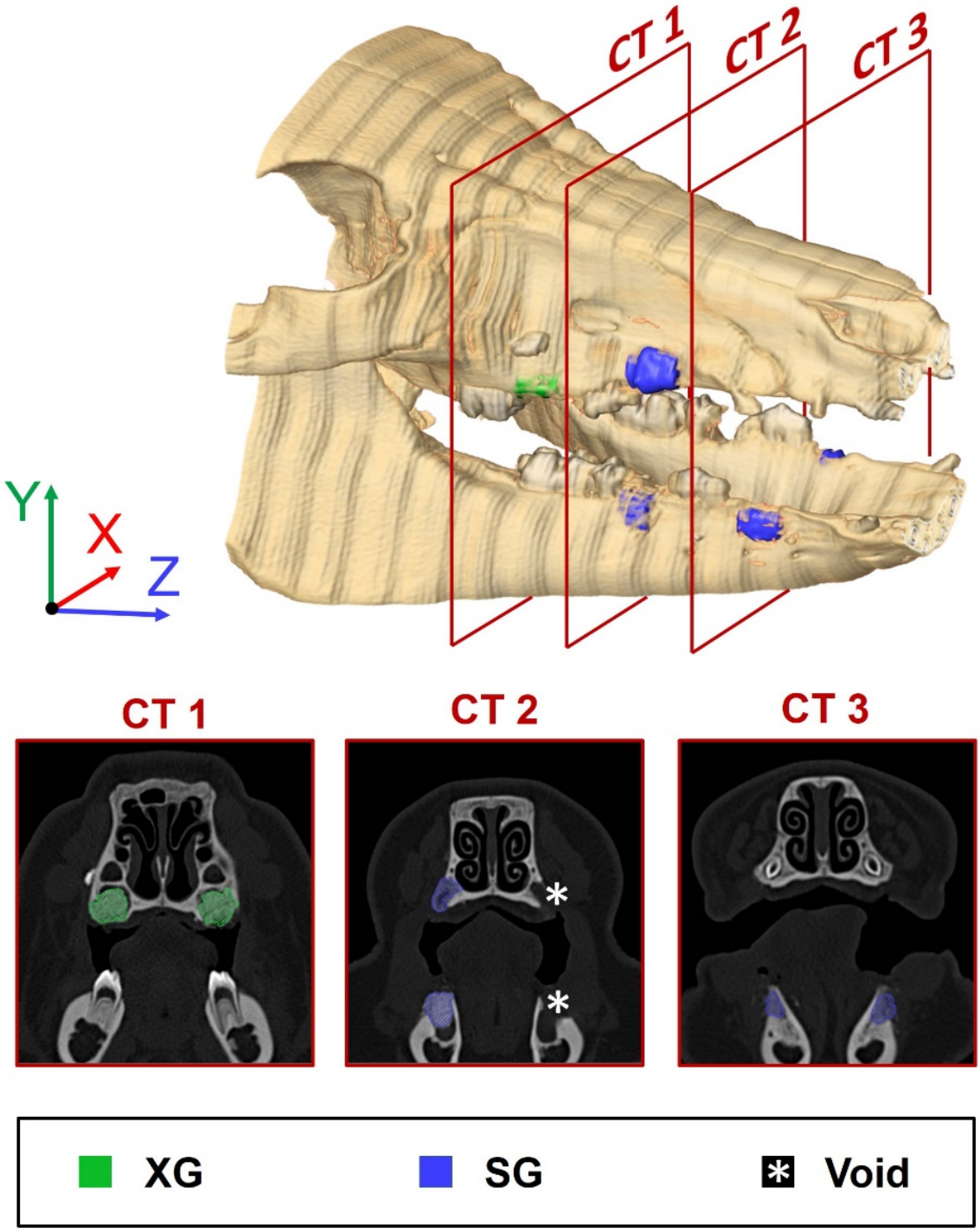

Fig. 2.2 Top: Reconstruction of the CT scan and grey-values 3D segmentation of the different three-wall bone defects. Bottom: Three representative slices of the CT scan representing the segmentation of the different bone substitutes.

Volumetric CT quantification

A sample of each BG was scanned and used to determine the radiopacity thresholds of each biomaterial. Ranges of 442 – 948 HU and 847 – 1435 HU were established for XG and SG, respectively. Then, the defect regions were identified by a trained observer based on the recognition of its anatomical location. The grafted volume was calculated at each time point and for each identified defect region using a grayscale-based automated segmentation process. The segmentation consisted in performing grey-value thresholding followed by an erosion-dilation filtering operation to remove segmentation artefacts external to the grafted region bulk, and finally, running an algorithm to fill the holes on the segmented region to eliminate possible pores inside the grafted region.

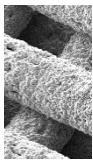

The grafted volumes of each defect at each time-point were calculated with the following equation [23]:

$$V_k = \sum_{i=0}^{n} A_{k,i} \cdot \Delta z \ (k = 0,\ 6,\ 12\ ) \qquad \textbf{Equation 2.1}$$

Where V_k corresponds to the total grafted volume at each time-point (*i.e.* k = 0, 6 or 12 weeks after surgery), $A_{k,i}$ is the grafted area calculated for one slice of the stack (i) at one time point (k), and Δz represents the elemental increment in the z scan direction (**Fig. 2.2**) determined by the CT configuration (*i.e.* 500 µm). The percent variation of the grafted volume (ΔV) after 6 or 12 weeks for the XG and SG was calculated using **Equation 2.2**:

$$\Delta V = \frac{V_f - V_i}{V_i} \cdot 100\ [\%] \qquad \textbf{Equation 2.2}$$

Where V_0 corresponds to the volume of the grafted region in the initial CT scan (one day after surgery, k=0) and V_f corresponds to the volume of the grafted region at the final time point (euthanised either at k=6 or k=12 weeks), calculated with **Equation 2.1**. The segmentation and quantification process was performed with the image analysis software BoneJ (BoneJ, Fiji, ImageJ [24]) in a randomised blinded configuration.

Four samples (corresponding to the conditions 6w-XG-ULP, 6w-SG-LLP, 12w-SG-LRA, 12w-SG-LLA) were dismissed as the grafted region could not be clearly identified.

2.2.6 Histological Analysis

After explantation, four randomly selected samples per BG group and regeneration time were chosen for micromorphological analysis. For this purpose, samples underwent the following process: First, the explanted samples were kept in a 4% formaldehyde solution for 1 week. Then, the defect regions were cut (diamond band saw, Exakt 300, EXAKT Technologies, Norderstedt, Germany) parallel to the coronal plane in 10 mm to 15 mm pieces. The samples were dehydrated by immersion in increasing ethanol concentrations of 30, 70, 80, 90 and 100% in water. Then, ethanol was gradually replaced by methyl methacrylate resin (Tecnovit 7200 VLC, Kulzer,

Hanau, Germany) in successive solutions of 30, 70, 80, 90 and 100% in ethanol to ensure a complete infiltration. During all the resin infiltration process, samples were kept in a dark environment under vacuum. Samples were then polymerised (Photopolymerisation lamp, Exakt 520, EXAKT Technologies, Norderstedt, Germany) and the resulting blocks were cut in multiple 300 µm slices with the Exakt 300 bandsaw and polished down to 30-50 µm (Micro grinder, Exakt 400 CS, Exakt AW110, EXAKT Technologies, Norderstedt, Germany). One slice per sample was stained using Masson-Goldner trichrome staining. Stained samples were observed using a bright-field optical microscope (AF7000, Leica, Switzerland) with and without a polarising filter. Another slice was coated with a thin carbon layer and observed in a scanning electron microscope (SEM, Jeol J-6510, Tokyo, Japan) with a backscattered electron detector (BSD).

2.2.7 Statistical Analysis

The results of the volumetric CT quantification were processed through a statistical analysis software (Minitab 18.1, Minitab Inc., PA, USA) focusing on obtaining a global perspective of the role of each of the recorded surgery factor in the bone regeneration.

Firstly, all the data were checked for normal distributions and equivalence of variances (*i.e.* homoscedasticity) (Supplementary information: Least squares assumptions validation). Subsequently, an outlier test was run to remove possible outliers (Supplementary information: Outlier test). One outlier was found (for the condition 12 weeks - XG) and excluded from the statistical analysis. Then, a linear mixed-effects model (LMM) was fit to further understand the influence of the different factors on the grafted volume preservation (*i.e.* observed response). Such model allowed to consider both fixed and random effects [25]. The type of bone graft, regeneration time, jaw type (*i.e.* mandible vs maxilla) and anatomic site within each jaw (*i.e.* anterior or posterior) were included in the LMM as fixed effects, whereas the animal was included as a random effect (**Table 2.1**). Second- and third-order interactions between factors were also included in the model. The estimation method of this process followed the least-squares criterion. The correlations between factors were considered in the model. Most of the factors presented a cross-correlation due to the balanced design of the study and the random assignation of the defect anatomic sites to the different bone grafts. The exception was the unavoidable correlation between each animal and the corresponding regeneration time assigned. The nesting of these two factors was included in the LMM. During the fitting process, first the third-order interactions with a p-value above the significance level (set to 5%) were excluded from the model. Then, the same procedure was repeated with the second-order interactions. Finally, the same was carried out with the main factors (Supplementary information: Linear mixed-effects model fitting).

Table 2.1. Factors included in the linear mixed-effects model and corresponding levels and reference names.

	Factor	Levels	Ref.
Fixed factors	Bone graft (BG)	Synthetic graft / Xenograft	SG / XG
	Regeneration time	6 weeks / 12 weeks	6w / 12w
	Jaw	Upper / Lower	U / L
	Anatomic site	Anterior / Posterior	A / P
Random factors	Animal	1 – 8	1 – 8

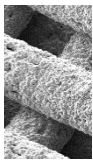

2.3 Results

2.3.1 Computerised Tomography (CT)

Qualitative CT evaluation

None of the grafts was lost during the healing period and both BGs presented a stable filling of the granules inside the defects. It was also observed that the surgical procedure effectively reduced the buccal bone plate by half and preserved the lingual bone plate. The radiopacity of the SG was higher than that of the XG, as shown in **Fig. 2.3**. In addition, no bone regeneration was found in the empty defects, suggesting that they were critical-sized and, for this reason, they are not included in the following results.

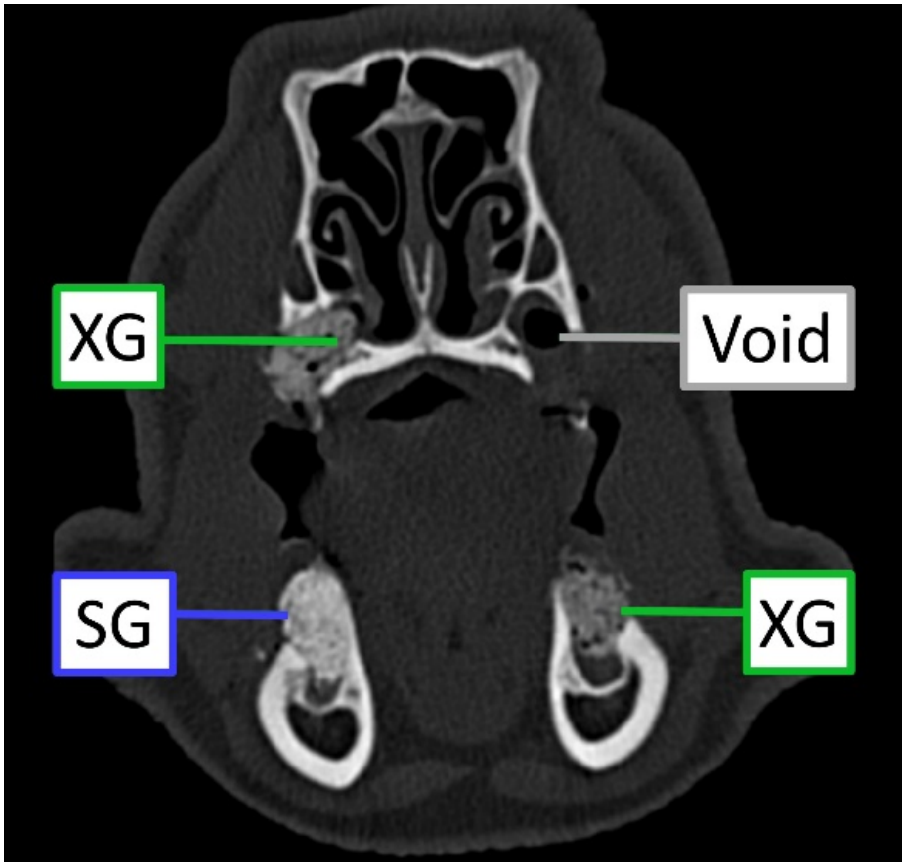

Fig. 2.3 Coronal slice of a CT scan showing four premolar grafted defects.

Quantitative CT results

The data were analysed using a linear mixed-effects model, considering all the fixed effects (including their second- and third-order interactions) and the random effects. The non-statistically significant factors were successively removed until fitting a model with only significant factors. The parameters that were found to be significant were all the main factors, except “Jaw” type. The results of the fitted linear mixed-effects model are displayed in **Table 2.2** and the main effects plot is shown in **Fig. 2.4**.

Table 2.2. Linear mixed-effect model fit: p-value indicating the significance of each factor in the model. Determination of the positive-negative effect on the response for each level of each factor (+/- effect). Coefficient of each factor in the fitted regression equation. (The complete process can be found in the Supplementary information: Linear mixed-effects model fitting).

Factor	p-value	+ effect	- effect	Coef.
Bone Graft (BG)	0.001	SG	XG	11.83
Anatomic Site	0.028	A	P	7.61
Regeneration Time	0.037	12w	6w	7.20
Constant	0.002	N/A	N/A	-10.84

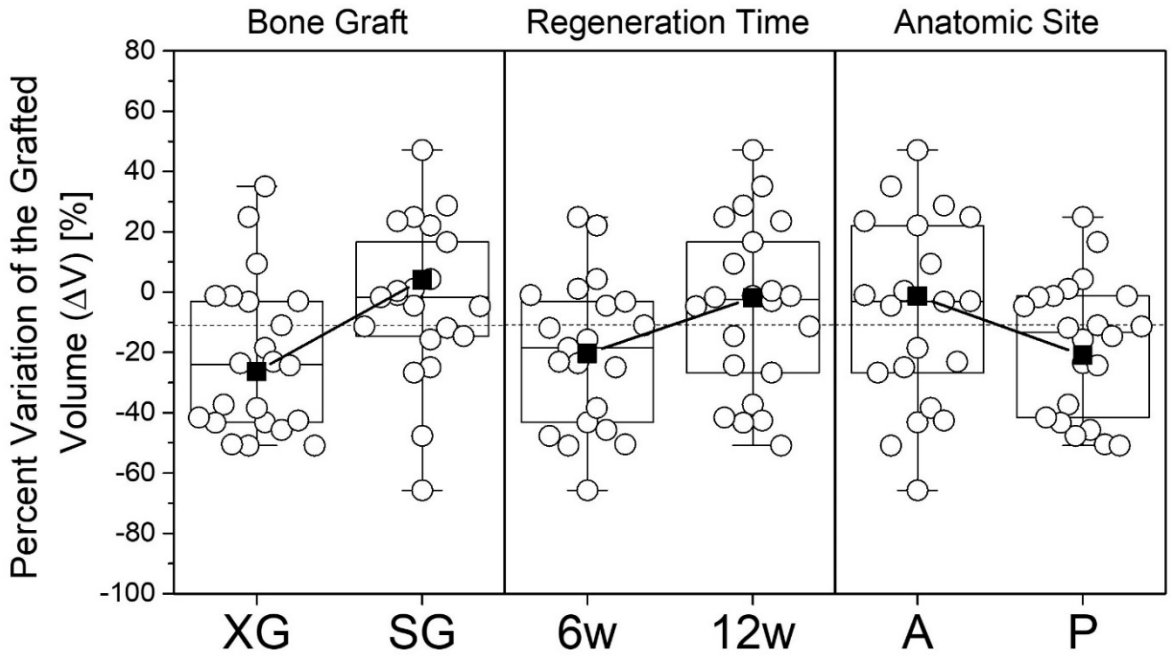

Fig. 2.4. Individual experimental observations (white dots) of the percent variation of the grafted volume (ΔV) grouped by the different significant factors according to the linear mixed-effects model (*i.e.* BG type, regeneration time and anatomic site). Boxplot indicating the median and quartiles of the observed population distribution. Overlayed main effects plot (solid squares and trendlines) illustrating the mean responses for each level of the factors fitted in the model (**Table 2.2**). Constant coefficient represented in a horizontal dashed line.

Additionally, the results of the variation of grafted bone volume are plotted as a function of the BG type and the regeneration time (**Fig. 2.5**). After 6 weeks, bone preservation

percentages (mean value ± standard deviation) of -30.81 ± 17.13% and -10.82 ± 27.32% were observed for the XG and the SG, respectively. After 12 weeks, these percentages increased by approximately 16% being -14.68 ± 29.17% and 5.72 ± 22.67% for the XG and the SG, respectively, which overall demonstrates better volume preservation by the SG.

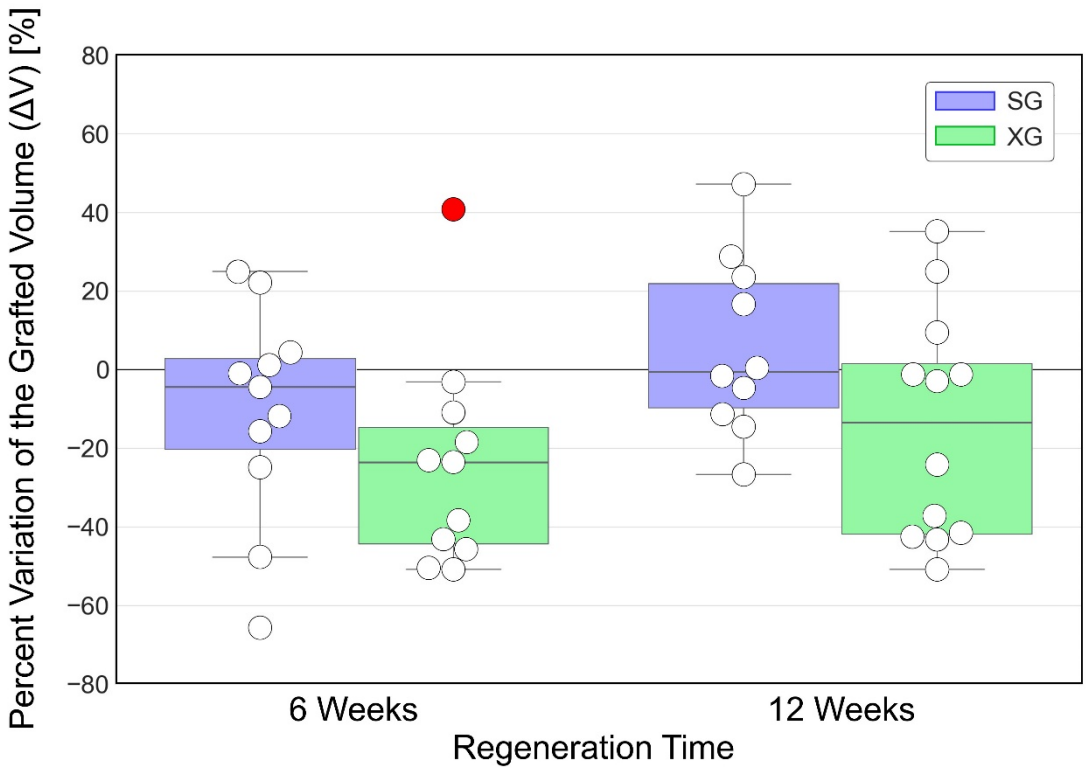

Fig. 2.5. Percent variation of the grafted volume (ΔV) for the different BG types (SG and XG) after 6 and 12 weeks of regeneration. Boxplots superimposed to scatterplots with white points representing the analysed data and red points representing the outliers.

2.3.2 Qualitative Histological Evaluation

The histological evaluation (**Fig. 2.6**) revealed the biocompatibility of the two bone grafts. No signs of inflammation, degeneration areas nor bone necrosis were observed at any time point. Moreover, an active process of new bone formation was observed in both BGs, which showed osteoconductive properties and excellent osseointegration. This active new bone formation was observed with approximately the same intensity after 6 and 12 weeks in both biomaterials. After 6 weeks, most of the samples showed thin bone trabeculae with irregular alveolar bone crests and no corticalisation. At 12 weeks, a higher number of samples presented thick bone trabeculae and smooth alveolar crests.

Additionally, the histological slides were observed by linearly polarised light (LPL). LPL images allow identifying birefringent materials, which display optical anisotropy. In birefringent materials, the differences in light refraction result in variations of brightness, whereas materials without this feature are seen as opaque. Collagen is easily identified through LPL due to its birefringent properties [26]. In **Fig. 2.6** several

regions with varying brightness corresponding to the oriented collagen fibres were observed. Whilst in SGs one could notice this phenomenon occurring only in newly formed bone, in XGs the granules were also bright, which can be attributed to its biological origin.

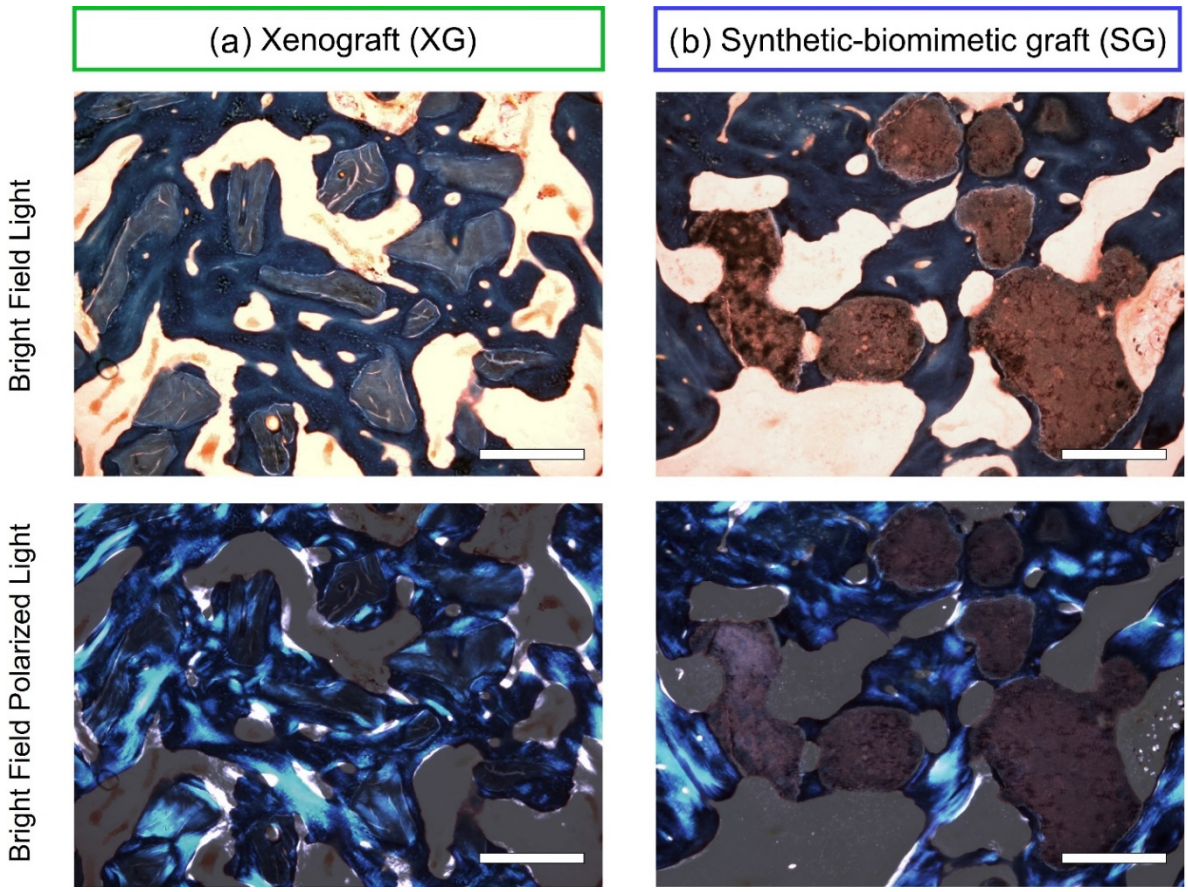

Fig. 2.6. Histological views showing the grafted regions with XG **a** and SG **b** after 12 weeks of regeneration stained with Masson–Goldner trichrome technique. Top: Bright field light microscopy where the newly formed bone appears in blue, the XG in grey and the SG in brown. Bottom: Bright field polarised light microscopy images (with overlaid original image at 75% of transparency) of the same region evidencing the collagen orientation in the forming bone. Scale bars represent 500 μm.

A closer observation of the histological slides of the SG at 12-weeks revealed some resorption areas (indicated with black arrows in **Fig. 2.7 a** and **b** in the outline of the vascular spaces between the biomaterial granules. The altered morphology of some of the granules contrasted with the original spheroidal morphology (presented in **Fig. 2.7 c**, and was ascribed to osteoclastic resorption of the material.

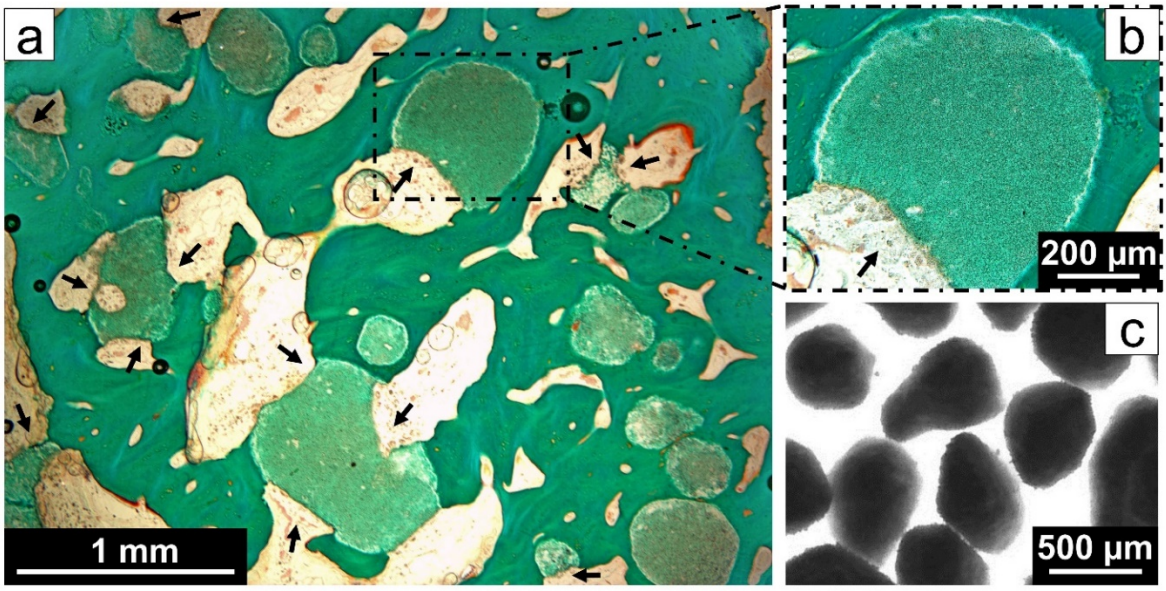

Fig. 2.7. a, b Histological section stained with Masson's trichrome showing a defect grafted with SG at 12 weeks post-surgery. Arrows indicate the regions where the rounded morphology of the BG has been altered by the osteoclastic resorption. **c** Optical microscopy image showing the morphology of the SG granules before surgery.

The SEM images of the samples (**Fig. 2.8**) evidenced for both BGs an excellent osseointegration, with the newly formed bone not only surrounding the grafts, but in direct contact with them. Additionally, lamellar bone was found around the Haversian canals (asterisks) in all samples. No differences in bone quantity and distribution were observed between 6 and 12 weeks nor between the BG type used (**Fig. 2.8 Row a**). Mature bone with Haversian structure was found in the grafted regions in all BGs. Osteons were clearly visible, with the Haversian canal surrounded by concentric bone lamellae and an interconnected network of osteocyte lacunae (white arrows) in the adjacent woven bone (**Fig. 2.8 Row b**).

Higher magnification images (**Fig. 2.8 Row c**) revealed the differences in microstructure of the two BGs. With a lamellar structure and the presence of some pores associated to osteocyte lacunae, the XG showed the typical microstructure of bone, due to its xenogenic origin. SGs, on the other hand, had a more porous microstructure, which resulted from the entangled network of calcium-deficient hydroxyapatite nanocrystals obtained during the biomimetic fabrication process [27], [28]. Moreover, it was observed that the new bone surrounding the XG fragments was woven bone, whereas more mature lamellar structures were seen in direct contact with the SG granules.

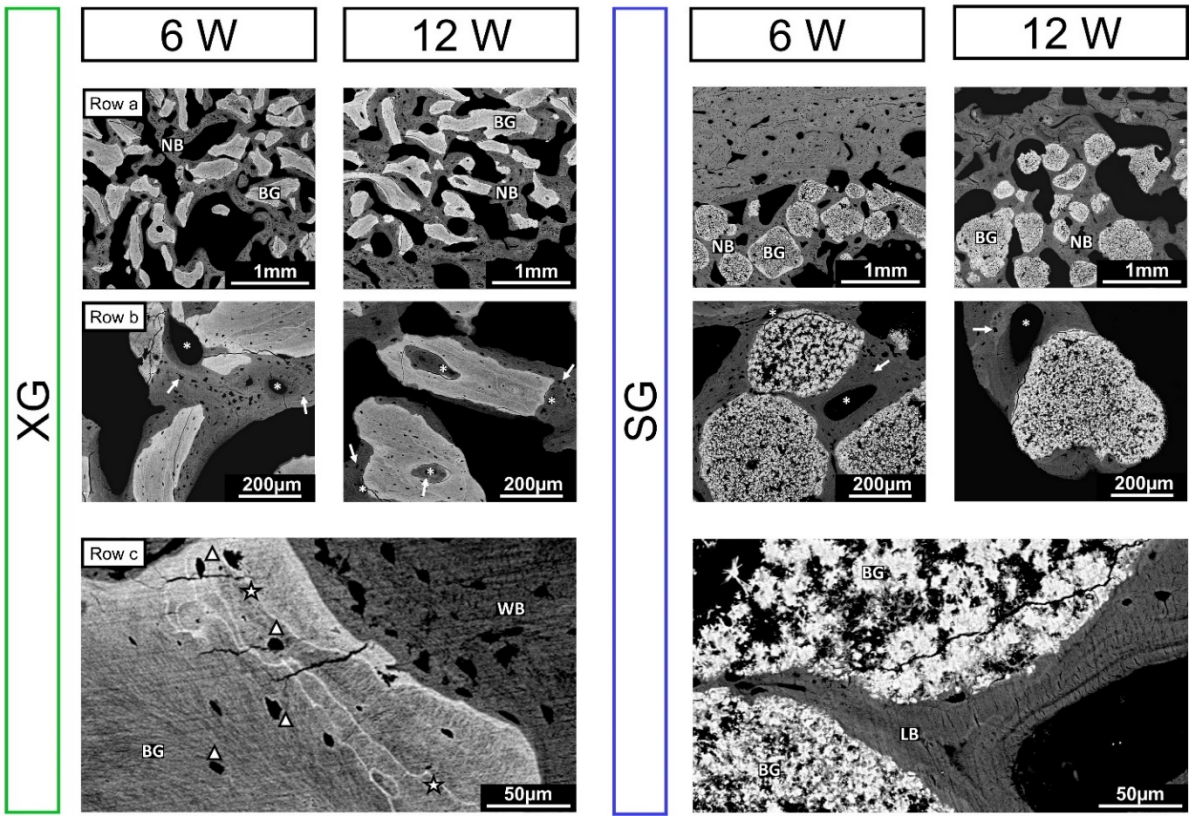

Fig. 2.8 SEM images of grafted regions after 6 and 12 weeks of surgery. Row **a**: Lower magnification micrographs showing the good integration between the bone graft (BG) and newly formed bone (NB). Row **b**: Higher magnification images allow identifying the Haversian canals (asterisks) and osteocyte lacunae (arrows) indicating the presence of osteons and of a mature bone structure in both BGs. Row **c**: A closer look into the BGs reveals the different microstructures. On the XG one can observe osteocyte lacunae (triangles) and mineralisation bands (star) of the original bovine bone constituting the biomaterial, in a lighter shade than the newly formed woven bone (WB) surrounding it. In the SG it is possible to distinguish the calcium-deficient hydroxyapatite (CDHA) nano-crystal network typical of biomimetic calcium phosphates, surrounded by a new bone deposit with a lamellar structure (LB).

2.4 Discussion

Volume stability is critical, not only to avoid the implant neck or thread exposure, but also to ensure treatment predictability and long-term success of the tooth reconstruction [29]. This study compares the performance, in terms of volume preservation, of two different bone grafts in a three-wall alveolar ridge defect in Landrace minipigs after 6 and 12 weeks. This type of bone defect has been widely studied in the literature [30,31] and represents a more challenging situation compared to four-wall defects [32], but without reaching the complexity of vertical or horizontal bone augmentations.

The potential of biomimetic calcium phosphates for bone augmentation applications was assessed in a previous study, which evaluated the vertical bone formation of the same bone grafts tested in the present work, on the calvaria of rats [21]. Faster bone regeneration was observed for the biomimetic SG group compared to XGs. However,

the relevance of that indication for clinical research is limited [33]. Therefore, in the present study, the material was tested in a large animal model, in an indication that is more similar to the clinical situation. In fact, minipigs are considered to be an animal model much closer to humans, not only in terms of the anatomy and composition of bone tissue, but also in terms of the bone regeneration and remodelling process [34].

The primary outcome of the study, 3D-volume preservation by CT analysis, was defined to match the current follow-up technique of bone grafting procedures in the dental offices, with the goal of resembling the clinical setup. It is common in preclinical and clinical studies in the dental field to use radiological data as the main outcome [12,13,35,36].

A linear mixed-effects model data analysis allowed to identify the effect of each parameter on the preservation of the grafted bone volume as well as the existence of possible interactions between them. Randomisation and a high number of replicates allowed this approach. Interestingly, the type of bone graft used resulted to be the most influential parameter, followed by the anatomic site and the regeneration time, which had a similar influence. In contrast, the placement of the defect in either the mandible or the maxilla was not found to have a significant effect. The levels of each factor in the mixed-effects model that resulted in higher bone preservation were synthetic grafts, longer regeneration times (*i.e.* 12 weeks) and anterior positions. Regarding the effect of bone graft in the volume preservation, the SG presented a limited volume loss of around 11% on average at 6 weeks and a volume gain of 6% at 12 weeks, whereas the xenograft lost between 31 and 15% of the initial grafted volume at 6 and 12 weeks, respectively (**Fig. 2.5**). These findings regarding the XG are in agreement with previous studies [12,13,37,38], and may be attributed to the packing of the xenograft flakes, as schematised in **Fig. 2.9**, rather than to a resorption process, which is known to be very limited for this bone substitute [39]. This packing process may only occur soon after surgery, when the biomaterial is not osseointegrated, and explains why Younes *et al.* observed a reduction in the grafted volume only during the first three months, remaining stable thereafter (up to 2 years) [38]. Moreover, the fact that the regeneration time was also statistically significant and had a positive influence on the regenerated bone volume can be attributed to the natural bone remodelling process occurring in the bone defects. Finally, the mixed-effects model revealed also a significant effect of the anatomic site, with better volume preservation on anterior positions. Although, it is not clear that the results can be extrapolated across species, this finding is in agreement with previous studies in dental research reporting a higher turnover rate in anterior alveolar bone, associated to the higher ratio of trabecular bone [40].

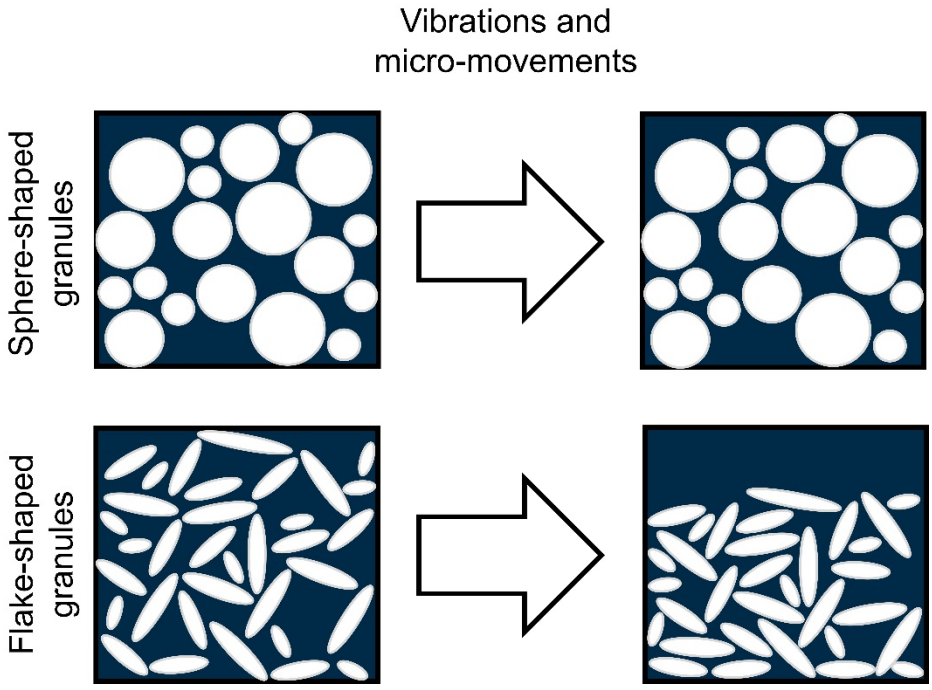

Fig. 2.9. Schema representing the packing effect of different granules morphologies after vibrations and micromovements.

The histological observations proved that both biomaterials had excellent osteointegrative properties and biocompatibility, since a direct bone ingrowth on the particles was observed without any graft encapsulation. The Haversian bone structure observed in the samples indicated a mature stage of bone remodelling with stress-oriented tissue, thus denoting a mechanically stable architecture [41]. The presence of these structures through the whole sample at the shortest time-point (6 weeks) supported the high osteoconductivity on both BG types. Additionally, the biomimetic synthetic grafts presented newly formed bone in a more mature stage than the xenografts in the regions surrounding the biomaterial, suggesting a faster remodelling process.

As far as degradation is concerned, biomimetic synthetic bone grafts with very similar compositions and microstructures to the SG analysed in the current study have been shown to sustain cell-mediated degradation [42,43], as demonstrated by the observation of the typical Howship's Lacunae and cutting cones in close contact with the materials. In the same vein, Mai *et al.* observed, in a miniature swine mandible model grafted with an apatitic bone cement, that the biomaterial underwent a process of resorption that occurred simultaneously to bone formation [44]. This is consistent with the observation of concave morphologies in the SGs in the present study (**Fig. 2.7**), compatible with osteoclastic resorption. However, this did not lead to a volume shrinkage at 12 weeks, but rather the opposite, which suggests that the SG resorption was incorporated in the physiological remodelling process of natural bone. This hypothesis is further supported by the mature lamellar structures found in direct contact with the SG (**Fig. 2.8 Row c**), in contrast to the woven bone surrounding the XG (**Fig. 2.8 Row c**).

Regarding the biodegradation of the XG, this is in fact a controversial topic in the literature. Numerous clinical studies report proper osseointegration and bone

regeneration but a slow or inexistent degradability. Skoglund *et al.* performed alveolar ridge augmentation procedures and observed non-resorbed particles after 44 months, showing doubts as to whether the material should be considered resorbable [45]. Similar observations were done by Duda *et al.* after a 30-month study [46]. In a longer-term study, Schlegel *et al.* described the absence of clinical or histological signs of granule resorption after 6 years [47]. Nor was the degradation of the XG observed in other studies combining the XG with autologous bone (80/20 mixture). For instance, Hallman *et al.* did not find signs of resorption after 6 months in maxillary sinus floor augmentation [48], and Mordenfeld *et al*. concluded, through histomorphometric measurements, that no significant changes in the particle size were observed after 11 years in maxillary sinus augmentation procedures [39]. However, other studies have reported cell-mediated degradation for this same material [49-52]. The discrepancies in the results could be attributed to different factors, such as the grafting site or the local mechanical environment. In this respect, Araújo *et al.* tested an orthodontic procedure to move a tooth into a XG-grafted region in a canine model, concluding that there was a tension-dependent resorption of the material. Whilst in the unloaded regions the graft remained unaltered, in the regions adjacent to the tooth subjected to mechanical stress the osteoclastic resorption of the granules was accentuated [53]. In the present study, the histological assessment provided no evidence of XG resorption. This contrasts with a previous work that used the same animal model and defect location, where cell-mediated resorption was identified in the histological studies of the same XG [54]. An important point to consider is that the size of the defect was considerably larger (30 × 15 × 13 mm^3) than the one used in the present study. As the defect size undoubtedly influences the biomechanical stimuli that the graft receives, this could be the cause of the discrepancies between the two studies.

To determine more in depth the role of each bone graft in the bone regeneration process would require additional characterisation techniques [55], which are beyond the scope of this study. For instance, performing immunohistochemical staining of some selected decalcified samples would allow to better assess the osteoclastic activity around the BG granules and better understand the resorption process in both conditions. Additionally, by real-time polymerase chain reaction (qPCR) the gene expression of key genes for bone regeneration (*e.g.* type I collagen, ALP, osteonectin, osteocalcin, BMP-2, osteopontin) could be quantitatively assessed and compared between the two BGs.

One last aspect to consider, regarding the scope and limitations of this study, is that we opted to perform standardised defects, in order to guarantee a more comparable scenario and reduce as much as possible the variability associated with defect morphology. However, this is achieved at the expense of renouncing to use a chronified model, which would be more representative of the common clinical situation. Moreover, it would be interesting to address the mechanical stability of the grafted region and the interaction with dental implants, which are important aspects of the bone graft performance that should be considered in future studies.

In summary, the efficacy of two commercially available bone grafts was assessed in a preclinical study, mimicking the clinical setup of a three-wall defect in the alveolar crest. The two BGs analyzed showed excellent osteoconduction, guiding the formation of new bone in the defect. Additionally, the results obtained from the three-dimensional CT Scan analysis revealed that volume preservation was better achieved with the biomimetic synthetic graft, suggesting that the morphology of the granules plays an important role in this respect.

2.5 References

[1] R. L. Duncan and C. H. Turner, “Mechanotransduction and the functional response of bone to mechanical strain” *Calcif. Tissue Int.*, vol. 57, no. 5, pp. 344–358, Nov. 1995, doi: 10.1007/BF00302070.

[2] M. G. Araujo and J. Lindhe, “Dimensional ridge alterations following tooth extraction. An experimental study in the dog” *J. Clin. Periodontol.*, vol. 32, no. 2, pp. 212–218, Feb. 2005, doi: 10.1111/j.1600-051X.2005.00642.x.

[3] M. Esposito, M. G. Grusovin, P. Coulthard, and H. V Worthington, “The efficacy of various bone augmentation procedures for dental implants: a Cochrane systematic review of randomized controlled clinical trials” *Int. J. Oral Maxillofac. Implants*, vol. 21, no. 5, pp. 696–710.

[4] A. S. Greenwald, S. D. Boden, V. M. Goldberg, Y. Khan, C. T. Laurencin, and R. N. Rosier, “Bone-Graft Substitutes: Facts, Fictions, and Applications” *J. Bone Jt. Surgery-American Vol.*, vol. 83, pp. 98–103, 2001, doi: 10.2106/00004623-200100022-00007.

[5] D. I. Zeugolis, M. Keeney, E. Collin, G. Fontana, and A. Pandit, “Xenogenic Tissues and Biomaterials for the Skeletal System” in *Comprehensive Biomaterials*, vol. 2, Elsevier, 2011, pp. 387–404.

[6] C. Kunert-Keil, T. Gredes, and T. Gedrange, “Biomaterials Applicable for Alveolar Sockets Preservation: In Vivo and In Vitro Studies” in *Implant Dentistry - The Most Promising Discipline of Dentistry*, InTech, 2011.

[7] H. V. Precheur, “Bone Graft Materials” *Dent. Clin. North Am.*, vol. 51, no. 3, pp. 729–746, 2007, doi: 10.1016/j.cden.2007.03.004.

[8] M.-P. Ginebra, M. Espanol, Y. Maazouz, V. Bergez, and D. Pastorino, “Bioceramics and bone healing” *EFORT Open Rev.*, vol. 3, no. 5, pp. 173–183, May 2018, doi: 10.1302/2058-5241.3.170056.

[9] J. M. Sadowska, F. Wei, J. Guo, J. Guillem-Marti, M.-P. Ginebra, and Y. Xiao, “Effect of nano-structural properties of biomimetic hydroxyapatite on osteoimmunomodulation” *Biomaterials*, vol. 181, no. July, pp. 318–332, Oct. 2018, doi: 10.1016/j.biomaterials.2018.07.058.

[10] A. Barba *et al.*, “Osteogenesis by foamed and 3D-printed nanostructured calcium phosphate scaffolds: Effect of pore architecture” *Acta Biomater.*, vol. 79, no. 2, pp. 135–147, Oct. 2018, doi: 10.1016/j.actbio.2018.09.003.

[11] A. Barba *et al.*, “Osteoinduction by Foamed and 3D-Printed Calcium Phosphate Scaffolds: Effect of Nanostructure and Pore Architecture” *ACS Appl. Mater. Interfaces*, vol. 9, no. 48, pp. 41722–41736, Dec. 2017, doi: 10.1021/acsami.7b14175.

[12] R. Kirmeier, M. Payer, M. Wehrschuetz, N. Jakse, S. Platzer, and M. Lorenzoni, “Evaluation of three-dimensional changes after sinus floor augmentation with different grafting materials” *Clin. Oral Implants Res.*, vol. 19, no. 4, pp. 366–372, Apr. 2008, doi: 10.1111/j.1600-0501.2007.01487.x.

[13] F. Mazzocco, D. Lops, L. Gobbato, A. Lolato, E. Romeo, and M. Del Fabbro, “Three-Dimensional Volume Change of Grafted Bone in the Maxillary Sinus” *Int. J. Oral Maxillofac. Implants*, vol. 29, no. 1, pp. 178–184, 2014, doi: 10.11607/jomi.3236.

[14] A. F. Schilling *et al.*, “Resorbability of bone substitute biomaterials by human osteoclasts” *Biomaterials*, vol. 25, no. 18, pp. 3963–3972, Aug. 2004, doi: 10.1016/j.biomaterials.2003.10.079.

[15] J. M. Sadowska and M.-P. Ginebra, “Inflammation and biomaterials: role of the

immune response in bone regeneration by inorganic scaffolds" *J. Mater. Chem. B*, vol. 8, no. 41, pp. 9404–9427, 2020, doi: 10.1039/D0TB01379J.

[16] M. V. Thomas and D. A. Puleo, "Infection, inflammation, and bone regeneration: A paradoxical relationship" *J. Dent. Res.*, vol. 90, no. 9, pp. 1052–1061, 2011, doi: 10.1177/0022034510393967.

[17] K. D. Hankenson, M. Dishowitz, C. Gray, and M. Schenker, "Angiogenesis in bone regeneration" *Injury*, vol. 42, no. 6, pp. 556–561, 2011, doi: 10.1016/j.injury.2011.03.035.

[18] B. Flautre, M. Descamps, C. Delecourt, M. C. Blary, and P. Hardouin, "Porous HA ceramic for bone replacement: role of the pores and interconnections - experimental study in the rabbit." *J. Mater. Sci. Mater. Med.*, vol. 12, no. 8, pp. 679–82, Aug. 2001, doi: https://doi.org/10.1023/A:1011256107282.

[19] L. E. Rustom *et al.*, "Multiscale Porosity Directs Bone Regeneration in Biphasic Calcium Phosphate Scaffolds" *ACS Biomater. Sci. Eng.*, vol. 3, no. 11, pp. 2768–2778, 2017, doi: 10.1021/acsbiomaterials.6b00632.

[20] L. L. Hench and J. Wilson, *An Introduction to Bioceramics*. World Scientific Pub Co Inc, 1993.

[21] A. Hoornaert *et al.*, "Vertical Bone Regeneration with Synthetic Biomimetic Calcium Phosphate onto the Calvaria of Rats" *Tissue Eng. Part C Methods*, vol. 25, no. 1, pp. 1–11, Jan. 2019, doi: 10.1089/ten.tec.2018.0260.

[22] A. R. Rissolo and J. Bennett, "Bone grafting and its essential role in implant dentistry" *Dent. Clin. North Am.*, vol. 42, no. 1, pp. 91–116, Jan. 1998, Accessed: Apr. 12, 2017.

[23] Y. Uchida, M. Goto, T. Katsuki, and Y. Soejima, "Measurement of maxillary sinus volume using computerized tomographic images" *Int. J. Oral Maxillofac. Implants*, vol. 13, no. 6, pp. 811–8, 1998.

[24] M. Doube *et al.*, "BoneJ: Free and extensible bone image analysis in ImageJ" *Bone*, vol. 47, no. 6, pp. 1076–1079, Dec. 2010, doi: 10.1016/j.bone.2010.08.023.

[25] J. C. Pinheiro and D. M. Bates, *Mixed-Effects Models in S and S-PLUS*. New York: Springer-Verlag, 2000.

[26] T. G. Bromage, H. M. Goldman, S. C. McFarlin, J. Warshaw, A. Boyde, and C. M. Riggs, "Circularly polarized light standards for investigations of collagen fiber orientation in bone" *Anat. Rec.*, vol. 274B, no. 1, pp. 157–168, Sep. 2003, doi: 10.1002/ar.b.10031.

[27] M. P. Ginebra *et al.*, "Setting Reaction and Hardening of an Apatitic Calcium Phosphate Cement" *J. Dent. Res.*, vol. 76, no. 4, pp. 905–912, Apr. 1997, doi: 10.1177/00220345970760041201.

[28] N. Roveri and M. Iafisco, "Evolving application of biomimetic nanostructured hydroxyapatite" *Nanotechnol. Sci. Appl.*, p. 107, Nov. 2010, doi: 10.2147/NSA.S9038.

[29] T. Jemt and U. Lekholm, "Measurements of Buccal Tissue Volumes at Single-Implant Restorations after Local Bone Grafting in Maxillas: A 3-Year Clinical Prospective Study Case Series" *Clin. Implant Dent. Relat. Res.*, vol. 5, no. 2, pp. 63–70, Aug. 2003, doi: 10.1111/j.1708-8208.2003.tb00185.x.

[30] P. V. P. Oltramari *et al.*, "Evaluation of bone height and bone density after tooth extraction: an experimental study in minipigs" *Oral Surgery, Oral Med. Oral Pathol. Oral Radiol. Endodontology*, vol. 104, no. 5, pp. e9–e16, Nov. 2007, doi: 10.1016/j.tripleo.2007.06.015.

[31] B. Ruehe, S. Niehues, S. Heberer, and K. Nelson, "Miniature pigs as an animal model

for implant research: bone regeneration in critical-size defects" *Oral Surgery, Oral Med. Oral Pathol. Oral Radiol. Endodontology*, vol. 108, no. 5, pp. 699–706, Nov. 2009, doi: 10.1016/j.tripleo.2009.06.037.

[32] C. E. Misch and J. B. Suzuki, "Tooth Extraction, Socket Grafting, and Barrier Membrane Bone Regeneration" in *Contemporary Implant Dentistry*, 3rd ed., 2008, pp. 870–904.

[33] Y. Li, S.-K. Chen, L. Li, L. Qin, X.-L. Wang, and Y.-X. Lai, "Bone defect animal models for testing efficacy of bone substitute biomaterials" *J. Orthop. Transl.*, vol. 3, no. 3, pp. 95–104, Jul. 2015, doi: 10.1016/j.jot.2015.05.002.

[34] S. Wang, Y. Liu, D. Fang, and S. Shi, "The miniature pig: a useful large animal model for dental and orofacial research" *Oral Dis.*, vol. 13, no. 6, pp. 530–537, Nov. 2007, doi: 10.1111/j.1601-0825.2006.01337.x.

[35] A. Dasmah, A. Thor, A. Ekestubbe, L. Sennerby, and L. Rasmusson, "Particulate vs. block bone grafts: Three-dimensional changes in graft volume after reconstruction of the atrophic maxilla, a 2-year radiographic follow-up" *J. Cranio-Maxillofacial Surg.*, vol. 40, no. 8, pp. 654–659, Dec. 2012, doi: 10.1016/j.jcms.2011.10.032.

[36] T. Jensen *et al.*, "Volumetric changes of the graft after maxillary sinus floor augmentation with Bio-Oss and autogenous bone in different ratios: a radiographic study in minipigs" *Clin. Oral Implants Res.*, vol. 23, no. 8, pp. 902–910, Aug. 2012, doi: 10.1111/j.1600-0501.2011.02245.x.

[37] D. Salem, A. Alshihri, E. Arguello, R. Jung, H. Mohmed, and B. Friedland, "Volumetric Analysis of Allogeneic and Xenogeneic Bone Substitutes Used in Maxillary Sinus Augmentations Utilizing Cone Beam Computed Tomography: A Prospective Randomized Pilot Study" *Int. J. Oral Maxillofac. Implants*, vol. 34, no. 4, pp. 920–926, Jul. 2019, doi: 10.11607/jomi.7318.

[38] F. Younes, J. Cosyn, T. De Bruyckere, R. Cleymaet, and A. Eghbali, "A 2-year prospective case series on volumetric changes, PROMs, and clinical outcomes following sinus floor elevation using deproteinized bovine bone mineral as filling material" *Clin. Implant Dent. Relat. Res.*, vol. 21, no. 2, pp. 301–309, 2019, doi: 10.1111/cid.12730.

[39] A. Mordenfeld, M. Hallman, C. B. Johansson, and T. Albrektsson, "Histological and histomorphometrical analyses of biopsies harvested 11 years after maxillary sinus floor augmentation with deproteinized bovine and autogenous bone" *Clin. Oral Implants Res.*, pp. 961–970, May 2010, doi: 10.1111/j.1600-0501.2010.01939.x.

[40] S. Sakka and P. Coulthard, "Bone Quality: A Reality for the Process of Osseointegration" *Implant Dent.*, vol. 18, no. 6, pp. 480–485, Dec. 2009, doi: 10.1097/ID.0b013e3181bb840d.

[41] J.-Y. Rho, L. Kuhn-Spearing, and P. Zioupos, "Mechanical properties and the hierarchical structure of bone" *Med. Eng. Phys.*, vol. 20, no. 2, pp. 92–102, Mar. 1998, doi: 10.1016/S1350-4533(98)00007-1.

[42] A. Barba *et al.*, "Impact of Biomimicry in the Design of Osteoinductive Bone Substitutes: Nanoscale Matters" *ACS Appl. Mater. Interfaces*, vol. 11, no. 9, pp. 8818–8830, 2019, doi: 10.1021/acsami.8b20749.

[43] E. Cuzmar, R. A. Perez, M.-C. Manzanares, M.-P. Ginebra, and J. Franch, "In Vivo Osteogenic Potential of Biomimetic Hydroxyapatite/Collagen Microspheres: Comparison with Injectable Cement Pastes" *PLoS One*, vol. 10, no. 7, p. e0131188, Jul. 2015, doi: 10.1371/journal.pone.0131188.

[44] R. Mai *et al.*, "Histologic study of incorporation and resorption of a bone cement–collagen composite: an in vivo study in the minipig" *Oral Surgery, Oral Med. Oral*

Pathol. Oral Radiol. Endodontology, vol. 105, no. 3, pp. e9–e14, Mar. 2008, doi: 10.1016/j.tripleo.2007.09.016.

[45] A. Skoglund, P. Hising, and C. Young, “A Clinical and Histologic Examination in Humans of the Osseous Response to Implanted Natural Bone Mineral” *Int. J. Oral Maxillofac. Implants*, vol. 12, no. 2, pp. 194–199, 1997.

[46] M. Duda and J. Pajak, “The issue of bioresorption of the Bio-Oss xenogeneic bone substitute in bone defects” *Ann Univ Mariae Curie Sklodowska Med.*, vol. 59(1), pp. 269–77, 2004.

[47] A. Schlegel and K. Donath, “BIO-OSS® - A resorbable bone substitute?” *J. Long. Term. Eff. Med. Implants*, vol. 8 3–4, pp. 201–9, 1998.

[48] M. Hallman, A. Cederlund, S. Lindskog, S. Lundgren, and L. Sennerby, “A clinical histologic study of bovine hydroxyapatite in combination with autogenous bone and fibrin glue for maxillary sinus floor augmentation: Results after 6 to 8 months of healing” *Clin. Oral Implants Res.*, vol. 12, no. 2, pp. 135–143, 2001, doi: 10.1034/j.1600-0501.2001.012002135.x.

[49] E. S. Tadjoedin, G. L. De Lange, A. L. J. J. Bronckers, D. M. Lyaruu, and E. H. Burger, “Deproteinized cancellous bovine bone (Bio-Oss®) as bone substitute for sinus floor elevation. A retrospective, histomorphometrical study of five cases” *J. Clin. Periodontol.*, vol. 30, no. 3, pp. 261–270, 2003, doi: 10.1034/j.1600-051X.2003.01099.x.

[50] D. Zaffe, G. C. Leghissa, J. Pradelli, and A. R. Botticelli, “Histological study on sinus lift grafting by Fisiograft and Bio-Oss” *J. Mater. Sci. Mater. Med.*, vol. 16, no. 9, pp. 789–793, 2005, doi: 10.1007/s10856-005-3574-5.

[51] S. E. McAllister, Bradley S.; Margolin, Mark D.; Cogan, Allan G.; Buck, Dave; Hollinger, Jeffrey O.; Lynch, “Eighteen-Month Radiographic and Histologic Evaluation of Sinus Grafting with Anorganic Bovine Bone in the Chimpanzee” *Int. J. Oral Maxillofac. Implants*, vol. 14, no. 3, pp. 361–368, 1999.

[52] S. Sartori, M. Silvestri, F. Forni, A. Icaro Cornaglia, P. Tesei, and V. Cattaneo, “Ten-year follow-up in a maxillary sinus augmentation using anorganic bovine bone (Bio-Oss). A case report with histomorphometric evaluation” *Clin. Oral Implants Res.*, vol. 14, no. 3, pp. 369–372, May 2003, doi: 10.1034/j.1600-0501.2003.140316.x.

[53] M. G. Araújo, D. Carmagnola, T. Berglundh, B. Thilander, and J. Lindhe, “Orthodontic movement in bone defects augmented with Bio-Oss®. An experimental study in dogs” *J. Clin. Periodontol.*, vol. 28, no. 1, pp. 73–80, 2001, doi: 10.1034/j.1600-051x.2001.280111.x.

[54] E. Rumpel *et al.*, “The biodegradation of hydroxyapatite bone graft substitutes in vivo” *Folia Morphol. (Warsz).*, vol. 65, no. 1, pp. 43–48, 2006.

[55] G. S. Stein and J. B. Lian, “Molecular Mechanisms Mediating Proliferation/Differentiation Interrelationships During Progressive Development of the Osteoblast Phenotype” *Endocr. Rev.*, vol. 14, no. 4, pp. 424–442, Aug. 1993, doi: 10.1210/edrv-14-4-424.

2.6 Supplementary Information

Detailed information on the statistical analysis performed to the CT scan volumetric quantification of percent variation of the grafted volume (ΔV) is supplied in this appendix.

2.6.1 Least Squares Assumptions Validation

The residuals for the percent variation of the grafted volume were examined to verify if the ordinary least squares assumptions were being met and consequently, we could validate the use of a linear regression model. The linearity observed in the normal probability plot (**Fig. S2.1 A**) and the normal distribution observed in the histogram (**Fig. S2.1 C**) validates the assumption that the errors do not derive substantially from a normal distribution. The residual versus fit plot (**Fig. S2.1 B**) evidences the presence of factor levels in the data and guarantees that all the errors of these factor levels have a similar and constant variance. Finally, the residual versus observation order plot guarantees that the errors are independent and thus, random (**Fig. S2.1 D**). This way, it was proved that the residuals were normally distributed, independent and had equal variances.

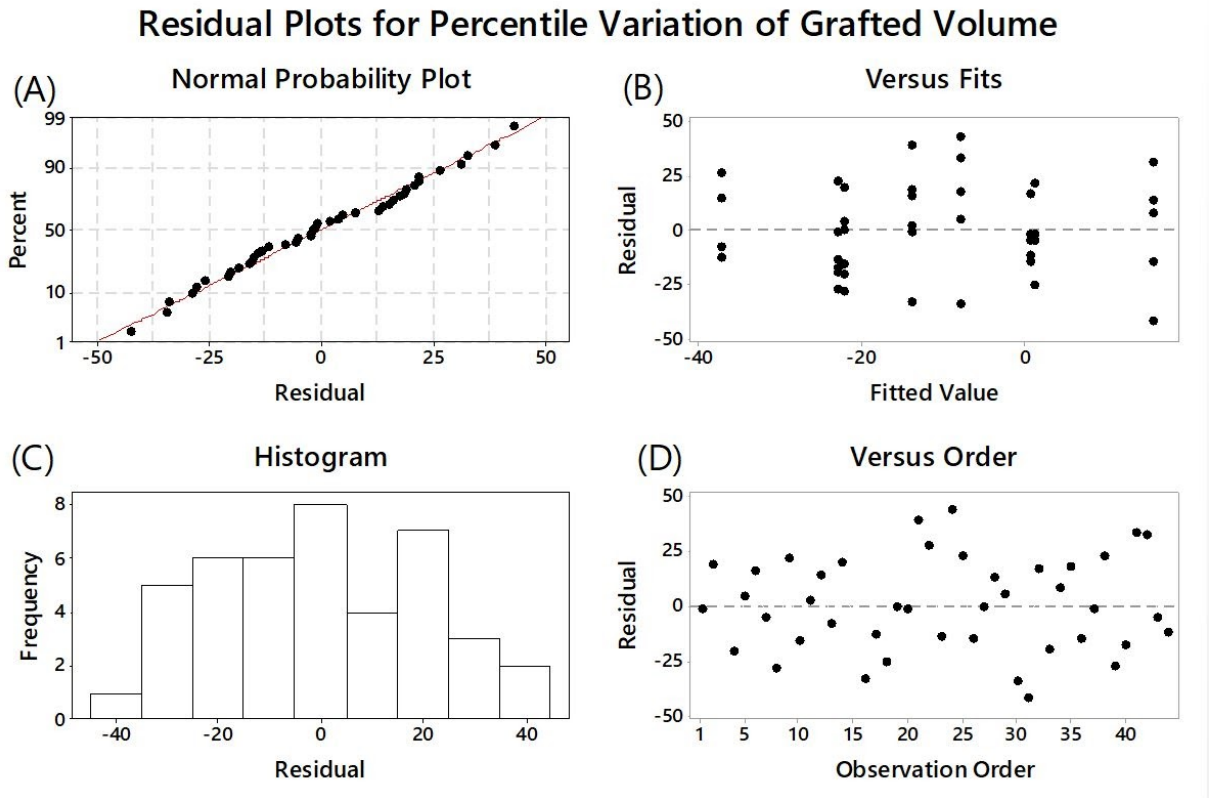

Fig. S2.1. A Normal probability plot of the residuals, **B** Residuals versus fits, **C** Histogram of the residuals and **D** Residuals versus observation order (animal).

2.6.2 Outlier test

Results of the outlier test performed on the data to remove from the model statistically significant outliers are shown in **Fig. S2.2**.

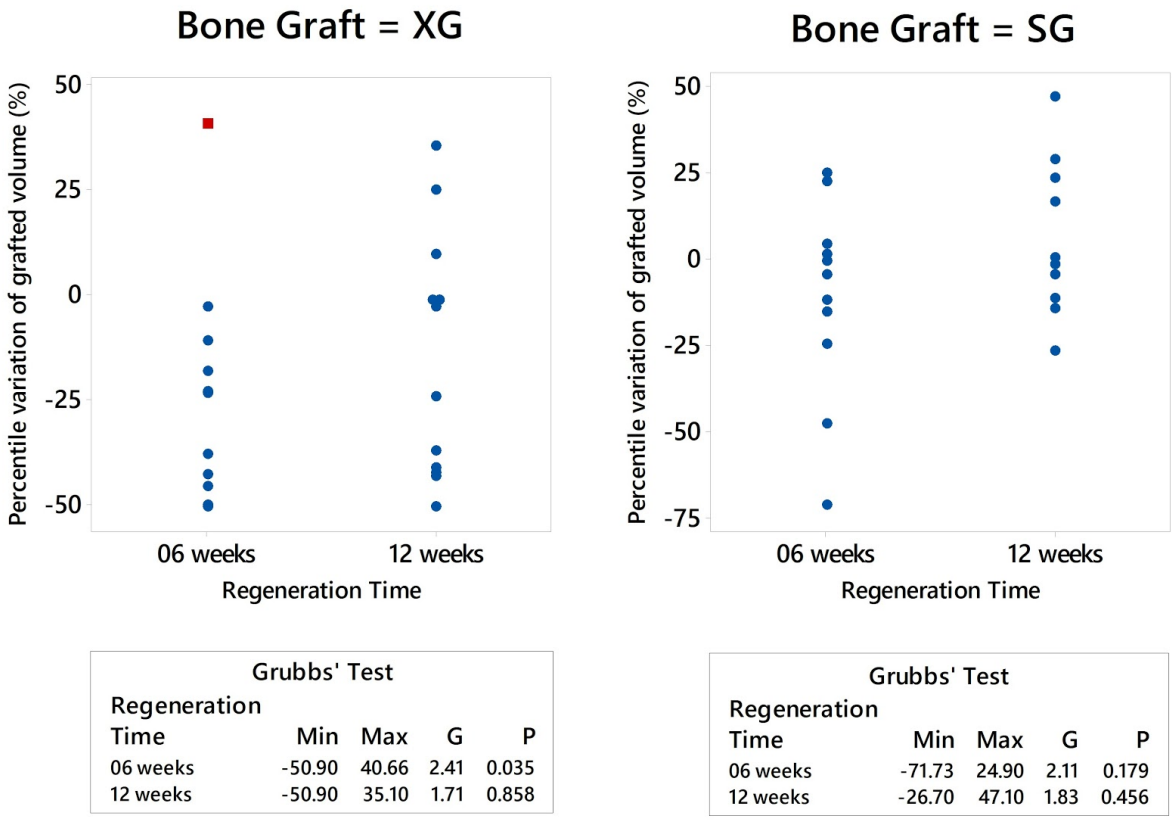

Grubbs' Test

Regeneration Time	Min	Max	G	P
06 weeks	-50.90	40.66	2.41	0.035
12 weeks	-50.90	35.10	1.71	0.858

Grubbs' Test

Regeneration Time	Min	Max	G	P
06 weeks	-71.73	24.90	2.11	0.179
12 weeks	-26.70	47.10	1.83	0.456

Fig. S2.2. Outlier test performed for the percentile variation of grafted volume data. Outliers indicated with red squared icons and not-outliers indicated with blue dots.

Table S2.1. Factors information including factor name, factor type (random or fixed), number of levels of each factor and values for these levels. The factor nesting arrangement implicit in the names of the factors and value (indicated in brackets).

Factor	Type	Levels	Values
Animal (Regeneration time)	Random	8	1(12w), 2(6w), 3(6w), 4(12w),5(12w), 6(6w), 7(12w), 8(6w)
Regeneration time	Fixed	2	12w, 6w
Jaw	Fixed	2	L, U
Anatomic site	Fixed	2	A, P
Bone graft	Fixed	2	SG, XG

Table S2.2. Outcome of the linear mixed-effects model fit considering all the factors, second- and third-order interactions.

Term	F-Value	P-Value
Regeneration time	1.70	0.203
Jaw	1.76	0.195
Anatomic site	2.52	0.124
Bone graft	2.92	0.099
Regeneration time*Jaw	1.36	0.253
Regeneration time*Anatomic site	2.83	0.103
Regeneration time*Bone graft	0.79	0.382
Jaw*Anatomic site	1.41	0.246
Jaw*Bone graft	0.30	0.587
Anatomic site*Bone graft	0.26	0.615
Regeneration time*Jaw*Anatomic site	0.03	0.866
Regeneration time*Jaw*Bone graft	0.36	0.555
Regeneration time*Anatomic site*Bone graft	0.01	0.929
Jaw*Anatomic site*Bone graft	0.19	0.666

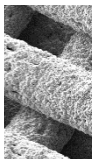

Table S2.3. Outcome of the linear mixed-effects model fit after removing all the non-significant third-order interactions.

Term	F-Value	P-Value
Regeneration time	3.85	0.059
Jaw	2.65	0.114
Anatomic site	6.62	0.015
Bone graft	4.74	0.037
Regeneration time*Jaw	3.65	0.065
Regeneration time*Anatomic site	4.01	0.054
Regeneration time*Bone graft	2.24	0.144
Jaw*Anatomic site	2.18	0.149
Jaw*Bone graft	0.49	0.487
Anatomic site*Bone graft	0.31	0.582

Table S2.4. Outcome of the linear mixed-effects model fit after removing all the non-significant third- and second-order interactions.

Term	F-Value	P-Value
Regeneration time	4.71	0.036
Jaw	1.04	0.314
Anatomic site	5.53	0.024
Bone graft	9.52	0.004

Table S2.5. Outcome of the linear mixed-effects model fit after removing all the non-significant interactions and factors.

Term	F-Value	P-Value
Regeneration time	4.67	0.037
Anatomic site	5.24	0.028
Bone graft	12.65	0.001

Table S2.6. Coefficients of the final linear mixed-effects regression fit.

Term	+ effect	- effect	Coef.	SE Coef.	DF	T-Value	P-Value
Constant	–	–	-10.841884	3.317823	39	-3.267770	0.002
Regeneration time	12w	6w	7.199971	3.332635	39	2.160444	0.037
Anatomic site	A	P	7.612659	3.325574	39	2.289126	0.028
Bone graft	SG	XG	11.826295	3.325574	39	3.556167	0.001

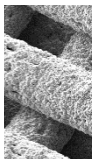

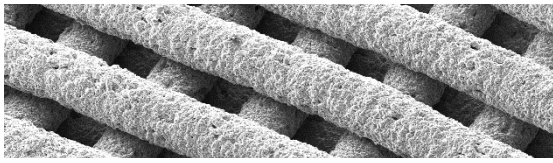

Chapter 3

Accelerated Hardening of Nanotextured 3D-Plotted Self-Setting Calcium Phosphate Inks

ACCELERATED HARDENING OF NANOTEXTURED 3D-PLOTTED SELF-SETTING CALCIUM PHOSPHATE INKS

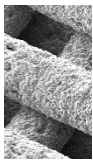

Abstract

Direct ink writing (DIW) techniques open up new possibilities for the fabrication of patient-specific bone grafts. Self-setting calcium phosphate inks, which harden at low temperature, allow obtaining nanostructured scaffolds with biomimetic properties and enhanced bioactivity. However, the slow hardening kinetics hampers the translation to the clinics. We explored different hydrothermal treatments for the consolidation of DIW scaffolds fabricated with an α-tricalcium phosphate/pluronic F127 ink, comparing them with a biomimetic treatment. Three different scaffold architectures were analysed. The hardening process, associated to the conversion of α-tricalcium phosphate to hydroxyapatite was drastically accelerated by the hydrothermal treatments, reducing the time for complete reaction from 7 days to 30 minutes, while preserving the scaffold architectural integrity and retaining the nanostructured features. β- tricalcium phosphate was formed as a secondary phase, and a change of morphology from plate-like to needle-like crystals in the hydroxyapatite phase was observed. The binder was largely released during the treatment. The hydrothermal treatment resulted in a 30% reduction of the compressive strength, associated to the residual presence of β-tricalcium phosphate. Biomimetic and hydrothermally treated scaffolds supported the adhesion and proliferation of rat mesenchymal stem cells, indicating a good suitability for bone tissue engineering applications.

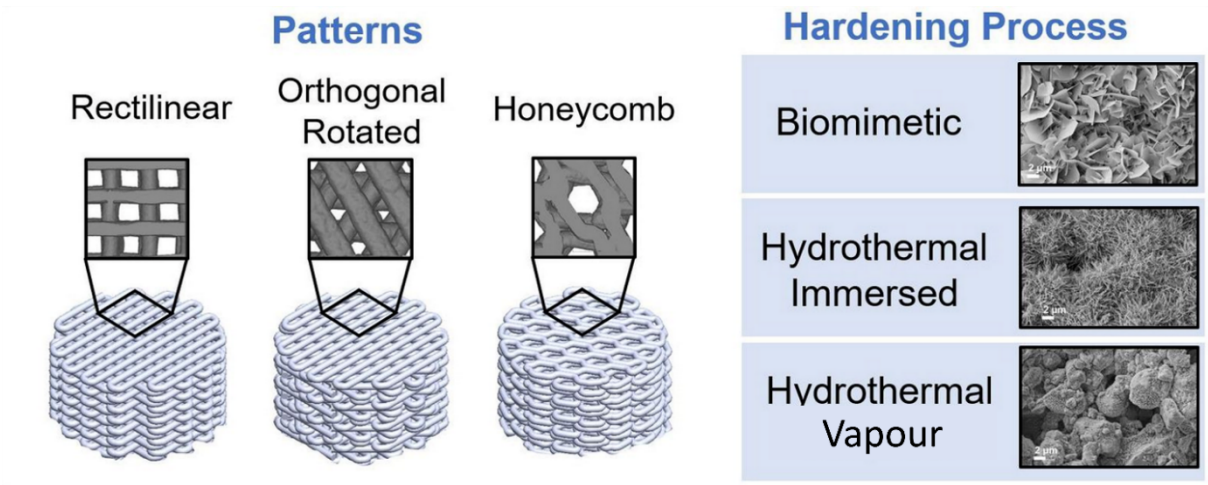

3.1 Introduction

The recent developments in three-dimensional (3D) printing technologies have opened vast opportunities for the development of patient-specific bone grafts, which is expected to have a particularly high impact on dental and maxillofacial surgery as well as in trauma and orthopaedic surgery. Whereas autologous or allogenic bone grafts are still the gold standard in the frequent bone grafting surgical procedures performed nowadays [1,2], the possibility to fabricate customised scaffolds based on digitalised medical imaging techniques has provided a real boost to the applications of synthetic bone grafts. The novel fabrication approaches referred to as 3D printing techniques are based on computer aided design (CAD) and computer aided manufacturing (CAM) and result in a patient-specific bone grafting therapy. Such technologies allow the design of personalised synthetic bone grafts, matching the specificity of every defect in terms of both the metabolic and anatomic characteristics, opening new perspectives in this field [3].

Previous works reported the use of such techniques employing polymers, ceramics, or even metal alloys [4,5]. In the case of bioceramics, the works revolve around either powder bed printing, which consists in dispensing a liquid binder or reactive fluid onto a powder bed in a layer by layer process [6], or in filament-based direct ink writing (DIW), also referred to as robocasting, microextrusion or three-dimensional plotting [7] which consists in dispensing layer by layer an ink composed of ceramic particles homogenously dispersed in a binder following an *in silico* designed pattern. The main advantage of filament-based direct ink writing over powder bed printing is that there is no need to clean the printed object from remaining particles from the bed that can provoke adverse inflammatory responses of the host tissue. The design of the inks plays a central part in this technology. They must present a pseudoplastic behaviour in order to withstand the weight of the superimposed layers and must be completely injectable, allowing a continuous printing [8]. Furthermore, by tailoring the ink composition it is possible to tune the physicochemical properties of the scaffolds in terms of chemistry, textural properties and multiscale porosity.

The use of DIW with calcium phosphate (CaP)-based inks for the fabrication of bone implants and scaffolds for bone tissue engineering was proposed for the first time in 2005 [9]. Several works have reported the fabrication and properties of robocasted scaffolds made of hydroxyapatite (HA) [9-11], beta tricalcium phosphate (β-TCP) [12, 13], biphasic combinations of β-TCP and HA [11,14-17] and bioactive glasses [18-24].

Nonetheless, in all these pioneer works, after DIW the samples had to be consolidated by sintering at high temperature. The effects of sintering conditions on the chemical, structural and mechanical properties of those samples have been deeply studied [11,16,25,26].

Recently, the possibility to fabricate low-temperature self-setting inks that do not require the sintering step has been proposed, using formulations based on beta-calcium silicate (β-$CaSiO_3$) [20,27], magnesium phosphates [28] or calcium phosphates [29,30]. Most calcium phosphate self-setting inks are based on alpha-tricalcium phosphate (α-TCP), which can be combined with different binders, like gelatine [29], type I collagen [31], hydroxypropyl methylcellulose (HPMC) [32], Polysorbate 80 (Tween 80) and short-chain triglycerides (Miglyol 812) [30,33,34], polyvinyl alcohol [33] and alginic acid [33].The hardening process of these inks is due to the hydrolysis of α-TCP to a calcium deficient hydroxyapatite (CDHA), resulting in nano/micro structured crystals that are much closer to the mineral phase of bone than

sintered CaPs. In this work, we propose to exploit the inverse-thermoresponsive properties of pluronic F127, using it as a new binder for an α-TCP self-setting ink. We showed in a previous work that the combination of pluronic F127 hydrogel with α-TCP resulted in a paste exhibiting a sequential gelling/hardening behaviour and enhanced injectability. Moreover, the presence of pluronic did not hinder the self-hardening reaction of α-TCP [35].

However, while the low-temperature chemical consolidation of these scaffolds allows obtaining a biomimetic product, closer to bone mineral than the high-temperature sintered scaffolds, the self-setting reaction of the α-TCP-based inks is slow, and therefore the hardening process of the 3D-printed scaffolds is long. This makes the translation of this technology to the clinic complex, and impairs its application, particularly in emergencies where time is valuable and limited. It is therefore necessary to accelerate the hardening process. With this objective in mind, in this work we analyse different post-printing treatments for DIW scaffolds fabricated with a pluronic F127/α-TCP self-setting ink, and their effect on the nano/microstructure, composition and mechanical performance, as well as on the ability to sustain the proliferation of mesenchymal stem cells.

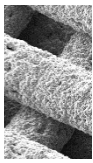

3.2 Materials and Methods

3.2.1 Preparation of the Self-setting Ink

The solid phase of the self-setting ink was composed of α-TCP synthesised as described elsewhere [36]. The α-TCP block was milled in an agate planetary ball mill (Fritsch, Pulverisette) during 15 min at 450 rpm with 10 agate balls (30 mm diameter). The resulting powder was then sieved during 30 min with a 40 μm sieve (Filtra, Spain), introducing 145 g of powder together with 200 g of Zirconia balls (1.5 mm diameter; Tosoh, Japan). The binder phase of the ink was prepared introducing 30 g of pluronic F127 (Sigma Aldrich P2443) together with 50 ml of distilled water in a 150 ml polypropylene (PP) recipient (Dürmann, Germany) and mixed in a dual asymmetric centrifugal mixer (DAC 150, Speedmixer, USA) at 3500 rpm during 1 min. Water was then added to a total volume of 100 ml and the mixture was homogenised in the DAC mixer at 3500 rpm for 5 min. The ceramic ink was finally produced by introducing 6 g of α-TCP powder together with 3 g of binder solution (binder to powder ratio of 0.5 g g^{-1}) into a PP recipient of 50 ml and mixed for 1 min at 3500 rpm in the DAC mixer.

3.2.2 Computer Aided Design and DIW Process

Cylindrical samples (6 mm diameter and 12 mm height) were designed with the help of a CAD software (Solidworks, Dassault Systems, France) and exported into a standard triangle language (STL) file. The resulting STL file was then transferred to the open-source software Slic3r (slic3r.org) in order to adjust the fabrication parameters. As described in **Fig. 3.1,** three patterns with different architectures were fabricated. The orthogonal pattern (O) corresponded to a 90° rotation at each layer of a linear parallel grid. The orthogonal rotated (OR) pattern corresponded to a 45° rotation at each layer of the linear parallel grid. The honeycomb (HC) pattern was composed of hemi-hexagonal segments which were rotated 120° at each layer, composing hexagons when the structure was projected onto the XY plane. In all cases the nozzle size (theoretical strand diameter) was set to 250 μm, the layer height to 225

μm (corresponding to a layer overlapping of 10% along the Z axis), the filling density was set to 45% and the deposition speed was set to 10 mm s^{-1}. This information was saved in a numerical control programming language (G-code).

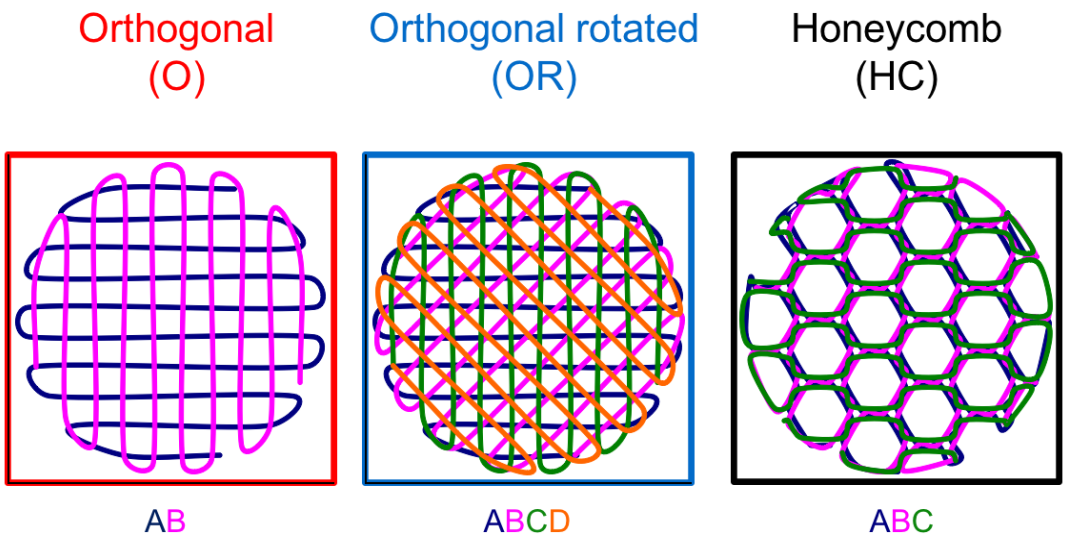

Fig. 3.1. Different patterns employed for the scaffolds.

Prior to printing the scaffolds, the self-setting ink was introduced into the cartridge (3cc Optimum® Syringe Barrels, Nordson EFD, U.S.A.). Then, a tapered dispending tip (Gauge 25 SmoothFlow Tapered Tips, Nordson EFD, U.S.A.) was coupled to the cartridge, and the whole assembly was installed into the DIW device (Pastecaster, Fundació CIM, Spain). Afterwards, batches of 15 scaffolds were fabricated at room temperature in a time span of 1.5 h.

3.2.3 Post-printing Hardening Treatments

The fabricated scaffolds were then subjected to three different post-printing processes, as described in **Fig. 3.2**: (a) biomimetic treatment, where the scaffolds were immersed in water at 37 ºC for up to 6 d, using a fixed volume of 100 ml per scaffold. Prior to immersion, the scaffolds were kept in a water vapour saturated atmosphere at 37 ºC for 24 h to ensure good cohesion; (b) hydrothermal-immersed treatment, where the specimens were immersed in water (100 ml per scaffold) and autoclaved at 121 ºC and 2 atm of absolute pressure for different time lengths, up to 30 min; (c) hydrothermal-vapour treatment, where the scaffolds were autoclaved at 121 ºC and 2 atm of absolute pressure for different time lengths, up to 100 min. Prior to both hydrothermal treatments, the specimens were kept in a vapour saturated atmosphere at 100 ºC and 1 atm for 10 min.

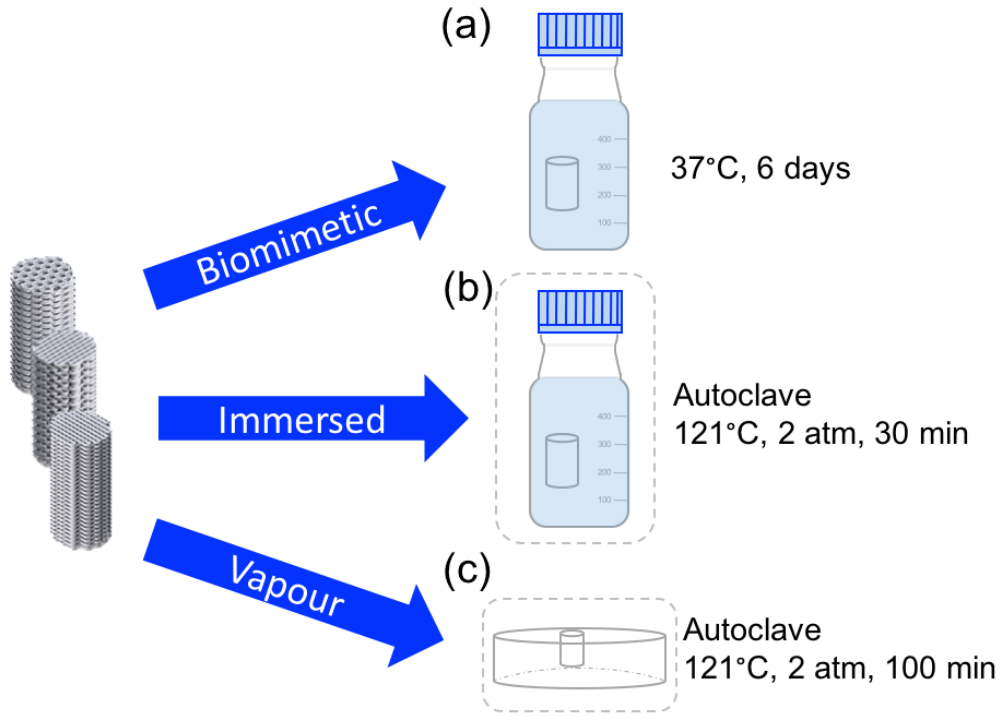

Fig. 3.2. Schematic representation of the different post-printing treatments tested in this study: **a** Biomimetic treatment, **b** Hydrothermal-immersed treatment, and **c** Hydrothermal-vapour treatment.

3.2.4 Scaffold Characterisation – Phase Composition and Microstructure

Phase composition was assessed at different reaction times by X-ray powder diffraction on the powder obtained for each hardening condition after manually crushing the scaffolds in an agate mortar. In the case of scaffolds subjected to the biomimetic treatment, samples were immersed in isopropanol during 15 min prior to the analysis to stop the hardening reaction at selected times. The diffractometer (D8 Advance, Bruker) equipped with a Cu Kα X-ray tube was operated at 40 kV and 40 mA. Data were collected in 0.02° steps over the 2θ range of 10–80° with a counting time of 2 s per step. Phase quantification was performed using the reference intensity ratio method (EVA, Bruker) comparing diffraction patterns of the crystalline structures of α-TCP (ICDD PDF 00-029-0359), CDHA (ICDD PDF 01-086-1201) and β-TCP (ICDD PDF 00-003-0681).

The microstructure of the scaffolds hardened in different conditions was observed under a field emission scanning electron microscope (FIB/SEM, Zeiss Neon 40) at 5 kV, after coating the surface with a thin carbon layer.

3.2.5 Scaffold Characterisation – Scaffold Architecture, Porosity and Specific Surface Area

X-ray computed microtomography (μ-CT) analysis was conducted using the GE phoenix v|tome|x L 240 system equipped with a 180 kV/20 W maximum power nanofocus X-ray tube and high contrast flat panel detector DXR250. The tomographic measurement was performed with an acceleration voltage of 80 kV and an X-ray current of 150 μA. The X-ray spectrum of tungsten target was modified by using a 0.5 mm thick aluminium filter. The exposure time per projection was 400 ms and 1800 projections were taken around 360°. The isotropic linear voxel size (voxel resolution) of the obtained volume was 15 μm. The sample tomographic reconstruction was performed with GE phoenix datos|x 2.0 software, using the object shifting correction and the beam hardening correction in the different material modes. The visualisation of the samples, as well as the structural parameter quantifications, were performed using VG Studio MAX 2.2 software. Three scaffolds were scanned at the same time allowing the use of the same threshold values for segmentation. Surface determination tool within VG Studio was used to display the sample volume in virtual reconstructions.

In addition, open porosity and pore entrance size distribution were analysed in the range between 0.006 and 360 μm by mercury intrusion porosimetry (MIP, AutoPore IV Micromeritics). The volume of nano-micropores normalised per unit of mass (V_{micro}) was measured from the sum of the incremental mercury intrusion in the pores smaller than 10 μm. The skeletal density of the scaffolds (ρ_{skel}) was assessed by helium pycnometry (AccuPyc 1330, Micromeritics, USA). The apparent density of the scaffolds (ρ_{app}) was calculated as the quotient of the scaffold mass over the scaffold equivalent cylinder volume obtained from the measurements of the scaffold diameter and height. The value of the total porosity (P_{TOT}) was calculated with the **Equation 3.1** [37]:

$$P_{TOT}(\%) = \left(1 - \frac{\rho_{app}\left[\frac{g}{cm^3}\right]}{\rho_{skel}\left[\frac{g}{cm^3}\right]}\right) \cdot 100 \qquad \textbf{Equation 3.1}$$

The nano-microporosity (P_{micro}) was calculated with the **Equation 3.2**:

$$P_{micro}(\%) = \left(V_{micro}\left[\frac{cm^3}{g}\right] \cdot \rho_{app}\ \left[\frac{g}{cm^3}\right]\right) \cdot 100 \qquad \textbf{Equation 3.2}$$

The macroporosity (P_{macro}) was calculated as the difference between the total porosity and the nano-micro porosity (**Equation 3.3**)

$$P_{macro}(\%) = P_{TOT}(\%) - P_{micro}(\%) \qquad \textbf{Equation 3.3}$$

Finally, the specific surface area (SSA) was determined by nitrogen adsorption using the BET (Brunauer-Emmett-Teller) method (ASAP 2020, Micromeritics). Prior to measurement, samples were outgassed in vacuum conditions (10 mmHg) at a holding temperature of 100 ºC for 2 h.

3.2.6 Scaffold Characterisation – Binder Content Thermogravimetric Analysis and FTIR

Thermogravimetric analysis (TGA) was performed with the aim to determine the amount of binder remaining in the scaffolds after the different consolidation methods. The measurements were performed under the heating rate of 10 ºC min^{-1} from 25 to 550 ºC in an oxygen saturated atmosphere. The amount of polymer contained in the scaffolds was determined by comparing the TGA curves of each sample with those of a pluronic-free counterpart, consisting of α-TCP mixed with water with the same L/P ratio and subjected to the same treatment as the corresponding sample.

Fourier-transform infrared spectroscopy (FTIR) analysis was performed in a Nicolet 6700 FTIR spectrometer using the KBr pellet method using 2 mg sample per 300 mg KBr. Spectra were recorded in the 4000 to 400 cm^{-1} range, at 128 scans accumulation and 2 cm^{-1} resolution.

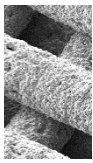

3.2.7 Scaffold Characterisation – Mechanical Characterisation

A universal testing machine (Bionix, MTS) was employed to perform uniaxial compressive tests at a rate of 1 mm min^{-1}. The load was applied perpendicular to the printing plane (XY plane), *i.e.* in the Z direction. HC patterned scaffolds subjected to different post-printing treatments were tested, as well as scaffolds fabricated with different pattern architectures and hardened under biomimetic conditions. Samples were tested in wet state in order to be closer to the *in vivo* situation. A total of 12 scaffolds were tested for each condition. The Weibull modulus was calculated applying a Weibull statistical analysis on the ultimate compressive stress values (**Equation 3.4**).

$$Ln\left(Ln\left(\frac{1}{P_s}\right)\right) = m(Ln(\sigma) - Ln(\sigma_0)) \qquad \textbf{Equation 3.4}$$

Where:

P_s = Probability of survival

σ = ultimate compressive strength of the sample

σ_0 = constant corresponding to the stress for which 100% of the samples will not fail

m = Weibull modulus

3.2.8 Scaffold Characterisation – Cell Culture

The influence of the post-printing treatment on cell response was studied in static 3D culture conditions in samples fabricated with O architecture. Scaffolds (discs of 6 mm in diameter and 2 mm in height) were placed in 24-well cell culture plates, sterilised with ethanol (70%, Sigma and Aldrich) during 30 min and rinsed 3 times with phosphate-buffered saline (PBS, Gibco). Samples were then preconditioned for 2 h with 1 ml of advanced Dulbecco's Modified Eagle Medium supplemented with 10% fetal bovine serum, 2 mM L-glutamine, 50 U ml^{-1} penicillin, 50 µg ml^{-1} streptomycin and 20 mM HEPES. Afterwards, the medium was removed and $5x10^5$ rat mesenchymal stem cells (rMSC; extracted from bone marrow of long bones of Lewis

rats; in passages 3 to 5) were seeded on each scaffold in a 25 µl medium drop. rMSC were allowed to attach during 1 h at 37 °C and 5% CO_2 and then 1 ml of fresh medium was gently added. After 3 and 7 d of static cell culture, the scaffolds were moved to a new well plate, rinsed with PBS and the remaining cells on the scaffolds were lysed with 500 µl of M-PER (mammalian protein extraction reagent, Thermo Scientific, Waltham, MA, USA). The cell number was quantified using a commercial lactate dehydrogenase (LDH) detection kit (Roche Applied Science, Penzberg, Germany). The LDH activity in the lysates was measured spectrophotometrically at a wavelength of 492 nm with PowerWave HT Microplate Reader (BioTek Instruments, Inc., Winooski, VT). A calibration curve with decreasing number of cells was used to express the results of LDH activity in cell number. Experiments were performed in triplicates for statistical analysis.

Immunofluorescent staining was used to visualise cell morphology. After 7 d of culture the scaffolds were rinsed in PBS–glycine and cells were fixed for 20 min in 4% paraformaldehyde solution. Cells were permeabilised for 15 min with Triton X-100 (0.05%) and blocked for 30 min in PBS–bovine serum albumin (BSA; 1%). Actin filaments were stained with TRITC-conjugated phalloidin (Sigma-Aldrich, USA) and nuclei were counterstained with DAPI (4',6-diamidino-2-phenylindole, 1 µg ml^{-1}). Images were acquired with an E600 fluorescence microscope (Nikon, Japan) and treated with Cell F software (Olympus, Japan).

3.2.9 Statistical analysis

Data were analysed using one-way analysis of variance and Tukey's multiple-comparison test to determine statistical differences between specimens. A confidence interval of 95% (α=0.05) was used and the resulting means and standard deviations are shown in **Figs. 3.8** and **3.11**.

3.3 Results and Discussion

3.3.1 Effect of the Post-printing Treatment on Composition, Microstructure and Porosity

The hardening of the scaffolds is associated to the hydrolysis of the α-TCP contained in the ink, which transforms to a calcium deficient hydroxyapatite (CDHA) according to the following reaction (**Equation 3.5**):

$$3\alpha\text{-}Ca_3(PO_4)_2\ (s) + H_2O\ (l) \rightarrow Ca_9(HPO_4)(PO_4)_5OH\ (s) \qquad \textbf{Equation 3.5}$$

The reaction mechanism involves the dissolution of the α-TCP particles followed by the nucleation and growth of CDHA crystals. This mechanism has been extensively studied in the field of calcium phosphate cements for the development of injectable bone grafting materials [38,39]. Moreover, in a previous work we demonstrated that the addition or pluronic F127 in α-TCP pastes slightly delayed the setting reaction in the early stages but did not hinder the full transformation to calcium-deficient hydroxyapatite [35]. The results obtained with the robocast scaffolds confirm these results since, as shown in **Fig. 3.3 a**, under biomimetic conditions α-TCP fully transformed to CDHA in 3 to 7 days.

The hydrolysis of α-TCP under hydrothermal-immersed conditions (**Fig. 3.3 b**) displayed similarities with respect to the biomimetic conditions. However, the time required to yield the maximum conversion into CDHA decreased to 15 min. The faster reaction kinetics is in agreement with previous studies which report that hydrolysis of α-TCP occurs more rapidly at increased temperatures [40,41], and must be interpreted taking into account the retrograde solubility of both α-TCP and hydroxyapatite [42, 43]. Thus, although the solubility of α-TCP is smaller at the higher temperature of the hydrothermal treatment, also the solubility of CDHA is reduced, thus fostering the precipitation of this compound and resulting in a higher reaction rate. Furthermore, β-TCP appeared as a result of the treatment, indicating that while α-TCP reacted to form CDHA, α-TCP also underwent allotropic phase transformation to form its low-temperature beta polymorph. As a result, the yield in CDHA formation was reduced to around 90%.

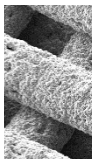

The final composition of the scaffolds after the hydrothermal-vapour condition was significantly different from the other two treatments (**Fig. 3.3 c**). In this case, the final composition of the scaffold consisted in a mixture of CDHA (60%), β-TCP (17%) and unreacted α-TCP (23%). The reaction time was around 60 min.

The formation of β-TCP as a second phase in addition to CDHA after the hydrothermal treatment of α-TCP was reported in previous studies [44], although longer treatment times were applied. The formation of β-TCP was surprising since this phase is generally obtained by solid state reaction above 700 ºC. The results obtained suggest that the pressure applied lowers the transition temperature between the β and α-TCP, which is close to 1120 ºC, thus favouring the allotropic transformation of α-TCP into β-TCP. This transformation coexists with the hydrolysis of α-TCP to CDHA.

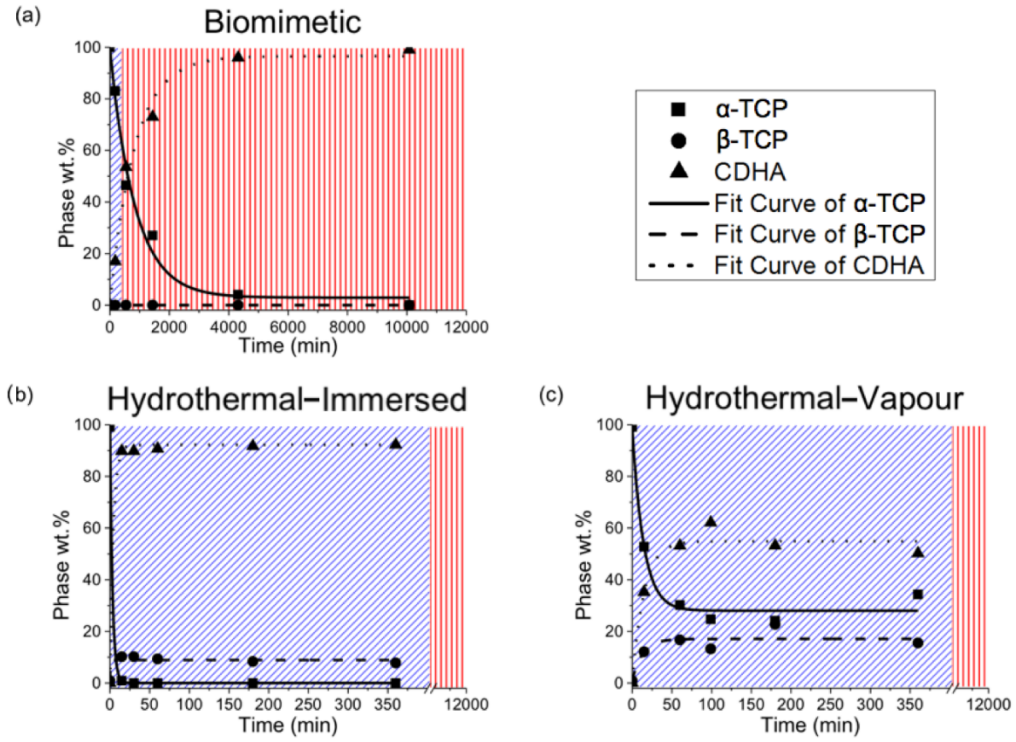

Fig. 3.3. Phase transformation kinetics determined by XRD analysis for the different hardening conditions.

The post-printing treatment affected not only the phase transformation taking place in the scaffolds, but also the presence of binder after its consolidation. The nominal amount of binder added in the ink was calculated to be 14.3 wt.%. The binder remaining in the scaffolds after the different post-printing treatments, once the phase transformation was complete (7 d, 30 min and 100 min for the biomimetic, hydrothermal-immersed and hydrothermal-vapour respectively), was measured by TGA (**Fig. 3.4 a**). The decomposition temperature of pluronic F127 was 200 ºC. Interestingly, a significant weight loss was observed in the control samples, that is, the samples prepared without pluronic. This can be attributed to the loss of water associated to the CDHA phase, both the evaporation of surface-adsorbed water, below 200 ºC, and further loss of the lattice water at higher temperatures [45,46]. The fact that this was more pronounced for the biomimetic sample than for the ones subjected to hydrothermal treatments can be associated to the higher amount of CDHA present in the specimens on one hand, and on the other hand to a higher water content in the former specimens. In fact, the shape of the curves suggests that specimens obtained by the biomimetic treatment had a higher amount of adsorbed water, which is associated to the weight loss below 200 ºC, whereas the amount of lattice water seemed to be similar to the samples subjected to the hydrothermal treatment, as reflected by the similar slopes of the curves above 200 ºC. Concerning the DIW scaffolds, the highest weight loss was observed for the hydrothermal vapour treatment, whereas the other two treatments, that is biomimetic and hydrothermal immersed, showed similar decomposition patterns of the binder, with lower weight loss observed. In **Fig. 3.4 b** the calculated values of the binder's amount in the different samples is displayed. As expected, in the hydrothermal vapour condition the content of pluronic F127 in the treated specimens was the same as for the initial ink used (14.3%). In contrast, the amount of binder in the samples treated under biomimetic and hydrothermal immersed conditions was reduced to 0.36 and 0.53%, demonstrating that during the immersion in water, either at 37 or 121 ºC, the binder contained in the scaffolds was almost completely released.

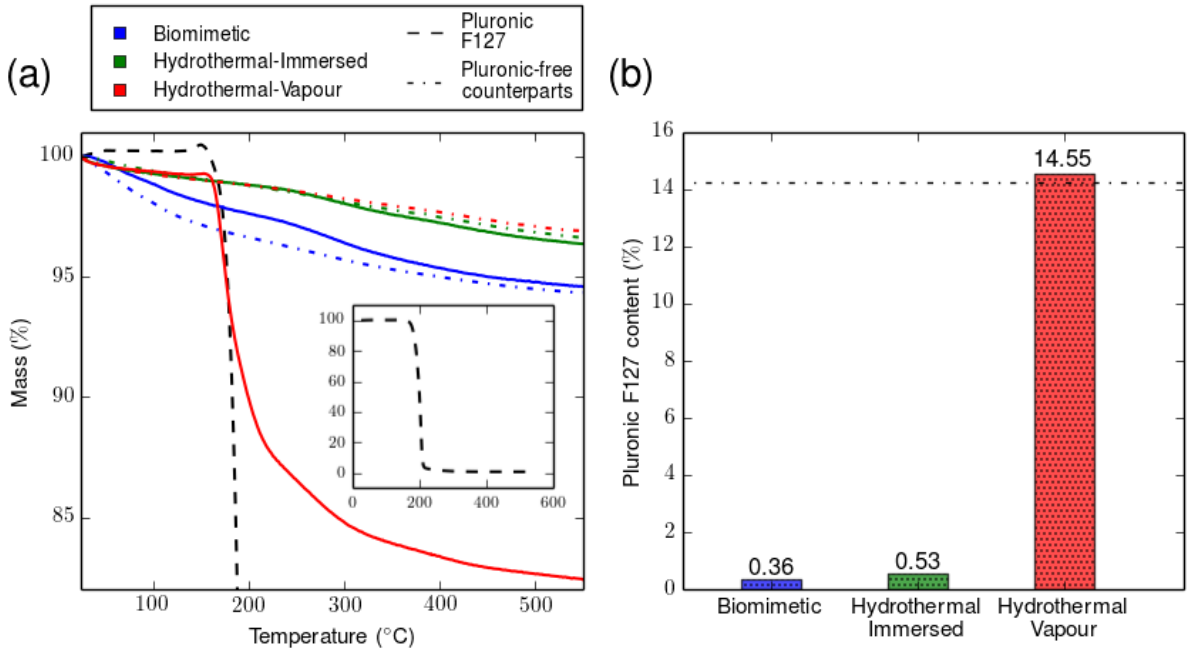

Fig. 3.4. a Thermogravimetric mass loss of the samples subjected to the different post-printing treatments, where the continuous and the dashed lines correspond to the studied scaffolds and their pluronic-free counterparts respectively. The mass loss for the pure pluronic F127 is represented in the inset; **b** amount of pluronic F127 calculated from the TGA data, where the dashed line indicates the binder nominal concentration in the ink.

The FTIR spectra of the different specimens are displayed in **Fig. 3.5**. The typical bands characteristic of the different PO_4 vibration modes of (v1~980, v2~363, v3~1082 and v4~515 cm^{-1}) [47] present in calcium phosphates were identified in all samples. Moreover, all samples, regardless of the hardening treatment used, presented the absorption bands of HPO_4^{2-} (~870 cm^{-1}) and OH^-(~631 and ~3570 cm^{-1}) which are characteristic of calcium deficient hydroxyapatite [48,49]. Although α-TCP and β-TCP were observed in the XRD patterns, these two phases were hardly distinguished in the FTIR spectra due to the overlapping of their infrared spectral bands with those of CDHA.

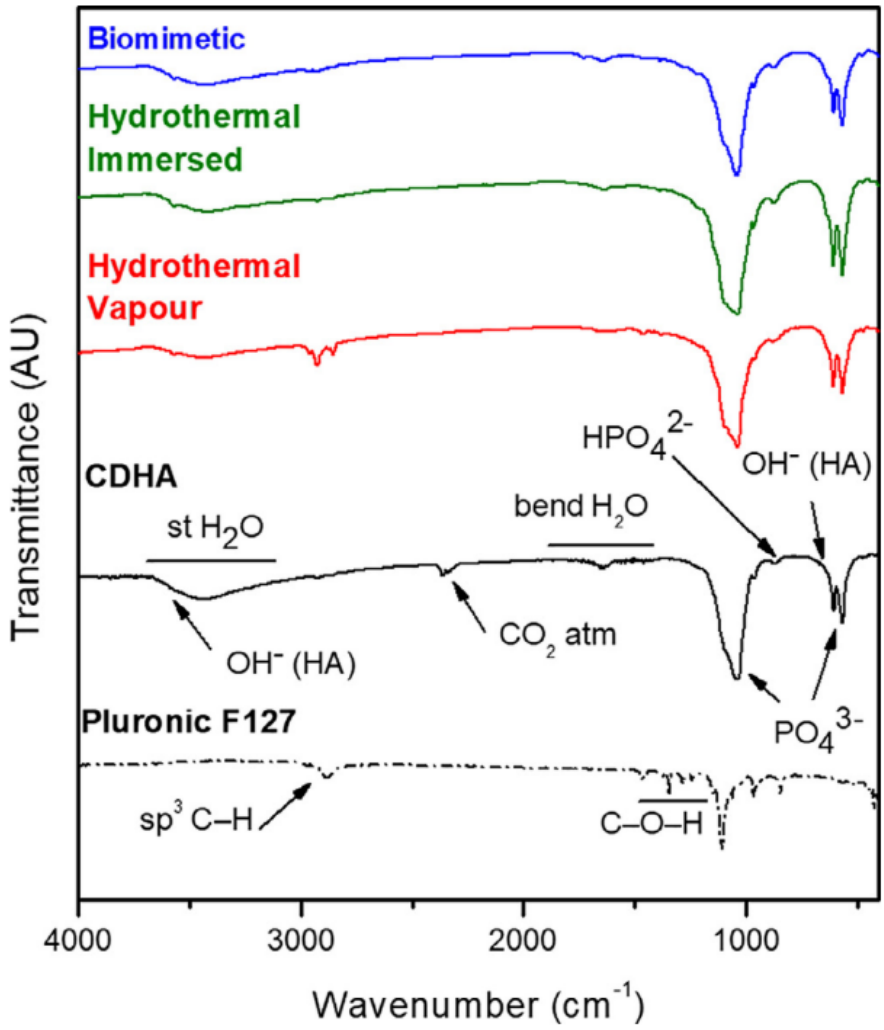

Fig. 3.5. KBr-Fourier Transformed Infrared spectroscopy diagrams of the scaffolds subjected to the different post-printing treatments.

In addition, in the samples subjected to the hydrothermal-vapour process, C-H stretching bands (~2850 cm^{-1}) corresponding to sp3 carbon hydrogen bonds and C-O stretching bands (~1110 cm^{-1}) corresponding to alkoxy bond characteristic of aliphatic ethers, confirming the presence of pluronic F127 in the scaffolds [50], in agreement with the TGA results (**Fig. 3.4**).

The microstructure of the scaffold strands after complete reaction for the different treatments (7 d, 30 min and 100 min for the biomimetic, hydrothermal-immersed and hydrothermal-vapour respectively) is shown in **Fig. 3.6**. The biomimetic treatment resulted in an entangled network of plate-like CDHA crystals (**Fig. 3.6 a**), which is in agreement with the microstructure developed under biomimetic conditions in calcium phosphate cements prepared with coarse particles, similar to the ones used in the self-setting ink [51]. In contrast, in the hydrothermal-immersed condition the CDHA crystals exhibited a needle-like morphology (**Fig. 3.6 b**), as also reported in previous studies [52]. Under hydrothermal-vapour condition, the microstructure of the scaffold was consistent with a lower rate of transformation to CDHA, the original α-TCP particles being still visible, although covered with a layer of CDHA nanometric crystals (**Fig. 3.6**

c) that, according to XRD, represented 60% of the composition of the scaffold. The lack of liquid environment hindered ionic diffusion and therefore the precipitated crystals were localised in close contact with the reactant particles. Although water vapour could be condensed on the surface of the particles, the ions produced by the dissolution of the α-TCP could not migrate to form an entangled network of CDHA crystals. Instead, the precipitated CDHA formed a compact shell that impaired the dissolution of the remaining α-TCP core.

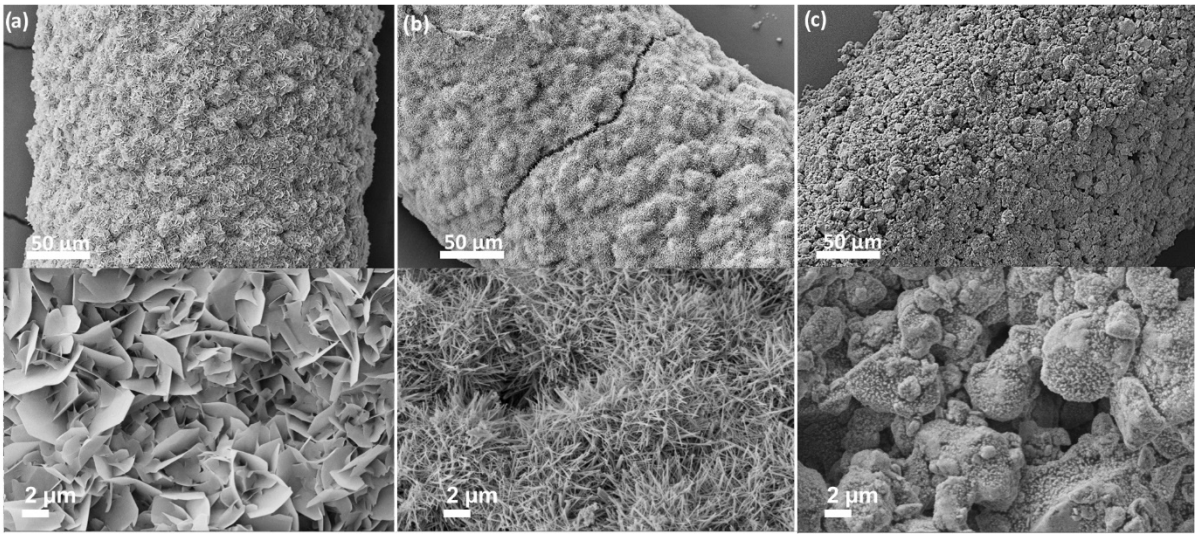

Fig. 3.6. Representative Field Emission-Scanning Electron Microscopy images of the microstructures obtained at two different magnifications after the different post-printing treatments: **a** Biomimetic, 7 d; **b** Hydrothermal-immersed, 30 min; and **c** Hydrothermal-vapour, 100 min.

The SSA values were 12.345 ± 0.004, 11.664 ± 0.033 and 2.342 ± 0.018 $m^2 g^{-1}$ for the biomimetic, hydrothermally-immersed and hydrothermal-vapour samples, respectively, which are in good agreement with the microstructural observations.

The pore entrance size distribution of the scaffolds consolidated under the different methods determined by MIP is presented in **Fig. 3.7**. In general, a bimodal pore entrance size distribution can be observed for each consolidation method. The pores larger than 10 µm corresponded to the macroporosity between strands. All the scaffolds used for the MIP were printed following the HC pattern, which made the entrance macropore size distribution overlap in all cases. In contrast, the entrance pore size distribution below 10 µm (nano-microporosity within the strands) presented significant differences between consolidation methods, due to the different microstructures obtained. The smallest micropores were observed for the scaffolds consolidated with the biomimetic approach, with pore entrance sizes bellow 0.1 µm. The hydrothermal-immersed samples presented slightly bigger pore entrance sizes (around 0.2 µm). This is consistent with previous results obtained with calcium phosphate cements with similar composition, where it was shown that plate-like CDHA crystal networks resulted in smaller-size pore interconnections than the needle-like crystal networks [37]. Finally, the biggest pore entrance size (2 to 3 µm) was observed for the hydrothermal-vapour treatment. As it can be observed in **Fig. 3.6**, the spaces

between polyhedral particles in this sample are considerably larger than the spaces between plate- or needle-like crystals of the other samples.

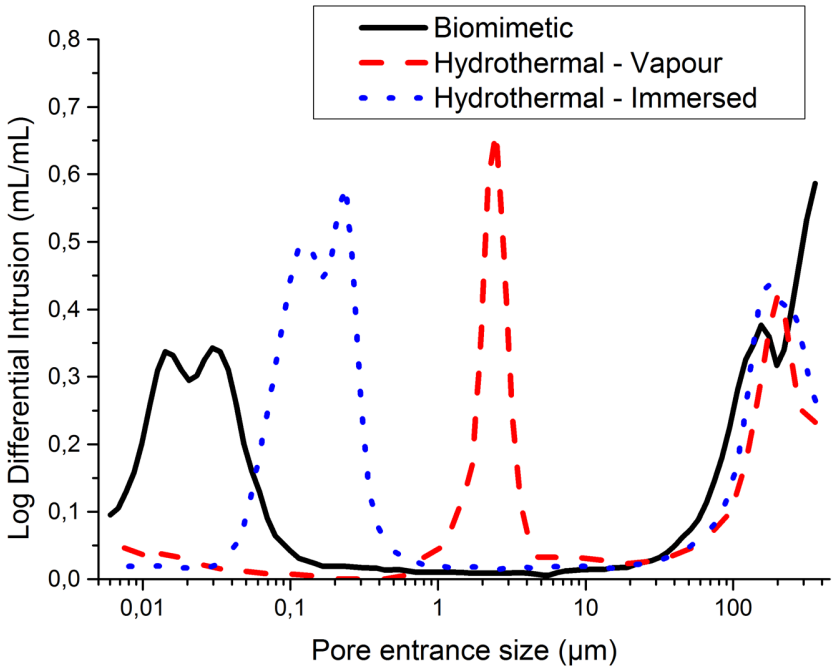

Fig. 3.7. Pore entrance size distribution obtained by mercury intrusion porosimetry (MIP) for HC pattern scaffolds subjected to the different post-printing treatments.

The quantification of the nano-microporosity measured by MIP, as well as the total porosity calculated according to **Equation 3.1** and the macroporosity according to **Equation 3.3** is displayed in **Fig. 3.8 a**. Remarkable differences were found in nano-micro porosity with values of 23.9, 26.7 and 15.3% for the biomimetic, hydrothermal-immersed and hydrothermal-vapour respectively. These differences explain the values found in the total porosity, which follow the same trend. The macroporosity was very similar for the three post-printing treatments (44.8, 45.9 and 44.0% for the biomimetic, hydrothermal-immersed and hydrothermal-vapour respectively) as expected since all the specimens were printed with the HC pattern.

3.3.2 Effect of the Post-printing Treatment on the Mechanical Properties

Fig. 3.8 b shows the compressive strength and Weibull modulus of scaffolds with HC pattern, after the different post-printing treatments. The hydrothermal treatments led to lower compressive strength and Weibull modulus compared to the biomimetic condition, with the hydrothermal-vapour presenting the lowest values. No correlation was observed between porosity and compressive strength, which suggests that the differences in microstructure plays a determinant role. In fact, previous studies on calcium phosphate cements revealed that the mechanism responsible for the hardening of these materials was the mechanical interlocking between the precipitated crystals, and that the mechanical strength was directly related to the amount of precipitated phase formed in the setting reaction [38,53]. This trend is clearly

maintained in the present study, where the scaffolds under the hydrothermal-vapour treatment presented the lowest conversion into CDHA and the microstructure lacked entangled CDHA crystals. In contrast, the hydrothermal-immersed and the biomimetic scaffolds presented an increasing conversion into CDHA which resulted in higher compressive strengths, which are within the range of the compressive strength of cancellous bone (between 2 and 12 MPa) [54]. An additional parameter that may contribute to the lower compressive strength of the hydrothermal-vapour samples is the plasticising effect of the binder, which was retained in much higher amounts (14.55%) than in the other treatments (**Fig. 3.4 b**). Moreover, the Weibull modulus of the biomimetic scaffolds was bigger than that of the hydrothermal-immersed scaffolds, which indicates that this last treatment results in less reliable samples (*i.e.* with a higher variability in the compressive strength). Since the mechanical reliability of brittle materials such as the CDHA scaffolds depends on the distribution of defects, it can be hypothesised that the presence of some β-TCP in the material can result in a more heterogeneous structure, this creating stress concentration sites. It would be important, therefore, to find strategies to enhance the reliability and toughness of this kind of structures.

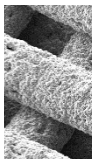

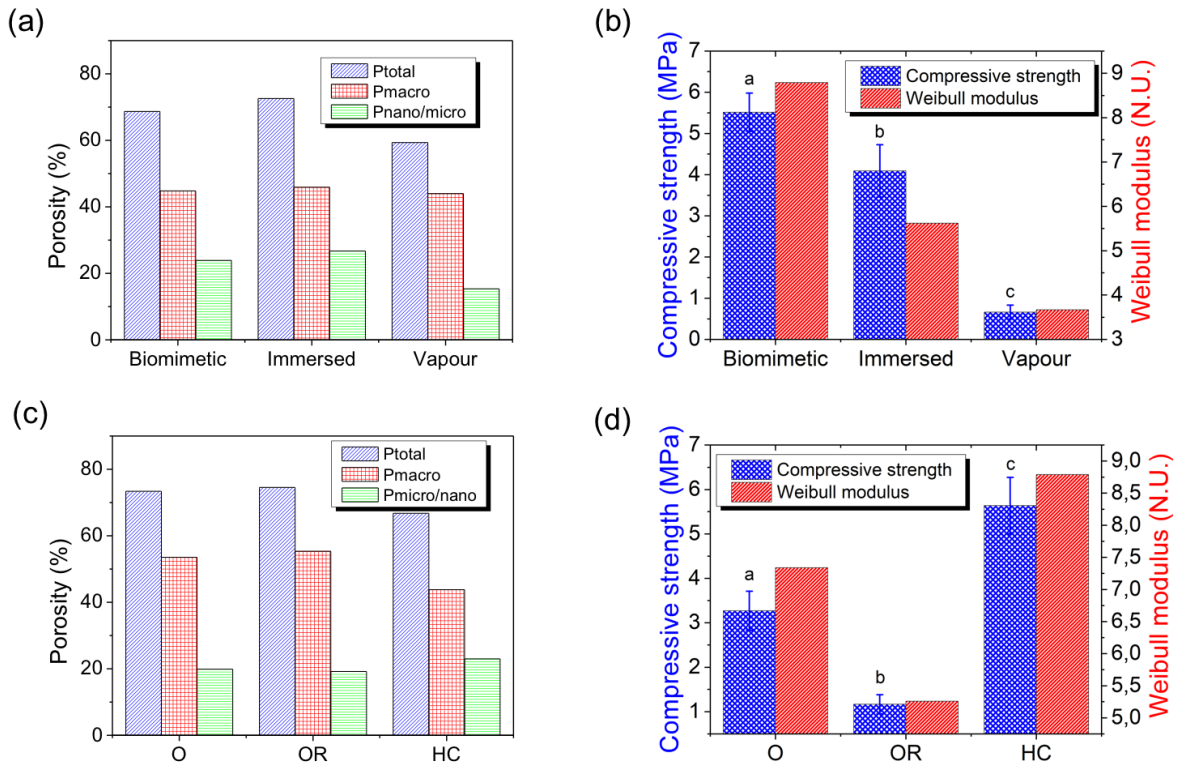

Fig. 3.8. a Porosity and **b** compressive strength and Weibull modulus of the scaffolds printed with HC pattern and subjected to the different post-printing treatments. **c** Porosity, and **d** compressive strength and Weibull modulus of the scaffolds set by the biomimetic treatment printed with different patterns. Statistically significant differences between treatments **(**b) and between patterns (d) are marked with different letters.

3.3.3 Effect of Scaffold Pattern on Mechanical Properties

Scaffolds with different structures subjected to the biomimetic post-treatment were compared in terms of mechanical properties. Representative μ-CT reconstructions of the scaffolds fabricated following different patterns are shown in **Fig. 3.9**, where a representative unit cell for each pattern obtained by μ-CT analysis is also displayed. For the O pattern, the macropore size, measured as the distance between adjacent parallel strand surfaces was $L_x = L_y = 332 \pm 18$ μm in the printing plane projection (XY plane), and $L_Z = 195 \pm 15$ μm in the lateral projection. These distances were the same in the OR scaffolds, but the 45º rotation applied every layer created a more complex pore shape. The HC scaffold presented vertical hexagonal channels with average diameter of 556 ± 46 μm.

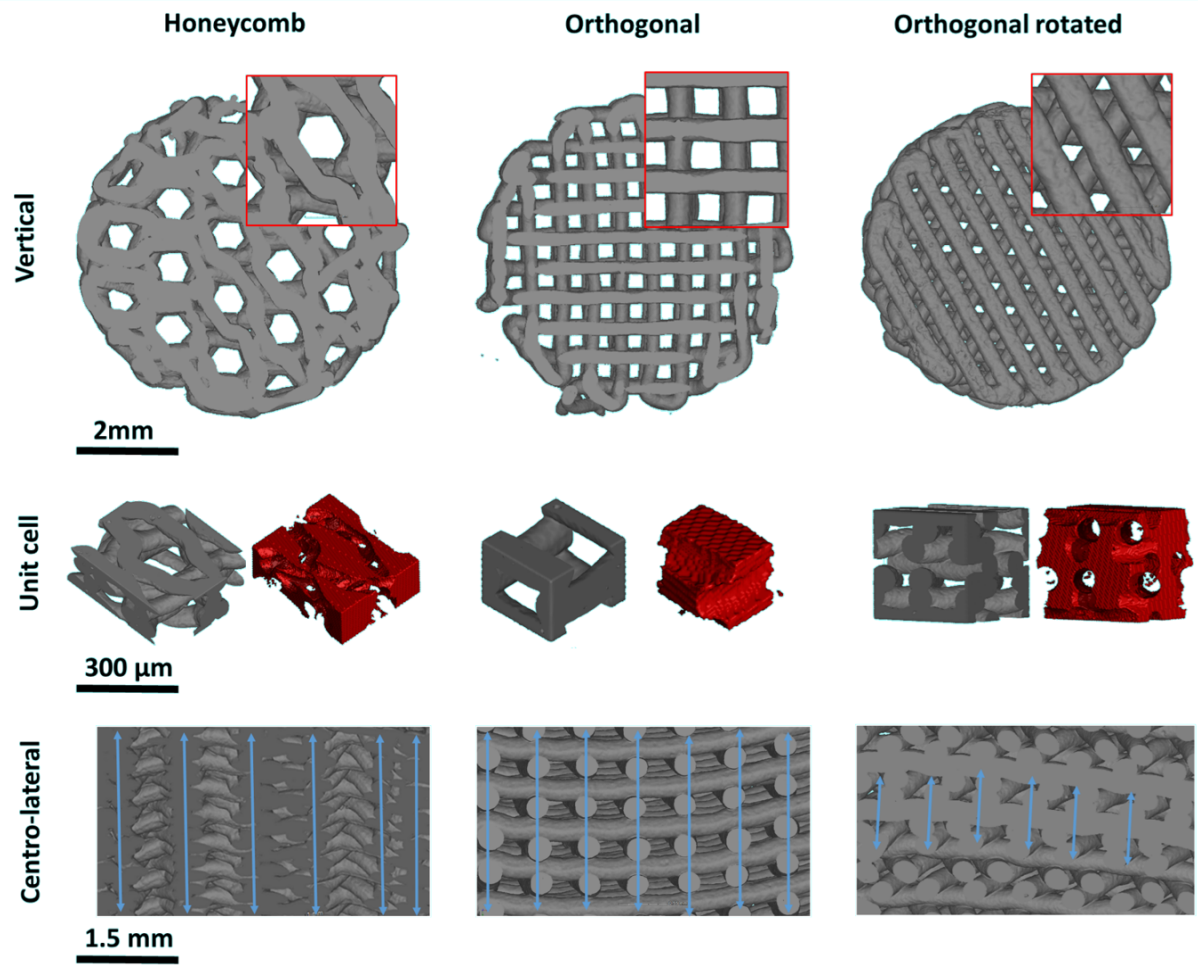

Fig. 3.9. Virtual reconstructions from μ-CT data of scaffolds printed with different patterns. Top: vertical view from the printing plane; middle: unit cells representing the solid part of the cell (light grey) and rendered porosity (red); bottom: centro-lateral view showing the pillars that transfer the mechanical load during compression strength test, blue arrows show the continuity of the pillars in the direction of loading.

As expected, the different patterns resulted in different macroporosities, as shown in **Fig. 3.8 c**. The HC pattern exhibited the lowest macroporosity (43.8%), followed by

the O pattern (53.5%) and, finally, the OR (55.4%). Regarding the nano-micro porosity, the three conditions presented similar values (19.9, 19.2 and 23.0% for O, OR and HC respectively), as all the samples were subjected to the same biomimetic setting treatment.

The compressive strength and Weibull modulus for the scaffolds with different patterns, all of them subjected to the biomimetic treatment are shown in **Fig. 3.8 d**. The highest compressive strength and Weibull modulus corresponded to the HC scaffold, followed by the O and OR scaffolds.

No correlation was found between compressive strength and macroporosity. The trends observed can be rather explained by the strand architecture in the different scaffolds. Thus, in the HC pattern the strands form tubular-like walls aligned in the direction of the applied load, and in the case of the O patterned scaffold, the intersection points of the strands in the different layers also form longitudinal pillars (**Fig. 3.10**). As previously described [11,29,55], the failure of the structure is due to the bending of these pillars. The higher Weibull modulus of the HC pattern indicates that this structure is mechanically more reliable than the O pattern in the direction perpendicular to the printing plane. In the OR structure, the overlapping points between strands are shifted every two layers, which results in a drastic reduction of vertical pillars, leading to a significantly lower compressive strength. The percentage of area within the XY projection where the strands are overlapped in consecutive layers of a repetition unit (**Fig. 3.10**), that is, the effective section, was 22% of the cross-section area for the O pattern, only 11% for the OR and 28% for the HC pattern, which is in good agreement with the trends observed for the compressive strengths measured for the different structures (**Fig. 3.8 d**).

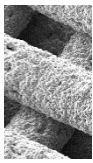

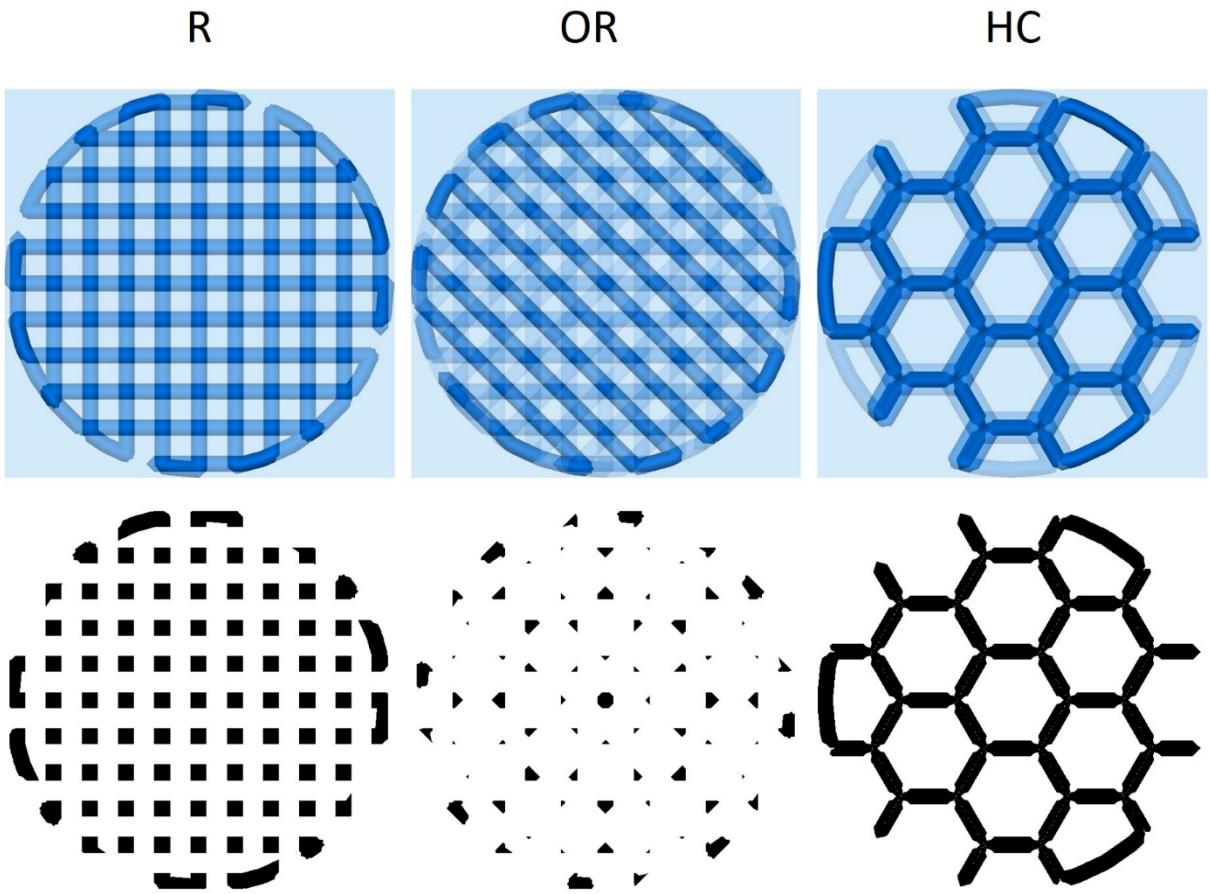

Fig. 3.10. Top: Overlapped axial view of the repetition units for each pattern. Bottom: Regions of the cross sections that are common in all the layers. This pattern renders immediate comprehension of the scaffold pillars morphology. The image is a result of a Boolean AND operation with the binarised images of the cross sections constituting the repetition unit.

It is difficult to compare the mechanical properties of the biomimetic scaffolds with analogous ceramic scaffolds fabricated by DIW, due to different porosities and architectures. Although in general higher compressive strengths were reported for sintered scaffolds, for example 47 and 15 MPa, for hydroxyapatite and beta tricalcium phosphate with O structure respectively [11,16], it has to be considered that pore size and strut diameter were different from the ones in the present study, and especially, the total porosity was much smaller, around 40%, whereas the biomimetic O scaffolds exhibited 73% of total porosity.

3.3.4 *In Vitro* Response of Rat Mesenchymal Stem Cells

In order to assess the effect of the post-printing treatments on the ability of the scaffolds to support cell adhesion and growth, rMSC were seeded on O scaffolds subjected to the different conditions. As shown in **Fig. 3.11**, scaffolds hardened under biomimetic conditions supported cell adhesion, with a stable number of cells over time, while the number of cells slightly increased in the case of the scaffolds subjected to

the hydrothermal-immersed treatment. In contrast, the number of cells on the hydrothermal-vapour treated scaffolds was significantly lower and decreased over time. Confocal microscopy images after 7 d of culture confirmed the presence of cells covering all the surface of the strands on the biomimetic and hydrothermal-immersed scaffolds, whereas for the hydrothermal-vapour condition, spaces free of cells were found on the strands (**Fig. 3.11 b**). This can be associated to the higher amount of pluronic F127 present in the hydrothermal-vapour scaffolds, as measured by TGA (**Fig. 3.4**), since during the vapour treatment there is no chance for pluronic to be released prior to the cell culture, which could lead to a reduction of cell adhesion and compromise the cytocompatibility of the scaffold [56]. It can be concluded, therefore, that the immersion of the scaffold during hydrothermal treatment is a requisite not only to enhance the transformation of α-TCP to CDHA, with the consequent improvement of the mechanical properties, but also to facilitate the release of the binder and increase the cytocompatibility of the scaffold. Indeed, both biomimetic and hydrothermal-immersed treatments allowed cell colonisation. This is a promising result that supports the use of these scaffolds in cell-based bone tissue engineering therapies and the development of *in vitro* bone models.

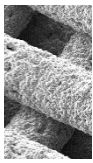

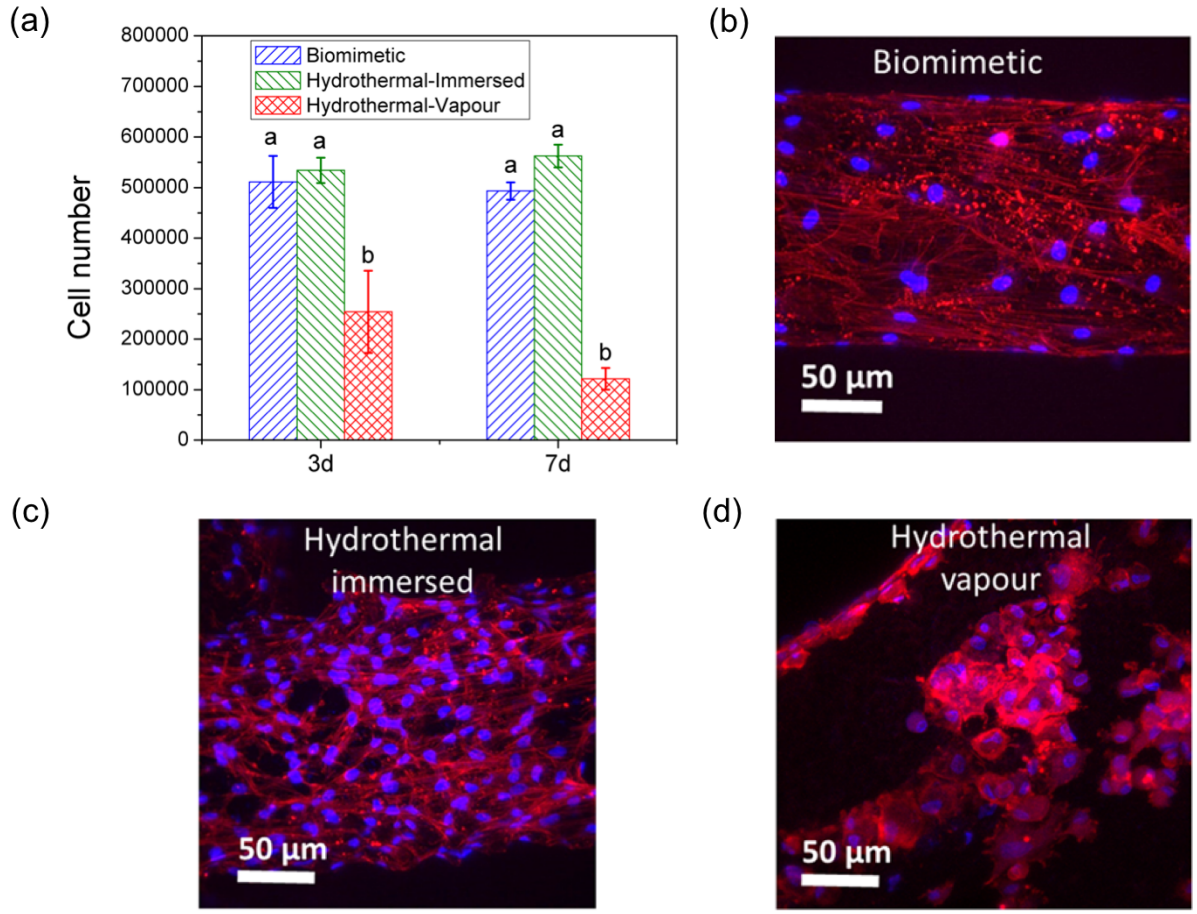

Fig. 3.11. Results of the cell culture study: **a** Number of rMSC determined by LDH assay after 3 and 7 d of 3D static cell culture on O scaffolds subjected to the different post-printing treatments where different letters indicate statistically significant differences; and **b-d** confocal microscope images of cells attached to these scaffolds after 7 d of 3D static cell culture. Actin cytoskeleton is shown in red and nuclei in blue.

3.4 Conclusion

In this study, we developed a hydrothermal method that allows a significant reduction in the consolidation time of DIW α-TCP scaffolds, without losing the biomimetic features. The hydrothermal treatment of DIW scaffolds immersed in water significantly accelerated the hydrolysis of α-TCP into CDHA, reducing the hardening time to 30 minutes. This offers the possibility to fabricate scaffolds on-demand in a very short lapse of time (*e.g.* few hours), including the time for patient imaging, scaffold architecture selection, DIW and consolidation. This can represent a paramount advantage, in particular to treat clinical emergencies such as car, labour or sport accidents, in a patient-specific way. The hydrothermal treatment of the scaffolds resulted in a change in microstructure and promoted the allotropic transformation of α-TCP into its β polymorph, which reduced the yield in CDHA formation and resulted in a slight decrease of strength and reliability. Both the biomimetic and hydrothermal-immersed treatments resulted in scaffolds with compressive strengths similar to trabecular bone. Whereas a compressive strength of 5.51 MPa was obtained in HC scaffolds with 68.7% porosity with the biomimetic treatment, the hydrothermal-immersed treatment resulted in a compressive strength of 4.09 MPa for HC scaffolds with 72.6% porosity. The Weibull modulus was higher in the biomimetic treatment than in the hydrothermal-immersed treatment (8.79 vs. 5.62 respectively), indicating higher reliability. In addition, both treatments allowed the scaffold colonisation by rMSC, suggesting that the two treatments are suitable to produce synthetic patient-specific bone grafts. However, due to the intrinsic brittleness of these materials, the use of such scaffolds in load bearing applications would require a further enhancement of their mechanical properties or the combination with additional mechanical fixation systems.

3.5 References

[1] C. G. Finkemeier, “Bone-grafting and bone-graft substitutes” *J. Bone Joint Surg. Am.*, vol. 84-A, no. 3, pp. 454–64, Mar. 2002.

[2] M. Bohner, “Resorbable biomaterials as bone graft substitutes” *Materials Today*, vol. 13, no. 1–2. Elsevier Ltd, pp. 24–30, Jan-2010, doi:10.1016/S1369-7021(10)70014-6.

[3] B. Stevens, Y. Yang, A. Mohandas, B. Stucker, and K. T. Nguyen, “A review of materials, fabrication methods, and strategies used to enhance bone regeneration in engineered bone tissues” *J. Biomed. Mater. Res. Part B Appl. Biomater.*, vol. 85B, no. 2, pp. 573–582, May 2008, doi:10.1002/jbm.b.30962.

[4] S. Bose, S. Vahabzadeh, and A. Bandyopadhyay, “Bone tissue engineering using 3D printing” *Mater. Today*, vol. 16, no. 12, pp. 496–504, Dec. 2013, doi:10.1016/j.mattod.2013.11.017.

[5] D. Tang, R. S. Tare, L.-Y. Yang, D. F. Williams, K.-L. Ou, and R. O. C. Oreffo, “Biofabrication of bone tissue: approaches, challenges and translation for bone regeneration” *Biomaterials*, vol. 83, pp. 363–382, Mar. 2016, doi:10.1016/j.biomaterials.2016.01.024..

[6] A. Butscher, M. Bohner, S. Hofmann, L. Gauckler, and R. Müller, “Structural and material approaches to bone tissue engineering in powder-based three-dimensional printing” *Acta Biomater.*, vol. 7, no. 3, pp. 907–920, Mar. 2011, doi:10.1016/j.actbio.2010.09.039..

[7] J. I. Cesarano, T. A. Baer, and P. Calvert, “Recent developments in freeform fabrication of dense ceramics from slurry deposition” *International Solid Freeform Fabrication symposium*, Nov. 1997, doi:10.2172/554831.

[8] J. E. Smay, J. Cesarano, and J. A. Lewis, “Colloidal Inks for Directed Assembly of 3-D Periodic Structures” *Langmuir*, vol. 18, no. 14, pp. 5429–5437, Jul. 2002, doi:10.1021/la0257135.

[9] S. Michna, W. Wu, and J. A. Lewis, “Concentrated hydroxyapatite inks for direct-write assembly of 3-D periodic scaffolds” *Biomaterials*, vol. 26, no. 28, pp. 5632–5639, Oct. 2005, doi:10.1016/j.biomaterials.2005.02.040.

[10] A. Kumar, A. R. Akkineni, B. Basu, and M. Gelinsky, “Three-dimensional plotted hydroxyapatite scaffolds with predefined architecture: comparison of stabilization by alginate cross-linking versus sintering” *J. Biomater. Appl.*, vol. 30, no. 8, pp. 1168–1181, Mar. 2016, doi:10.1177/0885328215617058.

[11] P. Miranda, A. Pajares, E. Saiz, A. P. Tomsia, and F. Guiberteau, “Mechanical properties of calcium phosphate scaffolds fabricated by robocasting” *J. Biomed. Mater. Res. Part A*, vol. 85A, no. 1, pp. 218–227, Apr. 2008, doi:10.1002/jbm.a.31587.

[12] P. Miranda, E. Saiz, K. Gryn, and A. P. Tomsia, “Sintering and robocasting of β-tricalcium phosphate scaffolds for orthopaedic applications” *Acta Biomater.*, vol. 2, no. 4, pp. 457–466, Jul. 2006, doi:10.1016/j.actbio.2006.02.004.

[13] Y. Zhang *et al.*, “Mesoporous bioactive glass nanolayer-functionalized 3D-printed scaffolds for accelerating osteogenesis and angiogenesis” *Nanoscale*, vol. 7, no. 45, pp. 19207–19221, Dec. 2015, doi:10.1039/C5NR05421D.

[14] M. Houmard, Q. Fu, M. Genet, E. Saiz, and A. P. Tomsia, “On the structural, mechanical, and biodegradation properties of HA/β-TCP robocast scaffolds” *J. Biomed. Mater. Res. Part B Appl. Biomater.*, vol. 101, no. 7, pp. 1233–1242, Oct. 2013, doi:10.1002/jbm.b.32935.

[15] C. Mangano *et al.*, “In Vivo Behavior of a Custom-Made 3D Synthetic Bone Substitute

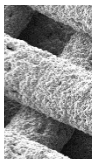

in Sinus Augmentation Procedures in Sheep" *J. Oral Implantol.*, vol. 41, no. 3, pp. 240–250, Jun. 2015, doi:10.1563/AAID-JOI-D-13-00053.

[16] J. Franco, P. Hunger, M. E. Launey, A. P. Tomsia, and E. Saiz, "Direct write assembly of calcium phosphate scaffolds using a water-based hydrogel" *Acta Biomater.*, vol. 6, no. 1, pp. 218–228, Jan. 2010, doi:10.1016/j.actbio.2009.06.031.

[17] S. Ishack, A. Mediero, T. Wilder, J. L. Ricci, and B. N. Cronstein, "Bone regeneration in critical bone defects using three-dimensionally printed β-tricalcium phosphate/hydroxyapatite scaffolds is enhanced by coating scaffolds with either dipyridamole or BMP-2" *J. Biomed. Mater. Res. Part B Appl. Biomater.*, vol. 105, no. 2, pp. 366–375, Feb. 2017, doi:10.1002/jbm.b.33561.

[18] Q. Fu, E. Saiz, and A. P. Tomsia, "Bioinspired Strong and Highly Porous Glass Scaffolds" *Adv. Funct. Mater.*, vol. 21, no. 6, pp. 1058–1063, Mar. 2011, doi:10.1002/adfm.201002030.

[19] X. Liu, M. N. Rahaman, G. E. Hilmas, and B. S. Bal, "Mechanical properties of bioactive glass (13-93) scaffolds fabricated by robotic deposition for structural bone repair" *Acta Biomater.*, vol. 9, no. 6, pp. 7025–7034, Jun. 2013, doi:10.1016/j.actbio.2013.02.026.

[20] Y. Luo, A. Lode, C. Wu, and M. Gelinsky, "3D Plotting of Bioceramic Scaffolds under Physiological Conditions for Bone Tissue Engineering" in *Advanced Bioactive Inorganic Materials for Bone Regeneration and Drug Delivery*, CRC Press, 2013, pp. 83–116, doi:10.1201/b13926-5.

[21] C. Wu, Y. Luo, G. Cuniberti, Y. Xiao, and M. Gelinsky, "Three-dimensional printing of hierarchical and tough mesoporous bioactive glass scaffolds with a controllable pore architecture, excellent mechanical strength and mineralization ability" *Acta Biomater.*, vol. 7, no. 6, pp. 2644–2650, Jun. 2011, doi:10.1016/j.actbio.2011.03.009.

[22] A. Motealleh, S. Eqtesadi, F. H. Perera, A. Pajares, F. Guiberteau, and P. Miranda, "Understanding the role of dip-coating process parameters in the mechanical performance of polymer-coated bioglass robocast scaffolds" *J. Mech. Behav. Biomed. Mater.*, vol. 64, pp. 253–261, Dec. 2016, doi:10.1016/j.jmbbm.2016.08.004.

[23] H. Yun, S. Kim, and Y. Hyeon, "Design and preparation of bioactive glasses with hierarchical pore networks" *Chem. Commun.*, no. 21, p. 2139, 2007, doi:10.1039/b702103h.

[24] S. Eqtesadi, A. Motealleh, P. Miranda, A. Lemos, A. Rebelo, and J. M. F. Ferreira, "A simple recipe for direct writing complex 45S5 Bioglass® 3D scaffolds" *Mater. Lett.*, vol. 93, pp. 68–71, Feb. 2013, doi:10.1016/j.matlet.2012.11.043.

[25] A. Vallés Lluch, A. Campillo Fernández, G. Gallego Ferrer, and M. Monleón Pradas, "Bioactive scaffolds mimicking natural dentin structure" *J. Biomed. Mater. Res. Part B Appl. Biomater.*, vol. 90B, no. 1, pp. 182–194, Dec. 2008, doi:10.1002/jbm.b.31272.

[26] D. J. Hoelzle, A. G. Alleyne, and A. J. Wagoner Johnson, "Micro-robotic deposition guidelines by a design of experiments approach to maximize fabrication reliability for the bone scaffold application" *Acta Biomater.*, vol. 4, no. 4, pp. 897–912, Jul. 2008, doi:10.1016/j.actbio.2008.02.018.

[27] C. Wu *et al.*, "3D-printing of highly uniform CaSiO3 ceramic scaffolds: preparation, characterization and in vivo osteogenesis" *J. Mater. Chem.*, vol. 22, no. 24, p. 12288, 2012, doi:10.1039/c2jm30566f.

[28] M. M. Farag and H. S. Yun, "Effect of gelatin addition on fabrication of magnesium phosphate-based scaffolds prepared by additive manufacturing system" *Mater. Lett.*, vol. 132, pp. 111–115, Oct. 2014, doi:10.1016/j.matlet.2014.06.055.

[29] Y. Maazouz *et al.*, “Robocasting of biomimetic hydroxyapatite scaffolds using self-setting inks” *J. Mater. Chem. B*, vol. 2, no. 33, pp. 5378–5386, 2014, doi:10.1039/C4TB00438H.

[30] A. Lode *et al.*, “Fabrication of porous scaffolds by three-dimensional plotting of a pasty calcium phosphate bone cement under mild conditions” *J. Tissue Eng. Regen. Med.*, vol. 8, no. 9, pp. 682–693, Sep. 2014, doi:10.1002/term.1563.

[31] W. J. Kim, H. Yun, and G. H. Kim, “An innovative cell-laden α-TCP/collagen scaffold fabricated using a two-step printing process for potential application in regenerating hard tissues” *Sci. Rep.*, vol. 7, no. 1, p. 3181, Dec. 2017, doi:10.1038/s41598-017-03455-9.

[32] N. Raja and H. Yun, “A simultaneous 3D printing process for the fabrication of bioceramic and cell-laden hydrogel core/shell scaffolds with potential application in bone tissue regeneration” *J. Mater. Chem. B*, vol. 4, no. 27, pp. 4707–4716, 2016, doi:10.1039/C6TB00849F.

[33] Y. Luo, A. Lode, F. Sonntag, B. Nies, and M. Gelinsky, “Well-ordered biphasic calcium phosphate–alginate scaffolds fabricated by multi-channel 3D plotting under mild conditions” *J. Mater. Chem. B*, vol. 1, no. 33, p. 4088, 2013, doi:10.1039/c3tb20511h.

[34] A. R. Akkineni, Y. Luo, M. Schumacher, B. Nies, A. Lode, and M. Gelinsky, “3D plotting of growth factor loaded calcium phosphate cement scaffolds” *Acta Biomater.*, vol. 27, pp. 264–274, Nov. 2015, doi:10.1016/j.actbio.2015.08.036.

[35] Y. Maazouz, E. B. Montufar, J. Malbert, M. Espanol, and M.-P. P. Ginebra, “Self-hardening and thermoresponsive alpha tricalcium phosphate/pluronic pastes” *Acta Biomater.*, vol. 49, pp. 563–574, Feb. 2017, doi:10.1016/j.actbio.2016.11.043.

[36] E. B. Montufar, Y. Maazouz, and M. P. Ginebra, “Relevance of the setting reaction to the injectability of tricalcium phosphate pastes” *Acta Biomater.*, vol. 9, no. 4, pp. 6188–6198, Apr. 2013, doi:10.1016/j.actbio.2012.11.028.

[37] D. Pastorino, C. Canal, and M.-P. Ginebra, “Multiple characterization study on porosity and pore structure of calcium phosphate cements” *Acta Biomater.*, vol. 28, pp. 205–214, Dec. 2015, doi:10.1016/j.actbio.2015.09.017.

[38] M. P. Ginebra *et al.*, “Setting Reaction and Hardening of an Apatitic Calcium Phosphate Cement” *J. Dent. Res.*, vol. 76, no. 4, pp. 905–912, Apr. 1997, doi:10.1177/00220345970760041201.

[39] M.-P. Ginebra, E. Fernández, F. C. M. Driessens, and J. A. Planell, “Modeling of the Hydrolysis of α-Tricalcium Phosphate” *J. Am. Ceram. Soc.*, vol. 82, no. 10, pp. 2808–2812, Dec. 2004, doi:10.1111/j.1151-2916.1999.tb02160.x.

[40] M. P. Ginebra *et al.*, “The effects of temperature on the behaviour of an apatitic calcium phosphate cement” *J. Mater. Sci. Mater. Med.*, vol. 6, no. 12, pp. 857–860, Dec. 1995, doi:10.1007/BF00134332.

[41] C. Durucan and P. W. Brown, “Kinetic Model for α-Tricalcium Phosphate Hydrolysis” *J. Am. Ceram. Soc.*, vol. 85, no. 8, pp. 2013–2018, Aug. 2002, doi:10.1111/j.1151-2916.2002.tb00397.x.

[42] C. Rey, C. Combes, C. Drouet, D. Grossin, G. Bertrand, and J. Soulié, “Bioactive Calcium Phosphate Compounds: Physical Chemistry” in *Comprehensive Biomaterials II*, Elsevier, 2017, pp. 244–290, doi:10.1016/B978-0-12-803581-8.10171-7.

[43] R. G. Carrodeguas and S. De Aza, “α-Tricalcium phosphate: Synthesis, properties and biomedical applications” *Acta Biomater.*, vol. 7, no. 10, pp. 3536–3546, Oct. 2011, doi:10.1016/j.actbio.2011.06.019.

[44] L. Galea *et al.*, “Textured and hierarchically structured calcium phosphate ceramic

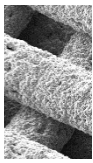

blocks through hydrothermal treatment" *Biomaterials*, vol. 67, pp. 93–103, Oct. 2015, doi:10.1016/j.biomaterials.2015.07.026.

[45] T. I. Ivanova, O. V. Frank-Kamenetskaya, A. B. Kol'tsov, and V. L. Ugolkov, "Crystal Structure of Calcium-Deficient Carbonated Hydroxyapatite. Thermal Decomposition" *J. Solid State Chem.*, vol. 160, no. 2, pp. 340–349, Sep. 2001, doi:10.1006/jssc.2000.9238.

[46] J. C. Elliott, "General Chemistry of the Calcium Orthophosphates" in *Studies in Organic Chemistry*, vol. 18, 1994, pp. 1–62, doi:10.1016/B978-0-444-81582-8.50006-7.

[47] V. M. Bhatnagar, "Infrared spectrum of strontium hydroxyapatite" *Experientia*, vol. 23, no. 9, pp. 697–699, Sep. 1967, doi:10.1007/BF02154118.

[48] R. M. Wilson, J. C. Elliott, S. E. P. Dowker, and L. M. Rodriguez-Lorenzo, "Rietveld refinements and spectroscopic studies of the structure of Ca-deficient apatite" *Biomaterials*, vol. 26, no. 11, pp. 1317–1327, Apr. 2005, doi:10.1016/j.biomaterials.2004.04.038.

[49] M. Mir *et al.*, "XRD, AFM, IR and TGA study of nanostructured hydroxyapatite" *Mater. Res.*, vol. 15, no. 4, pp. 622–627, 2012, doi:10.1590/S1516-14392012005000069.

[50] C. Guo, H.-Z. Liu, and J.-Y. Chen, "A Fourier transform infrared study of the phase transition in aqueous solutions of Ethylene oxide-propylene oxide triblock copolymer" *Colloid Polym. Sci.*, vol. 277, no. 4, pp. 376–381, Apr. 1999, doi:10.1007/s003960050395.

[51] M. Espanol, R. A. Perez, E. B. Montufar, C. Marichal, A. Sacco, and M. P. Ginebra, "Intrinsic porosity of calcium phosphate cements and its significance for drug delivery and tissue engineering applications" *Acta Biomater.*, vol. 5, no. 7, pp. 2752–2762, Sep. 2009, doi:10.1016/j.actbio.2009.03.011.

[52] K. Ioku, G. Kawachi, S. Sasaki, H. Fujimori, and S. Goto, "Hydrothermal preparation of tailored hydroxyapatite" *J. Mater. Sci.*, vol. 41, no. 5, pp. 1341–1344, Mar. 2006, doi:10.1007/s10853-006-7338-5.

[53] S. Gallinetti, C. Canal, and M.-P. Ginebra, "Development and Characterization of Biphasic Hydroxyapatite/β-TCP Cements" *J. Am. Ceram. Soc.*, vol. 97, no. 4, pp. 1065–1073, Apr. 2014, doi:10.1111/jace.12861.

[54] D. W. Hutmacher, J. T. Schantz, C. X. F. Lam, K. C. Tan, and T. C. Lim, "State of the art and future directions of scaffold-based bone engineering from a biomaterials perspective" *J. Tissue Eng. Regen. Med.*, vol. 1, no. 4, pp. 245–60, doi:10.1002/term.24.

[55] P. Miranda, A. Pajares, E. Saiz, A. P. Tomsia, and F. Guiberteau, "Fracture modes under uniaxial compression in hydroxyapatite scaffolds fabricated by robocasting" *J. Biomed. Mater. Res. Part A*, vol. 83A, no. 3, pp. 646–655, Dec. 2007, doi:10.1002/jbm.a.31272.

[56] T. Tharmalingam, H. Ghebeh, T. Wuerz, and M. Butler, "Pluronic Enhances the Robustness and Reduces the Cell Attachment of Mammalian Cells" *Mol. Biotechnol.*, vol. 39, no. 2, pp. 167–177, Jun. 2008, doi:10.1007/s12033-008-9045-8.

Chapter 4

Hydrothermal Processing of 3D-Printed Calcium Phosphate Scaffolds Enhances Bone Formation *In Vivo*: a Comparison with Biomimetic Treatment

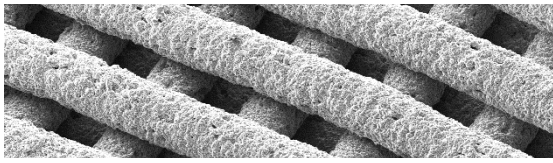

HYDROTHERMAL PROCESSING OF 3D-PRINTED CALCIUM PHOSPHATE SCAFFOLDS ENHANCES BONE FORMATION *IN VIVO*: A COMPARISON WITH BIOMIMETIC TREATMENT

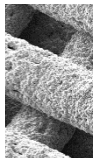

Abstract

Hydrothermal (H) processes accelerate the hydrolysis reaction of α-TCP compared to the long-established biomimetic (B) treatments. They are of special interest for patient-specific 3D-printed bone graft substitutes, where the manufacturing time represents a critical constraint. Altering the reaction conditions has implications for the physicochemical properties of the reaction product. However, the impact of the changes produced by the hydrothermal reaction on the *in vivo* performance was hitherto unknown. The present study compares the bone regeneration potential of 3D-printed α-TCP scaffolds hardened using these two treatments in rabbit condyle monocortical defects. Although both consolidation processes resulted in scaffolds with excellent biocompatibility, osseointegrative and osteoconductive properties, the amount of newly formed bone increased by one third in the hydrothermal vs the biomimetic samples. B and H scaffolds consisted mostly of high specific surface area calcium deficient hydroxyapatite (38 and 27 m^2 g^{-1}, respectively), with H samples containing also 10 wt.% β-TCP. The shrinkage produced during the consolidation process was shown to be very small in both cases, below 3%, and smaller for H than for B samples. The differences in the *in vivo* performance were mainly attributed to the distinct crystallisation nanostructures, which proved to have a major impact on permeability and protein adsorption capacity, using BSA as a model protein, with B samples being highly impermeable. Given the crucial role that soluble proteins play in osteogenesis, this is proposed to be a relevant factor behind the distinct *in vivo* performances observed for the two materials.

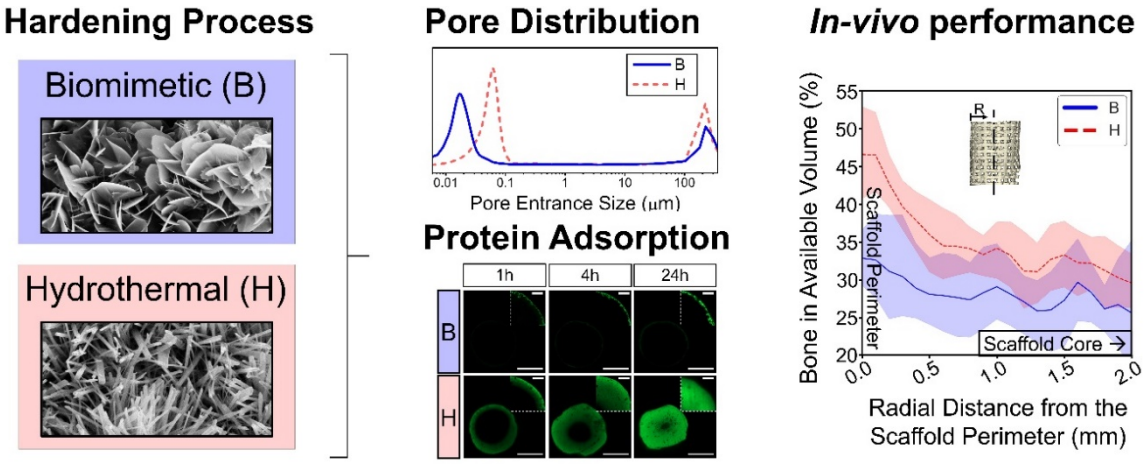

4.1 Introduction

In recent years, the democratisation of additive manufacturing technologies has opened a wide variety of applications in the medical field [1]. Among them, patient-specific bone grafts and implants are one of the most straight forward and promising uses. These are already a reality in the medical industry. Personalised bone grafts are ideal for complex indications, *e.g.* defects that are non-confined, geometrically complex, large, or that require vertical regeneration. The traditional solutions to these cases are autologous bone harvesting (usually fibula [2] and iliac crest [3]) or standard xenogenic or synthetic blocks [4]. The main advantages of personalised bone scaffolds are: (1) Possibility of implementing a virtual surgical planning and more precisely tackle complex geometrical reconstructions [5-8]. (2) Shortening of the surgical time compared with the current available solutions [9,10]. (3) Reduction of the patient's morbidity by avoiding any additional surgery [11,12].

Among the wide variety of existing printing techniques, filamentary-based direct ink writing (DIW) stands as one of the most convenient for the fabrication of ceramic parts. This technology, consisting of the layer by layer microextrusion of a pasty ink [13], enables introducing high ceramic loads in the printed parts, presents low to non-existent waste of raw material, which is critical when using priced biomaterials, and, is simple and affordable. It has been widely used with calcium phosphates [8,14-16], the most used materials for bone regeneration, due to their similarity to the natural bone and high biocompatibility [17]. Typically, calcium phosphate-based inks require a sintering process after printing the green body to achieve hardening of the printed structure.

Recently, self-setting calcium phosphate inks were developed, based on the hydrolysis of alpha tricalcium phosphate (α-TCP) [18,19]. In this case, the printed structures do not require a high-temperature sintering process, since the hardening is due to a cementitious reaction that takes place in the printed paste at room temperature. A further advantage is that the reaction product of the hydrolysis of α -TCP is a calcium deficient hydroxyapatite (CDHA), with a composition closer to the bone mineral than that of the sintered calcium phosphates [20,21]. These biomimetic CDHA DIW scaffolds have been proved to exhibit an excellent osteogenic properties [22-26,27]. However, the slowness of the hydrolysis reaction requires long times for the hardening of the 3D-printed structures, from 3 to 10 d depending on the powder reactivity and the nature of the ink binder used [18,19,26,28,29]. This limits the implementation of this technique in clinical applications, where bone grafts have to be designed and manufactured on-demand usually in a reduced time span.

In this respect, it has been shown that it is possible to accelerate the hydrolysis reaction of α-TCP by hydrothermal routes [30,31]. This is a promising approach to reduce the lead time of DIW personalised bone grafts [32]. However, besides accelerating the hydrolysis process, the hydrothermal process introduces modifications both in the chemistry and the microstructure of the final product, which can have implications in the final performance of the printed scaffolds. Although recent studies have shown the key role of surface texture and crystal morphology in the osteogenic properties of calcium phosphates, [33-36], the impact that this specific hydrothermal treatment may have on the bone regeneration potential is unknown.

With this in mind, the aim of this work is to shed light on the effect of the biomimetic and hydrothermal processing on the morphological and physicochemical features of 3D-printed calcium phosphate scaffolds and to analyse the effect of the resulting composition and textural parameters on the *in vivo* performance of the 3D-printed scaffolds in an orthotopic rabbit model.

4.2 Materials and Methods

4.2.1 Scaffold Preparation

An ink consisting of a ceramic suspension was obtained by mixing a 30 wt.% poloxamer 407 aqueous solution with α-tricalcium phosphate powder at a liquid to powder ratio of 0.45 wt./wt. The mixture was extruded with a custom-made direct ink writing 3D printer. The scaffolds were printed with a nozzle with an orifice diameter of 413 μm (22ga Tappered Tip, Fisnar, WI, USA) following an orthogonal pattern, with a strand-to-strand separation of 250 μm and a layer height of 307 μm. Two scaffold geometries were printed: cubic samples with 8 mm side and cylindrical samples with 8 mm in diameter and height. The samples were hardened using two different processes, either i) a biomimetic treatment consisting of a 7-day immersion in water at 37 ºC; or ii) a hydrothermal treatment, using temperature to accelerate the process, specifically autoclaving at 121 ºC, as described in a previous work [32]. After the hardening process, the cylindrical samples were water sanded in their lateral face with P1200-grain sandpaper down to a final diameter of 5 mm for the *in vivo* experiments. The particles that originated during the sanding process were removed by three rinsing and sonication steps in distilled water. The hydrothermally set scaffolds were sterilised by wet heat in an autoclave, while the biomimetic samples were sterilised by gamma irradiation (25 KGy dose) to avoid heating them above the physiological temperature.

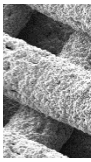

4.2.2 Characterisation of the Scaffolds

Chemical Characterisation

The phase composition of the scaffolds was assessed by X-ray diffraction (XRD) using a diffractometer (D8 Advance Eco, Bruker AXS GmbH, Karlsruhe, Germany) equipped with a Cu K-α beam, a Ni filter and a LynxEye detector. Measurements were acquired in the 3-65º 2θ range with a step size of 0.02º and a sampling step time of 3 s. The quantification of the crystalline phases and the determination of amorphous content were performed by Rietveld refinement (TOPAS 5, Bruker, MA, USA). The amount of amorphous phase was indirectly determined by the addition of corundum as internal standard (a known amount between 30 and 40 wt.%). The amorphous content (A) was deduced from the overestimation of the quantity of internal standard following **Equation 4.1** [37]:

$$A = \frac{100\%}{100\% - R} \cdot 100\% \cdot \left(1 - \frac{R}{R_R}\right) \qquad \textbf{Equation 4.1}$$

where R corresponds to the added amount of internal standard and R_R corresponds to the percentage of corundum calculated in the Rietveld refinement. In the refinement process, the following crystal structures were employed: calcium deficient hydroxyapatite (COD-9002214), β-tricalcium phosphate (ICSD-006191) and

corundum (ICSD-033639), obtained either from the inorganic crystal structure database (ICSD) or the crystallography open database (COD). The following parameters were adjusted in the refinement: lattice parameters, phase scale factors, zero-shift error, peak shape parameters and preferred orientation (supplementary information).

Raman spectra of the powdered scaffolds were recorded using a inVia™ Qontor® spectrometer (Renishaw, Gloucestershire, UK). A 532 nm laser with a 10 mW output power was used as the excitation source. All the spectra were collected with a 50x objective, in the 400 – 4000 cm^{-1} range, using an integration time of 10 s and 5 accumulations. The spectral resolution was ca. 1 cm^{-1}.

Microstructure, Porosity and Pore Architecture

Different techniques were used to assess the morphology of the scaffolds at different magnifications. The microstructure of the samples was observed through scanning electron microscopy (FIB/SEM, Neon 40, Zeiss, Oberkochen, Germany) run at 5 kV and acquired with a through-the-lens electron detector. Prior to the acquisition, samples were sputter-coated with a thin electron-conductive carbon layer to prevent electrostatic charges (Emitech 950x carbon evaporator, Montigny-le-Bretonneux, France). The specific surface area was determined by nitrogen sorption using the Brunauer-Emmett-Teller (BET) method (ASAP 2020, Micromeritics, GA, USA). Before the analysis, the samples were degassed by holding them at 100 ºC for 2 h under a 10 mmHg vacuum atmosphere. The skeletal density (ρ_{skel}) of the specimens was determined by helium pycnometry (AccuPyc 1330, Micromeritics, GA, USA). The apparent density (ρ_{app}) of the scaffolds was calculated as the quotient of the dry scaffold's mass over its equivalent volume measured on the cubic samples (n=15), and the total porosity was determined as $[1-(\rho_{app}/\rho_{skel})]\cdot 100$. The pore entrance size distribution in the range of 0.006 to 360 µm was determined by mercury intrusion porosimetry (MIP). The MIP results were combined with the skeletal density to determine the internal porosity of the strands (intrastrand porosity), according to **Equation 4.2**:

$$P_{intrastrand} = \left(\frac{V_{(p<10\mu m)}}{V_{(p<10\mu m)}+V_{mat}}\right)\cdot 100 = \left(\frac{V_{(p<10\mu m)}}{V_{(p<10\mu m)}+{}^{1}/_{\rho_{skel}}}\right)\cdot 100 \qquad \textbf{Equation 4.2}$$

where $V_{(p<10\mu m)}$ is the volume of pores smaller than 10 µm normalised per unit of mass, obtained from the sum of the incremental mercury intrusion in the pores below this size in the pore entrance size distribution curves, and V_{mat} is the specific volume of the material, which is the reciprocal of the skeletal density.

The morphology of the scaffold's architecture was assessed by micro-computed tomography (µ-CT) (Skyscan 1272, Bruker, MA, USA) operated with an X-ray current of 111 µA and an acceleration voltage of 90 kV. The X-ray beam was configured with an aluminium and a tungsten filter with respective thicknesses of 0.5 and 0.038 mm. The exposure time and step resolution around the 180º were set to 1650 ms and 0.2º per step respectively. No frame averaging was applied. The acquisition was performed with an isotropic voxel resolution of 18 µm. The data was processed with beam hardening correction and object shifting correction and reconstructed into tomographic image stacks (NRecon software, Bruker, MA, USA). Subsequently, the resulting

reconstructions were aligned to the printing axis (DataViewer software, Bruker, MA, USA). Different strategies were followed to evaluate the morphological differences between the printed structures and the theoretical geometry. First, the different orthogonal views of the structure were assessed with an image analysis software (ImageJ2, NIH, MD, USA [38]) to calculate the percentage of linear shrinkage in the three printer axis directions (*i.e.* X, Y and Z). For each direction, the distance corresponding to five repetition units was measured and compared with the theoretical dimensions calculating the percentual deviation. Five samples per condition were analysed. Subsequently, the macroporosity generated during the printing process was measured (CTAn v1.16 software, Bruker, MA, USA) and compared to that of the theoretical structure, generated through CAD software (SolidWorks, Dassault Systèmes, Vélizy-Villacoublay, France) based on the dimensions introduced in the printing configuration, transformed to image stack (Mimics, Materialise, Leuven, Belgium), and analysed with the same procedure used for the μ-CT experimental acquisitions. Finally, the two different structures were compared with the theoretical mesh design: A 3D mesh of a representative sample was obtained for each condition by segmenting the μ-CT acquisition (Slicer v4.10.2, 3D Slicer, NIH, USA [39]) and a design of the theoretical structure was created with CAD software (MeshMixer v3.5, Autodesk, CA, USA). Then, a 3D point cloud comparison software (ClowdCompare v2.11.2, EDF R&D, France) was used to assess the deviation of the printed structures with respect to the reference theoretical design. Briefly, a point cloud was sampled from the mesh of the printed and the normal distance from each point of the 3D cloud to the reference mesh was calculated. A colour map of the deviation distances on the 3D structure was obtained. Moreover, the sample deviation distance of each point of the 3D cloud was recorded for both conditions and compared in a histogram.

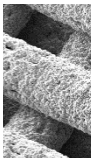

Mechanical Characterisation

The compressive strength of the scaffolds was assessed in 8 mm cubic scaffolds in the Z printing direction by monotonic compressive test (Bionix servo-hydraulic test system, MTS Systems, M.N., USA) in displacement-control mode at a displacement rate of 1 mm min^{-1}. Before the test, the scaffolds were immersed in water and stored at 37 ºC overnight and were tested in wet conditions to better simulate the *in vivo* situation. Fifteen samples were tested per condition and the strain-stress curves, elastic modulus, ultimate compressive strength and Weibull modulus were determined.

Protein Adsorption Study

To analyse the relevance of microstructural features in the interaction with proteins in solution, a study was carried out with bovine serum albumin (BSA) as a model protein. BSA (Sigma Aldrich, MO, USA) was dissolved in phosphate-buffered saline (PBS, Gibco, Thermo Fisher Scientific, MA, USA) at two different concentrations, 600 μg ml^{-1} and 6000 μg ml^{-1}. BSA was fluorescently marked with 3-(4-carboxybenxoyl) quinoline-2-carboxaldehyde (CBQCA, Invitrogen, Thermo Fisher Scientific, MA, USA) following the manufacturer indications. In order to visualise the protein penetration in the strands' cross-section, 5 mm-length spare strands of each material were immersed in 150 μl of each BSA solution, for different incubation times (*i.e.* 30 min, 1 h, 2 h, 4 h, 8 h and 24 h). The adsorbed protein was imaged by means of a fluorescence confocal

microscope (LSM 800, Zeiss, Oberkochen, Germany) using a wavelength of 488 nm. A flat surface of the strand cross-section was obtained by embedding the samples in two-part epoxy resin (Sei Whale, R*Concept, Barcelona, Spain) and water sanding them down to 4000P grain size (EcoMet 4 grinder polisher, Buehler, IL, USA). Additionally, an indirect quantification of the kinetics of protein adsorption was performed. For each of the studied time points, 5 mg of B and H strands were incubated in 100 µl of both BSA solutions. The supernatants were collected and their fluorescence intensity measured in a microplate reader (Synergy HTX, BioTek Instruments, VT, USA). Data were correlated to a calibration curve to establish the BSA concentration remaining in the supernatants. These concentrations were subtracted from the initial known solutions' concentration to determine the amount of protein adsorbed by the strands. The results were normalised by the sample weight and SSA of each material.

4.2.3 *In Vivo* Study

Study Design

All animal procedures were performed in compliance with the Guide for Care and Use of Laboratory Animals [40] and the European Community Guidelines (Directive 2010/63/EU) for the protection of animals used for scientific purposes and under the permission of the National Animal Ethics Committee on Human and Animal Experimentation (Approval # CEAAH 4683). This study was part of a larger study to analyse the bone regeneration capacity of scaffolds with different configurations. In total ten adult female New Zealand white rabbits with a body weight ranging from 4.8–5.5 kg and an age range of 8–12 months were used. The animals were purchased from a professional stock breeder (Charles River, Saint Aubin les Elboeuf, France) and housed in individual boxes of two square meters each one and an acclimatisation period of two weeks was established prior to surgery. Health status was determined by physical and orthopaedic examination, radiographic examination of the rear limbs and results of hematologic and serum biochemical profiles.

Cylindrical 3D-printed scaffolds with 5 mm in diameter and 8 mm in height, fabricated by either the biomimetic or the hydrothermal protocols (n = 7 for each condition) were randomly inserted in bilateral defects drilled in the medial aspect of the femoral condyle. One single time point at 8 weeks was evaluated.

Surgical Procedure

The surgical procedure was performed under standard sterile conditions. The animals were pre-anaesthetised using butorphanol, midazolam and medetomidine. Anaesthesia was induced with propofol and maintained with inhaled isoflurane in an oxygen carrier by mask. Both limbs stifle areas were clipped and subsequently scrubbed with chlorhexidine gluconate solution for an aseptic preparation of the surgical field. With the animals in dorsal recumbency and after a small skin subcutaneous and joint capsule incision, the medial aspect of both femoral condyles was exposed by a medial parapatellar incision (**Fig. 4.1 ii**). Using a 2.5 mm drill bit and under copious physiological saline irrigation to avoid thermal necrosis, a monocortical bone defect was performed in the centre point of the medial aspect of the condyle (**Fig. 4.1 iii**). Afterwards, the defect was enlarged with a 5 mm drill always under continuous physiological saline irrigation (**Fig. 4.1 iv**). The depth of the defect

was fixed to 10 mm. The cylindrical scaffolds with a diameter of 5 mm and a height of 10 mm were then press-fitted in each bone defect (**Fig. 4.1 v, 4.1 vi**). After assuring the good stability of the implants, the joint capsule, the subcutaneous tissue and the skin were sutured in layers in a routine way (**Fig. 4.1 vii, 4.1 viii**).

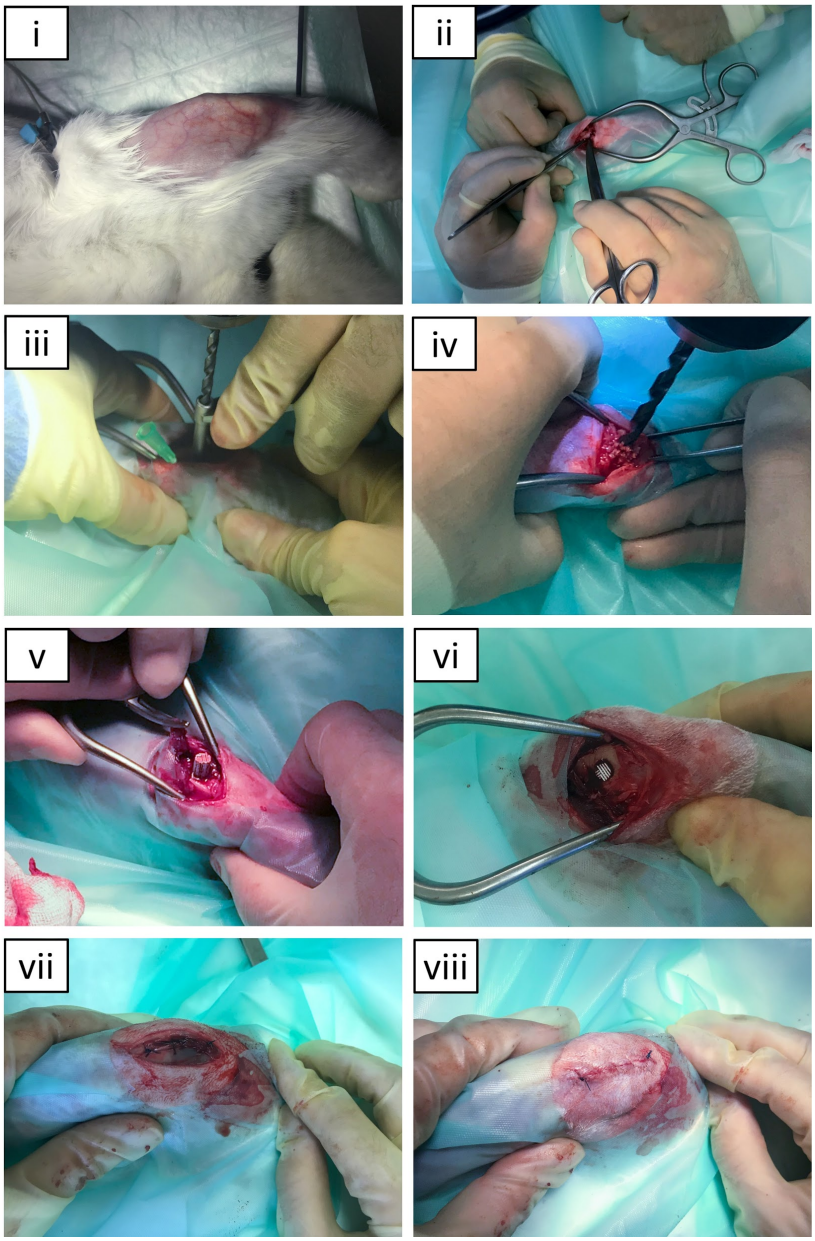

Fig. 4.1. i Defect region pre-operatory preparation. **ii** Medial parapatellar incision in the femoral condyle. **iii** 2.5 mm drilling in the centre point of the medial aspect of the femoral condyle guided by a drill guide. **iv** Expansion of the initial guide hole to 5 mm. **v**, **vi** Press-fit grafting of the cylindrical scaffold. **vii** Suture of the joint capsule. **viii** Suture of the skin.

Once recovered from the anaesthesia, the animals were housed in the same individual boxes and allowed to full weight-bearing. During the postoperative period, analgesic and antibiotic treatments were given to the animals for 7 d.

The animals were euthanised 8 weeks after the surgical procedure with an overdose of sodium pentobarbital according to the legislation of the American Veterinary Medical Association (AVMA). A pre-euthanasia sedation of midazolam and medetomidine was used for animal welfare reasons.

After euthanasia, the condylar regions of the femur were explanted and fixed in 10% neutral buffered formalin solution for two weeks and dehydrated in an increasing series of ethanol solutions.

Histomorphometric Analysis

This process was based on X-ray micro-computed tomography (μ-CT) of the explants and allowed to quantify in 3-dimensions the amount and distribution of the newly formed bone into the scaffold. The analysis was composed of the following steps:

- *Acquisition:* The dehydrated samples were analysed by μ-CT, adjusting the settings described in section 4.2.2 to a higher resolution, to properly distinguish the different tissue regions. The exposure time per projection was 2600 ms, 1800 projections were done along the 360º and an averaging of 3 frames per projection was chosen. An isotropic voxel size of 10 μm was used. The acquisitions were reconstructed using the same procedure previously described.

- *Segmentation:* The reconstructed stacks were first oriented in the Z printing direction and the X and Y printing axis were aligned to the image axis (Data Viewer, Bruker, Kontich, Belgium). Then, a cylindrical volume of interest (VOI) corresponding to the scaffold region (**Fig. 4.2 i**) was defined (CTAn, Bruker, Kontich, Belgium). The images of each z-stack were processed individually by fitting a univariate Gaussian mixture model with four components to their pixel grayscale level distributions [41]. This approach modelled the grayscale image histograms as a weighted sum of four Gaussian distributions corresponding to biomaterial, bone, non-mineralised tissue and outer VOI. (**Fig. 4.2 ii**). The model allowed clustering each pixel into one of the four tissue-type groups according to its greyscale value (**Fig. 4.2 iii**). This process was run iteratively for each image of the stack along the Z-direction. Subsequently, the segmented images were processed with a median filter with a disk-shaped structuring element of radius 50 μm to remove the segmentation artefacts attributed to the noise in the image (**Fig. 4.2 iv**).

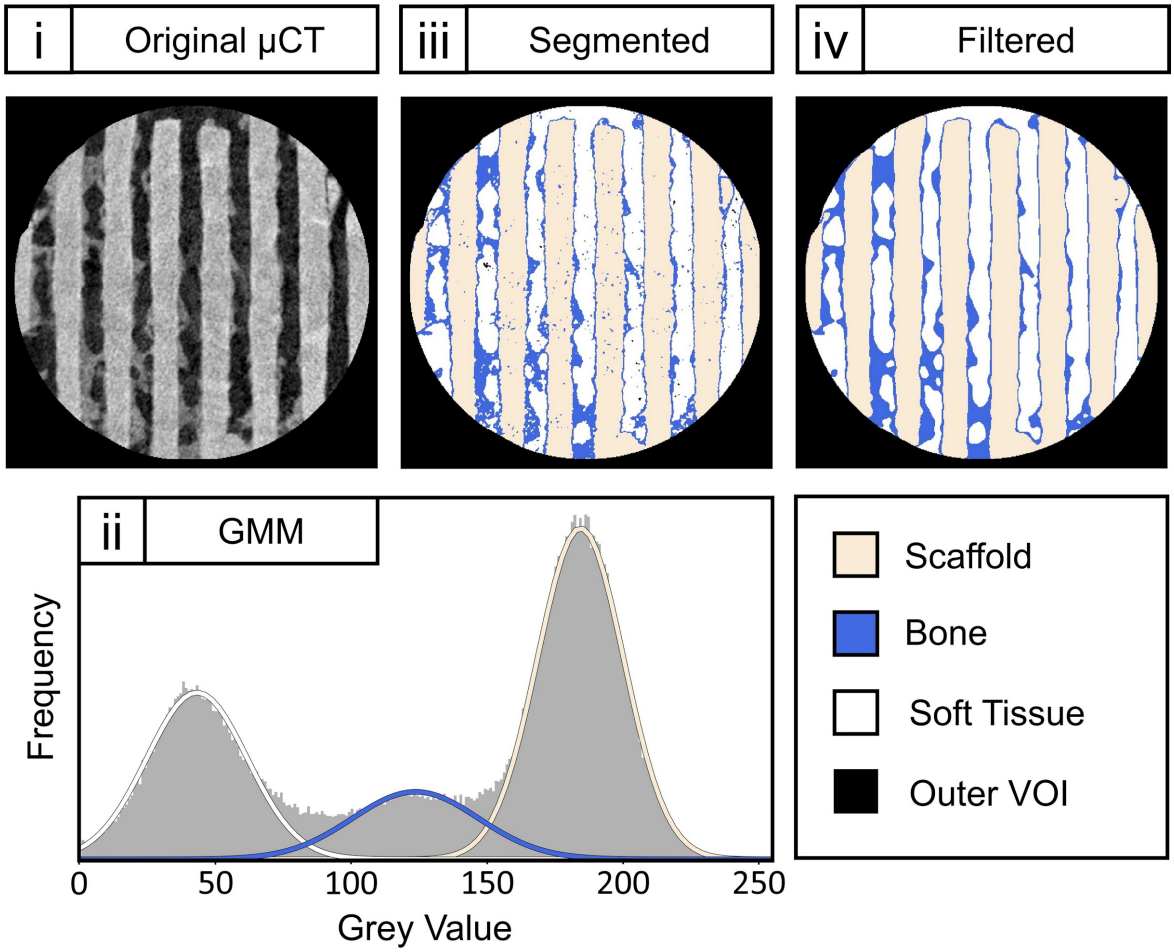

Fig. 4.2. Segmentation process: **i** slice image of the stack after orientation through Z printing axis and definition of a VOI, **ii** grey values histogram (background) with the Gaussian Mixture Model (GMM) distributions fitted for each tissue type, **iii** image after segmentation with the three model sub-populations and **iv** segmented image after applying median filter (disc-shaped structuring element with radius 50 µm) to correct for erroneously assigned pixels due to image noise. For visualisation purposes, pixels corresponding to outer VOI background have been excluded from the histogram representation.

- *Quantification of the Bone Volume Percentage*: For each sample, the total number of segmented pixels classified under the different tissue-type labels were quantified. Then, the bone volume percentage was calculated as the total number of bone pixels over the total number of available volume pixels.

- *Quantification of the Radial Bone Intrusion Curves:* The bone fraction in the scaffolds was measured and plotted as a function of the radial distance from the surface. To do so, the samples were analysed in radial bands using a thinning algorithm based on a morphological erosion transformation [42]. For each image of the Z stack, the perimeter of the VOI was taken as a departure point to determine a 100 µm-thick band by using a disc erosion operation. Then the percentage of bone in available volume was calculated for this band. This process was repeated successively departing from the new perimeter obtained after subtracting the previous band moving through the centre of the scaffold with each iteration.

- *Representation of the Bone Distribution Axial Colormaps:* For each condition, all the segmented stacks were added into a single 3-dimensional matrix stacking them along the Z printing axis (*i.e.* the axial direction of the cylindrical VOI*).* Then, the bone fraction of the resulting matrix was calculated for the Z projection. As a result, a 2D image representing in each pixel the average bone fraction of all the samples for the corresponding X-Y coordinate was obtained and plotted as a colourmap.

The program developed to perform the image analysis was written in Python (Python 3.9.0, www.python.org), its main stages are detailed in the supplementary information and the code is available in a Git repository

(https://github.com/YAGORAYMOND/uCT-image-analysis).

Histological Assessment

After µ-CT analysis, the dehydrated samples were immersed in solutions with increasing concentrations (*i.e.* 25, 50, 75 and 100%) of methyl methacrylate resin (Technovit 7200 VLC, Kulzer, Germany). The embedded samples were stored overnight under vacuum and photo polymerised in a UV lamp (EXAKT 520, Exakt Technologies, Norderstedt, Germany). The resulting blocks were cut through the central axis of the scaffolds cylinder with a precision diamond band saw (EXAKT 300 CP, Exakt Technologies, Norderstedt, Germany).

The cut surface of the first half sample was water sanded down to P4000 grain size (Surface grinder, EXAKT 400 CS, AW110, Exakt Technologies, Norderstedt, Germany), coated with a thin carbon layer and observed with a scanning electron microscope (SEM, Phenom XL, Phenom world, Thermo Fischer Scientific, MA, USA) operated at 10 kV and using a backscattered electron detector. Mappings of the full samples were acquired with the SEM automatic image mapping scan utility (Automated image mapping software, Phenom ProSuite, Phenom World, Thermo Fischer Scientific, MA, USA).

A 300 µm slice of the second half-sample was cut with a precision band saw with a diamond blade, glued to a PMMA 3 mm sample holder (precision adhesive press, EXAKT 402, Exakt Technologies, Norderstedt, Germany), polished down to 30-50 µm and stained using Masson-Goldner trichrome staining. The stained samples were observed with a bright-field optical microscope (BX51-P, Olympus, Tokyo, Japan).

4.2.4 Statistical Analysis

The compressive strength and the dimensional evaluation of the structures are reported as mean values ± standard deviations. The histomorphometric analysis is reported with a boxplot indicating the median and quartiles. A statistical analysis software (Minitab®19, MiniTab Inc., State College, PA) was used in all the cases to determine statistically significant differences between specimens by one-way analysis of variance (ANOVA) followed by Tukey's post hoc test. A confidence interval of 95% (α=0.05) was considered.

4.3 Results

4.3.1 Scaffolds Characterisation

Chemical Composition

Differences in chemical composition were observed by X-ray diffraction (XRD) of both biomaterials (**Fig. 4.2 i**). Whilst all diffraction peaks in the biomimetic scaffold, apart from the corundum peaks corresponding to the internal standard, were attributed to calcium-deficient hydroxyapatite (CDHA), the hydrothermal scaffolds presented a biphasic composition consisting of CDHA and beta-tricalcium phosphate (β-TCP). Additionally, differences in the sharpness of the peaks were readily visible for the hydrothermal condition when compared to the biomimetic one. Better resolved peaks indicating a higher degree of crystallinity were observed for the hydrothermally treated scaffolds (**Fig. 4.2 ii**). In addition, in both XRD spectra, the peak appearing at 25.9º corresponding to the (002) reflection of CDHA, was substantially sharper than the rest of the peaks of the same phase, indicating a preferential crystal growth along the *c* axis direction. Changes in the relative intensity of the peaks were also detected in the 31.0-33.5º 2θ range, which were attributed to both the peak overlapping of the additional phase encountered and the texturisation of the anisotropic crystals during the sample preparation. Moreover, although XRD provides direct information on crystalline phases, the addition of a known amount of an internal standard mixed with the powdered scaffolds allows also an indirect determination of the amount of amorphous phases present in the samples [37]. The resulting XRD spectra along with the results of phase quantification by Rietveld refinement, revealed that the biomimetic treatment resulted in 92.9% of CDHA and 7.1% of amorphous phase, compared to 78.7% of CDHA, 10.1% β-TCP and 11.2% of amorphous phase obtained with the hydrothermal treatment.

The analysis by Raman spectroscopy showed similar results for both treatments presenting the characteristic PO_4 vibration v_1 band at ≈960 cm^{-1}. Furthermore, two v_2 (PO_4^{3-}) vibrations corresponding to the doubly degenerate bending mode O-P-O appearing at 447 and 433 cm^{-1}, the v_3 (PO_4^{3-}) vibrations corresponding to the triply degenerate asymmetric stretching mode (P-O) appearing in the region from 1030 to 1100 cm^{-1} and the v_4 (PO_4^{3-}) triply degenerate bending mode vibrations appearing in the region 550-630 cm^{-1} [43]. The weak band at ≈1005 cm^{-1} is assigned to the symmetric stretching of the HPO_4^{2-} ions, the band at ≈880 cm^{-1} to the stretching of P-(OH^-) in HPO_4^{2-} and the band at 3572 cm^{-1} is associated with the stretching mode of the OH^- group [44].

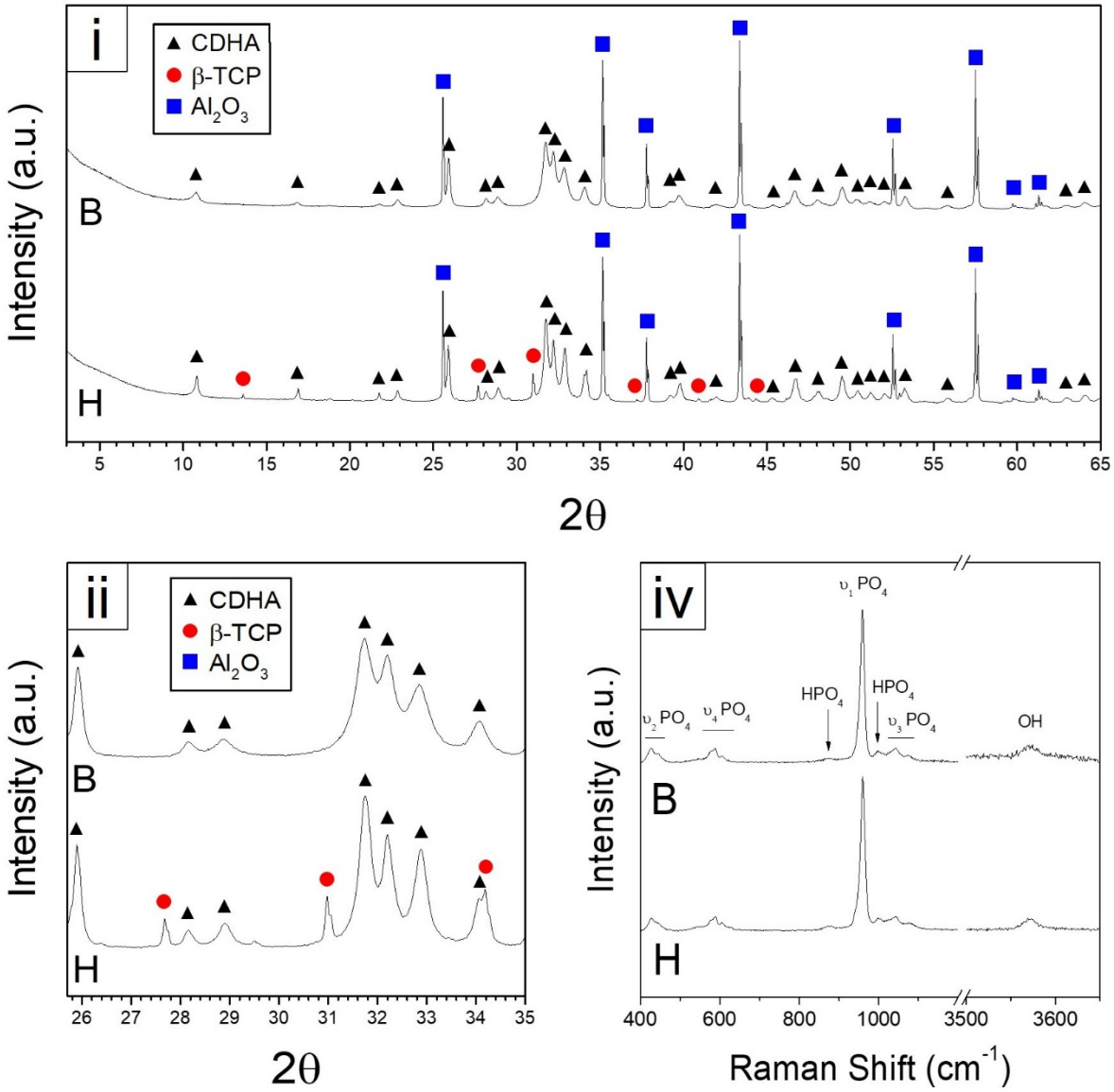

iii

	Crystalline Phase		Amorphous Phase
	CDHA	β-TCP	
Biomimetic	92.9 %	–	7.1 %
Hydrothermal	78.7 %	10.1 %	11.2 %

Fig. 4.3. Comparison of the samples set through the biomimetic (B) and hydrothermal (H) treatments. **i** X-ray diffraction pattern of the whole acquired 2θ range (3-65º) with symbols identifying the crystalline phases found in each sample, *i.e.* calcium-deficient hydroxyapatite (CDHA), β-tricalcium phosphate (β-TCP) and corundum (Al_2O_3), the internal pattern added to the pristine samples to quantify the amorphous phase. **ii** zoomed region of the XRD diffractogram. **iii** Rietveld refinement crystalline and amorphous phase quantification. **iv** Raman spectra of the B and H samples.

Microstructure, Porosity, Mechanical Properties and Protein Adsorption

The scaffolds presented remarkable differences in the microstructure. Whilst the samples set under biomimetic conditions presented a microstructure consisting of entangled plate-like hydroxyapatite nanocrystals, the samples hardened by hydrothermal routes showed interlocked acicular needle-shaped nanocrystals, with a much larger aspect ratio, as displayed in **Fig. 4.4**. The plate-like crystals of the biomimetic samples resulted in a larger SSA of 38.54 $m^2 g^{-1}$ compared to 27.11 $m^2 g^{-1}$ for the hydrothermal samples.

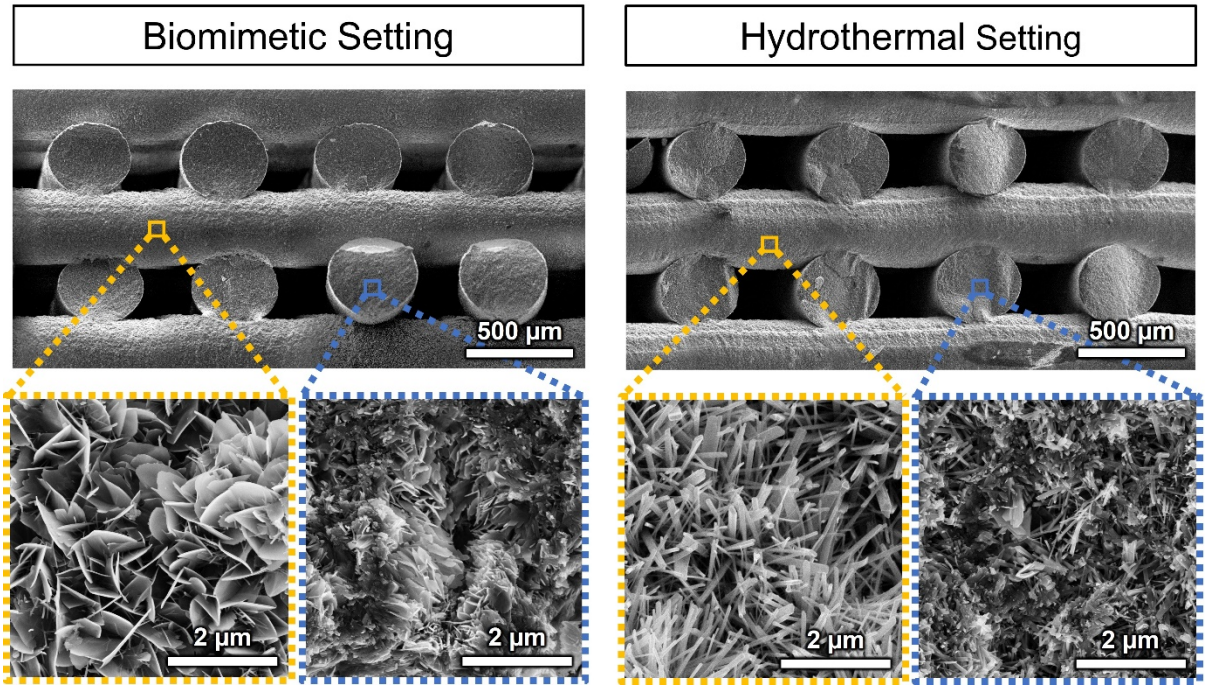

Fig. 4.4. Comparison of the macro- and microstructure of the scaffolds set under biomimetic and hydrothermal treatments assessed by scanning electron microscopy.

The total porosity of the scaffolds, determined by gravimetric methods, was similar in the two scaffold types, irrespective of the consolidation method (**Table 4.1**). The macroporosity (P_{macro}) calculated by µ-CT (**Table 4.1**) was slightly smaller for the hydrothermal than for the biomimetic samples. In both conditions, the values were slightly above the theoretical values. Regarding size distribution as determined by MIP, both samples presented a bimodal pore entrance size distribution (**Fig. 4.5 i**), with two peaks corresponding to the intrastrand porosity, which was in the nanometric range and the inter-strand porosity or macroporosity. Due to their large dimensions, the macropores fell partially outside the range detectable by this technique. Remarkable differences were found both in the intrastrand nanoporosity (**Table 4.1**) and nanopore size. Whereas the biomimetic samples presented a nanoporosity of 48.4% and nanopore sizes centred at 0.017 µm, the hydrothermally treated samples had a higher nanoporosity of 57.1%, with larger pore entrance sizes of 0.062 µm.

Table 4.1. Textural parameters of the scaffolds hardened using biomimetic or hydrothermal treatments: macroporosity (P_{macro}) obtained by μ-CT; intrastrand nanoporosity ($P_{intrastrand}$) measured combining MIP and He pycnometry according to Eq. 4.2; total porosity (P_{total}) determined by gravimetric methods; skeletal density (ρ_{skel}) determined by He pycnometry and specific surface area (SSA) by nitrogen adsorption through the BET method.

	P_{macro} [%]	$P_{intrastrand}$ [%]	P_{total} [%]	ρ_{skel} [$g.cm^{-3}$]	SSA [$mm^2.g^{-1}$]
Biomimetic	44.47 ± 0.74*	48.41	74.71 ± 2.02**	3.01	38.54
Hydrothermal	41.08 ± 1.50*	57.07	75.79 ± 1.07**	3.06	27.11
Theoretical	39.58	-	-	-	-

* Statistically significant differences observed between hardening methods ($p<0.05$).

** No statistically significant differences noted between hardening methods ($p>0.05$).

The assessment of the scaffolds' architecture by μ-CT revealed that both hardening treatments resulted in a small linear shrinkage. This shrinkage was mainly observed in the directions of the printing plane (*i.e.* X and Y) with a more accentuated contraction of ~3% for the biomimetic condition compared to ~1.5% for the hydrothermal samples (**Fig. 4.5 ii**), although the differences were not statistically significant. Accordingly, the 3D mesh comparison of the printed structures (μ-CT) with the theoretical design showed a global deviation through the negative values. This was noticeable in the colourmap, with predominant lime-green colours, and in the histogram, with a shift through the left of both distributions (**Fig. 4.5 iii**).

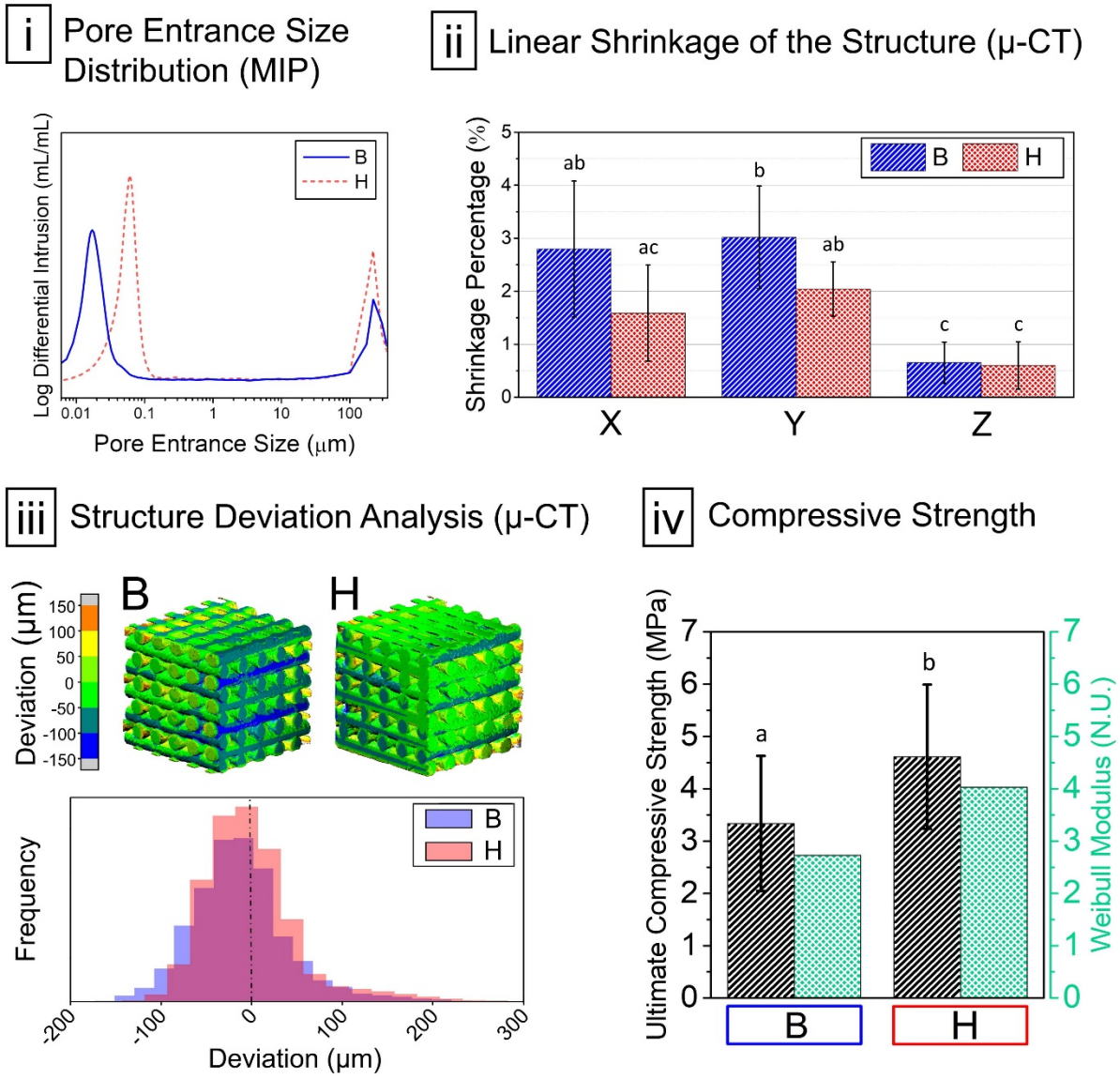

Fig. 4.5. i Pore entrance size distribution of the biomimetic and hydrothermally treated scaffolds determined by mercury intrusion porosimetry (MIP). **ii** Linear shrinkage percentage calculated from μ-CT acquisitions. **iii** 3D-mesh-based analysis of the scaffold morphology deviation compared to the theoretical structure. Meshes of each condition obtained by μ-CT segmentation. Colourmap representing the local deviations in each region of the structure (top) and histogram representing the point-cloud deviation distribution (bottom). **iv** Ultimate compressive strength and Weibull modulus of the scaffolds treated with the hydrothermal and biomimetic conditions. Different letters in sections (ii) and (iv) indicate statistically significant differences ($p<0.05$)

Fig. 4.5 iv displays the compressive strength of the scaffolds determined by uniaxial compressive testing. The hydrothermally treated samples presented higher values of ultimate compressive strength, 4.61 ± 1.29 MPa and elastic modulus, 366.21 ± 157.06 MPa compared to 3.34 ± 1.38 MPa and 236.97 ± 84.15 MPa respectively, for the samples obtained with the biomimetic treatment. Indeed, both differences were statistically significant ($p<0.05$). The Weibull modulus was also higher for the hydrothermally set samples, 4.03 compared to 2.73 for the biomimetic specimens.

Protein Adsorption

Remarkable differences were found in the BSA adsorption patterns of the two materials. The penetration of the protein into the material was significantly higher in the H samples than in the B samples, as visualised in **Fig. 4.6 i**. While in B samples the protein was detected only in a superficial layer of the strand, penetrating only a few microns even after 24h immersion, in H samples the BSA the protein diffused through the material progressively with incubation time. This was amplified in the solution with higher BSA concentration. These results were in good agreement with the values of BSA adsorbed in each material calculated from the remaining protein in solution, as shown in **Fig. 4.6 ii** for both H and B samples.

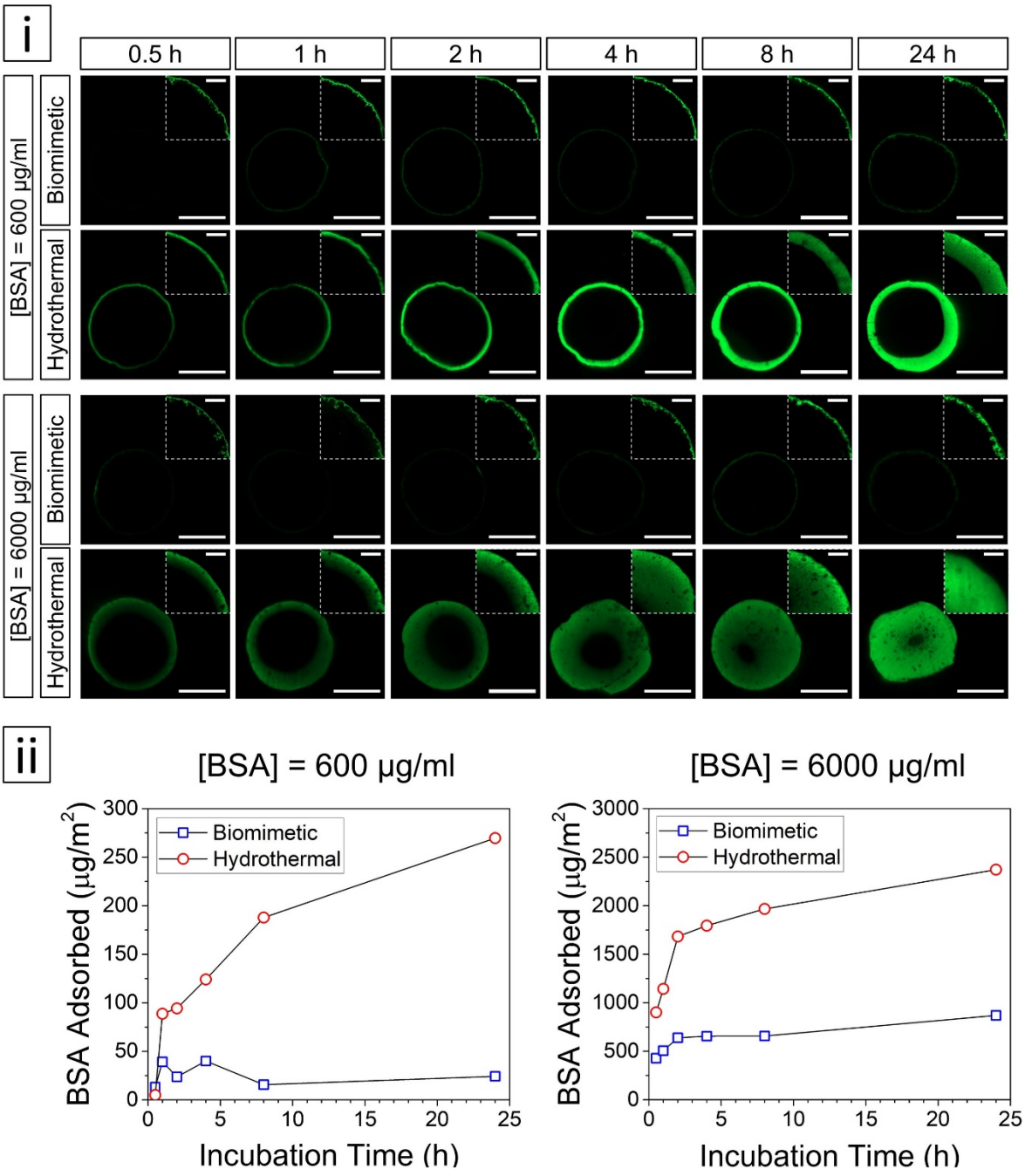

Fig. 4.6. Comparison of the protein adsorption properties of the biomimetic and hydrothermally treated samples incubated in two different BSA concentrations. **i** Fluorescent confocal microscopy images of the strand's cross-sections illustrating the penetration of BSA (in green) at different incubation times. Main images acquired with normalised settings for a better comparison between conditions. Scalebar = 200 µm. Inserts showing a close-up view of the surface penetration with optimised settings individually adjusted for each image. Scalebar = 50 µm. **ii** BSA adsorbed by the strands after incubation in the protein solutions. Results normalised by sample weight and SSA of each condition.

4.3.2 *In vivo* Performance

Surgeries were uneventful. However, one of the animals did not fully recover from the surgery, did not gain weight and finally died a few days after the procedure, which resulted in the loss of two samples, both belonging to group B. The rest of the animals completed a normal postoperative period without any clinical complication. No signs of infection, wound dehiscence, weight loss, behaviour changes, implant migration or lameness were observed along the postoperative period.

Histomorphometric Assessment

The percentage of newly formed bone was quantified in three dimensions. Scaffolds hardened under hydrothermal conditions presented a significantly higher amount of newly formed bone with a 37.3 ± 4.7% compared to the 28.8 ± 5.3% obtained with the biomimetic treatment (**Fig. 4.7 i**). A more detailed analysis of the bone distribution inside the scaffolds revealed that the percentage of bone was higher along the entire cross-section in the hydrothermal scaffolds as compared to the biomimetic ones, and that the difference was more pronounced at the external region of the scaffold, in contact with the surrounding bone (**Fig. 4.7 ii**). This is in good agreement with **Fig. 4.7 iii**, where the colourmaps representing the cumulative value of the average of the percentage of bone on the axial projection (*i.e.* printing plane) for all the specimens are displayed.

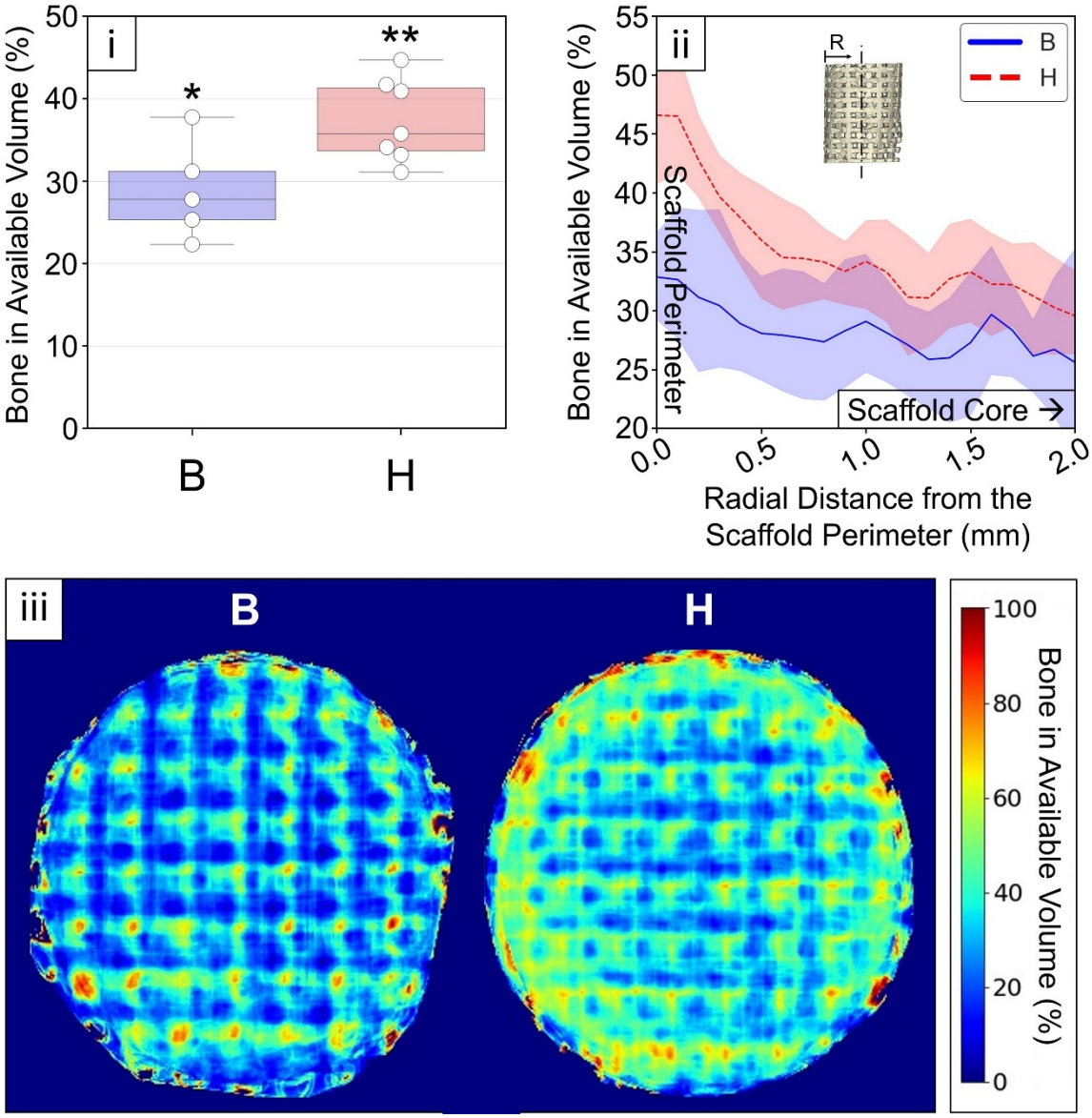

Fig. 4.7. µ-CT histomorphometric analysis: **i** Box plot and overlaid scatter plot of individual events representing the percentage of bone volume in available volume. Statistically significant differences indicated with a different number of asterisks (p-value = 0.024). **ii** Radial intrusion of bone into the scaffold. The X-axis represents the distance from the external perimeter of the scaffold. The average bone fraction is represented with a darker-coloured line and the 95% confidence interval for that estimate is represented with a softer-coloured region. **iii** Cumulative mapping showing the percentage of newly formed bone in available volume along the printing-plane projection (average of all the specimens).

Histological Evaluation

Both scaffold types presented newly formed bone growing in direct contact with the biomaterial (**Fig. 4.8** and **4.9**) and a widespread blood vessels network dispersed inside the interconnected macroporosity (**Fig. 4.9 i-iii, vii-ix).** The new bone was

mainly found surrounding the biomaterial and accumulated in the strand intersections, and consisted of a mixture of woven bone and some lamellar structures. The regions of lamellar bone were more abundant in the hydrothermal specimens, with numerous Haversian channels surrounded by successive osteonal lamellae, as well as Howship's lacunae in the osseous surfaces of the larger vascular channels, suggestive of an active remodelling process.

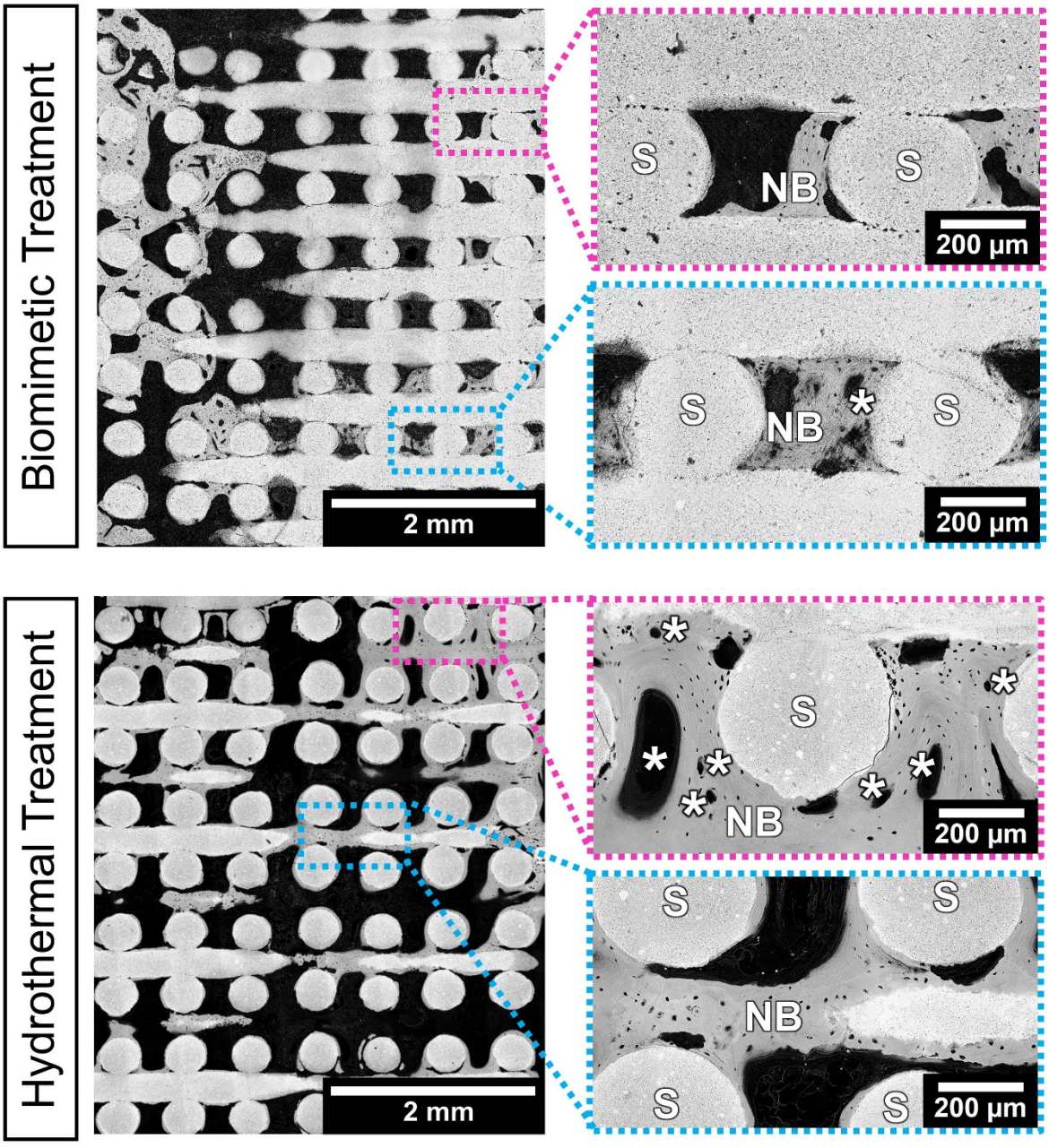

Fig. 4.8. Scanning electron micrographs of the scaffolds set through biomimetic and hydrothermal treatments after 8 weeks of implantation. The scaffold (S) appears in light grey in direct contact with the newly formed bone (NB), in darker grey. Haversian canals (asterisks) surrounded by concentrically arranged lamellae are visible in the regions where the bone is at a more advanced stage of remodelling.

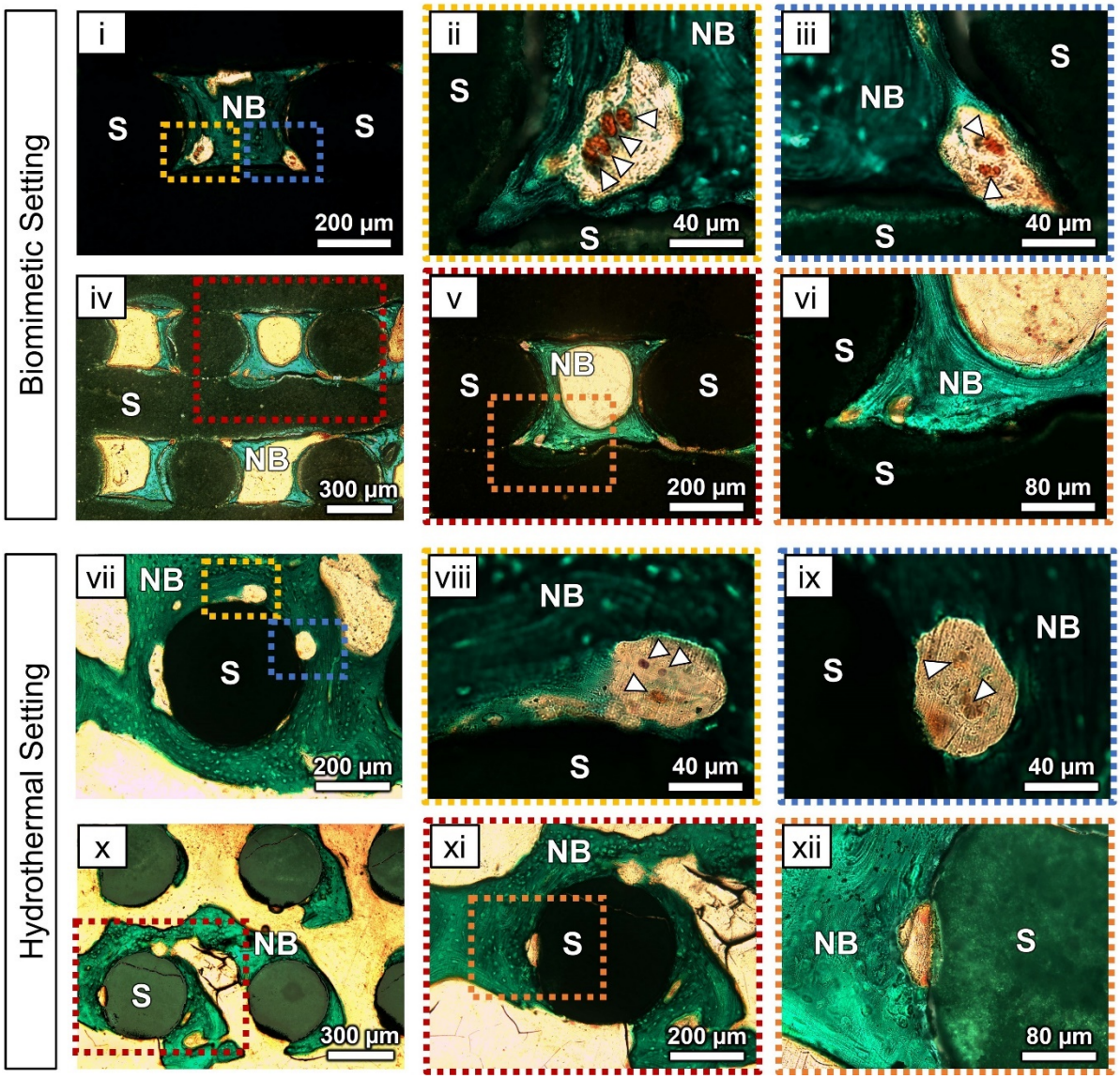

Fig. 4.9. Micrographs of undecalcified Masson-Goldner trichrome stained histological sections of biomimetically hardened (Top) and hydrothermally hardened (Bottom) 3D scaffolds. Both conditions showed a proper interaction of the scaffold (S) with the newly formed bone (NB), stained in green. Osteocytes inside lacunae are recognizable along all the calcified bone matrix and a network of blood vessels (white arrowheads) is identified in both materials (ii, iii, viii, ix).

4.4 Discussion

Using a hydrothermal hardening process for setting α-TCP-based synthetic bone grafts instead of the traditional biomimetic treatment is a strategy of major industrial interest as the processing time can be significantly reduced [32]. Moreover, contrary to what happens with high-temperature ceramic treatments, it allows obtaining solid structures with high specific surface areas and nanostructured surfaces, similarly to biomimetic treatments. The aim of this study was to shed light on the effects that the two treatments have at a chemical and structural level and especially in terms of the *in vivo* response.

4.4.1 Physicochemical Properties

The hydrothermal treatment of the α-TCP-poloxamer green scaffolds resulted in two types of changes compared to the biomimetic route: slight alterations in the composition (**Fig. 4.3**) and a change in the shape of the precipitated crystals (**Fig. 4.4**). The differences in composition were attributed to an allotropic α-TCP to β-TCP transformation, associated with the temperature and pressure of the process, which coexist with the main reaction, the hydrolysis of α-TCP to CDHA [45]. Moreover, the higher reaction energy of this process favoured the nucleation of apatite with a higher crystallinity [46]. In addition, a small percentage of amorphous phase was detected (≈10% for the hydrothermal and ≈7% for the biomimetic). The presence of intermediate amorphous phases has been previously detected in the precipitation of many apatitic products, including the hydrolysis of α -TCP, as they facilitate the nucleation of apatite crystals [47]. Moreover, accurate NMR and spectroscopic analyses on precipitated nanoapatite crystals have persistently observed an amorphous-like layer (hydrated-layer) covering the surface of existing nanocrystals [27]. These two sources of amorphous content could explain the presence of amorphous phase detected in the samples.

Concerning the results from Raman spectroscopy, both scaffolds had very similar features in their phosphates, hydrogen phosphate and hydroxyl bands, despite the different hydrolysis settings: hydrothermal versus biomimetic. In both cases CDHA was characterised by a small hydroxyl band which, similar to biological bone apatites, indicates a very small amount of hydroxyl groups compared to highly pure stoichiometric hydroxyapatites [48]. This lack of OH^- ions is a common feature of non-stoichiometric calcium-deficient and hydroxyl-deficient apatites [49]. In addition, the HPO_4^{2-}, which is common in biological bone apatite (but not in stoichiometric hydroxyapatite) is also typically observed in the hydrolysis of α-TCP [50].

On the other hand, remarkable differences in crystal shape were observed. Whilst the biomimetic treatment led to plate-like structures, the hydrothermal setting resulted in needle-like crystals elongated along the *c*-axis and larger in size. Crystallite anisotropy for both, plates and needles, was confirmed by XRD, from the anomalously sharp peak corresponding to the (002) reflection (2θ=25.9º), which indicates preferential crystal growth along the [001] direction, *i.e.* along the *c*-axis. Similar results were previously reported [31,51-53]. The reason why the shape of the crystals is altered is still unclear as too many variables such as temperature, pressure, pH, time, supersaturation, etc. can play a role. Moreover, the existence of negatively charged phosphate-rich *a*-surfaces and positively charged calcium-rich *c*-surfaces in hydroxyapatite leads to surface energy anisotropy, which also affects crystal growth. Ultimately, the morphology of the crystal depends on the competing growth of the *a*-surface *versus* the *c*-surface [31]. Analogously to the present observations, a similar difference in crystal morphology was observed when comparing calcium phosphates obtained by biomimetic setting treatments of α-TCP powders with fine and coarse particle sizes (*i.e.* d_{50} = 2.22 and 10.88 μm, respectively). In that case, a smaller particle size led to a higher reactivity conducing to the nucleation of needle-shaped crystals, whereas larger particles were less reactive and resulted in the nucleation of plate-like crystals, although larger than those obtained in the present study [54].

The different crystal morphology had also implications in the pore size distribution recorded by MIP. Thus, the acicular crystals of the hydrothermal scaffolds gave rise

to a more open and interconnected network, with larger pore entrance size (around 60-80 nm), and larger intrastrand porosity (57%) in contrast to the plate-shaped crystals of the biomimetic scaffolds, with very small pore entrance size (around 10-20 nm) and lower porosity (48%) (**Fig. 4.5 i**), in agreement with previous results [55]. Although the differences in the amount of nanoporosity and nanopore size may appear small, they had a great impact on the interaction with physiological fluids, as revealed when analysing the BSA adsorption by the different substrates (**Fig. 4.6**). Whereas in the biomimetic scaffolds the protein was unable to enter the porous network in spite of its high porosity, the hydrothermal scaffolds, were highly permeable to the diffusion of the protein, due to the higher porosity but, above all, the larger pore entrance size [56]. This resulted in a much higher amount of adsorbed protein in the H scaffolds despite their smaller specific surface area, a factor that may play a role in the distinct *in vivo* behaviour observed for the two materials notwithstanding the similarity in chemical composition.

4.4.2 Scaffold Morphology and Mechanical Properties

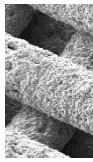

Shrinkage is one of the most critical aspects that has to be closely monitored for the design of personalised bone grafts by 3D printing. After printing, the green bodies obtained by the extrusion of ceramic powder inks are normally subjected to drying and sintering treatments. Both, the removal of the binder and the formation of inter-particle necks during the sintering process result in the shrinkage of the structure, and its magnitude depends on a multitude of factors, like the material, the ink solid fraction or the temperature and time of the thermal treatments among others [57], and typically ranges from 10 to 40% for DIW processes [15,58]. However, in the present work, the ink was composed of a reactive α-TCP powder, able to harden at a low temperature by a chemical consolidation process which allows circumventing the sintering step. As a result, much smaller shrinkages, below 3%, were recorded (**Fig. 4.5 ii**).

The self-setting reaction is driven by the progressive dissolution of α-TCP and consequent precipitation of CDHA [20]. Fernandez *et al*. determined that the dimensional changes associated with the hydrolysis reaction of α-TCP to CDHA in calcium phosphate cements were as small as 0.10% [59]. Previous studies regarding its application to DIW considered shrinkage of these self-setting inks to be negligible [60,61]. Nonetheless, other works reported the existence of dimensional changes in the strands during the setting treatment, leading to longitudinal cracking [28,29]. To the best of our knowledge, the shrinkage associated with DIW calcium phosphate cement scaffolds had not been quantified so far.

In the present study, we were able to quantify by μ-CT a small but statistically significant linear shrinkage, more pronounced for the biomimetic scaffolds than for the hydrothermal ones, which was anisotropic, considerably larger in the X and Y printing directions than in the Z (vertical) direction (**Fig. 4.5 ii**, **4.5 iii**). This small contraction may be the result of a combination of multiple events occurring at different stages of the scaffold fabrication process [62]: i) gravitational shrinkage, which may occur during the printing process when the ink has not yet solidified. It is caused by the strand's own weight and it affects only the vertical direction (Z) [63,64,65]; ii) evaporation shrinkage, which may take place just after extrusion due to the evaporation of the binder's solvent. It gives rise to longitudinal shrinkage, which affects mainly the printing plane directions (*i.e.* X and Y) [62]; iii) shrinkage linked to the removal of the binder, by release in solution during the setting treatment. Some authors have reported

swelling instead of contraction associated with the interaction of the binder with water [28,29]; iv) finally, dimensional changes associated with the consolidation process, in the present study the crystal entanglement during the cement-like reaction. These are much smaller than those observed in sintering processes due to the interparticle necking, and in both cases are isotropic [59,64,66].

The small shrinkage detected in the present work was observed preferentially in the XY direction, and was negligible in the Z direction. This can be attributed on one hand to the robust gel-embedded powder suspension used, with good pseudoplastic properties [67], and on another hand to the fixed layer height and the large layer overlap employed (25.7% of the strand diameter), which allowed each layer to compensate for potential vertical shrinkage in the previous layers. Similar trends were reported by other studies with calcium phosphate-poloxamer 407 inks, reporting more accentuated shrinkages in the printing plane directions than in the vertical direction [15,62]. The shrinkage observed could be associated with the evaporation of water during the printing process, or the release of the binder during the setting of the scaffolds. However, although the release of the binder when immersed in water during setting is almost total [32], this does not result in a high shrinkage, contrary to what happens during debinding for most ceramic inks. This could be explained by the fact that simultaneously with the binder dissolution, the reaction of the ceramic powder takes place, which results in the precipitation of an entangled network of newly precipitated crystals.

The difference between the two consolidation treatments was not statistically significant, although a more pronounced shrinkage was observed in the B condition. This may be related to the differences in binder's washout during the different setting treatments, being B a slower process. In the same vein, a previous study in CPC robocasted structures observed different shrinkage behaviours attributed to different cement setting treatments [28]. Moreover, the higher shrinkage of the B condition is consistent with the smaller intrastrand porosity of the structure observed by MIP (**Fig. 4.5** and **Table 4.1**). In summary, the precise determination of the shrinkage has confirmed the high dimensional stability associated with this type of inks and the advantage over the sintering-based approach. The values of shrinkage observed are compatible with the levels of shape accuracy required for patient-specific applications, as the resolution of the technique itself involves larger variability.

Regarding the mechanical properties, higher compressive strength was recorded for the hydrothermally treated scaffolds (**Fig. 4.5 iv**). Since both scaffolds had similar total porosity, this trend seems to be associated with the levels of inter-strand macroporosity, which was lower for the hydrothermal scaffolds than for the biomimetic ones, and affected the mechanical behaviour more markedly than the internal porosity of the strands, that was higher for the hydrothermal than for the biomimetic samples (**Table 4.1**). An additional parameter to be considered, besides porosity, is that the mechanical interlocking of the needle-shaped crystals can be more efficient than that provided by plate-like microstructures. This is in agreement with a previous study analysing the effect of the microstructure on the mechanical properties of calcium phosphate cements [54].

4.4.3 *In Vivo* Performance

The histological evaluation showed bone growth in direct contact with both biomaterials. No evidence of fibrous encapsulation nor foreign body reaction were observed in any of the samples (**Figs. 4.8** and **4.9**). This confirms the excellent biocompatibility of the low-temperature set (*i.e.* hydrolysed) CDHA biomaterials, which has been already reported in several studies [24,26,68,69]. The newly formed bone was homogeneously distributed along the axial direction and followed a gradient in the radial direction, evidencing the good osteoconductive properties of the material. Moreover, the interconnected porosity of the 3D-printed scaffolds allowed for the formation of widespread blood vessels along the structure.

Performing a μ-CT-based volumetric quantification was crucial for a complete histomorphometric assessment of such a patterned structure. Unlike in isotropic architectures, like foams, where a two-dimensional analysis may be representative, in this case, the porosity of the cross-section is very dependent on the orientation. The percentages of bone found in the grafted structures (**Fig. 4.7 i**) were similar to the ones found in the original trabecular defect region, assessed in the surrounding tissue. Additionally, this approach allowed to obtain further information to the classical bone surface over total surface (BS/TS) or bone volume over total volume (BV/TV) ratios. In this regard, bone intrusion could be assessed quantitatively (**Fig. 4.7 ii**). No differences in the trend of the bone intrusion curves were identified between sample conditions, indicating that both materials presented similar osteoconduction properties. However, the vertical offset observed in the hydrothermal curve indicated a more advanced regeneration stage which is in agreement with the bone volume quantifications. Furthermore, the average bone percentage mappings corroborated both observations (**Fig. 4.7 iii**). In both plots, a texture could also be identified which is associated with the pattern of the strands constituting the scaffold's structure.

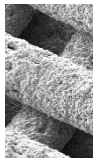

In spite of the great similarity between the two materials compared, significantly higher percentages of newly formed bone were obtained in the hydrothermal condition (**Fig. 4.7 i**). The distinctive features were the presence of 10% of β-TCP in the H samples, and the difference in microstructure, *i.e.* the needle-shaped vs plate-shaped morphology of the precipitated crystals in the H and B samples respectively, as well as a lower SSA for the former. Regarding the presence of β-TCP, one could hypothesise that it could increase the release of calcium in the surrounding tissues due to its higher solubility. However, previous studies showed that despite having a higher solubility, the release of Ca from β-TCP was smaller than that from biomimetic CDHA, due to the poor crystallinity and higher SSA of the latter [70]. Moreover, when increasing amounts of β-TCP were introduced in CDHA cements it was shown that calcium release was unaffected since β-TCP remained hidden within the CDHA matrix, which is also the case in the present material [71]. For these reasons, it seems that the cause of the different behaviours should rather be associated with the microstructural changes. Previous *in vivo* studies found a direct correlation between the microstructure of calcium phosphates and the bone regeneration process, being the needle-shaped microstructures the ones presenting the most promising results [33,35,72-74]. Specifically, in agreement with the results obtained in the present work, an earlier study comparing biomimetic CDHA with needle-like crystals vs plate-like crystals concluded that the needle-shaped microstructure resulted in accelerated osteoinductive and osteogenic properties [34]. This evidence of the benefits of the needle-like morphology has led to the development of hydrothermal methods for the

production of microtextured coatings on stable CaP ceramics such as biphasic calcium phosphates [72].

One aspect that could also contribute to the distinct *in vivo* behaviour is the fact that the two scaffold types exhibited large differences in permeability to physiological fluids and soluble proteins, as seen in the BSA adsorption study. This is known to be a relevant factor regarding osteogenesis, where soluble proteins play a crucial role [75,76]. In this sense, the extremely low permeability of the biomimetic scaffolds may be considered a detrimental aspect for their *in vivo* performance.

Finally, the morphological features of the osseous tissue found in the hydrothermal samples suggested a higher level of maturity. A greater number of lamellae was visible surrounding the Haversian channels of the larger and numerous osteons (**Fig. 4.8**). The cement lines visible in the lamellar bone around the scaffolds (**Fig. 4.9**) further indicated a longer bone remodelling process. The bone present in the biomimetic samples was mostly woven bone, with some osteons surrounded by a limited number of lamellae (**Fig. 4.8**).

4.5 Conclusion

The aim of this work was to compare two different hardening processes in 3D-printed CDHA scaffolds: one biomimetic and another hydrothermal. For the first time, we quantified the shrinkage associated with the α-TCP setting reaction to CDHA on 3D-printed scaffolds, concluding that it represents a minimal distortion to the global scaffold´s structure. Both the biomimetic and hydrothermal treatments resulted in scaffolds with excellent biocompatibility and osteoconductive properties. However, the differences in the microstructure, nanoporosity and nanopore size turned out to be key in both the interaction with proteins in solution and the osteogenic capacity of the materials. The specific features obtained by the hydrothermal process were found to be more favourable, resulting in significantly more bone. The implications for the clinical translation are clear, due to the reduced processing times required in the hydrothermal routes compared to the widely studied biomimetic methods.

4.6 References

[1] C. L. Ventola, “Medical Applications for 3D Printing: Current and Projected Uses” *P T*, vol. 39, no. 10, pp. 704–11, Oct. 2014.

[2] D. A. Hidalgo, “Fibula free flap: a new method of mandible reconstruction” *Plast. Reconstr. Surg.*, vol. 84, no. 1, pp. 71–9, Jul. 1989.

[3] M. K. Sen and T. Miclau, “Autologous iliac crest bone graft: Should it still be the gold standard for treating nonunions?” *Injury*, vol. 38, no. 1, pp. S75–S80, Mar. 2007, doi: 10.1016/j.injury.2007.02.012.

[4] P. Felice *et al.*, “Vertical ridge augmentation of the atrophic posterior mandible with interpositional bloc grafts: bone from the iliac crest vs. bovine anorganic bone. Clinical and histological results up to one year after loading from a randomized-controlled clinical tria” *Clin. Oral Implants Res.*, vol. 20, no. 12, pp. 1386–1393, Dec. 2009, doi: 10.1111/j.1600-0501.2009.01765.x.

[5] J. Parthasarathy, “3D modeling, custom implants and its future perspectives in craniofacial surgery” *Ann. Maxillofac. Surg.*, vol. 4, no. 1, p. 9, 2014, doi: 10.4103/2231-0746.133065.

[6] R. J. Mobbs, M. Coughlan, R. Thompson, C. E. Sutterlin, and K. Phan, “The utility of 3D printing for surgical planning and patient-specific implant design for complex spinal pathologies: case report” *J. Neurosurg. Spine*, vol. 26, no. 4, pp. 513–518, Apr. 2017, doi: 10.3171/2016.9.SPINE16371.

[7] H. Saijo *et al.*, “Maxillofacial reconstruction using custom-made artificial bones fabricated by inkjet printing technology” *J. Artif. Organs*, vol. 12, no. 3, pp. 200–205, Sep. 2009, doi: 10.1007/s10047-009-0462-7.

[8] J. Cesarano *et al.*, “Customization of Load-Bearing Hydroxyapatite Lattice Scaffolds” *Int. J. Appl. Ceram. Technol.*, vol. 2, no. 3, pp. 212–220, May 2005, doi: 10.1111/j.1744-7402.2005.02026.x.

[9] P. Tack, J. Victor, P. Gemmel, and L. Annemans, “3D-printing techniques in a medical setting: a systematic literature review” *Biomed. Eng. Online*, vol. 15, no. 1, p. 115, Dec. 2016, doi: 10.1186/s12938-016-0236-4.

[10] N. Martelli *et al.*, “Advantages and disadvantages of 3-dimensional printing in surgery: A systematic review” *Surgery*, vol. 159, no. 6, pp. 1485–1500, Jun. 2016, doi: 10.1016/j.surg.2015.12.017.

[11] J. C. Banwart, M. A. Asher, and R. S. Hassanein, “Iliac Crest Bone Graft Harvest Donor Site Morbidity” *Spine (Phila. Pa. 1976).*, vol. 20, no. 9, pp. 1055–1060, May 1995, doi: 10.1097/00007632-199505000-00012.

[12] J. P. Anthony, J. D. Rawnsley, P. Benhaim, E. F. Ritter, S. H. Sadowsky, and M. I. Singer, “Donor Leg Morbidity and Function after Fibula Free Flap Mandible Reconstruction” *Plast. Reconstr. Surg.*, vol. 96, no. 1, pp. 146–152, Jul. 1995, doi: 10.1097/00006534-199507000-00022.

[13] J. A. Lewis and G. M. Gratson, “Direct writing in three dimensions” *Mater. Today*, vol. 7, no. 7–8, pp. 32–39, Jul. 2004, doi: 10.1016/S1369-7021(04)00344-X.

[14] P. Miranda, E. Saiz, K. Gryn, and A. P. Tomsia, “Sintering and robocasting of β-tricalcium phosphate scaffolds for orthopaedic applications” *Acta Biomater.*, vol. 2, no. 4, pp. 457–466, Jul. 2006, doi: 10.1016/j.actbio.2006.02.004.

[15] J. Franco, P. Hunger, M. E. Launey, A. P. Tomsia, and E. Saiz, “Direct write assembly of calcium phosphate scaffolds using a water-based hydrogel” *Acta Biomater.*, vol. 6, no. 1, pp. 218–228, Jan. 2010, doi: 10.1016/j.actbio.2009.06.031.

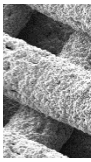

[16] C. F. Marques *et al.*, “Biphasic calcium phosphate scaffolds fabricated by direct write assembly: Mechanical, anti-microbial and osteoblastic properties” *J. Eur. Ceram. Soc.*, vol. 37, no. 1, pp. 359–368, Jan. 2017, doi: 10.1016/j.jeurceramsoc.2016.08.018.

[17] M. Vallet-Regí and J. M. González-Calbet, “Calcium phosphates as substitution of bone tissues” *Prog. Solid State Chem.*, vol. 32, no. 1–2, pp. 1–31, 2004, doi: 10.1016/j.progsolidstchem.2004.07.001.

[18] A. Lode *et al.*, “Fabrication of porous scaffolds by three-dimensional plotting of a pasty calcium phosphate bone cement under mild conditions” *J. Tissue Eng. Regen. Med.*, vol. 8, no. 9, pp. 682–693, Sep. 2014, doi: 10.1002/term.1563.

[19] Y. Maazouz *et al.*, “Robocasting of biomimetic hydroxyapatite scaffolds using self-setting inks” *J. Mater. Chem. B*, vol. 2, no. 33, pp. 5378–5386, 2014, doi: 10.1039/C4TB00438H.

[20] M. P. Ginebra *et al.*, “Setting Reaction and Hardening of an Apatitic Calcium Phosphate Cement” *J. Dent. Res.*, vol. 76, no. 4, pp. 905–912, Apr. 1997, doi: 10.1177/00220345970760041201.

[21] M.-P. Ginebra, M. Espanol, Y. Maazouz, V. Bergez, and D. Pastorino, “Bioceramics and bone healing” *EFORT Open Rev.*, vol. 3, no. 5, pp. 173–183, May 2018, doi: 10.1302/2058-5241.3.170056.

[22] J.-P. Carrel, A. Wiskott, S. Scherrer, and S. Durual, “Large Bone Vertical Augmentation Using a Three-Dimensional Printed TCP/HA Bone Graft: A Pilot Study in Dog Mandible” *Clin. Implant Dent. Relat. Res.*, vol. 18, no. 6, pp. 1183–1192, Dec. 2016, doi: 10.1111/cid.12394.

[23] J.-P. Carrel, A. Wiskott, M. Moussa, P. Rieder, S. Scherrer, and S. Durual, “A 3D printed TCP/HA structure as a new osteoconductive scaffold for vertical bone augmentation” *Clin. Oral Implants Res.*, vol. 27, no. 1, pp. 55–62, Jan. 2016, doi: 10.1111/clr.12503.

[24] P. Diloksumpan *et al.*, “Orthotopic Bone Regeneration within 3D Printed Bioceramic Scaffolds with Region-Dependent Porosity Gradients in an Equine Model” *Adv. Healthc. Mater.*, vol. 1901807, pp. 1–11, 2020, doi: 10.1002/adhm.201901807.

[25] L. Vidal *et al.*, “Regeneration of segmental defects in metatarsus of sheep with vascularized and customized 3D-printed calcium phosphate scaffolds” *Sci. Rep.*, vol. 10, no. 1, p. 7068, Dec. 2020, doi: 10.1038/s41598-020-63742-w.

[26] A. Barba *et al.*, “Osteogenesis by foamed and 3D-printed nanostructured calcium phosphate scaffolds: Effect of pore architecture” *Acta Biomater.*, vol. 79, no. 2, pp. 135–147, Oct. 2018, doi: 10.1016/j.actbio.2018.09.003.

[27] T. Ahlfeld *et al.*, “Toward Biofabrication of Resorbable Implants Consisting of a Calcium Phosphate Cement and Fibrin—A Characterization In Vitro and In Vivo” *Int. J. Mol. Sci.*, vol. 22, no. 3, p. 1218, Jan. 2021, doi: 10.3390/ijms22031218.

[28] A. R. Akkineni *et al.*, “3D plotting of growth factor loaded calcium phosphate cement scaffolds” *Acta Biomater.*, 2015, doi: 10.1016/j.actbio.2015.08.036.

[29] T. Ahlfeld *et al.*, “Design and Fabrication of Complex Scaffolds for Bone Defect Healing: Combined 3D Plotting of a Calcium Phosphate Cement and a Growth Factor-Loaded Hydrogel” *Ann. Biomed. Eng.*, vol. 45, no. 1, pp. 224–236, Jan. 2017, doi: 10.1007/s10439-016-1685-4.

[30] L. Galea *et al.*, “Textured and hierarchically structured calcium phosphate ceramic blocks through hydrothermal treatment” *Biomaterials*, vol. 67, pp. 93–103, Oct. 2015, doi: 10.1016/j.biomaterials.2015.07.026.

[31] S. Murakami, K. Kato, Y. Enari, M. Kamitakahara, N. Watanabe, and K. Ioku, “Hydrothermal synthesis of porous hydroxyapatite ceramics composed of rod-shaped particles and evaluation of their fracture behavior” *Ceram. Int.*, vol. 38, no. 2, pp. 1649–1654, 2012, doi: 10.1016/j.ceramint.2011.09.056.

[32] S. Raymond *et al.*, “Accelerated hardening of nanotextured 3D-plotted self-setting calcium phosphate inks” *Acta Biomater.*, vol. 75, pp. 451–462, Jul. 2018, doi: 10.1016/j.actbio.2018.05.042.

[33] A. Barba *et al.*, “Osteoinduction by Foamed and 3D-Printed Calcium Phosphate Scaffolds: Effect of Nanostructure and Pore Architecture” *ACS Appl. Mater. Interfaces*, vol. 9, no. 48, pp. 41722–41736, Dec. 2017, doi: 10.1021/acsami.7b14175.

[34] A. Barba *et al.*, “Impact of Biomimicry in the Design of Osteoinductive Bone Substitutes: Nanoscale Matters” *ACS Appl. Mater. Interfaces*, vol. 11, no. 9, pp. 8818–8830, 2019, doi: 10.1021/acsami.8b20749.

[35] N. Davison *et al.*, “Submicron-scale surface architecture of tricalcium phosphate directs osteogenesis in vitro and in vivo” *Eur. Cells Mater.*, vol. 27, no. April, pp. 281–297, Apr. 2014, doi: 10.22203/eCM.v027a20.

[36] R. Duan, D. Barbieri, X. Luo, J. Weng, J. D. de Bruijn, and H. Yuan, “Submicron-surface structured tricalcium phosphate ceramic enhances the bone regeneration in canine spine environment” *J. Orthop. Res.*, vol. 34, no. 11, pp. 1865–1873, Nov. 2016, doi: 10.1002/jor.23201.

[37] T. Westphal, T. Füllmann, and H. Pöllmann, “Rietveld quantification of amorphous portions with an internal standard—Mathematical consequences of the experimental approach” *Powder Diffr.*, vol. 24, no. 3, pp. 239–243, Sep. 2009, doi: 10.1154/1.3187828.

[38] C. T. Rueden *et al.*, “ImageJ2: ImageJ for the next generation of scientific image data” *BMC Bioinformatics*, vol. 18, no. 1, p. 529, Dec. 2017, doi: 10.1186/s12859-017-1934-z.

[39] A. Fedorov *et al.*, “3D Slicer as an image computing platform for the Quantitative Imaging Network” *Magn. Reson. Imaging*, vol. 30, no. 9, pp. 1323–1341, 2012, doi: 10.1016/j.mri.2012.05.001.

[40] N. R. Council, *Guide for the Care and Use of Laboratory Animals*. Washington, D.C.: National Academies Press, 2011.

[41] C. Bishop, *Pattern Recognition and Machine Learning*. Springer, 2005.

[42] R. C. Gonzalez and R. E. Woods, *Digital Image Processing*, 4th Editio. Pearson, 2018.

[43] S. Koutsopoulos, “Synthesis and characterization of hydroxyapatite crystals: A review study on the analytical methods” *J. Biomed. Mater. Res.*, vol. 62, no. 4, pp. 600–612, Dec. 2002, doi: 10.1002/jbm.10280.

[44] M. Markovic, B. O. Fowler, and M. S. Tung, “Preparation and comprehensive characterization of a calcium hydroxyapatite reference material” *J. Res. Natl. Inst. Stand. Technol.*, vol. 109, no. 6, p. 553, Nov. 2004, doi: 10.6028/jres.109.042.

[45] L. Galea *et al.*, “Textured and hierarchically structured calcium phosphate ceramic blocks through hydrothermal treatment” *Biomaterials*, vol. 67, pp. 93–103, 2015, doi: 10.1016/j.biomaterials.2015.07.026.

[46] L. M. Rodríguez-Lorenzo and M. Vallet-Regí, “Controlled crystallization of calcium phosphate apatites” *Chem. Mater.*, vol. 12, no. 8, pp. 2460–2465, 2000, doi: 10.1021/cm001033g.

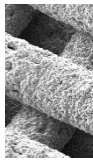

[47] X. Wei, O. Ugurlu, and M. Akinc, “Hydrolysis of α-Tricalcium Phosphate in Simulated Body Fluid and Dehydration Behavior During the Drying Process” *J. Am. Ceram. Soc.*, vol. 90, no. 8, pp. 2315–2321, Aug. 2007, doi: 10.1111/j.1551-2916.2007.01682.x.

[48] C. Rey, C. Combes, C. Drouet, and M. J. Glimcher, “Bone mineral: update on chemical composition and structure” *Osteoporos. Int.*, vol. 20, no. 6, pp. 1013–1021, Jun. 2009, doi: 10.1007/s00198-009-0860-y.

[49] C. Drouet, “Apatite Formation: Why It May Not Work as Planned, and How to Conclusively Identify Apatite Compounds” *Biomed Res. Int.*, vol. 2013, pp. 1–12, 2013, doi: 10.1155/2013/490946.

[50] M. Espanol, J. Portillo, J.-M. Manero, and M.-P. Ginebra, “Investigation of the hydroxyapatite obtained as hydrolysis product of α-tricalcium phosphate by transmission electron microscopy” *CrystEngComm*, vol. 12, no. 10, p. 3318, 2010, doi: 10.1039/c001754j.

[51] M. Yoshimura, H. Suda, K. Okamoto, and K. Ioku, “Hydrothermal synthesis of biocompatible whiskers” *J. Mater. Sci.*, vol. 29, no. 13, pp. 3399–3402, Jul. 1994, doi: 10.1007/BF00352039.

[52] K. Ioku, S. Nishimura, Y. Eguchi, and S. Goto, “Hydrothermal Preparation of Porous Hydroxyapatite Ceramics” *Rev. HIGH Press. Sci. Technol.*, vol. 7, no. 8, pp. 1398–1400, Aug. 1998, doi: 10.4131/jshpreview.7.1398.

[53] K. Ioku, G. Kawachi, S. Sasaki, H. Fujimori, and S. Goto, “Hydrothermal preparation of tailored hydroxyapatite” *J. Mater. Sci.*, vol. 41, no. 5, pp. 1341–1344, Mar. 2006, doi: 10.1007/s10853-006-7338-5.

[54] M. P. Ginebra, F. C. M. Driessens, and J. A. Planell, “Effect of the particle size on the micro and nanostructural features of a calcium phosphate cement: A kinetic analysis” *Biomaterials*, vol. 25, no. 17, pp. 3453–3462, Aug. 2004.

[55] D. Pastorino, C. Canal, and M.-P. Ginebra, “Multiple characterization study on porosity and pore structure of calcium phosphate cements” *Acta Biomater.*, vol. 28, pp. 205–214, Dec. 2015, doi: 10.1016/j.actbio.2015.09.017.

[56] M. Espanol, R. A. Perez, E. B. Montufar, C. Marichal, A. Sacco, and M. P. Ginebra, “Intrinsic porosity of calcium phosphate cements and its significance for drug delivery and tissue engineering applications” *Acta Biomater.*, vol. 5, no. 7, pp. 2752–2762, Sep. 2009, doi: 10.1016/j.actbio.2009.03.011.

[57] F. Abdeljawad *et al.*, “Sintering processes in direct ink write additive manufacturing: A mesoscopic modeling approach” *Acta Mater.*, vol. 169, pp. 60–75, May 2019, doi: 10.1016/j.actamat.2019.01.011.

[58] A. Nommeots-nomm, P. D. Lee, and J. R. Jones, “Journal of the European Ceramic Society Direct ink writing of highly bioactive glasses” *J. Eur. Ceram. Soc.*, vol. 38, no. 3, pp. 837–844, 2018, doi: https://doi.org/10.1016/j.jeurceramsoc.2017.08.006.

[59] E. Fernández, M. P. Ginebra, O. Bermúdez, M. G. Boltong, F. C. M. Driessens, and J. A. Planell, “Dimensional and thermal behaviour of calcium phosphate cements during setting compared to PMMA bone cements” *J. Mater. Sci. Lett.*, vol. 14, no. 1, pp. 4–5, Jan. 1995, doi: 10.1007/BF02565267.

[60] A. Lode *et al.*, “Fabrication of porous scaffolds by three-dimensional plotting of a pasty calcium phosphate bone cement under mild conditions” *J. Tissue Eng. Regen. Med.*, vol. 8, no. 9, pp. 682–693, Sep. 2014, doi: 10.1002/term.1563.

[61] N. Raja, A. Sung, H. Park, and H. Yun, “Low-temperature fabrication of calcium deficient hydroxyapatite bone scaffold by optimization of 3D printing conditions” *Ceram. Int.*, vol. 47, no. 5, pp. 7005–7016, Mar. 2021, doi:

10.1016/j.ceramint.2020.11.051.

[62] E. B. Montufar *et al.*, “Factors governing the dimensional accuracy and fracture modes under compression of regular and shifted orthogonal scaffolds” *J. Eur. Ceram. Soc.*, vol. 40, no. 14, pp. 4923–4931, 2020, doi: 10.1016/j.jeurceramsoc.2020.03.045.

[63] J. Cesarano, “A Review of Robocasting Technology” *MRS Proc.*, vol. 542, p. 133, Feb. 1998, doi: 10.1557/PROC-542-133.

[64] S. Eqtesadi *et al.*, “Fabricating geometrically-complex B_4C ceramic components by robocasting and pressureless spark plasma sintering” *Scr. Mater.*, vol. 145, pp. 14–18, 2018, doi: 10.1016/j.scriptamat.2017.10.001.

[65] M. Houmard, Q. Fu, M. Genet, E. Saiz, and A. P. Tomsia, “On the structural, mechanical, and biodegradation properties of HA/β-TCP robocast scaffolds” *J. Biomed. Mater. Res. Part B Appl. Biomater.*, vol. 101, no. 7, pp. 1233–1242, Oct. 2013, doi: 10.1002/jbm.b.32935.

[66] Á. D. E. Pablos, M. Belmonte, M. I. Osendi, and P. Miranzo, “Cerámica y Vidrio Microstructural designs of spark-plasma sintered silicon carbide ceramic scaffolds” vol. 53, pp. 93–100, 2014, doi: 10.3989/cyv.132014.

[67] E. Feilden, “Additive manufacturing of ceramics and ceramic composites via robocasting” Imperial College London, 2017.

[68] H. GUO, J. SU, J. WEI, H. KONG, and C. LIU, “Biocompatibility and osteogenicity of degradable Ca-deficient hydroxyapatite scaffolds from calcium phosphate cement for bone tissue engineering” *Acta Biomater.*, vol. 5, no. 1, pp. 268–278, Jan. 2009, doi: 10.1016/j.actbio.2008.07.018.

[69] L. Ambrosio *et al.*, “Injectable calcium-phosphate-based composites for skeletal bone treatments” *Biomed. Mater.*, vol. 7, no. 2, p. 024113, Mar. 2012, doi: 10.1088/1748-6041/7/2/024113.

[70] A. Diez-Escudero, M. Espanol, S. Beats, and M.-P. Ginebra, “In vitro degradation of calcium phosphates: Effect of multiscale porosity, textural properties and composition” *Acta Biomater.*, vol. 60, pp. 81–92, Sep. 2017, doi: 10.1016/j.actbio.2017.07.033.

[71] S. Gallinetti, C. Canal, and M.-P. Ginebra, “Development and Characterization of Biphasic Hydroxyapatite/β-TCP Cements” *J. Am. Ceram. Soc.*, vol. 97, no. 4, pp. 1065–1073, Apr. 2014, doi: 10.1111/jace.12861.

[72] R. Duan, L. van Dijk, D. Barbieri, F. de Groot, H. Yuan, and J. de Bruijn, “Accelerated bone formation by biphasic calcium phosphate with a novel sub-micron surface topography” *Eur. Cells Mater.*, vol. 37, pp. 60–73, Jan. 2019, doi: 10.22203/eCM.v037a05.

[73] N. Davison, J. Su, H. Yuan, J. van den Beucken, J. de Bruijn, and F. Barrère-de Groot, “Influence of surface microstructure and chemistry on osteoinduction and osteoclastogenesis by biphasic calcium phosphate discs” *Eur. Cells Mater.*, vol. 29, pp. 314–329, Jun. 2015, doi: 10.22203/eCM.v029a24.

[74] S.-I. Roohani-Esfahani, S. Nouri-Khorasani, Z. Lu, R. Appleyard, and H. Zreiqat, “The influence hydroxyapatite nanoparticle shape and size on the properties of biphasic calcium phosphate scaffolds coated with hydroxyapatite–PCL composites” *Biomaterials*, vol. 31, no. 21, pp. 5498–5509, Jul. 2010, doi: 10.1016/j.biomaterials.2010.03.058.

[75] L. E. Rustom *et al.*, “Micropore-induced capillarity enhances bone distribution in vivo in biphasic calcium phosphate scaffolds” *Acta Biomater.*, vol. 44, pp. 144–154, Oct. 2016, doi: 10.1016/j.actbio.2016.08.025.

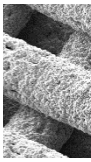

[76] S. K. Lan Levengood *et al.*, “Multiscale osteointegration as a new paradigm for the design of calcium phosphate scaffolds for bone regeneration” *Biomaterials*, vol. 31, no. 13, pp. 3552–3563, May 2010, doi: 10.1016/j.biomaterials.2010.01.052.

4.7 Supplementary Information

4.7.1 Rietveld Refinement

Rietveld refinement analyses were performed with the TOPAS software (TOPAS v4.2, Bruker AXS, Karlsruhe, Germany). For the refinement process, the starting model of the different structures was taken from the Inorganic Crystal Structure Database (ICSD) and the Crystallography Open Database (COD): COD-9002214 for calcium deficient hydroxyapatite (CDHA), ICSD-006191 for β-tricalcium phosphate and ICSD-033639 for corundum. The following parameters were refined: zero-shift error, background (as polynomial of 11th grade including 1/x) scale factor, mixing parameter for the pseudo-voigt function, Caglioti parameters to describe peak width (W, V, U), peak asymmetry (S/L and D/L) and March-Dollase parameter to model preferential orientation in the direction (002) for CDHA. Since the chemical composition of all phases was similar, no microabsorption corrections were made. The content of amorphous phase in the samples was indirectly determined with the addition of corundum as internal standard. For this purpose, a known amount (between 30 to 40 wt.%), was ground with the scaffolds and the amorphous content was deduced from the overestimation of the quantity of internal standard following the equation [1]:

$$A = \frac{100\%}{100\% - R} \cdot 100\% \cdot \left(1 - \frac{R}{R_R}\right) \qquad \textbf{Equation S4.1}$$

Where R corresponds to the added amount of internal standard and R_R to the percentage of corundum calculated from Rietveld refinement

The result from refinement of the biomimetic sample is shown in **Fig. S4.1**:

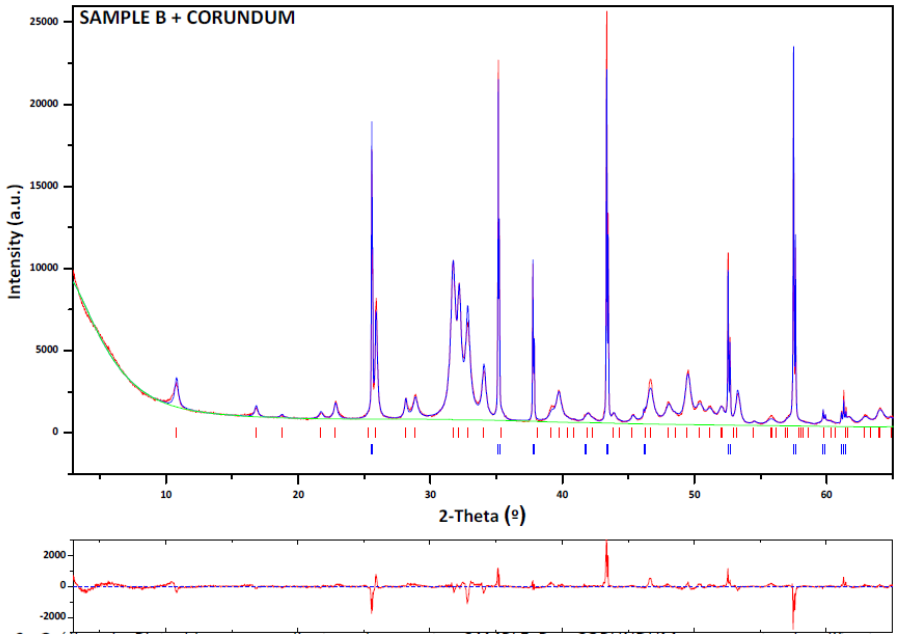

Fig. S4.1. Rietveld analysis pattern for the biomimetic sample. In red-experimental diffractogram, blue-calculated diffractogram, green-background, the difference curve is shown below in red colour. The vertical lines in the diffractogram indicate the position of the reflections corresponding to the CDHA phase in red and corundum in blue.

The Rietveld discrepancy values obtained upon refinement were: Re = 2.28%, Rp =4.44%, Rwp = 6.03% and GoF = 6.99.

The result from the refinement of the hydrothermal sample is shown in **Fig. S4.2**:

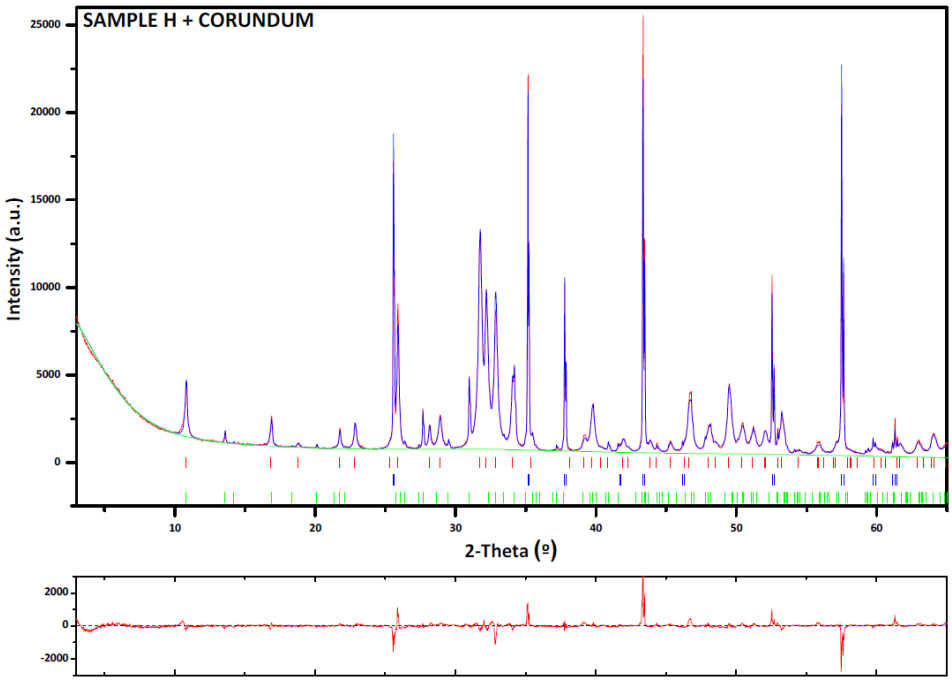

Fig. S4.2. Rietveld analysis patter for the hydrothermal sample. In red-experimental diffractogram, blue-calculated diffractogram, green-background, the difference curve is shown below in red colour. The vertical lines in the diffractogram indicate the position of the reflections corresponding to the CDHA phase in red, the corundum in blue and the β-TCP in green.

The Rietveld discrepancy values obtained upon refinement were: Re = 2.34%, Rp =4.25%, Rwp = 5.82% and GoF = 6.20.

Table S4.1: Summary of the content of the different phases obtained after refinement.

	CDHA	β-TCP	Amorphous Phase
Biomimetic	92.9%	N/A	7.1%
Hydrothermal	78.7%	10.1%	11.2%

4.7.2 Image Analysis

All image analysis was implemented using Python and can be found at

https://github.com/YAGORAYMOND/uCT-image-analysis

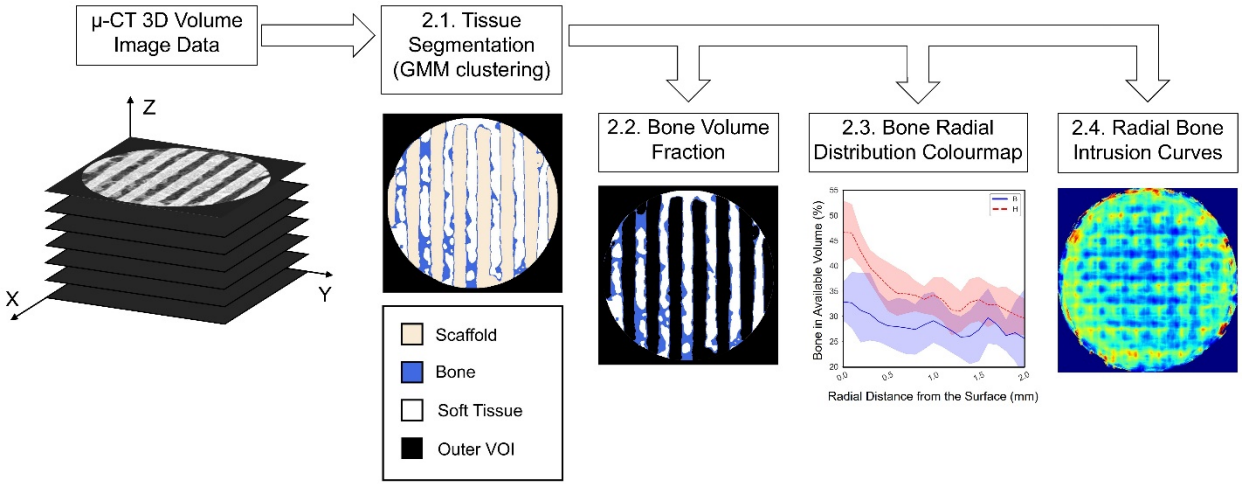

Fig. S4.3. Schema representing the main stages of the image analysis process.

The image analysis processing steps are described in more detail in the following four stages:

Segmentation

a) Load stacks of μ-CT reconstructions (.tiff format).

b) Reshape image as 1D array (flatten).

c) Fit a Gaussian Mixture model with 4 components.

d) Label the pixels according to the sorted means of the resulting GMM model. Assign pixels to the regions background (*i.e.* outside the VOI), void (*i.e.* non-mineralised tissue), bone and scaffold.

e) Apply a median filter using a disk-shaped structuring element of radius 50 μm (5 pixels).

Quantification of the Bone Volume Percentage

a) Determine volume of bone and void (*i.e.* non-mineralised tissue) regions.

b) Measure bone fraction as relative percentage of bone volume over available volume (100*(bone/(void+bone)).

Quantification of the Radial Bone Intrusion Curves

a) Iterate each z-stack.

b) Apply a thinning algorithm to each stack eroding the external perimeter of the sample in successive bands (21 layers, band size 200 μm).

c) Calculate bone fraction for each peeling band.

Representation of the Bone Distribution Axial Colormaps

a) Load segmented images.

b) Obtain the 2D z-projection of the volume.

c) Generate a 2D colormap representing bone fraction.

References

[1] T. Westphal, T. Füllmann, and H. Pöllmann, “Rietveld quantification of amorphous portions with an internal standard—Mathematical consequences of the experimental approach,” *Powder Diffr.*, vol. 24, no. 3, pp. 239–243, Sep. 2009, doi: 10.1154/1.3187828.

Chapter 5

3D Printing Non-Cylindrical Strands: Morphological and Structural Implications

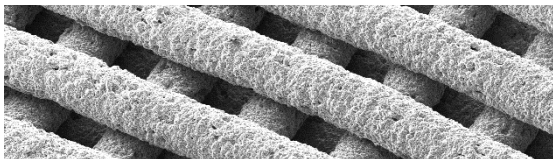

3D PRINTING NON-CYLINDRICAL STRANDS: MORPHOLOGICAL AND STRUCTURAL IMPLICATIONS

Abstract

Conventional direct ink writing uses circular nozzles and, therefore, results in cylindrical strands. 3D printing with non-circular nozzles adds new degrees of freedom to this versatile technology and allows obtaining structures with higher specific surface area or even introducing concave surfaces in the printed architecture. This is an enticing prospect for countless applications, including tissue engineering, chemical reaction catalysts, water evaporators and electrochemical energy storage devices. Despite this, it has been hardly explored by the 3D printing community. Herein, we develop for the first time 3D-printed structures with complex filament section morphologies using a custom-made modular nozzle and a self-setting ceramic ink. The fast elastic recovery of the ink allows obtaining good shape fidelity in the printed filaments, permitting the creation of intricate surfaces with up to 30% concavity and increasing up to 2.5 times the specific surface area compared to cylindrical strands. The use of non-circular nozzles introduces some specific constraints in the printing process. The geometry of the nozzle determines the stable printing directions, and nozzle orientation becomes a critical parameter to achieve a stable printing. Strand torsion, a phenomenon that remains unnoticed with circular nozzles, may result in relevant changes in the geometrical features of the printed structures.

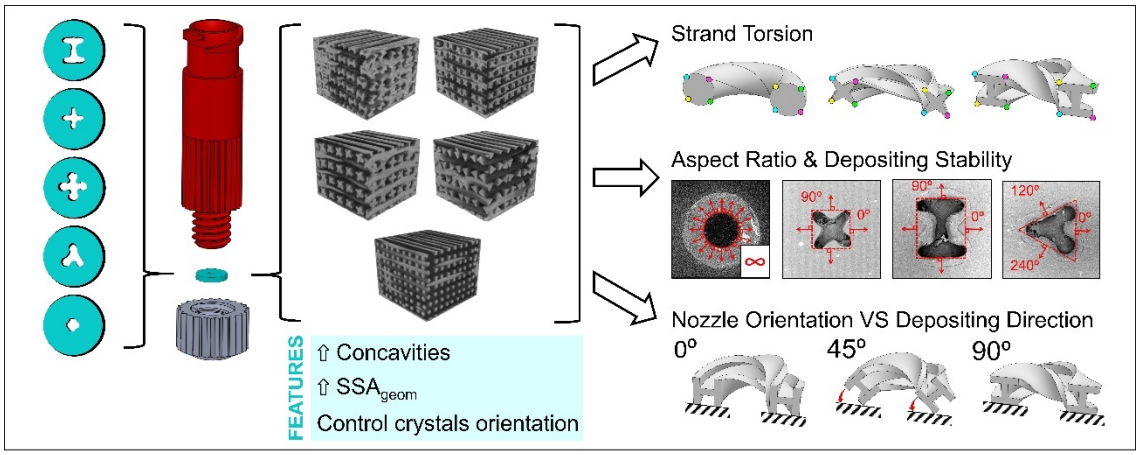

5.1 Introduction

Filament-based direct ink writing (DIW) is one of the additive manufacturing technologies that has attracted most attention in recent years due to its great versatility and the possibility of using different types of materials, from hydrogels to ceramics or metals. It is based on the extrusion of an ink or paste through a nozzle to obtain a continuous filament. This allows from the control of the printing path to the manufacturing of dense parts with complex geometries, and porous architectures with 3D periodic structures [1]. Conventional DIW uses circular nozzles and, therefore, results in cylindrical strands. Tuning the strand geometry would enable to introduce an additional level of control to the printed structures, opening up a wide range of new unexplored possibilities.

The most straightforward application is related to the possibility to increase the specific surface area (SSA) of the printed structures. In recent years, DIW manufacturing processes have raised an interest in applications where a high interaction surface is needed, due to the high SSA that can be achieved in the porous periodic 3D strand structures. Among all the shapes in two-dimensional space with the same area, the circle is the one with the smallest perimeter, therefore, with the smallest SSA [2]. The use of deposition nozzles with a higher aspect ratio would allow obtaining strand geometries with more intricate cross-sections than the circle, increasing the structure's SSA. Applications like chemical reaction catalysts [3,4], water evaporators [5], and electrochemical energy storage devices [6] would benefit from this increment of SSA, resulting in higher efficiency of the respective processes.

Furthermore, DIW is a promising technology for the fabrication of textured ceramics [7,8], *i.e.* materials with anisotropic polycrystalline microstructure, which can enhance a wide variety of properties *(e.g.* magnetic, superconductive, ion conductive, thermoelectric, piezoelectric, optical, thermally conductive, and structural) [9]. The fabrication of these structures through DIW allows three-dimensional geometrical freedom and fine control of the texture orientation. It represents a suitable strategy in applications where a certain degree of control over crystallographic orientation is required (*e.g.* cylindrical sonar projectors [10]). Textured ceramics are commonly obtained by templated grain growth (TGG). Briefly, large anisotropic single crystals dispersed into a fine granular powder matrix are oriented epitaxially and sintered to trigger nucleation and crystal growth [11]. The epitaxial orientation of the single crystals can be achieved by shear processes, where tape casting is one of the most common approaches. The extrusion process of a paste through a nozzle occurring in DIW also leads to crystal orientation. However, with traditional circular nozzles, this orientation is concentric and proportional to the shear stress of each region of the cross-section [7,12]. By using nozzles with rectangular high aspect ratio profiles, more similar to the ones used in tape casting [13], it would be possible to orient the crystals in one single crystallographic direction, achieving properties closer to those of the monocrystal.

Printing non-cylindrical strands could also find an application in the field of bone regeneration. DIW has been proposed as a promising technology for the fabrication of patient-specific synthetic bone grafts [14] based on the possibility of printing gel-based pastes with a high concentration of ceramic charges. Moreover, the design of self-setting ceramic inks opens the door to associating them with biological molecules, or combining them with cell-containing bioinks. In this application, the 3D-printed structure acts as a scaffold for bone formation and ingrowth. Recent studies have

shown that the geometrical features of the scaffold architecture play a key role in tissue regeneration. Rumpler *et al.* evidenced that the surface area and local curvature of the porosity has a strong influence on the tissue growth rate *in vitro* [15]. Moreover, Barba *et al.* proved that foam-like scaffolds with concave pores promoted bone formation and osteoinduction, contrary to 3D-printed scaffolds with convex surfaces. This was attributed to the microenvironment created in the confined cavities, that acted as osteogenic niches, conducive to cellular differentiation and functionality, ultimately leading to the formation of new bone [16]. Nevertheless, traditional DIW structures result in cylindrical strands and, therefore, convex surfaces. Using nozzles with the appropriate non-circular orifice geometry would allow introducing concave surfaces in the 3D-printed structures while also increasing the bone-biomaterial contact area, thus improving the potential of bone regeneration.

Even though the possibility of using square or hexagonal nozzles was put forward more than 15 years ago by Rao *et al.* [17], the use of non-circular nozzles has not been further explored by the 3D printing community, and the implications of the complex filament geometries in the printing process and the printed structures were not analysed in depth.

In the present work, we describe the fabrication of DIW ceramic structures with different strand morphologies by using a custom-made modular nozzle with interchangeable discs containing orifices with complex geometries. A self-setting calcium phosphate ink was used, which does not require any sintering step and does not exhibit shrinkage during the consolidation process [18]. One of the goals is to obtain strand cross-sections leading to a higher specific surface area of the filaments, and we describe for the first time the fabrication of strands with concave surfaces. Additionally, we describe the strand torsion occurring when changing the deposition direction, a phenomenon also occurring in the DIW of cylindrical strands that until the date went unnoticed due to the characteristic symmetry of this geometry. Furthermore, we discuss the implications of the strand geometry in the printing configuration and the restrictions and limitations that arise when using standard DIW positioning systems.

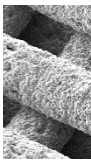

5.2 Materials and Methods

5.2.1 Nozzle Design

A custom modular nozzle that fits interchangeable thin discs with multiple orifice geometries was designed (SolidWorks, Dassault Systemes, Vélizy-Villacoublay, France) and machined in polyether ether ketone (PEEK) (**Fig. 5.1 A**). The orifices were designed with similar dimensions while exploring different simple geometries. Discs of 3 mm in diameter and six different orifice geometries were micromachined from Teonex® polyethylene naphthalate (PEN) films (150 µm thick) using a diode end-pumped neodymium-doped yttrium orthovanadate ($Nd:YVO_4$) laser (PowerLine E, Rofin-Sinar, MI, USA) emitting a TEM_{00} pulsed laser beam ($M^2 < 1.2$) at 355 nm wavelength (**Fig. 5.1 B**). The entire process was performed in an air atmosphere. The laser beam was focused on the surface of the PEN films using a F-theta lens with 235 mm in focal length. In consequence, the laser spot diameter on the surface of the sample was approximately 11 µm. Galvanometric mirrors were used to scan the laser beam across the polymeric samples. The processing parameters used for micromachining were: average laser power P=0.5 W, scanning speed v=8 mm s^{-1}, and

pulse frequency f=20 kHz. After processing, micromachined films were cleaned by ultrasonication in an acetone bath for 10 min followed by rinsing with distilled water to remove any residue on the surface.

5.2.2 3D Printing

Three-dimensional structures composed of different strand geometries were obtained by microextrusion of a calcium phosphate self-setting paste [19]. Here, α-tricalcium phosphate (α-TCP) powder was mixed with a poloxamer-based hydrogel obtaining a ceramic suspension, which was introduced in a 3 ml cartridge (QuantX™ 8001001 Syringe Barrel, Fisnar, MN, USA) and extruded through a nozzle using a direct ink writing device (Heavy Duty Paste Extruder, CIM-UPC, Barcelona, Spain). The nozzle orifice was aligned to the nozzle displacement path so that the vertical and horizontal directions of **Fig. 5.1 B** were lined up with the two orthogonal printing directions. Strands with the six different non-circular cross-sections (**Fig. 5.1 B**) were extruded and compared to a control strand obtained with a tapered dispensing tip (Smooth Flow Tapered Dispensing Tip, Gauge 22, Fisnar, MN, USA) with an inner diameter of 410 μm. The printing pattern consisted of an arrangement of successive layers of parallel strands, each layer oriented orthogonally to adjacent layers. The strand-to-strand separation was 250 μm and the layer overlapping was 15% of the nozzle size. The plunger extrusion rate was adjusted individually for each condition according to its respective orifice area to guarantee that the ink extrusion speed matched the nozzle displacement speed. Moreover, the printing speed was optimised according to the requirements of the nozzle orifice geometries. Cylindrical constructs of 10 mm in diameter and 5 mm in height were printed. The green structures were subjected to a hydrothermal treatment as described elsewhere [19] resulting in the hydrolysis of α-TCP to calcium-deficient hydroxyapatite (CDHA), with the subsequent hardening of the 3D-printed structures.

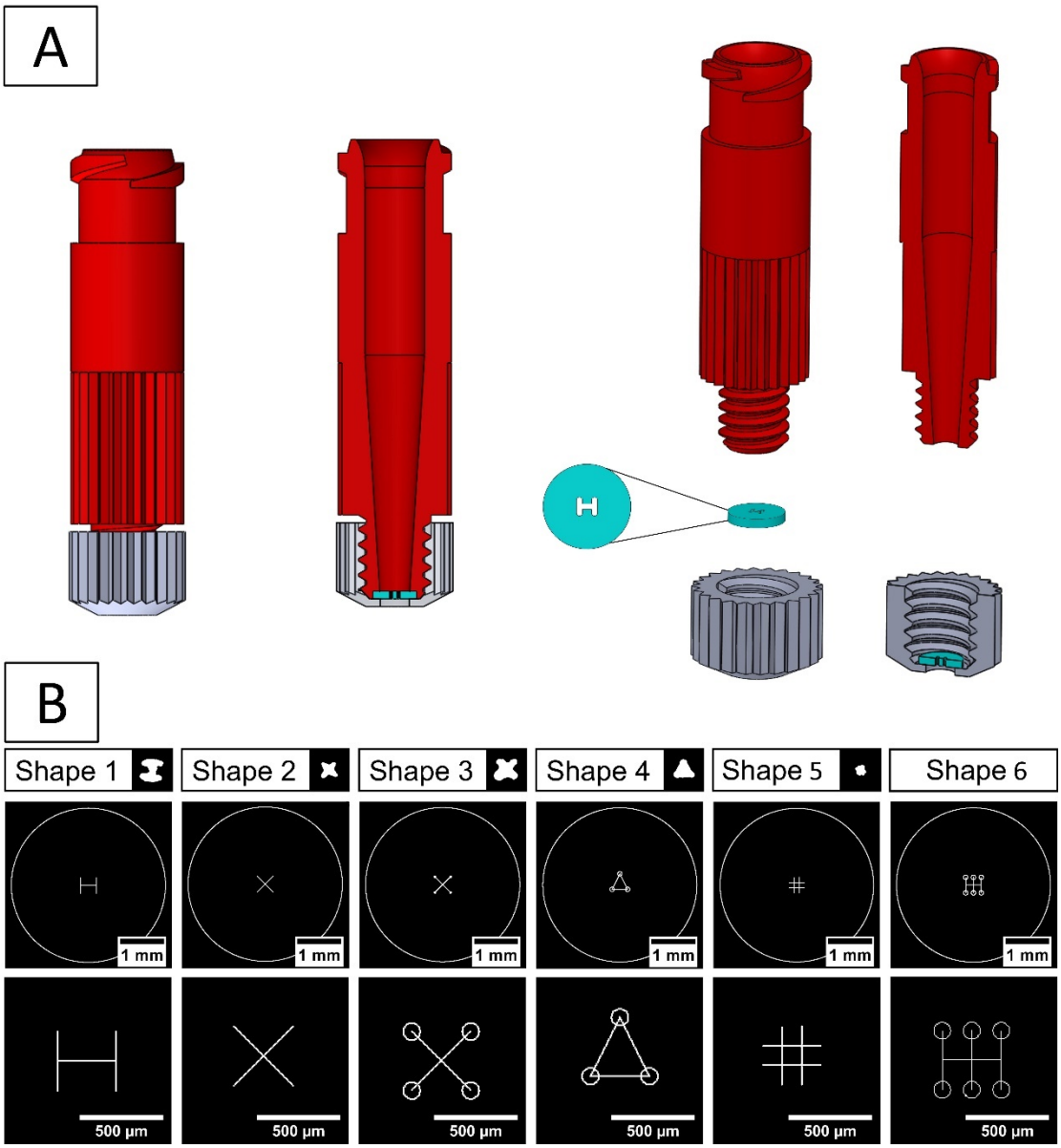

Fig. 5.1. A Scheme of the modular nozzle assembly. Nozzle body with Luer lock connector system at the upper side in red. Interchangeable disc with a laser-engraved orifice at the centre in turquoise. Disc holder in grey. **B** Drawing Exchange Format (DXF) designs of the laser-cut discs with the different orifice geometries.

5.2.3 Strand Shape Fidelity Assessment

The shape fidelity of the extrusion process was assessed by comparing the geometries of the nozzles with the strand cross-sections. The printed structures were embedded in PMMA resin (Technovit 7200, Heraeus Kulzer GmbH, Hanau, Germany) inside moulds and stored under vacuum conditions in a dark environment for 2 d. Then, the embedded samples were photopolymerised (Exakt 520, EXAKT Advanced Technologies, GmbH, Norderstedt, Germany) for 12 h under UV light followed by 12 h under white light. The resulting blocks were cut with a precision diamond band saw (Exakt 300, EXAKT Advanced Technologies, GmbH, Norderstedt, Germany) in a plane perpendicular to the strands cross-sections and through the central axis of the cylinders, and water-sanded down to P4000 grit size (Micro grinder, Exakt 400 CS,

EXAKT Advanced Technologies, GmbH, Norderstedt, Germany). The resulting cuts and the printing nozzles were coated with a thin carbon layer and observed by scanning electron microscopy (SEM, PhenomXL, Phenom World, Thermo Fisher Scientific MA, USA) with a beam intensity of 10 kV, using a backscattered electron detector (BSD).

The images were segmented and analysed with an image analysis software (Fiji, ImageJ [20]) to obtain the aspect ratio, perimeter and area of the different nozzles and filament sections. Moreover, the concavity of each geometry was quantified by determining the convex hull of each geometry, which is the minimum convex polygon that includes all the points [21,22]. Combining these data, two indexes that describe the concavity level were defined: i) the Perimeter Concavity Ratio (PCR), which is the ratio between the perimeter of the original shape and the perimeter of the convex hull, being 1 for a completely convex shape and increasing as the concavity of the original shape increases; ii) the Surface Concavity Percentage (SCP), which represents the percentage of area within the convex hull region that is occupied by a concave porosity. This index equals 0% for a completely convex shape and tends to 100% for shapes with higher concavity.

Additionally, a rheological evaluation was performed to determine the viscoelastic properties of the ink. For this purpose, a rheometer (Discovery HR-2, TA Instruments, DE, USA) equipped with a rough parallel plate geometry (20 mm Ø) and a solvent trap to prevent ink drying was used. The analysis was performed at a controlled temperature of 18 ºC and a geometry gap of 0.5 mm. A first strain sweep test was carried out under oscillatory mode at a frequency of 1 Hz from 0.01% to 1000%, to monitor the storage and loss modulus and to determine the linear viscoelastic region (LVR) and the flow point (FP). Those were used to determine the low and high shear strain levels used in the three interval thixotropy test (3ITT) performed under oscillatory mode (10 Hz) to assess the elastic recovery of the paste [23]. This test simulates the shear rate profile of the extrusion process and allows to assess the transition kinetics of the ink from fluid-like flow (second interval) to elastic shape retention (third interval) [24]. The assay consisted of a first interval applying a small amplitude oscillatory shear, corresponding to low shear strain (ϵ LVR) of 0.02% for 50 s followed by a second interval at a large amplitude oscillatory shear, corresponding to high shear strain (>FP) of 1000% for 50 s and a final interval applying the same conditions of the first interval, *i.e.* with low shear strain stage of 0.02%, for 100 s.

5.2.4 Structural Characterisation

Prior to the resin embedding process, 3D reconstructions of the structures were acquired (one sample per condition) by micro-computed tomography (µ-CT). The machine (SkyScan 1172, Bruker Micro-CT, Kontich, Belgium) was operated with a source voltage of 100 kV and source current of 100 µA. Images were collected with a step size of 0.2º, over the 0 - 180º range, with an exposure time of 3100 ms. A resolution of 26.3 µm per voxel with isotropic voxel size was used. Subsequently, acquisitions were reconstructed to image stacks with a previous beam-hardening correction and alignment optimisation process (NRecon, Bruker Micro-CT, Kontich, Belgium). After, stacks were rotated to align the reconstruction orientation to the original printing axis and cropped to a normalised volume of interest (VOI) of 5.42 mm (*i.e.* 206 px) in length and width, and 4.39 mm (*i.e.* 167 images) in height (Data Viewer,

Bruker Micro-CT, Kontich, Belgium). This way, the volume analysed was normalised and only the regular region of the structure was considered.

The images were binarised using an optimal grey-level threshold with Otsu's method (Fiji, ImageJ). Afterwards, the binarised images were transformed to 3D triangle meshes*, i.e.* Standard Triangle Language format (STL), with an image analysis software ("3D viewer" plugin, Fiji, ImageJ).

The volume of material (MV) and surface of material (MS) in the total volume of the VOI (TV) were measured by: (1) CTAn, an image analysis software dedicated to µ-CT analysis ("3D Analysis" tool, CTAn, Bruker Micro-CT, Kontich, Belgium); (2) Fiji, the polyvalent open-source image analysis software ("BoneJ" plugin [25], Fiji, ImageJ, NIH-LOCI, U.S.A.); (3) measurement on the 3D mesh using MeshLab, an open-source STL processing software (MeshLab, ISTI, Pisa, Italy [26]); and (4) a theoretical estimate based on the measurement of strand diameter and perimeter, VOI dimensions and the number of strands in the VOI.

Different geometrical attributes of the 3D-printed structures were assessed. The percentage of porosity was measured based on the proportion of MV in the TV. The pore size distribution was calculated using a sphere fitting algorithm [27] ("3D analysis" tool, CTAn, Bruker Micro-CT, Kontich, Belgium). Finally, the specific surface area (SSA) normalised by volume of strand (mm^2 mm^{-3}) and by length of strand (mm^2/strand mm) was calculated by dividing MS over MV and over the total length of the strands in each VOI respectively.

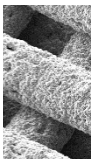

5.2.5 Finite Element Analysis

Linear static finite element simulation under elastic behaviour was performed on the different µ-CT-based STL reconstructions to assess the influence of the strand geometry on the stress distribution in the structure. The models used were first discretised using 4-node linear tetrahedral elements (C3D4). A uniaxial compression test under displacement-controlled loading along the Z printing axis was simulated.

The boundary conditions were defined on the nodes of the top and bottom faces of the mesh. Whereas the displacement of the bottom nodes was fixed in the Z direction, a vertical displacement of 0.0439 mm that corresponded to a compression strain of 0.1% was imposed for the top nodes. The Young modulus of the material after hydrothermal consolidation was experimentally determined by testing in compression massive cylinders (6 mm in diameter and 12 mm in height), under the same conditions applied in the simulation (quasi-static uniaxial compression loading, displacement control mode at 1 mm s^{-1}). The value obtained, 2.8 ± 0.9 GPa is congruent with the high porosity and microstructure of this type of self-setting ceramic materials, which consist of an entangled network of precipitated crystals [28,29]. A Poisson's ratio of 0.27 was selected for this analysis, as commonly reported for hydroxyapatite (HA) in the literature [30]. An elastic and isotropic model was used for this purpose. The finite element analysis (FEA) was performed on ABAQUS (Dassault Systèmes, France).

5.3 Results and Discussion

5.3.1 Strand Morphology and Shape Fidelity of the Microextrusion Process

The morphology of the nozzles and the corresponding strands are shown in **Fig. 5.2 A**. It is important to point out that a self-setting ink, which does not shrink during the hardening process [18], was chosen for this study in order to eliminate any dimensional change of the filament after extrusion. The strands retained to a large extent the shape of the extrusion nozzle, although some morphological deviations were observed at the regions where the orifice presented sharper curvatures (**Fig. 5.2 A**, red arrows). As a consequence, the strand section area was larger than the nozzle area for the nozzles exhibiting more intricate shapes (**Fig. 5.2 B**), and a decreasing trend of the concavity indicators was observed when comparing nozzles to strands (**Fig. 5.2 C-D**). The two concavity indicators used were able to quantify the geometries' concavity, showing the same trends, coherent with the morphology observations (**Fig. 5.2 A**). Nevertheless, the SCP resulted to be more sensitive and, therefore, a better indicator than the PCR.

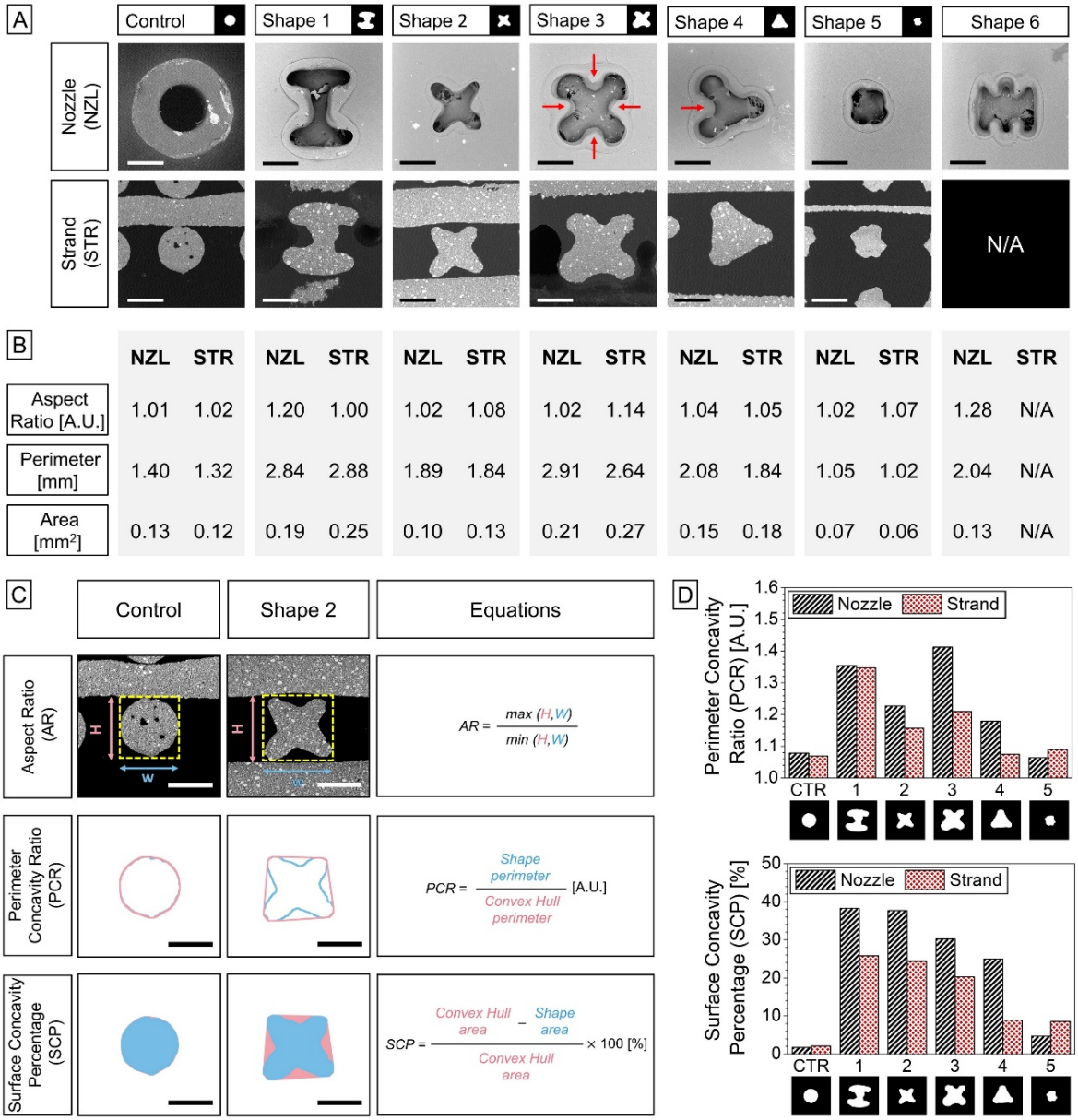

Fig. 5.2. A Comparison of the nozzle orifice (NZL) and the cross-section of the 3D-printed strands (STR) for the different tested geometries. Red arrows indicate sharp curvature regions of the nozzles, where the shape was less preserved. No strand is shown for shape 6 nozzle because it was not possible to print 3D structures with this nozzle geometry, as described in the text below. **B** Geometrical attributes measured both in the nozzles and strands (NZL and STR, respectively). **C** Scheme illustrating the measurement process for different geometrical indicators: Aspect Ratio (AR), Perimeter Concavity Ratio (PCR) and Surface Concavity Percentage (SCP). Examples of the control shape, with highly convex geometry, and shape 2, presenting some concave regions. **D** Results of the concavity indicators for the different geometries. Scale bars: 300 µm.

The discrepancies between the shape of the nozzle and the strand morphology can be attributed to two main possible causes, namely: i) the slow elastic recovery of the ink; or ii) the deformation of the nozzle during the extrusion process. The rheological tests showed that the ink exhibited a shear thinning behaviour, with an elastic modulus

G' in the viscoelastic region above 2 x 10^6 Pa, and a crossover of the G' and G'' (known as the flow point) at a shear strain around 40% (**Fig. 5.3 A**). Regarding the elastic recovery of the ink, the three interval thixotropy test (3ITT) (**Fig. 5.3 B**) evidenced that, upon the release of a high shear strain simulating the extrusion process, the transition from viscous prevalence (G''>G') to elastic prevalence (G'>G'') was quasi-instantaneous. These findings entail an optimum retention of the extruded strand shape, guaranteeing a high shape fidelity.

Having an ink with a fast viscosity recovery upon extrusion is of paramount importance to guarantee the strand shape fidelity when using nozzles with orifices other than circular, as the regions of the geometry with higher gradients of curvature will suffer the effects of surface tension, smoothing the edges and tending to the minimal-energy circular-cross-section geometry [31]. This phenomenon is accentuated in geometries with smaller curvature radii.

After ruling out the rheological behaviour of the ink as a cause of the strand shape deviations, the most likely explanation is the deformation of the polymeric disc that makes up the nozzle as a result of the high pressure during the extrusion process [32]. This deformation must be elastic, as no evidence of plastic deformation was found after inspecting used extrusion discs. The fact that greater deviations on the shape fidelity occur at overhanging features of the thin plastic discs is a further evidence that points towards this hypothesis. A solution to this problem would be to use more rigid materials (*e.g.* metallic) or thicker discs in the nozzles.

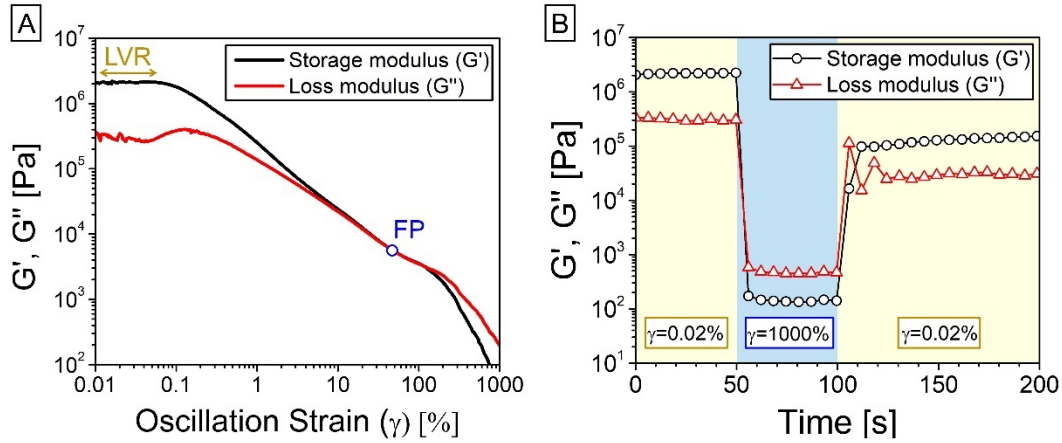

Fig. 5.3. A Storage modulus (G') and loss modulus (G'') of the ink measured in a strain sweep test. The linear viscoelastic region (LVR) and the flow point (FP) are indicated on the diagram. **B** Three interval thixotropy test (3ITT) showing the elastic recovery of the ink.

5.3.2 Implications of the Strand Geometry in the Printing Process

The µ-CT reconstruction of the VOI of the different 3D-printed structures evidenced that some strand shapes resulted in more regular structures than others (**Fig. 5.4**). The structures printed with the control nozzle and the shapes 2, 3 and 5 were the most regular ones. On the contrary, shapes 1 and 4 resulted in more irregular architectures, unevenly spaced and randomly oriented strands.

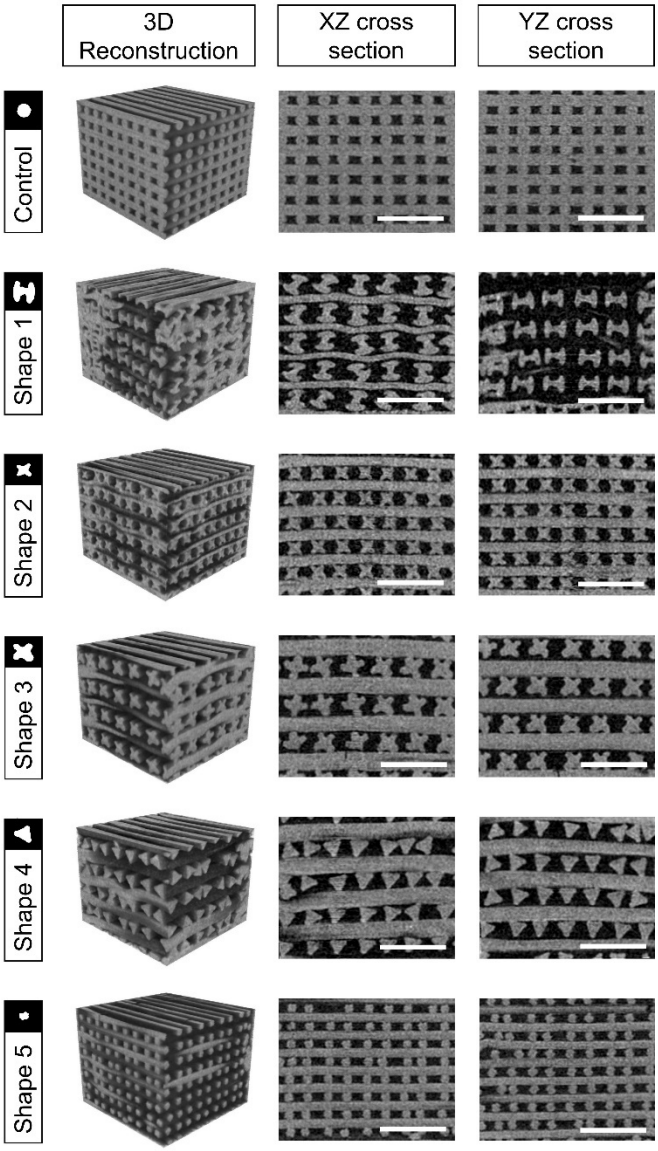

Fig. 5.4. 3D reconstruction and XZ and YZ cross-sections of the μ-CT images of the 3D structures printed with the different nozzle geometries. Scale bar: 2 mm.

This variable outcome emphasises the fact that using non-circular nozzles imposes some restrictions regarding the printing trajectories. Unlike the cylindrical strands, which are rotation-invariant and allow a stable deposition regardless of the direction, the alternative geometries tested in this work give rise to a more complex scenario. The geometry of the nozzle dictates the printing directions leading to the deposition of a stable strand. One can determine the planes of stable deposits and the associated normal vectors (represented in **Fig. 5.5 A** with dashed lines and arrows, respectively). To achieve a stable filament deposit, it is required that the direction of the normal vectors matches the deposition directions of the printing pattern. In the present work, the nozzle orientation was aligned to the printing directions of the orthogonal pattern (0 and 90º). Shapes 1, 2, 3, 5, and 6 present a suitable geometry for the orthogonal printing pattern used in this work. In contrast, shape 4 has the normal vectors in the 0 – 120 – 240º directions and, therefore, the strand deposition is unstable in the orthogonal (0 – 90º) deposition pattern (**Fig. 5.5 A**), although it would be appropriate

for another printing pattern matching the deposition orientations (*e.g.* honeycomb pattern, where the printing directions are 0 – 120 – 240º).

Another relevant parameter that has to be considered, which again highlights the relationship between nozzle geometry and the printing path, is the aspect ratio of the nozzle. If the layer height is fixed, as is the case in most currently available commercial devices, an aspect ratio close to one is required when printing structures that alternate different deposition directions in the successive layers. Otherwise, and especially if the aspect ratio of the orifice is high, it may become impossible to find a layer height that is suitable for all the printing directions. This may result in either wiggling of the strands, if the layer height is too large for one of the printing directions, or in flattened strands and damage on the previous layer if the layer height is set too low for the other printing direction. An example of this situation is shape 6 (**Fig. 5.2 B**), with an aspect ratio of 1.28, that did not allow printing stable structures. This limitation could be overcome by adjusting the layer height for each deposition direction, which is not possible in the current commercially available slicing software.

Another relevant phenomenon that is brought to light when printing non-cylindrical strands and goes unnoticed when using the conventional circular nozzles is strand torsion. It occurs when there is a change in direction of the deposition path, and is associated with the fixed orientation of the extrusion nozzle (**Figs. 5.5 B** and **5.5 F**). Although this happens independently of the shape of the filament, when the strand is cylindrical it is overlooked due to the rotation-invariant characteristic of the circular cross-section. Probably for this reason, to our knowledge it has never been pointed out before. As illustrated in **Fig. 5.5 B**, for 3 different strand cross-sections, when the nozzle changes its trajectory by 180º, the region of the strand that was first in the bottom is twisted, ending up in the top of the filament, which is a 180º torsion. If the nozzle changes its trajectory by making a 90-degree turn, the filament experiences a torsion of 90º, which depending on the nozzle symmetry, it can lead to a change in the orientation of the filament geometry in successive printing layers (**Fig. 5.5 C**). This is clearly visible in the μ-CT reconstruction of the scaffolds printed with shape 1 nozzle (**Fig. 5.4**), where alternated strand orientations are found in successive layers. Here, the orientation of the strands in the XZ cross-section is in "I" shape and in the YZ section is in "H" shape, *i.e.* the deposition of the strand occurs in alternated sides depending on the layer deposition direction.

In order to further assess the effect of nozzle alignment on the orientation of the printed strands, we printed 3D structures with the shape 1 nozzle aligning the nozzle at 45º with respect to the 0 – 90º deposition directions of the tested orthogonal pattern. In this setup, we observed an alternated deposition of in ¨H¨-like and in ¨ I¨-like orientations in adjacent strands (**Fig. 5.5 E**). We hypothesise that in this case the strands tend to lay down to a more stable position, and the preferred conformation is the one that minimises torsional forces when there is a change of deposition direction, as illustrated in **Fig. 5.5 D**.

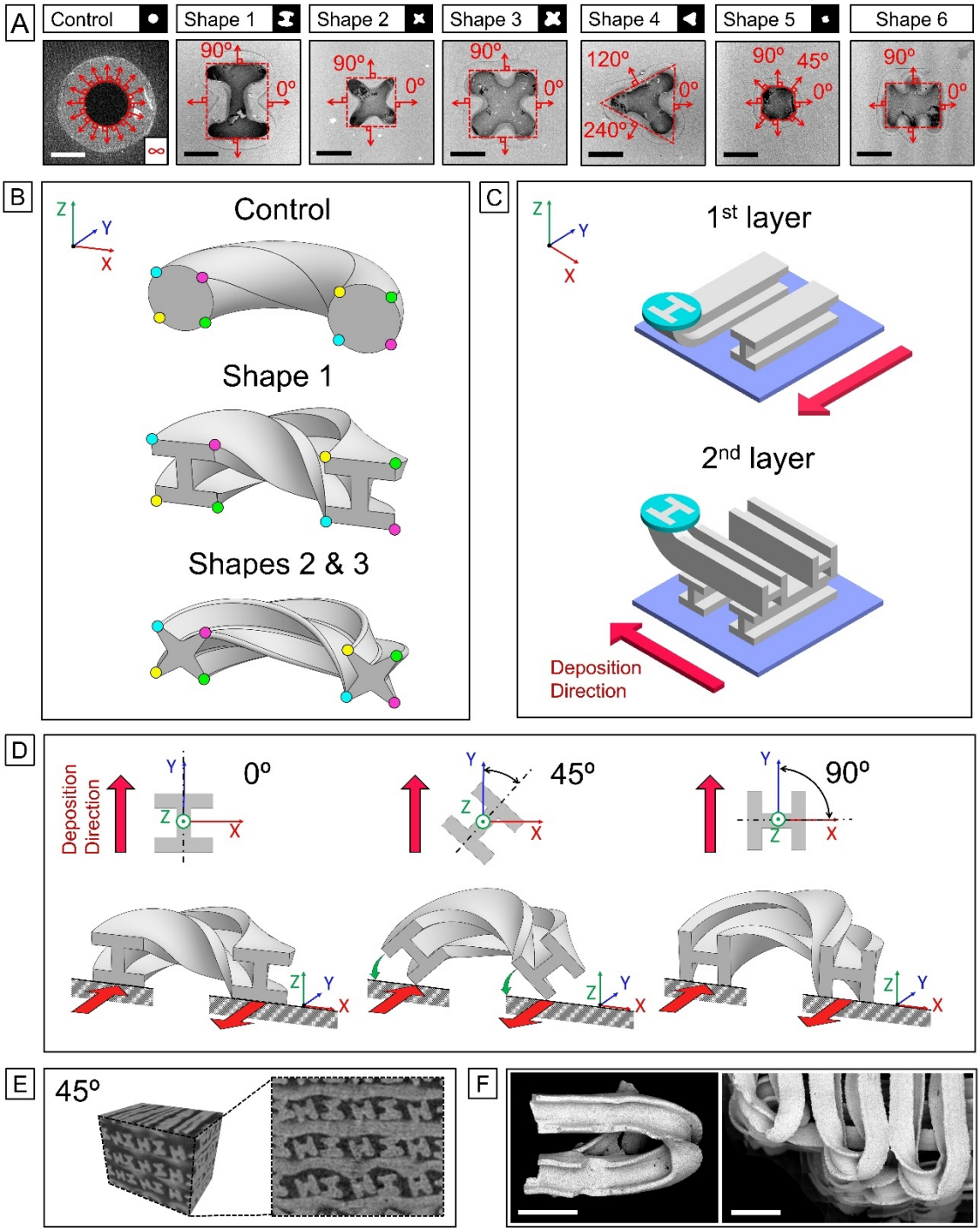

Fig. 5.5. A Stable deposition planes (red dashed lines) and their normal vectors (red arrows) for the different nozzle geometries. Scale bar: 300 µm. **B** Scheme illustrating the strand torsion phenomenon occurring at the 180º change of direction during printing. Colour points illustrate the trajectory of each region of the cross-section. **C** Representation of the deposition process of two successive layers with a non-rotating nozzle (turquoise) in an orthogonal deposition fashion leading to an inter-layer alternated orientation (*i.e.* H – I orientations). Red arrows indicate the deposition directions. **D** Effect of nozzle orientation (0º, 45º and 90º) on strand deposition during the change of printing direction (indicated with red arrows). **E** µ-CT reconstruction of a structure printed with the nozzle oriented at 45º with respect to the printing direction,

demonstrating the strand-to-strand alternated H-I deposition fashion. **F** SEM images showing the strand torsion phenomenon in the printed structures. Scale bar: 1 mm.

5.3.3 Morphological Analysis

The specific surface of the printed structures (**Fig. 5.6 A-B**) was assessed using four methods. CTAn and MeshLab approaches gave similar results although they were based on very different principles, whereas the Fiji software, which uses the same approach as CTAn presented a shift up bias, even though preserving the same trends. Finally, the theoretical approximation was also shifted up but with considerably higher variability.

As expected, the surface area normalised per strand length (**Fig. 5.6 A**) was directly correlated to the perimeter of the printed strands (**Fig. 5.2 B**), and there were clear differences between the different nozzles. The value not only depended on the surface concavity percentage, as observed when comparing strands with the same section like the control and shape 2, but also on the size of the nozzle orifice, with larger nozzles orifices resulting in strands with larger surface per unit length, as in the case of shape 1 or 3. To better assess the contribution of shape changes rather than size changes, the surface area was normalised by strand volume (**Fig. 5.6 B**). This allowed to isolate the morphological effect from the size effect and revealed clear differences between the different filament profiles. The control showed the smallest value, as expected, whereas the nozzle with shape 2 achieved the highest surface area per strand volume, doubling the value of the control.

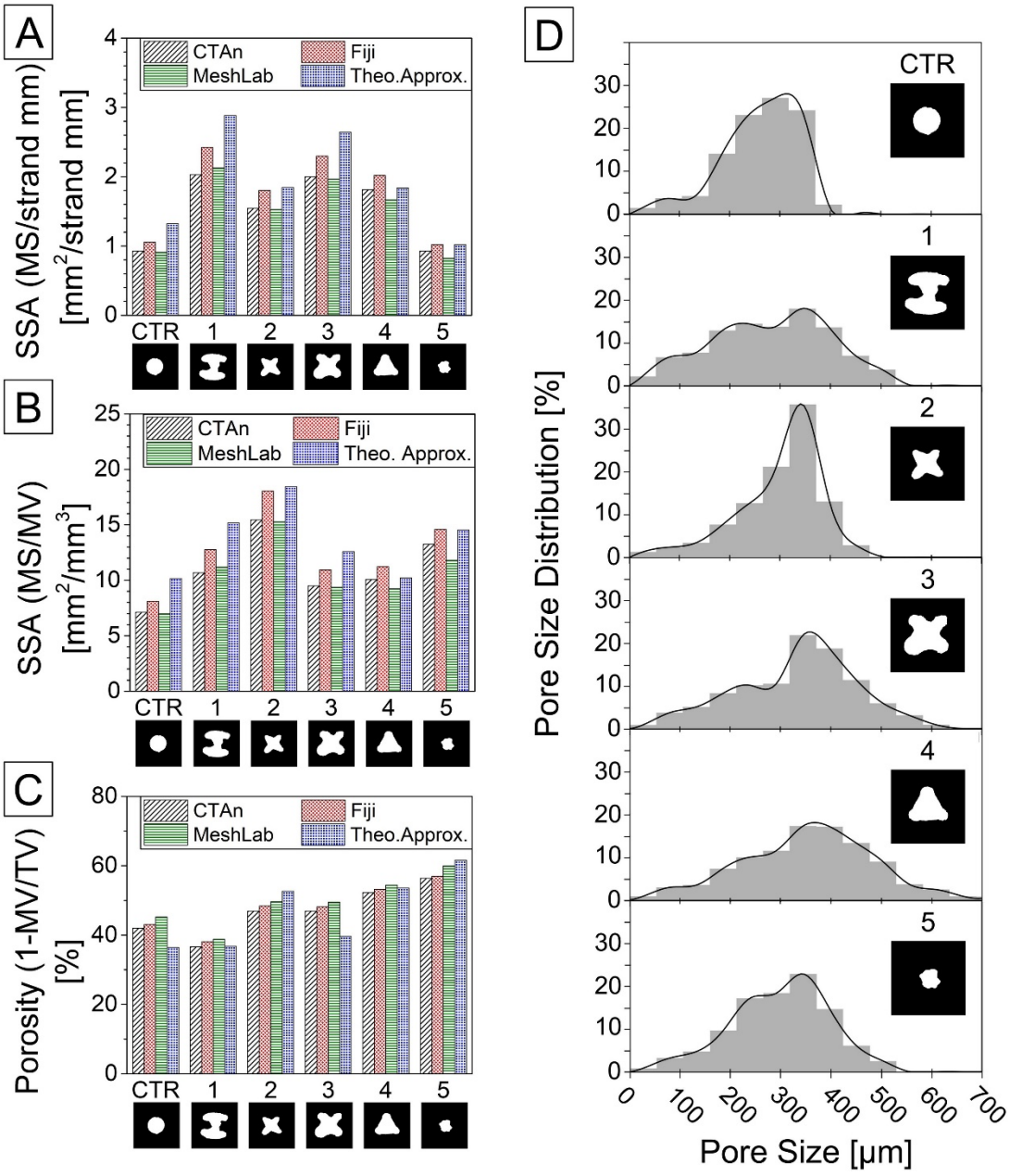

Fig. 5.6. Structural characterisation of the samples printed with different strand cross-sectional geometries: **A** Specific surface area (SSA) of the strands, calculated by normalising material surface (MS) per strand length; **B** SSA of the 3D-printed structures, calculated by normalising material surface (MS) per unit volume of strand (MV); **C** percentage of porosity, and **D** pore size distribution of the 3D-printed structures. A-C include four different quantification methods: Two of them based on the analysis of the µ-CT reconstruction using two alternative software (*i.e.* CTAn and Fiji); one third using the mesh obtained from the segmentation and meshing (STL) of the same µ-CT reconstruction (*i.e.* MeshLab); and one fourth using a theoretical estimation based on the SEM images of the strand cross-sections. The measurements of D are based on µ-CT analysis with CTAn software.

Regarding porosity quantification, there was a good agreement between the different methods, being the theoretical approximation the one with higher discrepancies, which can be explained by the fact that it was based on ideal structures rather than the real printed ones. Despite all the 3D structures being printed with a constant inter-strand separation of 250 µm in the XY plane, considerable differences in the porosity percentage were observed, which can be explained by (1) the different strand dimensions; (2) the morphological diversity of the nozzle designs. The influence of these two parameters into the percentage of porosity is illustrated in **Fig. 5.7**, which shows that with a fixed inter-strand separation, bigger strand dimensions lead to smaller porosities (*e.g.* percentage of porosity in shape 5 > control, shape 2 > shape 3). Moreover, when comparing strands with similar dimensions, a strand design with smaller cross-section area leads to higher porosities.

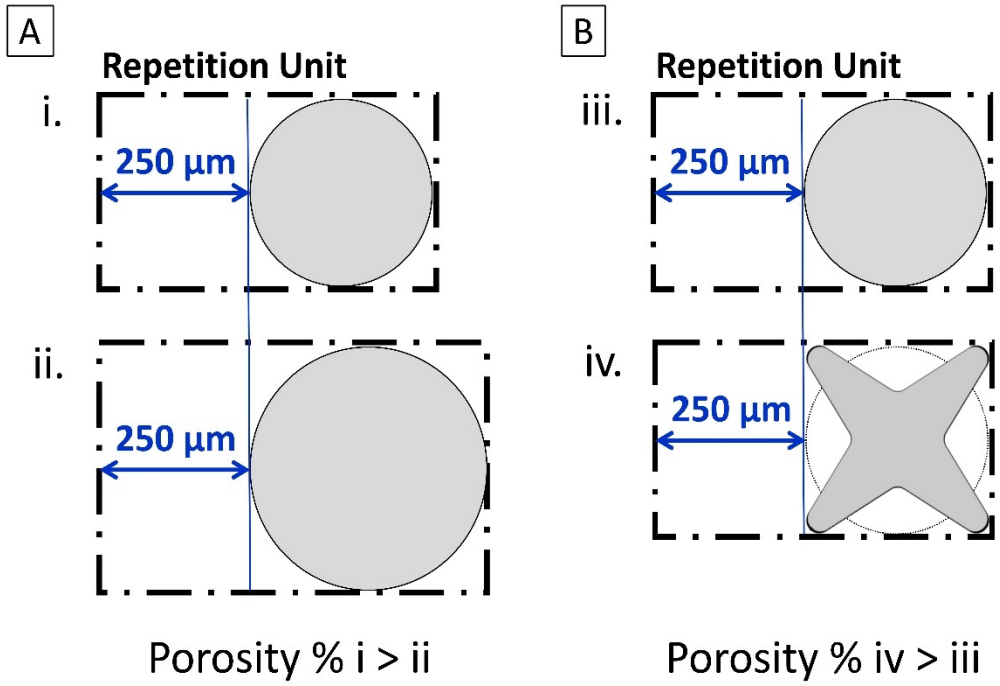

Fig. 5.7. Scheme showing the influence of strand size **A** and shape **B** into the porosity percentage, given a fixed inter-strand separation of 250 µm.

As expected, due to the nature of the DIW process and the rectilinear fill pattern used, which results in an interconnected pore network, most porosity was open. A residual amount of closed porosity (less than 0.2% in all the cases) was observed with CTAn software, which can be attributed to small air bubbles trapped in the ink during the mixing process, as observed, for instance, in the SEM image of the cross-section of the control sample (**Fig. 5.2 A**). Although all pores are interconnected and technically they can be considered as one single pore, the sphere-fitting algorithm allowed calculating the pore size distribution in the different 3D structures, which presented very dissimilar pore size distributions (**Fig. 5.6 D**). The maximum frequency was not centred in 250 µm but in 300 µm in most cases. This shift to larger dimensions when compared to the imposed 250 µm inter-strand separation can be attributed to the fact that this technique measures the pores volumetrically, and in some regions and orientations the pore dimensions can be larger than the defined inter-strand separation. Apart from that, a correlation was observed between the sharpness of the

distribution and the regularity of the printed structures, with the more regular structures like control and shape 2 nozzles (**Fig. 5.4**), presenting a sharper peak and a narrower pore size distribution.

5.3.4 Load Distribution: Finite Element Analysis

The maximal principal stress contours obtained from the simulation of a compressive strain of 0.1% in the elastic range are presented in **Fig. 5.8**. The structures cross-sections revealed a general trend in which the compression stresses were concentrated in the strand intersections, which act as structural pillars, whereas the regions of the strands linking these pillars are subjected to tensile stresses. This is coherent with the behaviour found in the literature for similar materials with brittle behaviour [33-36]. Miranda *et al.* reported a similar stress field distribution calculated by finite element method (FEM), which was correlated with the fracture mode assessed experimentally, observing initial cracking of the unsupported strand segments unifying the pillars propagating parallel to the load axis due to tensile stress accumulation in this region [33]. Additionally, as expected, the structures with larger strands (*e.g.* shape 1) presented fewer and wider pillars with attenuated compressive stress gradients. These observations were also in agreement with other studies comparing structures with different inter-layer contact areas [19,37]. It was also evidenced that the smaller curvature radius found at the strand unions acted as stress concentrators. The use of strand geometries with concavities and abrupt curvatures introduced additional stress concentrators. Finally, the regularity of the printing pattern also played a key role in the homogeneity of the stress distribution, with higher values of tensile stresses registered in structures with more irregular deposition patterns (*e.g.* shape 4). The Von Mises equivalent stress distribution, which may be of interest for understanding the behaviour of the structures when ductile materials are used is provided in the supplementary information.

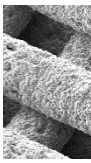

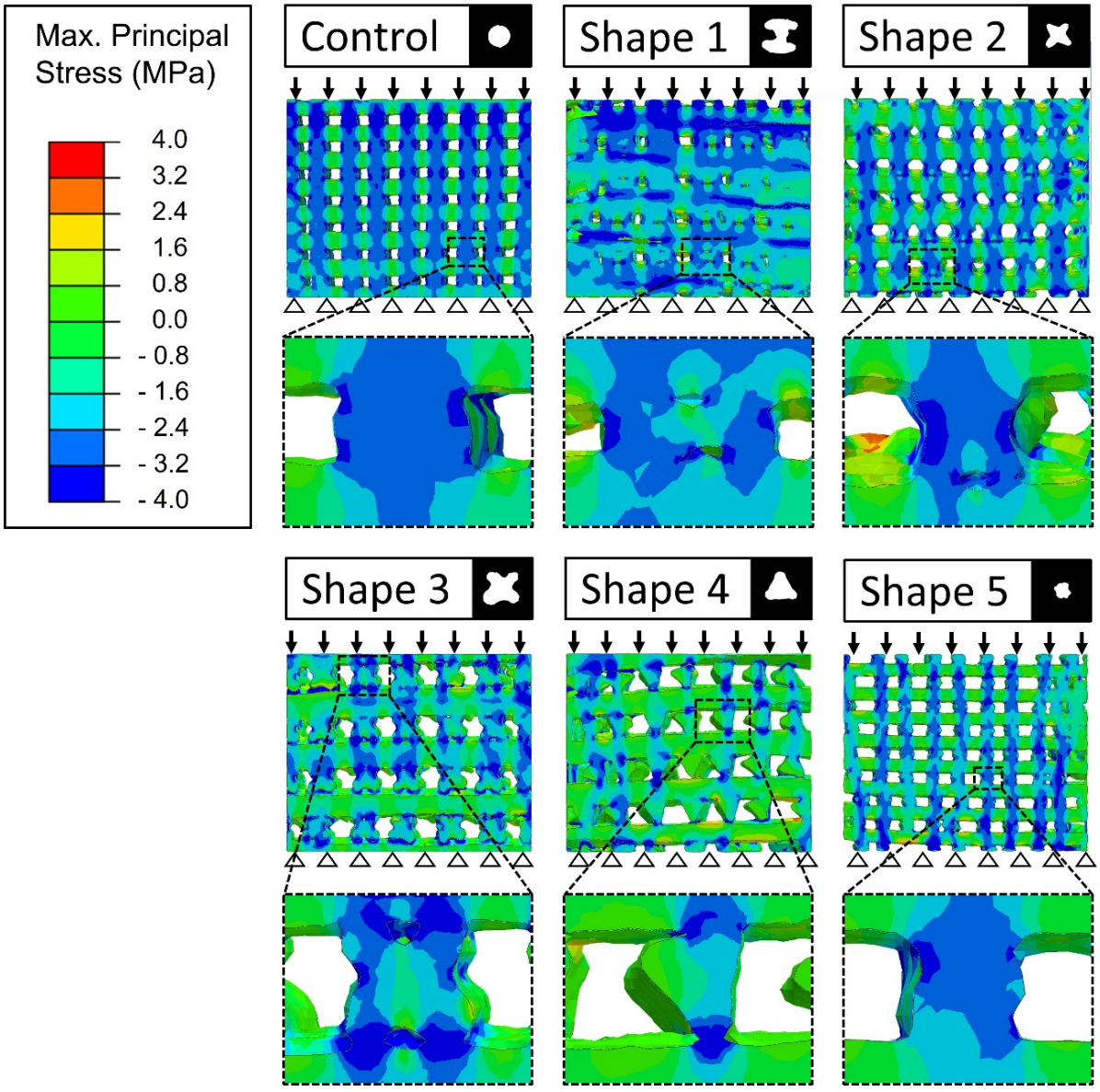

Fig. 5.8. Cross-section (XZ printing axis) of the structures obtained with different strand geometries showing the maximum principal stress contours obtained by finite element simulation. Compression in the elastic region with vertical (Z printing axis) strain 0.1% is indicated with arrows and vertically fixed bottom nodes are indicated with triangles. Normalised stress colormap ranging from 4 MPa tensile stress (red) to 4 MPa compressive stress (blue).

5.4 Conclusions

In summary, this study analyses the potential and the drawbacks of using non-circular nozzles in DIW, which can be exploited in a wide range of applications that already use this technique, like tissue engineering, chemical reaction catalysts, water evaporators and electrochemical energy storage devices. Amongst the benefits are the possibility to increase the specific surface area of the filaments and the 3D structures, or the introduction of concave surfaces, that can be beneficial for certain applications based on interfacial reactions or to create confined environments. Although modifying the geometry of the nozzle may seem of little relevance, it has enormous implications in the printing process and introduces an additional level of complexity in the 3D-printed structures. Printing with non-circular nozzles imposes some restrictions regarding the printing patterns since the stable deposition paths are limited and determined by the geometry of the printing nozzle. The alignment of the nozzle with the printing path and the aspect ratio of the nozzle become very important parameters to ensure the printing of stable and reproducible structures. Another relevant phenomenon that is brought to light when printing non-cylindrical strands while going unnoticed when using the conventional circular nozzles, is the strand torsion. This can result in different orientation of the strands in successive layers of print, or even in alternate filaments. The analysis of the specific design constraints has allowed identifying a series of technological implementations that may overcome the limitations and increase the possibilities of 3D printing with non-circular nozzles. Finally, it is worth mentioning that although this study was performed using a ceramic paste, the conclusions can be extended to other techniques which are also based on the extrusion of continuous filaments through a nozzle, such as fused deposition modelling (FDM).

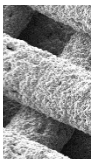

5.5 References

[1] J. A. Lewis and G. M. Gratson, “Direct writing in three dimensions” *Mater. Today*, vol. 7, no. 7–8, pp. 32–39, Jul. 2004, doi: 10.1016/S1369-7021(04)00344-X.

[2] J. E. Brothers and F. Morgan, “The isoperimetric theorem for general integrands” *Michigan Math. J.*, vol. 41, no. 3, pp. 419–431, 1994, doi: 10.1307/mmj/1029005070.

[3] J. N. Stuecker, J. E. Miller, R. E. Ferrizz, J. E. Mudd, and J. Cesarano, “Advanced Support Structures for Enhanced Catalytic Activity” *Ind. Eng. Chem. Res.*, vol. 43, no. 1, pp. 51–55, Jan. 2004, doi: 10.1021/ie030291v.

[4] C. Zhu *et al.*, “Toward digitally controlled catalyst architectures: Hierarchical nanoporous gold via 3D printing” *Sci. Adv.*, vol. 4, no. 8, 2018, doi: 10.1126/sciadv.aas9459.

[5] Y. Li *et al.*, “3D-Printed, All-in-One Evaporator for High-Efficiency Solar Steam Generation under 1 Sun Illumination” *Adv. Mater.*, vol. 29, no. 26, pp. 1–8, 2017, doi: 10.1002/adma.201700981.

[6] M. Wei, F. Zhang, W. Wang, P. Alexandridis, C. Zhou, and G. Wu, “3D direct writing fabrication of electrodes for electrochemical storage devices” *J. Power Sources*, vol. 354, pp. 134–147, Jun. 2017, doi: 10.1016/j.jpowsour.2017.04.042.

[7] Z. Fu, M. Freihart, L. Wahl, T. Fey, P. Greil, and N. Travitzky, “Micro- and macroscopic design of alumina ceramics by robocasting” *J. Eur. Ceram. Soc.*, vol. 37, no. 9, pp. 3115–3124, Aug. 2017, doi: 10.1016/j.jeurceramsoc.2017.03.052.

[8] M. Lorenz *et al.*, “Influence of platelet content on the fabrication of colloidal gels for robocasting: Experimental analysis and numerical simulation” *J. Eur. Ceram. Soc.*, vol. 40, no. 3, pp. 811–825, Mar. 2020, doi: 10.1016/j.jeurceramsoc.2019.10.044.

[9] G. L. Messing *et al.*, “Texture-engineered ceramics—Property enhancements through crystallographic tailoring” *J. Mater. Res.*, vol. 32, no. 17, pp. 3219–3241, Sep. 2017, doi: 10.1557/jmr.2017.207.

[10] S. F. Poterala, R. J. Meyer, and G. L. Messing, “Fabrication and properties of radially 〈001〉 C textured PMN-PT cylinders for transducer applications” *J. Appl. Phys.*, vol. 112, no. 1, p. 014105, Jul. 2012, doi: 10.1063/1.4730938.

[11] M. M. Seabaugh, I. H. Kerscht, and G. L. Messing, “Texture Development by Templated Grain Growth in Liquid-Phase-Sintered α-Alumina” *J. Am. Ceram. Soc.*, vol. 80, no. 5, pp. 1181–1188, Jan. 2005, doi: 10.1111/j.1151-2916.1997.tb02961.x.

[12] E. Feilden *et al.*, “3D Printing Bioinspired Ceramic Composites” *Sci. Rep.*, vol. 7, no. 1, p. 13759, Dec. 2017, doi: 10.1038/s41598-017-14236-9.

[13] A. Wonisch, P. Polfer, T. Kraft, A. Dellert, A. Heunisch, and A. Roosen, “A Comprehensive Simulation Scheme for Tape Casting: From Flow Behavior to Anisotropy Development” *J. Am. Ceram. Soc.*, vol. 94, no. 7, pp. 2053–2060, Jul. 2011, doi: 10.1111/j.1551-2916.2010.04358.x.

[14] H. N. Chia and B. M. Wu, “Recent advances in 3D printing of biomaterials” *J. Biol. Eng.*, vol. 9, no. 1, p. 4, Dec. 2015, doi: 10.1186/s13036-015-0001-4.

[15] M. Rumpler, A. Woesz, J. W. C. Dunlop, J. T. van Dongen, and P. Fratzl, “The effect of geometry on three-dimensional tissue growth” *J. R. Soc. Interface*, vol. 5, no. 27, pp. 1173–1180, Oct. 2008, doi: 10.1098/rsif.2008.0064.

[16] A. Barba *et al.*, “Osteoinduction by Foamed and 3D-Printed Calcium Phosphate Scaffolds: Effect of Nanostructure and Pore Architecture” *ACS Appl. Mater. Interfaces*, vol. 9, no. 48, pp. 41722–41736, Dec. 2017, doi: 10.1021/acsami.7b14175.

[17] R. B. Rao, K. L. Krafcik, A. M. Morales, and J. A. Lewis, “Microfabricated Deposition Nozzles for Direct-Write Assembly of Three-Dimensional Periodic Structures” *Adv. Mater.*, vol. 17, no. 3, pp. 289–293, Feb. 2005, doi: 10.1002/adma.200400514.

[18] A. Lode *et al.*, “Fabrication of porous scaffolds by three-dimensional plotting of a pasty calcium phosphate bone cement under mild conditions” *J. Tissue Eng. Regen. Med.*, vol. 8, no. 9, pp. 682–693, Sep. 2014, doi: 10.1002/term.1563.

[19] S. Raymond *et al.*, “Accelerated hardening of nanotextured 3D-plotted self-setting calcium phosphate inks” *Acta Biomater.*, vol. 75, pp. 451–462, Jul. 2018, doi: 10.1016/j.actbio.2018.05.042.

[20] J. Schindelin *et al.*, “Fiji: an open-source platform for biological-image analysis” *Nat. Methods*, vol. 9, no. 7, pp. 676–682, Jul. 2012, doi: 10.1038/nmeth.2019.

[21] R. Laurini, “Geographic Relations” in *Geographic Knowledge Infrastructure*, Elsevier, 2017, pp. 83–109.

[22] F. P. Preparata and M. I. Shamos, “Convex Hulls: Basic Algorithms” in *Computational Geometry*, New York, NY: Springer New York, 1985, pp. 95–149.

[23] T. G. Mezger, *The Rheology Handbook*. Vincentz Network, 2012.

[24] A. Schwab, R. Levato, M. D’Este, S. Piluso, D. Eglin, and J. Malda, “Printability and Shape Fidelity of Bioinks in 3D Bioprinting” *Chem. Rev.*, vol. 120, no. 19, pp. 11028–11055, Oct. 2020, doi: 10.1021/acs.chemrev.0c00084.

[25] M. Doube *et al.*, “BoneJ: Free and extensible bone image analysis in ImageJ” *Bone*, vol. 47, no. 6, pp. 1076–1079, Dec. 2010, doi: 10.1016/j.bone.2010.08.023.

[26] P. Cignoni, M. Callieri, M. Corsini, M. Dellepiane, F. Ganovelli, and G. Ranzuglia, “MeshLab: An open-source mesh processing tool” *6th Eurographics Ital. Chapter Conf. 2008 - Proc.*, no. January, pp. 129–136, 2008, doi: 10.1.1.649.4449.

[27] T. Hildebrand and P. Rüegsegger, “A new method for the model-independent assessment of thickness in three-dimensional images” *J. Microsc.*, vol. 185, no. 1, pp. 67–75, Jan. 1997, doi: 10.1046/j.1365-2818.1997.1340694.x.

[28] I. Ajaxon *et al.*, “Elastic properties and strain-to-crack-initiation of calcium phosphate bone cements: Revelations of a high-resolution measurement technique” *J. Mech. Behav. Biomed. Mater.*, vol. 74, no. June, pp. 428–437, Oct. 2017, doi: 10.1016/j.jmbbm.2017.06.023.

[29] M. Espanol, R. Perez, E. Montufar, C. Marichal, A. Sacco, and M. Ginebra, “Intrinsic porosity of calcium phosphate cements and its significance for drug delivery and tissue engineering applications” *Acta Biomater.*, vol. 5, no. 7, pp. 2752–62, 2009.

[30] N. Eliaz and N. Metoki, “Calcium Phosphate Bioceramics: A Review of Their History, Structure, Properties, Coating Technologies and Biomedical Applications” *Materials (Basel).*, vol. 10, no. 4, p. 334, Mar. 2017, doi: 10.3390/ma10040334.

[31] H. K. Kuiken, “Viscous sintering: the surface-tension-driven flow of a liquid form under the influence of curvature gradients at its surface” *J. Fluid Mech.*, vol. 214, no. 1, p. 503, May 1990, doi: 10.1017/S0022112090000234.

[32] F. N. Cogswell, “Converging flow of polymer melts in extrusion dies” *Polym. Eng. Sci.*, vol. 12, no. 1, pp. 64–73, Jan. 1972, doi: 10.1002/pen.760120111.

[33] P. Miranda, A. Pajares, E. Saiz, A. P. Tomsia, and F. Guiberteau, “Fracture modes under uniaxial compression in hydroxyapatite scaffolds fabricated by robocasting” *J. Biomed. Mater. Res. Part A*, vol. 83A, no. 3, pp. 646–655, Dec. 2007, doi: 10.1002/jbm.a.31272.

[34] Y. Maazouz *et al.*, “Robocasting of biomimetic hydroxyapatite scaffolds using self-

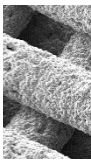

setting inks" *J. Mater. Chem. B*, vol. 2, no. 33, pp. 5378–5386, 2014, doi: 10.1039/C4TB00438H.

[35] P. Miranda, A. Pajares, E. Saiz, A. P. Tomsia, and F. Guiberteau, "Mechanical properties of calcium phosphate scaffolds fabricated by robocasting" *J. Biomed. Mater. Res. Part A*, vol. 85A, no. 1, pp. 218–227, Apr. 2008, doi: 10.1002/jbm.a.31587.

[36] B. Zhang, L. Guo, H. Chen, Y. Ventikos, R. J. Narayan, and J. Huang, "Finite element evaluations of the mechanical properties of polycaprolactone/hydroxyapatite scaffolds by direct ink writing: Effects of pore geometry" *J. Mech. Behav. Biomed. Mater.*, vol. 104, no. January, p. 103665, Apr. 2020, doi: 10.1016/j.jmbbm.2020.103665.

[37] M. Domingos *et al.*, "The first systematic analysis of 3D rapid prototyped poly(ε-caprolactone) scaffolds manufactured through BioCell printing: the effect of pore size and geometry on compressive mechanical behaviour and in vitro hMSC viability" *Biofabrication*, vol. 5, no. 4, p. 045004, Nov. 2013, doi: 10.1088/1758-5082/5/4/045004.

5.6 Supplementary Information

Von Mises equivalent stress contours:

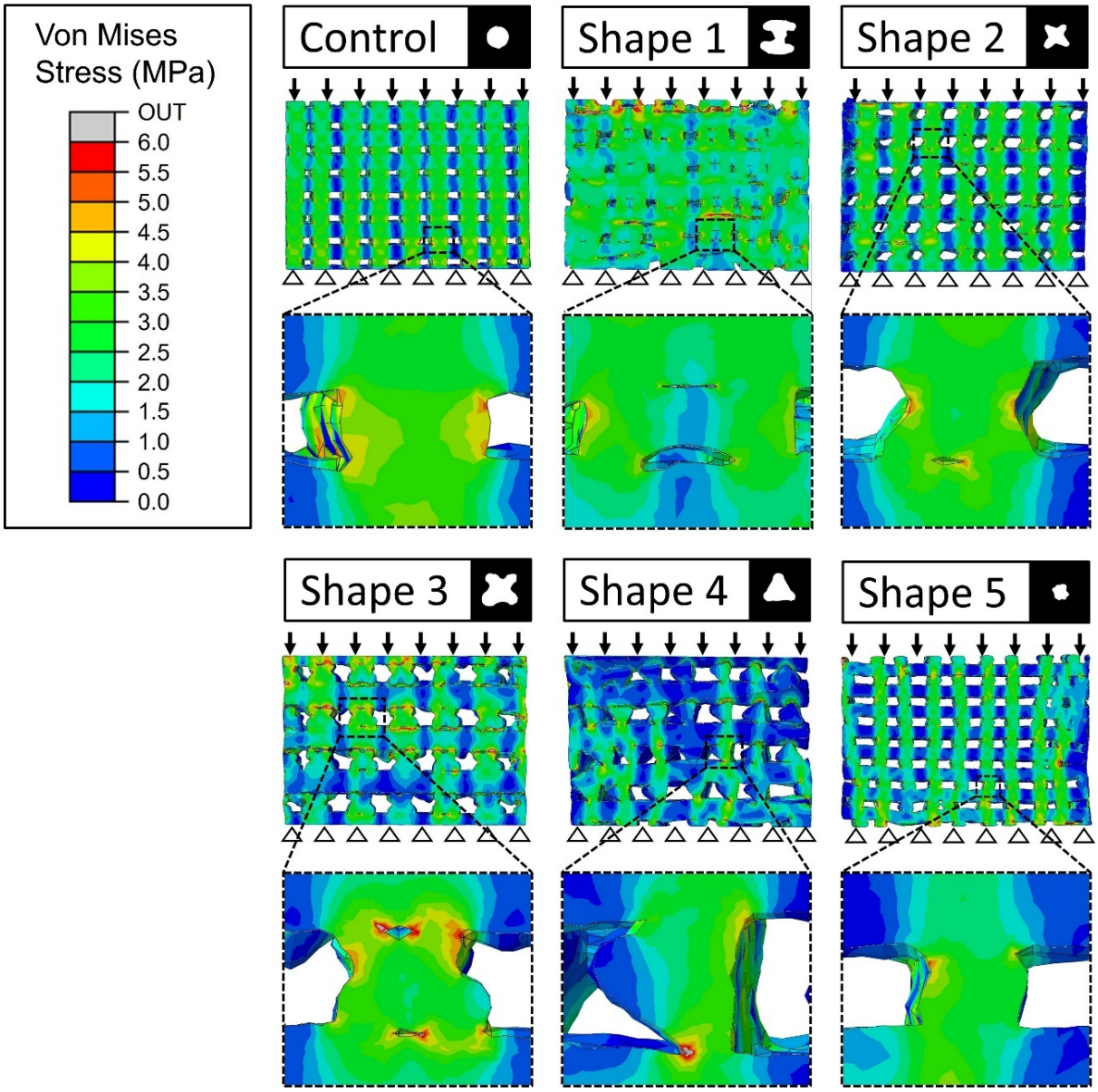

Fig. S5.1. Cross-section (XZ printing axis) of the structures elaborated with different strand geometries showing the Von Mises stress distribution obtained by finite element simulation. Compression in the elastic region with vertical (Z printing axis) strain 0.1% is indicated with arrows and vertically fixed bottom nodes are indicated with triangles. Normalised stress colormap ranging from 0 (blue) to 6 (red) MPa.

Chapter 6

3D Printing with Star-Shaped Strands: A New Approach to Enhance *In Vivo* Bone Regeneration

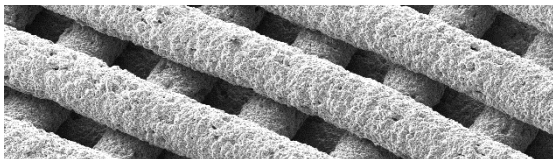

3D PRINTING WITH STAR-SHAPED STRANDS: A NEW APPROACH TO ENHANCE *IN VIVO* BONE REGENERATION

Abstract

Concave surfaces have shown to promote bone regeneration *in vivo*. However, bone scaffolds obtained by direct ink writing, one of the most promising approaches for the fabrication of personalized bone grafts, consist mostly of convex surfaces, since they are obtained by microextrusion of cylindrical strands. By modifying the geometry of the nozzle, it is possible to print 3D structures with non-cylindrical strands and concave surfaces. In this work, we compare the *in vivo* performance of 3D-printed calcium phosphate scaffolds with either conventional cylindrical strands or star-shaped strands, in a rabbit femoral condyle model. Monocortical defects were drilled in contralateral positions and randomly grafted with the two scaffold configurations, with identical composition. The samples were explanted eight weeks post-surgery and assessed by μ-CT and resin-embedded histological observations. The results revealed that the strands with concave surfaces enhanced bone regeneration and had better osteoconductive properties, guiding the newly formed bone faster towards the core of the scaffolds. This new approach can represent a turning point towards the optimisation of pore shape in 3D-printed bone grafts, further boosting the possibilities that direct ink writing technology offers for patient-specific applications.

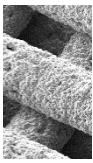

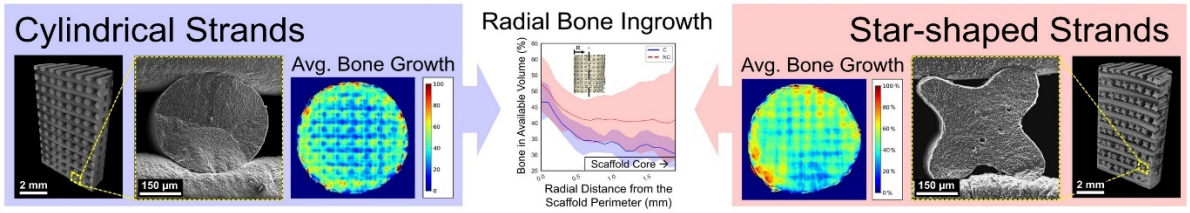

6.1 Introduction

The increasing development of additive manufacturing technologies has allowed, in recent years, the introduction of personalized medicine strategies in the field of bone regeneration [1]. Calcium phosphates (CaP) are among the best performing materials for this application, due to their similarity to the mineral phase of bone [2]. Biomimetic hydroxyapatite (HA), processed under physiological conditions outstands, as it accurately mimics the bone composition and microstructure [3].

A wide variety of additive manufacturing techniques have been used to print CaP 3D bone scaffolds [4]. Among them, filamentary-based direct ink writing (DIW) consists of extruding a pseudoplastic ink through a nozzle and controlling the deposition coordinates, in order to generate, layer by layer, the desired 3D structure [5]. Different ink formulations have been proposed, and amongst them, those using a hydrogel as a carrier for the ceramic powder present several advantages [6]. In addition to allowing a high volume fraction of ceramic particles, they are compatible with the use of reactive powders, which are at the origin of the self-hardening ceramic inks. In this case, the consolidation of the ceramic scaffold is not based on a high-temperature sintering process, but on a cement-like reaction that leads to the hardening of the structure at body temperature [7,8]. In contrast to high-temperature sintering, this mild consolidation setting can be combined with strategies involving biological molecules or even cells [9,10].

Porosity is a decisive factor in the performance of a scaffold for bone regeneration [11-13]. Ideally, a multi-scale porosity is required. On the one hand, an interconnected macropore network, with macropores ranging from 50 to 400 µm allows the vascularisation of the graft [11,12], required to supply oxygen and nutrients to the cells and remove the metabolic waste [13]. On the other hand, micropores, in addition to facilitating the permeability to oxygen and the physiological fluids, essential for cell proliferation [11], provide a larger surface area for interaction with the host tissue, including cells, soluble proteins, and extracellular matrix [14].

Besides pore size and pore interconnectivity, pore morphology also plays an important role in the biological performance of bone scaffolds. Numerous studies have demonstrated that the concavity of a surface is a determining factor in its ability to trigger bone formation [14-23]. For example, when comparing 3D-printed CaP scaffolds to foamed architectures with the same composition, despite the excellent osteoconductivity of both sample types, superior osteoinductive properties were found for the foamed samples when tested ectopically [24], which resulted also in higher osteogenesis also orthotopically [25]. This highlights the role played by pore architecture, and more specifically, by the curvature of the surface of the pores, convex in the case of the 3D-printed filaments, and concave for the foams. However, the underlying mechanisms are still unclear. Some studies relate this phenomenon with the microenvironments created within the concave pores, which may favour the differentiation of mesenchymal stem cells to osteoblasts. As they are protected from the flow of physiological fluids, the concentrations of soluble species, both proteins, and ions, in the concave regions may be different from those in their environment. For instance, in the case of calcium phosphate substrates, supersaturation levels of calcium and phosphate ions may be reached, from the dissolution or cell-mediated resorption of the scaffold. This, combined with the material capabilities of adsorbing endogenous molecular signals, may trigger the differentiation of the cells into osteogenic lineages [16-19,26]. Other investigations, rather than focusing on chemical

factors, attribute the curvature-driven tissue growth to physical or mechanical factors. Namely, tissue growth is the result of the reaction of cells to the mechanical forces induced by the geometries' curvature. Globally, the underlying physics would be analogous to that which governs processes as different as crystal growth, phase transformation, or membrane mechanics, where the tendency to minimise the system's energy results in the nucleation occurring in the regions with the lowest curvature radium and therefore lowest surface energy [20-23].

As previously mentioned, DIW has many advantages, including the possibility of tailoring both the external geometry and the internal porosity of the scaffolds [27-29,30]. However, the convex nature of the printed filaments, as circular nozzles are typically used, is a drawback when considering osteoinduction and bone formation. To overcome this limitation, in a recent work we developed for the first time 3D-printed CaP scaffolds with non-convex strand surfaces [31]. Briefly, custom-made non-circular nozzles were used to print strands with different cross-section geometries instead of the traditional cylindrical shape. A self-setting hydrogel-based alpha tricalcium phosphate (α-TCP) ink was used, which allowed to fabricate calcium deficient hydroxyapatite (CDHA) scaffolds with different filament morphologies. Nevertheless, the impact of filament geometry on their *in vivo* performance is still unknown. The present study aims to compare the *in vivo* performance of the concave-stranded structures obtained using a four-pointed-star nozzle (coded as NC-scaffolds, which stands for non-cylindrical) to the traditional cylindrical-stranded architectures (C-scaffolds), in a rabbit femoral condyle model.

6.2 Materials and Methods

6.2.1 Scaffolds Fabrication

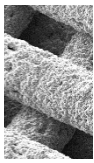

A powder phase consisting of α-tricalcium phosphate powder was mixed with a hydrogel consisting of a poloxamer 407 aqueous solution as described elsewhere [29]. The resulting ink was extruded through a custom-made direct ink writing device. Scaffolds with cylindrical strands (C-scaffolds) were printed with a commercial nozzle with a circular orifice of 410 µm (22ga Tappered Tip, Fisnar, WI, USA). To produce scaffolds with non-cylindrical strands (NC-scaffolds) a custom-made modular nozzle was used, as described in previous work [31], which had a four-point star-shaped orifice, and resulted in star-shaped strands. The cross-section area was very similar for the two strand geometries (0.12 and 0.13 mm^2 for the C and NC strands respectively) [31]. The scaffolds were printed with an orthogonal fill pattern consisting of 90º alternated deposition orientation in the XY printing plane and a theoretical infill percentage of 62%. That corresponded to an interstrand separation in the printing plane of 251 and 227 µm for the C and NC scaffolds, respectively. Scaffolds with two different geometries were printed: (1) Cylindrical samples with 8 mm in diameter and height, which were used, after grinding to 5 mm diameter, for the *in vivo* study and material characterisation. (2) 8 mm-side cubic samples used either directly or after grinding to 7 mm-side cubes for mechanical testing.

The as-printed scaffolds were subjected to a hydrothermal hardening process, comprising a first step of vapor pre-treatment followed by an autoclaving step immersed in water, as described in previous work [29]. Afterward, the samples were water sanded with P1200-grain sandpaper to obtain 5 mm-diameter cylinders and 7

mm-side cubic samples. Grinding was performed to remove the irregularities of the lateral faces of the scaffolds, where the filaments change direction. In this way, only the regular structure of the scaffold was retained, in order to better capture the effect of the strand geometry. After grinding the specimens were sonicated in distilled water in three successive 5 min washing steps to eliminate possible remaining sanded particles. Then, they were packaged in double sterilisation pouches and sterilised by wet heat in an autoclave.

6.2.2 Material Characterisation

Composition and Microstructure

The composition of the scaffolds was characterised by X-ray diffraction (XRD) and Fourier-transform infrared spectroscopy (FTIR). Prior to analysis, the samples were grinded in an agate mortar. The X-ray diffractograms were acquired with a diffractometer (D8 Advance, Bruker, Kontich, Belgium) equipped with a Cu Kα X-ray tube operated at 40 kV and 40 mA. Data were collected at 0.02º per step over the 2θ range 10 – 80º. Additionally, the amorphous content and the crystalline phases were quantified by Rietveld refinement adding an external standard (corundum, ICSD-033639) to the powder, that was analysed in a diffractometer (D8 Advance Eco, Bruker AXS GmbH, Karlsruhe, Germany) equipped with a Cu K-α beam, a Ni filter and a LynxEye detector scanning the 3 – 65º 2θ range with a step size of 0.02º. Two phases, additional to the external standard, were identified and quantified: calcium deficient hydroxyapatite (COD-9002214) and β-tricalcium phosphate (ICSD-006191). KBr-FTIR spectroscopy was performed by analysing hydraulic pressed pellets prepared from a mixture of 2 mg of sample and 300 mg of KBr. The spectrometer (Nicolet 6700, Thermo Fisher, MA, USA) scanned the sample absorbance along the wavelength spectra of 4000 to 400 cm^{-1} with a step resolution of 2 cm^{-1} and an accumulation of 256 scans per sampling step.

The microstructure of the samples was observed with a scanning electron microscope (FIB/SEM, Neon 40, Zeiss, Oberkochen, Germany) operated at 5 kV using a through-the-lens electron detector. Previously, the samples were coated by sputter deposition with a thin electron-conductive carbon layer before its analysis.

Porosity and Specific Surface Area

All the scaffolds prepared for the *in vivo* study were imaged by X-ray micro-computed tomography (μ-CT) prior to implantation. The images were acquired with the same machine setup used later for the explanted samples (explained in detail in the next section). However, as the high contrast between regions allowed it, the resolution was lowered to 18 μm $pixel^{-1}$, the scan rotation was set to 180º and a frame averaging of 1 was used to reduce the acquisition time. The resulting data were reconstructed in the same way as for the explanted samples and 3D renders were performed (CTvox v3.2.0 software, Bruker, Kontich, Belgium). The scaffolds were aligned to the cartesian axes and a volume of interest (VOI) of 5 repetition units in the three orthogonal axes was selected (DataViewer v1.5.2.4 software, Bruker, Kontich, Belgium). The reconstructions were segmented and the macroporosity percentage (P_{macro}) was determined (CTAn v1.12.0 software, Bruker, Kontich, Belgium). Additionally, this software allowed to quantify the scaffold envelope surface and to calculate the specific

surface area normalized by material volume (MV) (*i.e.* MS/MV) and by strand length (*i.e.* MS/strand mm).

Helium pycnometry (AccuPyc 1330, Micromeritics, GA, USA) was used to determine the skeletal density (ρ_{skel}) of the bulk material, and the apparent density (ρ_{app}) of the specimens was determined by measuring with a calliper the volume of cubic samples and weighting them (after drying overnight at 60 ºC in a stove). Both densities were combined as previously described by Pastorino *et al.* to determine the sample's total porosity (P_{tot}) by gravimetric routes [32]. The open porosity and pore entrance size distribution in the 0.006 – 360 µm range were measured by mercury intrusion porosimetry (MIP, AutoPore IV Micromeritics, GA, USA). Finally, the percentage of microporosity inside the strands was estimated from the MIP results and skeletal density measurements (**Equation 6.1**). First, the specific volume of micropores ($V_{micro\ (<10\mu m)}$, established as pores below 10 µm) was measured as the volume of mercury intruded in the pores with sizes comprised between 0.006 and 10 µm per gram of material. Then the specific material volume (V_{mat}) was calculated as the inverse of the skeletal density. Finally, the porosity inside the strands was obtained from the following equation:

$$P_{micro} = \left(\frac{V_{micro\ (<10\mu m)}}{V_{micro\ (<10\mu m)} + V_{mat}}\right) \cdot 100 = \left(\frac{V_{micro\ (<10\mu m)}}{V_{micro\ (<10\mu m)} + {}^{1}/_{\delta_{sk}}}\right) \cdot 100 \qquad \textbf{Equation 6.1}$$

The SSA_{BET} of both scaffold types was determined by nitrogen adsorption (ASAP 2020, Micromeritics, GA, USA) using the Brunauer- Emmett-Teller (BET) method. Samples were previously outgassed in a vacuum atmosphere (10 mmHg) for 2 h at 100 ºC.

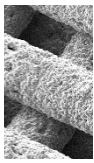

Mechanical Properties

The ultimate compressive strength (UCS) and the Weibull modulus of the scaffolds were assessed by uniaxial compressive testing (Bionix 858 uniaxial, MTS systems, MN, USA) under displacement-control conditions at a rate of 1 mm min^{-1} and using a load cell of 2.5 KN. C- and NC- cubic scaffolds were tested, with polished or unpolished lateral faces (*i.e.* 8-mm side or 7-mm side cubes, respectively), with 15 replicates per group. The specimens were immersed in water 1 h before the test and tested in wet conditions to better replicate the behaviour in a physiological environment.

The Weibull modulus was calculated by applying the Weibull probability distribution equation (**Equation 6.2**) to the obtained UCS of the samples, where P_s corresponds to the survival probability of the sample, σ corresponds to the UCS, σ_0 is a constant that represents the stress at which all the samples will survive and m corresponds to the Weibull modulus.

$$\ln\left(ln\left(\frac{1}{P_s}\right)\right) = m\big(ln(\sigma) - ln(\sigma_0)\big) \qquad \textbf{Equation 6.2}$$

6.2.3 Animals

Adult New Zealand white rabbits with an age ranging from 8 to 12 months and a bodyweight ranging from 4.8 to 5.5 kg were used. The animals were purchased from a professional stock breeder (Charles River, Saint Aubin les Elboeuf, France) and housed in individual 2 m^2 boxes during the course of the study. Prior to the surgery, a two-week acclimatisation period was established.

6.2.4 Study Design

The procedure was conducted in compliance with the European Community Guidelines (Directive 2010/63/EU) and the Guide for Care and Use of Laboratory Animals [33]. The study, which was part of a larger study to analyse the bone regeneration capacity of scaffolds with different configurations, obtained the permission of the local Animal Ethics Committee for Human and Animal Experimentation (Approval number: CEAAH 4683). A total of ten animals were used. A circular monocortical osteochondral defect was drilled bilaterally (2 defects per animal) in the medial aspect of the femoral condyle. The bone regeneration potential of the scaffolds with non-cylindrical strands was compared to a positive control group of scaffolds with cylindrical strands. Each defect was randomly grafted with a different scaffold type (n = 7 per each scaffold type). The outcome was evaluated 8 weeks post-surgery and consisted of a µ-CT volumetric assessment and a qualitative histological assessment of the scaffolds' cross-sections.

6.2.5 Surgical Procedure

The surgical procedure was performed under standard sterile conditions. After sedation, the animals were anesthetised with propofol and maintained with inhaled isoflurane (2%) in an oxygen carrier by mask. After aseptic preparation of the surgical site, the animals were placed in a dorsal recumbent position and a bilateral medial parapatellar skin incision was performed to expose the medial aspect of both femoral condyles. A first mono-cortical cylindrical defect with a depth of 10 mm was created in the centre of the femur condyle by using a Ø2.5 mm drill bit under copious saline solution irrigation to avoid thermal necrosis. Next, the defect was expanded to Ø5 mm. The defects were grafted with press-fitted cylindrical scaffolds of 5 mm in diameter and 10 mm in height. Two different scaffold conditions were used (C and NC). Afterward, the surgical wound was sutured in consecutive layers. Anaesthetic recovery of the animals was uneventful. At 8 weeks post-surgery, the animals were euthanized with a sodium pentobarbital overdose in compliance with the American Veterinary Medical Association legislation. Immediately after euthanasia, the condylar regions were explanted and fixed in neutral buffered formalin solution (10%) for two weeks and dehydrated in an increasing series of ethanol solutions.

6.2.6 Histomorphometric Assessment

Micro-Computed Tomography Acquisition

The dehydrated samples were analysed by µ-CT (Skyscan 1272, Bruker, Kontich, Belgium). The tomographic measurements were performed with an acceleration voltage of 90 kV and an X-ray current of 111 µA. The X-ray spectrum of the tungsten target was modified by using a 0.5 mm thick aluminium filter and a 0.038 mm thick

copper filter. The exposure time per projection was 2600 ms and 1800 projections were taken around 360º. An isotropic voxel resolution of 10 µm was selected. Object shifting correction and beam hardening correction were applied to the tomographic reconstructions of the acquisitions (NRecon software, Bruker, Kontich, Belgium).

Image Analysis

The segmentation and image analysis were based on a previous work where the process is reported in detail [34]. Briefly, the segmentation was performed by using a gaussian mixture model to cluster pixels according to scaffold, bone or soft tissue. Afterward, 3D reconstructions of the segmented data were rendered through a multiplanar reconstruction software (CTVox, Bruker, Kontich, Belgium). Then, for each sample, the percentage of newly formed bone normalized per volume available in the scaffold pores was calculated as the proportion of pixels labelled as bone over the sum of pixels corresponding to soft tissue and new bone and represented with a scatterplot of individual observations overlaid to a boxplot. Subsequently, the radial bone intrusion curves indicating the average bone fraction depending on the radial position were calculated for each individual sample. The combination of trendlines was represented with an average curve and a 95% CI region. Finally, the bone distribution axial colormaps representing the average bone fraction among all the samples of each condition depending on the position in the axial projection view were plotted. This analysis, based on previous work [34], was complemented by calculating the percentage of biomaterial surface covered by newly formed bone and the bone growth on the surface of the strands as a function of the offset distance.

The percentage of biomaterial surface covered by newly formed bone was calculated for each scaffold by dividing the surface of the scaffold covered by bone over the total surface of biomaterial available. The surface of biomaterial was calculated from the segmented stacks by subtracting to the biomaterial region the same region with one-pixel erosion. This way, a one-pixel thickness layer corresponding to the surface of the biomaterial was obtained. The bone surface in contact with the biomaterial was calculated by performing a conjunction (*i.e.* AND) Boolean operation to the combination of the one-pixel dilated biomaterial region and the bone region. The result consisted of a one-pixel thickness layer corresponding to the interface between regions. It was assumed that the number of pixels of these two calculated regions was directly proportional to the surfaces available (as the pixels are isotropic). The individual observations of the percentage of biomaterial surface covered by newly formed bone were plotted as a scatterplot and grouped in a boxplot.

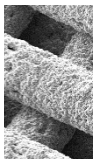

The percentage of bone growth on the surface of the strands as a function of the offset distance was calculated for each scaffold by defining successive 10 µm thick regions covering the biomaterial surface and calculating the percentage of bone over total volume in each of these regions. Then, the trend line of this percentage as a function of the distance from the biomaterial surface was calculated. For each condition, the average trend lines and 95% CI regions were plotted.

A detailed description of the image analysis workflow is provided in the supporting information section. The implementation codes in Python (Python 3.9.0, www.python.org) are available in the Git repository

https://github.com/YAGORAYMOND/uCT-image-analysis.

6.2.7 Histological Assessment

After µ-CT analysis, the dehydrated samples were successively immersed in ethanol solutions with increasing concentrations (*i.e.* 25, 50, 75, and 100 wt.%) of methyl methacrylate resin (Technovit 7200 VLC, Kulzer, Germany). The final resin embedding was held under vacuum overnight and photopolymerized in a UV lamp (EXAKT 520, Exakt Technologies, Norderstedt, Germany). Subsequently, the polymerized samples were cut with a diamond band saw (EXAKT 300 CP, Exakt Technologies, Norderstedt, Germany) through the central longitudinal cross-section of the scaffold. One half was polished (P4000 grain, Surface grinder, EXAKT 400 CS, AW110, Exakt Technologies, Norderstedt, Germany), sputter-coated with carbon, and observed through SEM (Phenom XL, Phenom world, Thermo Fischer Scientific, MA, USA) using a beam accelerating voltage of 10 kV and a secondary electron detector. The mapping scan utility (Automated image mapping software, Phenom ProSuite, Pehnom World, Thermo Fischer Scientific, MA, USA) was used to acquire images of the complete cross-sections. A 300 µm thick slice was cut from the other half sample, polished down to 30-50 µm, and stained with Goldner-Masson trichrome for histological observation under bright-field microscopy (BX51-P, Olympus, Tokyo, Japan).

6.2.8 Statistical Analysis

The scaffold's ultimate compressive strength is presented in a bar chart as mean values ± standard error. The µ-CT quantifications percentages of bone volume and biomaterial surface covered by bone are presented as boxplots (indicating the median and quartiles) with overlaid dots representing the individual observations. Statistically significant differences between specimens were calculated (Minitab®19, MiniTab Inc., State College, PA) by one-way analysis of variance (ANOVA) combined with Tukey's post hoc test. The confidence interval was set to 95% (α=0.05) for all the analyses.

6.3 Results

6.3.1 Material Characterisation

C- and NC-scaffolds were printed using a self-setting ink that hardens as a result of the hydrolysis of α-TCP to CDHA. The XRD analysis revealed the same phase composition irrespective of the geometry of the filaments of the scaffolds (**Fig. 6.1 I**). Rietveld quantification of the crystalline phases using an external standard revealed a composition of 78.8% CDHA, 10.1% β-tricalcium phosphate (β-TCP), and 11.2% amorphous phase. No unreacted α-TCP was detected in any of the samples.

The FTIR spectra (**Fig. 6.1 II**) showed the same absorption bands for both conditions, which correspond to the different vibration modes of PO_4^{3-} (*i.e.* v1~980, v2~363, v3~1082 and v4~515 cm^{-1}) [35] characteristic of the calcium phosphates. Moreover, the absorption bands of HPO_4^{2-} (*i.e.* ≈870 cm^{-1}) and OH^- (*i.e.* ≈631 and 3570 cm^{-1}), characteristic of calcium-deficient hydroxyapatite [36], were identified in both samples. Additionally, the H_2O stretching and bending bands corresponding to the humidity absorbed by the samples can be noticed at wavelengths of 3500 and 1500 cm^{-1}, respectively.

Images of the 3D-printed scaffold architectures with cylindrical and non-cylindrical strands, obtained by µ-CT are shown in **Fig. 6.1 III**. Scanning electron microscopy (SEM) observations revealed that both samples had the same microstructure,

consisting of an entangled network of acicular crystals, larger on the external surface of the filaments and smaller in the interior (**Fig. 6.1 IV**), and as expected had very similar specific surface area as determined by nitrogen adsorption (**Table 6.1**).

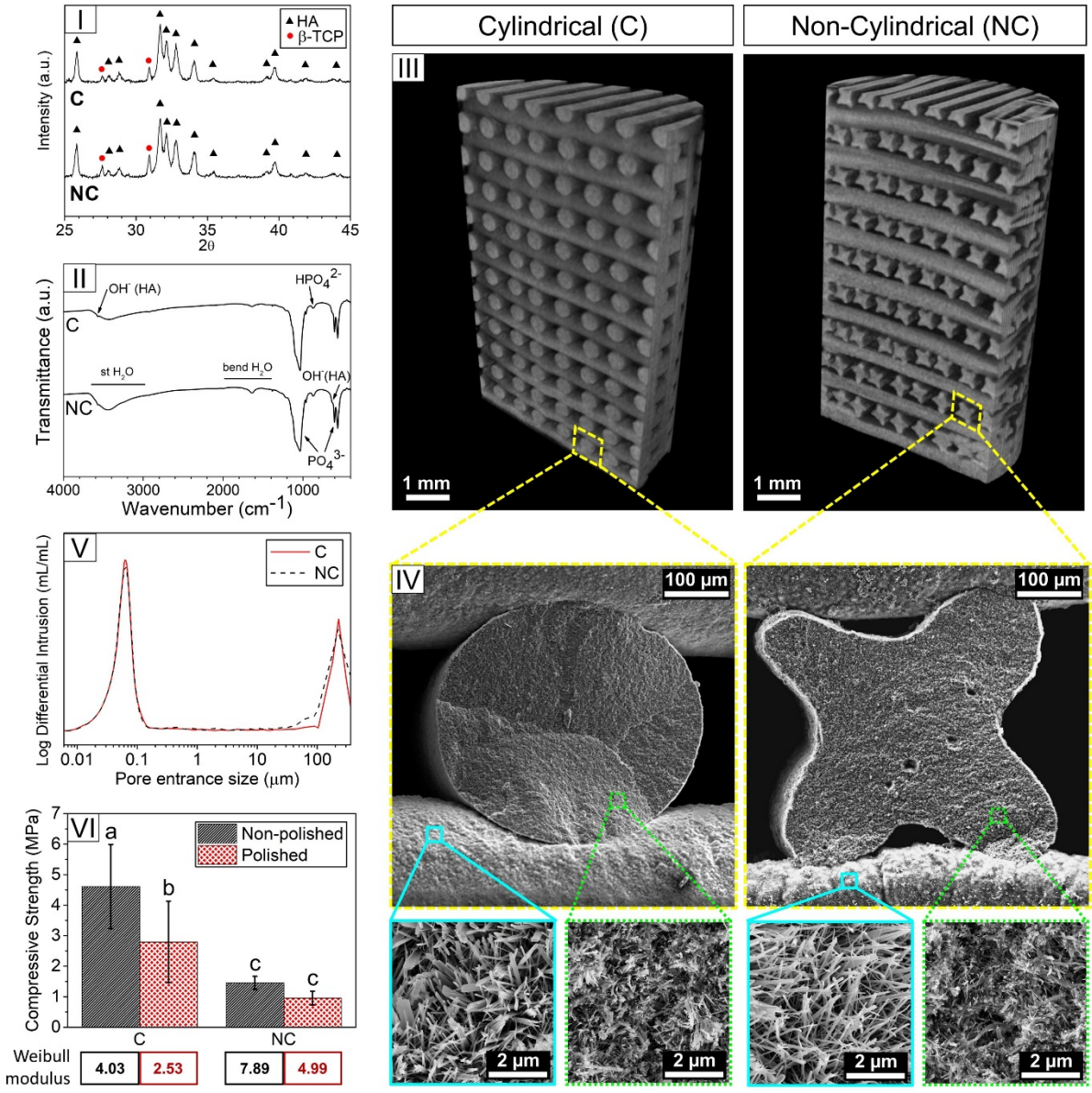

Fig. 6.1. I XRD patterns; **II** FTIR spectra; **III** Scaffold morphology obtained by μ-CT; **IV** scaffold microstructure observed by SEM; **V** Pore entrance size distribution as measured by MIP; **VI** Ultimate compressive strength and Weibull modulus, of the cylindrical and non-cylindrical-strand samples. Statistically significant differences are indicated with different letters ($p<0.05$).

The textural properties of the two scaffold types are displayed in **Table 6.1.** The macroporosity obtained in the 3D-printed structures during the printing process was quantified by μ-CT, obtaining values of 41.08 ± 1.50% and 48.38 ± 1.36% for the C- and NC-scaffolds respectively. The closed porosity represented less than 1% for both conditions. μ-CT also allowed to calculate the envelope specific surface area of the strands, which as expected was larger for the NC- than for the C-scaffolds. Both when

normalising the material surface (MS) per volume of material (MS/MV) and per strut length (MS/strand mm), the value was twice as high for the NC-scaffolds as for the control.

The pore entrance size distribution of the two scaffolds (**Fig. 6.1 V**) obtained by MIP, showed a similar bimodal porosity distribution, irrespective of the strand section geometry. The two pore entrance size levels correspond to the intrastrand and the interstrand porosity. For both sample types, the intrastrand porosity was in the range of 0.01 to 0.2 μm and the interstrand porosity was in the size range of 100 to 360 μm, where the larger threshold corresponds to the upper limit of detection of this technique. The total porosity measured by gravimetric methods was 75.78 and 78.72% for the C- and NC-scaffolds respectively. The intrastrand microporosity, assessed from the MIP results, was similar for both sample types, and the same stands for the specific surface area measured by nitrogen adsorption.

Table 6.1. Density and textural properties of the 3D-printed scaffolds composed of cylindrical and non-cylindrical strands.

Properties	**Cylindrical***	**Non-Cylindrical***
Skeletal Density (ρ_{skel})	3.06 g cm^{-3}	3.07 g cm^{-3}
Apparent Density (ρ_{app})	0.74±0.03 g cm^{-3}(a)	0.65±0.04 g cm^{-3}(b)
Total Porosity (P_{tot})	75.78±1.07%(a)	78.72±1.21%(b)
Intrastrand Microporosity (P_{micro})	56.67%	56.81%
Macroporosity (P_{macro})	41.08±1.50%(a)	48.38±1.36%(b)
Specific Surface Area (SSA_{BET})	27.11 m^2 g^{-1}	26.55 m^2 g^{-1}
Specific Surface Area (MS/MV) [μ-CT]	9.06±0.23 mm^2 mm^{-3}(a)	20.38±0.38 mm^2 mm^{-3}(b)
Specific Surface Area (MS/strand mm) [μ-CT]	1.18±0.03 mm^2 strand mm^{-1}(a)	2.04±0.04 mm^2 strand mm^{-1}(b)

* (a) and (b) indicate statistically significant differences between conditions ($p<0.05$).

The C-scaffolds had a significantly higher compressive strength, as shown in **Fig. 6.1 VI**, with 4.61 ± 1.38 MPa and 2.79 ± 1.34 MPa for the non-polished and polished specimens respectively, compared to the NC-scaffolds that resulted in 1.45 ± 0.21 MPa and 0.96 ± 0.23 MPa respectively. Moreover, a larger Weibull modulus was found in NC-scaffolds, indicating a more homogeneous flaw distribution and thus lower variability in the results. In both scaffold types, the grinding resulted in a reduction of the compressive strength and Weibull modulus.

6.3.2 *In Vivo* Study

All the animals completed the postoperative period with no clinical complications, weight loss, behaviour changes, or lameness. No signs of wound infection, wound dehiscence, or implant migration were observed. During the explantation and soft tissue removal process, one sample (belonging to the NC group) was damaged and dismissed from the study.

Bone was found in direct contact with the scaffolds and no immune rejection was observed, indicating the good biocompatibility of the material. Histological analysis was used to assess the bone morphology and degree of maturity and distribution. Additionally, μ-CT was used to quantify in three dimensions the amount of newly formed bone and identify the degree of penetration into the scaffolds.

Microscopic Assessment of the Bone Formation

SEM micrographs of the resin embedded scaffold cross-sections (**Fig. 6.2 I**) showed the scaffold porous structure (in light grey) surrounded by newly formed bone (dark grey) in direct contact with the biomaterial. Due to limitations in the precision of the resin-embedded-sample-cutting technique, the axes of the cross-sectional cuts were not perfectly aligned to the printing axis. This is a common occurrence when performing histological cuts of robocasted samples [25,37]. A positive consequence is that this allowed observing two regions of the scaffold in the same sample cut: the plane cutting the centre of the strand-intersection pillars (**Fig. 6.2 I-a**) and the plane cutting the centre of the Z-direction pores (**Fig. 6.2 I-b**). On the one hand, the region of strand intersections presented a similar bone distribution in both sample types, with newly formed bone growing on the concave surfaces formed by the strand intersections, linking the different strands (**Fig. 6.2 II-a** and **Fig. 6.2 III-a**). On the other hand, in the second region, bone was preferentially found in the non-cylindrical strands, deposited at the concave regions originated by its star-shaped geometry (**Fig. 6.2 III-b**).

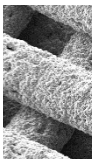

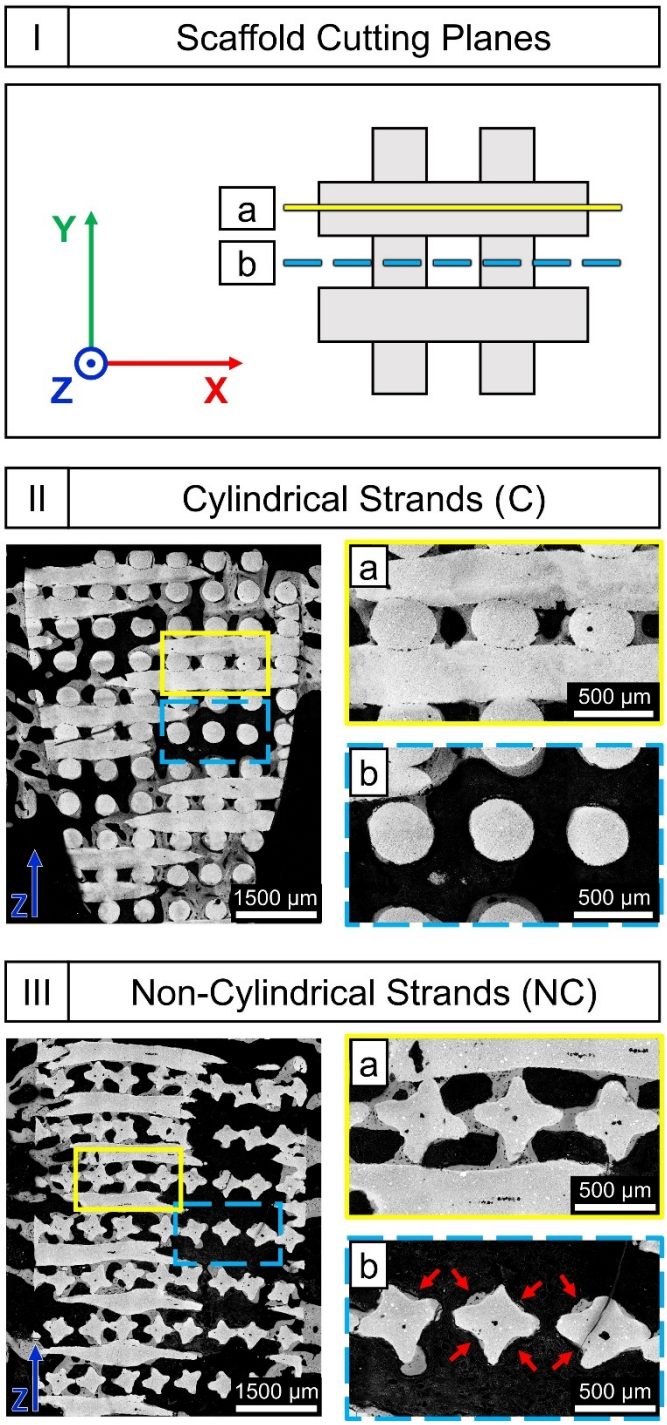

Fig. 6.2. I Schema illustrating the two cutting-planes observed in the histological cross-sections: **a** plane cutting the centre of the strand-intersections, and **b** plane cutting the centre of the Z-direction pores. **II** and **III** SEM images of the histological axial cross-section cuts for the cylindrical-stranded scaffolds and non-cylindrical-stranded scaffolds, respectively, where the **a** and **b** regions can be identified. Red arrows indicate the bone ingrowth on the concave strand surfaces in these second regions.

The histological assessment (**Fig. 6.3**) evidenced a high biocompatibility for both sample types, with a high degree of osseointegration and a proper osteoconduction throughout all the scaffolds. No signs of bone necrosis, inflammation areas nor

scaffold encapsulation were observed in any sample. Tissular continuity was found in both conditions (**Figs. 6.3 I**, **IV**, **VII**, and **X**). A close-up look at the histological slides revealed the presence of a broad network of vascular canals in the macropores of both sample types (**Figs. 6.3 VI**, **IX**, and **XII**). No differences in terms of bone structure and morphology were observed between sample conditions with this technique. Moving on to detailed observations of the higher magnification images, in **Fig. 6.3 III** lamellar bone is observed forming in apposition to pre-existent less mature woven bone located in the corner created by the intersection of two strands of consecutive layers. This suggests that the bone formation process has its origin in such regions. In **Fig. 6.3 V** a woven bone region is shown with three crossing vascular canals sectioned through the longitudinal axis by the histological section. On the right canal, aligned erythrocytes within a small blood vessel are observed, whereas in the centre canal an osteoclast-like multinucleated cell is visible. Such vascularisation favours the deposition of lamellar bone around the vascular canals indicating an active remodelling process. Similar dispositions are found for the NC condition in **Fig. 6.3 IX**, where a blood vessel inside the vascular canal is discerned. In this case, the structure surrounding the Haversian canal is at a more mature stage showing the striated layers of surrounding concentric lamellae. Finally, in **Fig. 6.3 XII** the transversal cut of a vascular canal with identifiable erythrocytes inside the vascular structure is visible. Moreover, in the upper left region of the vessel, the diapedesis process of a multinuclear cell is observed, which could be attributed to the initial stage in the formation of a cutting cone.

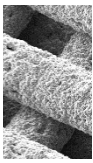

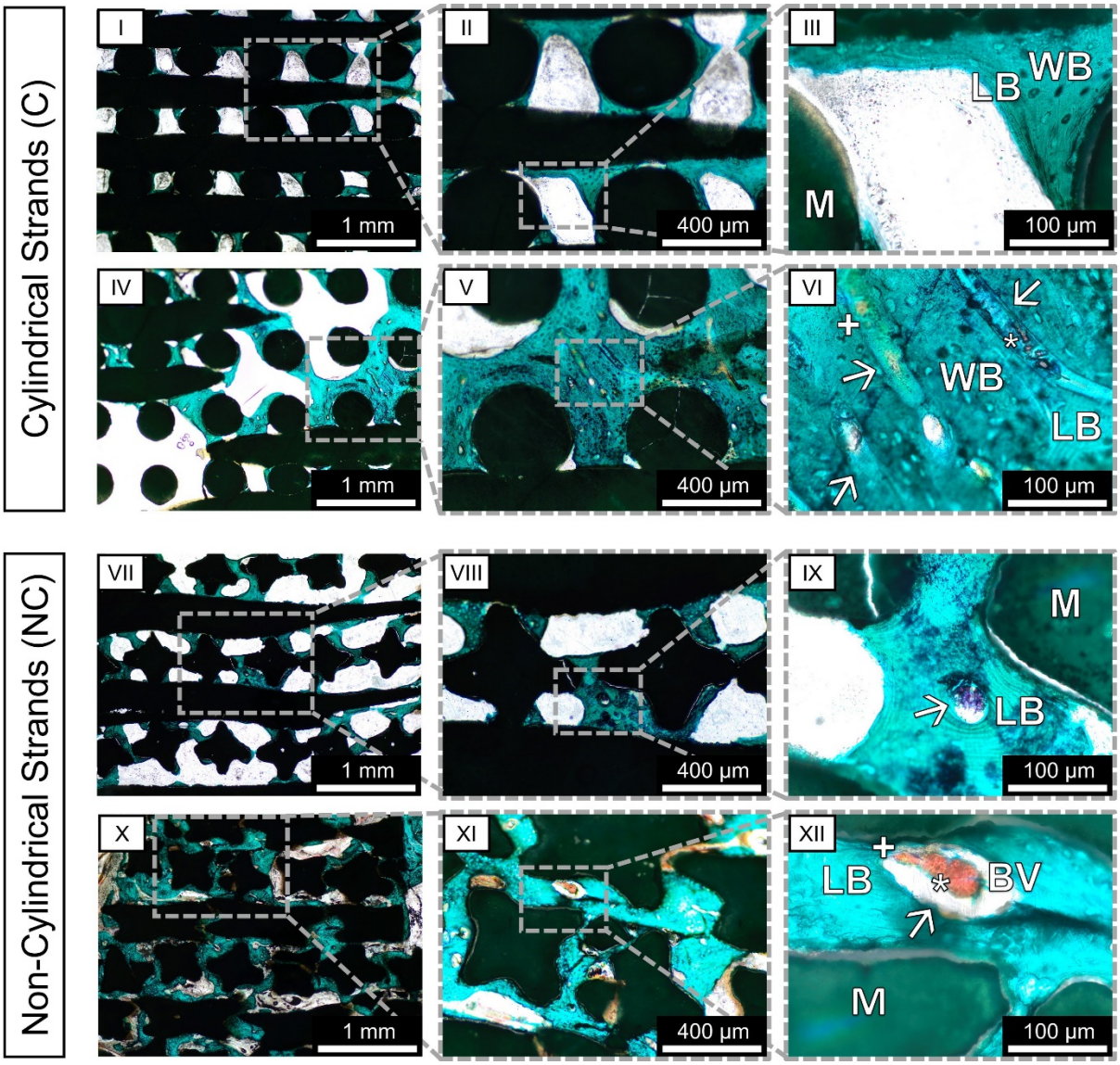

Fig. 6.3. Masson-Goldner trichrome staining of the histological slides of the cylindrical-stranded scaffolds (C) and non-cylindrical-stranded scaffolds (NC). Bone appears coloured in green-blue and biomaterial in dark. M = biomaterial, WB = woven bone, LB = lamellar bone, (→) = vascular canal, (*) = erythrocytes, (+) = multinucleated cell, BV= blood vessel.

µ-CT: 3D Reconstruction and Morphometric Quantification

3D reconstructions of the segmented µ-CT acquisitions (**Fig. 6.4**) allowed to assess the distribution of the newly formed bone within the scaffolds and compare the best and worst-case within each sample condition.

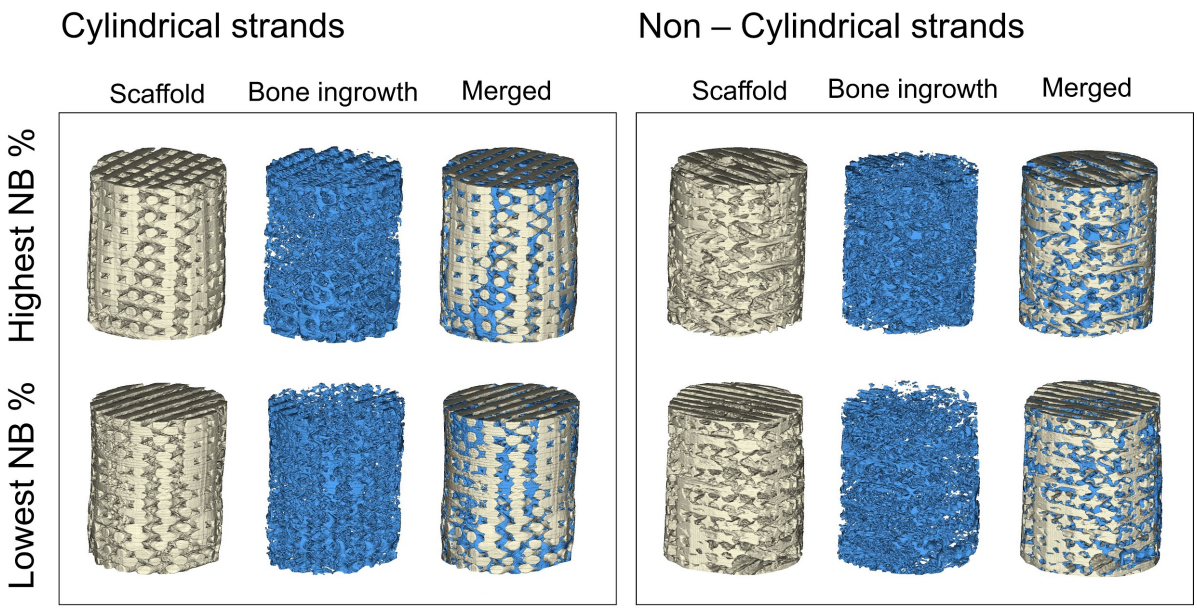

Fig. 6.4. Representative µ-CT reconstructions of the samples with highest and lowest percentage of newly formed bone (NB %) for the scaffolds printed with cylindrical (left) and non-cylindrical (right) strands.

The overall percentage of newly formed bone on available volume was higher for the non-cylindrical stranded scaffolds (43.60±10.32%) than for the cylindrical stranded scaffolds (37.34 ± 5.08%), although the difference was not statistically significant (**Fig. 6.5 I**). The bone distribution as a function of the radial distance from the scaffold surface is displayed in **Fig. 6.5 II**, which represents the degree of bone intrusion for both samples. Additionally, the degree of bone intrusion can also be shown by mapping the overall average bone percentage in a cumulated projection of the scaffold's axial cross-section, as displayed in **Fig. 6.5 III**. The colormap ranges from blue to red corresponding to 0 and 100% of newly formed bone in available volume respectively. The percentage of biomaterial surface covered by newly formed bone was also quantified, obtaining a 57.82 ± 11.28% and 65.11 ± 11.72% for the C and NC scaffolds respectively (**Fig. 6.5 IV**), although the difference was not statistically significant. Finally, the thickness of the bone grown on the surface of the strands with different geometries was quantified by determining the percentage of bone on available volume at different offset radial distances from the strand surface. The results are shown in **Fig. 6.5 V** with trendlines and 95% confidence intervals (CI) of the estimate.

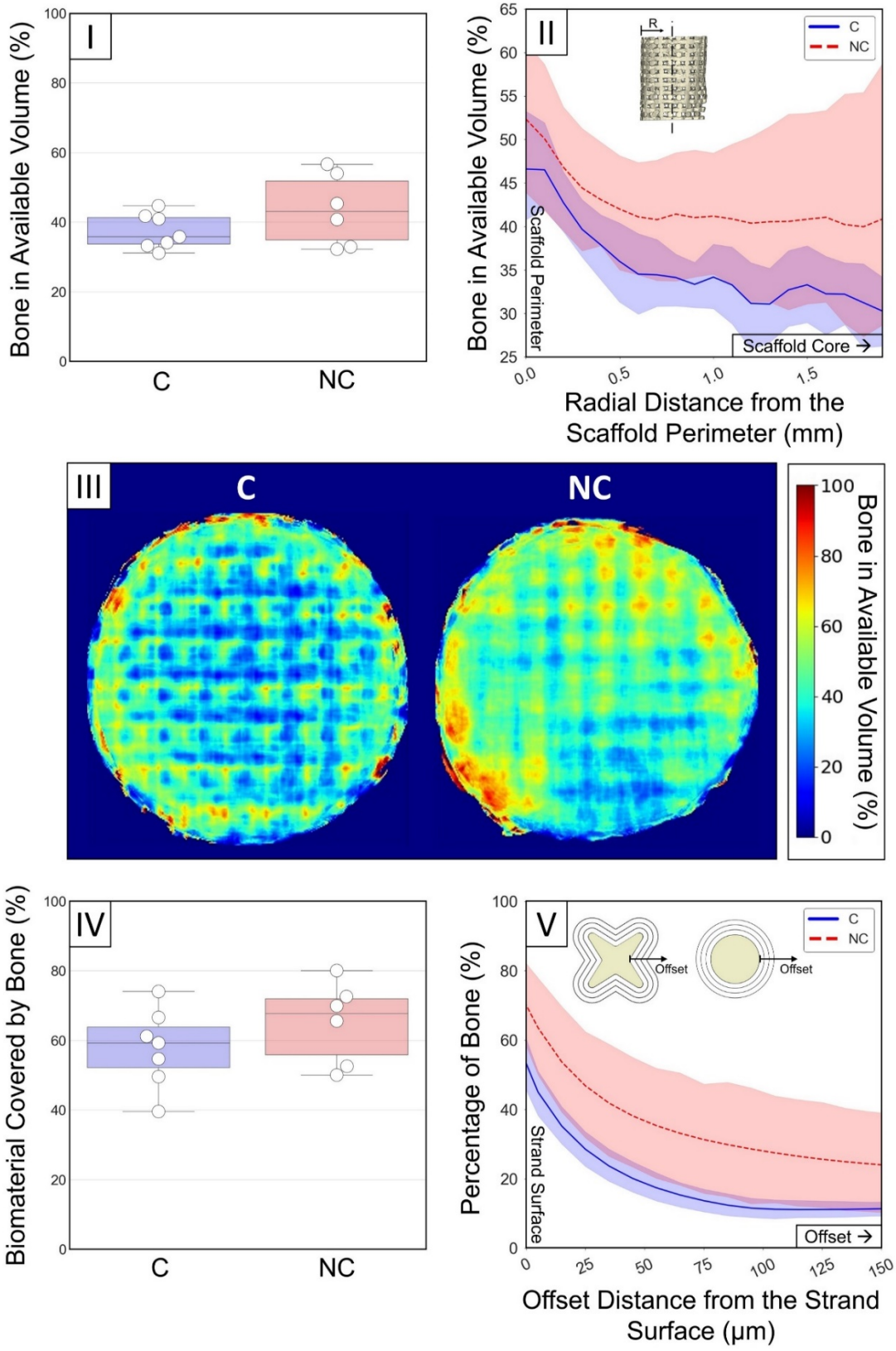

Fig. 6.5. I Quantification of the percentage of newly formed bone in the available volume; **II** radial bone intrusion into the scaffold. The solid and dashed lines represent the average value and the surrounding transparency-coloured regions represent the 95% CI for that estimate; **III** cumulate mapping of the percentage of newly formed bone

in available volume; **IV** percentage of biomaterial surface covered by newly formed bone and **V** bone growth on the surface of the cylindrical (C) and non-cylindrical (NC) strands. No statistically significant differences were found in sections I and IV ($p<0.05$).

6.4 Discussion

Surface curvature has been highlighted as a decisive parameter in tissue growth [20,21], and more specifically in bone formation [16,24]. Therefore, it should be taken into account as a design criterion for bone scaffolds. Some methods of manufacturing macroporous scaffolds, such as foaming or particle leaching, directly result in concave surfaces. This is not the case for microextrusion-based techniques, which typically use circular nozzles and therefore result in porous structures with convex surfaces. However, modification of the nozzle cross-section also allows the printing of non-cylindrical filaments with concave surfaces, introducing an additional degree of control to the pore geometry by this technique [31]. In this study, we analysed the impact of strand surface curvature of 3D-printed calcium phosphate scaffolds on the bone regeneration capacity in a rabbit model.

As shown by XRD and FTIR (**Figs. 6.1 I** and **II**), the two scaffold types, with different strand geometries, *i.e.* cylindrical vs. non-cylindrical, had the same composition, consisting mostly of CDHA with a small amount of β-TCP, as a result of the hydrothermal transformation of α-TCP [29,34]. FTIR confirmed the calcium-deficient nature of the HA, associated with the hydrolysis-based hardening reaction process [38]. SEM observations revealed similar microstructures for both scaffolds, consisting of an entangled network of acicular crystals characteristic of the HA obtained by hydrothermal processes [39]. Consequently, the specific surface area (SSA) measured by nitrogen adsorption was almost identical for both scaffolds. However, clear differences in crystal length were observed when comparing the internal and external microstructures in both scaffold types. This can be attributed to the available space for crystal growth at the surface, leading to longer needles.

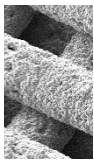

Despite the different strand morphologies, the total porosity of the two 3D-printed scaffold types was similar, and so were the micro and the macroporosity (**Table 6.1**). Regarding macroporosity, as both conditions were printed with the same printing pattern infill percentage, the small differences observed can be attributed to the different layer height and the different strand morphology. The micro and macropore size ranges (**Fig. 6.1 V**) were also very similar between the two scaffolds. Therefore, the differences observed in the *in vivo* performance of the scaffolds should be attributed mainly to the strand morphology.

However, as expected the strands with a fluted morphology led to a reduction in the scaffold compressive strength (**Fig. 6.1 VI**). This can be associated with the lower contact surface between successive layers, resulting in higher stress concentrations, as reported in a previous study [31]. It was also observed that grinding reduced the scaffold's compressive strength. This behaviour can be explained by the removal of the external layer of the scaffold, which has a lower porosity due to the bending of the strands when changing the printing direction.

As expected, bone grew throughout the porous structure in the two scaffold architectures (**Fig. 6.4**), as the scaffold material, a biomimetic calcium-deficient hydroxyapatite is known to be highly osteoconductive [40]. Moreover, the interconnected porosity of the 3D architecture led to a widespread vessel network,

resulting in a highly vascularized tissue, as observed in the Goldner-Masson-trichrome-stained histological slides (**Fig. 6.3**).

Although the differences found in the histomorphometric quantification were not statistically significant, all the results showed a clear trend indicating that the concave strands had a favourable effect in the amount of newly formed bone, the degree of bone penetration into the structure, and the thickness of the layer of bone formed on the strands. The μ-CT histomorphometric analysis allowed not only to quantify the amount of newly formed bone in three dimensions but also to determine its spatial distribution. A larger amount of regenerated bone was found when the scaffolds were printed with fluted star-shaped strands, although the increase was not statistically significant (**Fig. 6.5 I**). This is in agreement with previous studies reporting that the bone formation rate is accelerated on surfaces with smaller concave curvature radii [20,21,23]. The corrugation of the NC-scaffolds resulted in better osteoconductive properties, leading to a higher degree of bone intrusion towards the core of the structure, as shown in the radial bone intrusion trendlines of **Fig. 6.5 II** and in the average bone percentage mappings of **Fig. 6.5 III**. Whereas both scaffold types presented an initial exponential decrease of the bone percentage in the first 0.5 mm perimetral region, the amount of bone was constant from this point for the NC-scaffolds, while for the C-scaffolds it followed a decreasing trend towards the centre. Furthermore, the vertical offset also indicated a global larger amount of bone formation in NC-scaffolds with regards to C-scaffolds.

Consistent with these results, the mappings of bone percentage showed the highest amounts of bone in the perimetral areas of the scaffold. Moreover, the NC samples presented a higher percentage of bone than the C samples, and these differences became more remarkable in the core of the scaffolds, suggesting a higher level of osteoconduction for the NC samples. The architecture of both scaffolds was clearly identified in the mapping since in all the samples the orthogonal pattern was aligned. This was confirmed by the quantification of the surface of the strands covered by newly formed bone (**Fig. 6.5 IV**), resulting in higher values for the scaffolds with non-cylindrical strands compared to the cylindrical ones. These results are in agreement with previous studies reporting a positive effect of grooves patterned on metallic surfaces, enhancing and guiding bone formation [41,42] and improving osteoconductive properties [43]. The focus of these works was on guiding bone through the external surface of dental implants to maximize the degree of osseointegration and implant stability. In contrast, the current study harnessed this strategy to enhance bone ingrowth in a calcium phosphate scaffold. As this is a bioactive substrate, in addition to the purely geometrical effect, the impact of the geometry of the surface on the distribution of the ions exchanged with the surrounding fluids, with a possible confinement in the concavities, must be taken into account.

Moreover, the percentage of newly formed bone was calculated as a function of the offset distance from the strand surface (**Fig. 6.5 V**). Regardless of the strand geometry, bone started growing on the surface of the scaffold and progressively moved to the centre of the pore. This resulted in exponential decay trend lines for both samples, although there was an offset of about 10-15 % for the NC scaffolds, which showed also a higher variability. This is consistent with the higher amount of bone for the NC scaffolds in **Figs. 6.5 I**, **II**, and **III**. Furthermore, it is worth mentioning that the percentage of bone at z=0 in **Fig. 6.5 V** matched the results of **Fig. 6.5 IV**, the slight differences being attributed to the different quantification strategies employed. All together validates both quantification analyses.

In the same line, the SEM micrographs (**Fig. 6.2**) and histological observations (**Fig. 6.3**) revealed a double role of the filament concavities. In the first place, the triggering/acceleration of the bone formation process and, in the second place, an enhanced bone guiding function. Regarding the first one, the strand crossing regions presented the majority of the formed bone. This finding is in agreement with previous research that also found the bone starting to grow in more confined regions, such as concavities or corners [16,17,24]. Additionally, it was observed when comparing **Fig. 6.2 II-b** to **Fig. 6.2 III-b** that the strand fluting of the NC condition guided the bone growth through regions of the scaffolds that were hardly reached with the traditional strand configuration (*i.e.* the regions of the cantilever strands connecting the pillars).

The results shown in the present study demonstrate that the concave filaments were more efficient in terms of guiding bone formation, and hence, enhancing the global osteoconductive properties of the structure. However, the fact is that no significant increase in bone formation was observed, and the enhancement with respect to scaffolds with cylindrical struts was less remarkable than that obtained with a foamed architecture [24,25]. This can be explained by the fact that, despite having concave surfaces, pore interconnections in the NC-scaffolds were very large, and hence they lacked confined microenvironments like those found in foams with bottle-neck interconnections. Therefore, although the physical or mechanical factors associated with curvature-driven tissue formation [21] were indeed present, the chemical effects associated with the retention of soluble proteins and ions might be mitigated by the open nature of the macropore structure and the lack of confined volumes.

6.5 Conclusions

Controlling the morphology of the strands is a promising strategy to enhance bone regeneration on 3D-printed scaffolds. Strands with a fluted morphology appear to be capable of guiding bone faster through the core of the scaffolds than the traditional cylindrical morphologies. This represents a clear enhancement of the scaffold's osteogenic and osteoconductive properties.

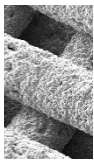

Although this work is a first step that proves the effectiveness of this approach for bone regeneration, further research is needed to fully understand the role of strand geometry, (testing multiple geometries and implantation times) and the interaction with the strand printing arrangement (using additional patterns to the orthogonal one). The configuration should be optimised to obtain conditions similar to bottle-neck pores and confined environments in order to turn the 3D-printed morphologies more efficient for bone regeneration.

6.6 References

[1] M. Javaid and A. Haleem, “Additive manufacturing applications in orthopaedics: A review” *J. Clin. Orthop. Trauma*, vol. 9, no. 3, pp. 202–206, Jul. 2018, doi: 10.1016/j.jcot.2018.04.008.

[2] W. Habraken, P. Habibovic, M. Epple, and M. Bohner, “Calcium phosphates in biomedical applications: materials for the future?” *Mater. Today*, vol. 19, no. 2, pp. 69–87, Mar. 2016, doi: 10.1016/j.mattod.2015.10.008.

[3] M.-P. Ginebra, M. Espanol, Y. Maazouz, V. Bergez, and D. Pastorino, “Bioceramics and bone healing” *EFORT Open Rev.*, vol. 3, no. 5, pp. 173–183, May 2018, doi: 10.1302/2058-5241.3.170056.

[4] R. Trombetta, J. A. Inzana, E. M. Schwarz, S. L. Kates, and H. A. Awad, “3D Printing of Calcium Phosphate Ceramics for Bone Tissue Engineering and Drug Delivery” *Ann. Biomed. Eng.*, vol. 45, no. 1, pp. 23–44, Jan. 2017, doi: 10.1007/s10439-016-1678-3.

[5] J. A. Lewis and G. M. Gratson, “Direct writing in three dimensions” *Mater. Today*, vol. 7, no. 7–8, pp. 32–39, Jul. 2004, doi: 10.1016/S1369-7021(04)00344-X.

[6] E. Feilden, E. G.-T. Blanca, F. Giuliani, E. Saiz, and L. Vandeperre, “Robocasting of structural ceramic parts with hydrogel inks” *J. Eur. Ceram. Soc.*, vol. 36, no. 10, pp. 2525–2533, Aug. 2016, doi: 10.1016/j.jeurceramsoc.2016.03.001.

[7] A. Lode *et al.*, “Fabrication of porous scaffolds by three-dimensional plotting of a pasty calcium phosphate bone cement under mild conditions” *J. Tissue Eng. Regen. Med.*, vol. 8, no. 9, pp. 682–693, Sep. 2014, doi: 10.1002/term.1563.

[8] Y. Maazouz *et al.*, “Robocasting of biomimetic hydroxyapatite scaffolds using self-setting inks” *J. Mater. Chem. B*, vol. 2, no. 33, pp. 5378–5386, 2014, doi: 10.1039/C4TB00438H.

[9] N. Raja and H. Yun, “A simultaneous 3D printing process for the fabrication of bioceramic and cell-laden hydrogel core/shell scaffolds with potential application in bone tissue regeneration” *J. Mater. Chem. B*, vol. 4, no. 27, pp. 4707–4716, 2016, doi: 10.1039/C6TB00849F.

[10] T. Ahlfeld *et al.*, “Design and Fabrication of Complex Scaffolds for Bone Defect Healing: Combined 3D Plotting of a Calcium Phosphate Cement and a Growth Factor-Loaded Hydrogel” *Ann. Biomed. Eng.*, vol. 45, no. 1, pp. 224–236, Jan. 2017, doi: 10.1007/s10439-016-1685-4.

[11] A. Kumar *et al.*, “Low temperature additive manufacturing of three dimensional scaffolds for bone-tissue engineering applications: Processing related challenges and property assessment” *Mater. Sci. Eng. R Reports*, vol. 103, pp. 1–39, May 2016, doi: 10.1016/j.mser.2016.01.001.

[12] V. P. Galván-Chacón and P. Habibovic, “Deconvoluting the Bioactivity of Calcium Phosphate-Based Bone Graft Substitutes: Strategies to Understand the Role of Individual Material Properties” *Adv. Healthc. Mater.*, vol. 6, no. 13, p. 1601478, Jul. 2017, doi: 10.1002/adhm.201601478.

[13] V. Karageorgiou and D. Kaplan, “Porosity of 3D biomaterial scaffolds and osteogenesis” *Biomaterials*, vol. 26, no. 27, pp. 5474–5491, Sep. 2005, doi: 10.1016/j.biomaterials.2005.02.002.

[14] O. Chan *et al.*, “The effects of microporosity on osteoinduction of calcium phosphate bone graft substitute biomaterials” *Acta Biomater.*, vol. 8, no. 7, pp. 2788–2794, Jul. 2012, doi: 10.1016/j.actbio.2012.03.038.

[15] M. J. Coathup *et al.*, “Effect of increased strut porosity of calcium phosphate bone graft

substitute biomaterials on osteoinduction" *J. Biomed. Mater. Res. Part A*, vol. 100A, no. 6, pp. 1550–1555, Jun. 2012, doi: 10.1002/jbm.a.34094.

[16] U. Ripamonti, J. Crooks, and A. N. Kirkbride, "Sintered porous hydroxyapatites with intrinsic osteoinductive activity: Geometric induction of bone formation" *S. Afr. J. Sci.*, vol. 95, no. 8, pp. 335–343, 1999.

[17] U. Ripamonti, P. W. Richter, and M. E. Thomas, "Self-Inducing Shape Memory Geometric Cues Embedded within Smart Hydroxyapatite-Based Biomimetic Matrices" *Plast. Reconstr. Surg.*, vol. 120, no. 7, pp. 1796–1807, Dec. 2007, doi: 10.1097/01.prs.0000287133.43718.89.

[18] G. Daculsi, T. Miramond, P. Borget, and S. Baroth, "Smart Calcium Phosphate Bioceramic Scaffold for Bone Tissue Engineering" *Key Eng. Mater.*, vol. 529–530, pp. 19–23, Nov. 2012, doi: 10.4028/www.scientific.net/KEM.529-530.19.

[19] U. Ripamonti, "Soluble osteogenic molecular signals and the induction of bone formation" *Biomaterials*, vol. 27, no. 6, pp. 807–822, Feb. 2006, doi: 10.1016/j.biomaterials.2005.09.021.

[20] M. Rumpler, A. Woesz, J. W. C. Dunlop, J. T. van Dongen, and P. Fratzl, "The effect of geometry on three-dimensional tissue growth" *J. R. Soc. Interface*, vol. 5, no. 27, pp. 1173–1180, Oct. 2008, doi: 10.1098/rsif.2008.0064.

[21] C. M. Nelson *et al.*, "Emergent patterns of growth controlled by multicellular form and mechanics" *Proc. Natl. Acad. Sci.*, vol. 102, no. 33, pp. 11594–11599, Aug. 2005, doi: 10.1073/pnas.0502575102.

[22] C. M. Bidan *et al.*, "How Linear Tension Converts to Curvature: Geometric Control of Bone Tissue Growth" *PLoS One*, vol. 7, no. 5, p. e36336, May 2012, doi: 10.1371/journal.pone.0036336.

[23] C. M. Bidan, K. P. Kommareddy, M. Rumpler, P. Kollmannsberger, P. Fratzl, and J. W. C. Dunlop, "Geometry as a Factor for Tissue Growth: Towards Shape Optimization of Tissue Engineering Scaffolds" *Adv. Healthc. Mater.*, vol. 2, no. 1, pp. 186–194, Jan. 2013, doi: 10.1002/adhm.201200159.

[24] A. Barba *et al.*, "Osteoinduction by Foamed and 3D-Printed Calcium Phosphate Scaffolds: Effect of Nanostructure and Pore Architecture" *ACS Appl. Mater. Interfaces*, vol. 9, no. 48, pp. 41722–41736, Dec. 2017, doi: 10.1021/acsami.7b14175.

[25] A. Barba *et al.*, "Osteogenesis by foamed and 3D-printed nanostructured calcium phosphate scaffolds: Effect of pore architecture" *Acta Biomater.*, vol. 79, no. 2, pp. 135–147, Oct. 2018, doi: 10.1016/j.actbio.2018.09.003.

[26] P. Habibovic, H. Yuan, C. M. van der Valk, G. Meijer, C. a van Blitterswijk, and K. de Groot, "3D microenvironment as essential element for osteoinduction by biomaterials" *Biomaterials*, vol. 26, no. 17, pp. 3565–3575, Jun. 2005, doi: 10.1016/j.biomaterials.2004.09.056.

[27] H. Shao *et al.*, "Bioactive glass-reinforced bioceramic ink writing scaffolds: sintering, microstructure and mechanical behavior" *Biofabrication*, vol. 7, no. 3, p. 035010, Sep. 2015, doi: 10.1088/1758-5090/7/3/035010.

[28] C. Wu, Y. Luo, G. Cuniberti, Y. Xiao, and M. Gelinsky, "Three-dimensional printing of hierarchical and tough mesoporous bioactive glass scaffolds with a controllable pore architecture, excellent mechanical strength and mineralization ability" *Acta Biomater.*, vol. 7, no. 6, pp. 2644–2650, Jun. 2011, doi: 10.1016/j.actbio.2011.03.009.

[29] S. Raymond *et al.*, "Accelerated hardening of nanotextured 3D-plotted self-setting calcium phosphate inks" *Acta Biomater.*, vol. 75, pp. 451–462, Jul. 2018, doi: 10.1016/j.actbio.2018.05.042.

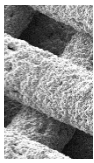

[30] L. Vidal *et al.*, “Regeneration of segmental defects in metatarsus of sheep with vascularized and customized 3D-printed calcium phosphate scaffolds” *Sci. Rep.*, vol. 10, no. 1, p. 7068, Dec. 2020, doi: 10.1038/s41598-020-63742-w.

[31] Y. Raymond *et al.*, “3D printing non-cylindrical strands: morphological and structural implications” *Manuscr. Submitt. Publ.*, 2021.

[32] D. Pastorino, C. Canal, and M.-P. Ginebra, “Multiple characterization study on porosity and pore structure of calcium phosphate cements” *Acta Biomater.*, vol. 28, pp. 205–214, Dec. 2015, doi: 10.1016/j.actbio.2015.09.017.

[33] N. R. Council, *Guide for the Care and Use of Laboratory Animals*. Washington, D.C.: National Academies Press, 2011.

[34] Y. Raymond *et al.*, “Biomimetic vs Hydrothermal α-TCP setting treatments: morphological and *in vivo* comparison” *Manuscr. Submitt. Publ.*, 2021.

[35] V. M. Bhatnagar, “Infrared spectrum of strontium hydroxyapatite” *Experientia*, vol. 23, no. 9, pp. 697–699, Sep. 1967, doi: 10.1007/BF02154118.

[36] M. Mir *et al.*, “XRD, AFM, IR and TGA study of nanostructured hydroxyapatite” *Mater. Res.*, vol. 15, no. 4, pp. 622–627, Jul. 2012, doi: 10.1590/S1516-14392012005000069.

[37] P. Diloksumpan *et al.*, “Orthotopic Bone Regeneration within 3D Printed Bioceramic Scaffolds with Region-Dependent Porosity Gradients in an Equine Model” *Adv. Healthc. Mater.*, vol. 1901807, pp. 1–11, 2020, doi: 10.1002/adhm.201901807.

[38] M. P. Ginebra *et al.*, “Setting Reaction and Hardening of an Apatitic Calcium Phosphate Cement” *J. Dent. Res.*, vol. 76, no. 4, pp. 905–912, Apr. 1997, doi: 10.1177/00220345970760041201.

[39] K. Ioku, G. Kawachi, S. Sasaki, H. Fujimori, and S. Goto, “Hydrothermal preparation of tailored hydroxyapatite” *J. Mater. Sci.*, vol. 41, no. 5, pp. 1341–1344, Mar. 2006, doi: 10.1007/s10853-006-7338-5.

[40] A. Barba *et al.*, “Impact of Biomimicry in the Design of Osteoinductive Bone Substitutes: Nanoscale Matters” *ACS Appl. Mater. Interfaces*, vol. 11, no. 9, pp. 8818–8830, 2019, doi: 10.1021/acsami.8b20749.

[41] J. Hall, P. Miranda-Burgos, and L. Sennerby, “Stimulation of Directed Bone Growth at Oxidized Titanium Implants by Macroscopic Grooves: An In Vivo Study” *Clin. Implant Dent. Relat. Res.*, vol. 7, no. s1, pp. s76–s82, Jun. 2005, doi: 10.1111/j.1708-8208.2005.tb00078.x.

[42] B. Chehroudi, D. McDonnell, and D. M. Brunette, “The effects of micromachined surfaces on formation of bonelike tissue on subcutaneous implants as assessed by radiography and computer image processing” *J. Biomed. Mater. Res.*, vol. 34, no. 3, pp. 279–290, Mar. 1997, doi: 10.1002/(SICI)1097-4636(19970305)34:3<279::AID-JBM2>3.0.CO;2-H.

[43] M. Hirao *et al.*, “Macro-structural effect of metal surfaces treated using computer-assisted yttrium-aluminum-garnet laser scanning on bone-implant fixation” *J. Biomed. Mater. Res. Part A*, vol. 73A, no. 2, pp. 213–222, May 2005, doi: 10.1002/jbm.a.30277.

6.7 Supplementary Information

All image analysis was implemented using Python and can be found at https://github.com/YAGORAYMOND/uCT-image-analysis

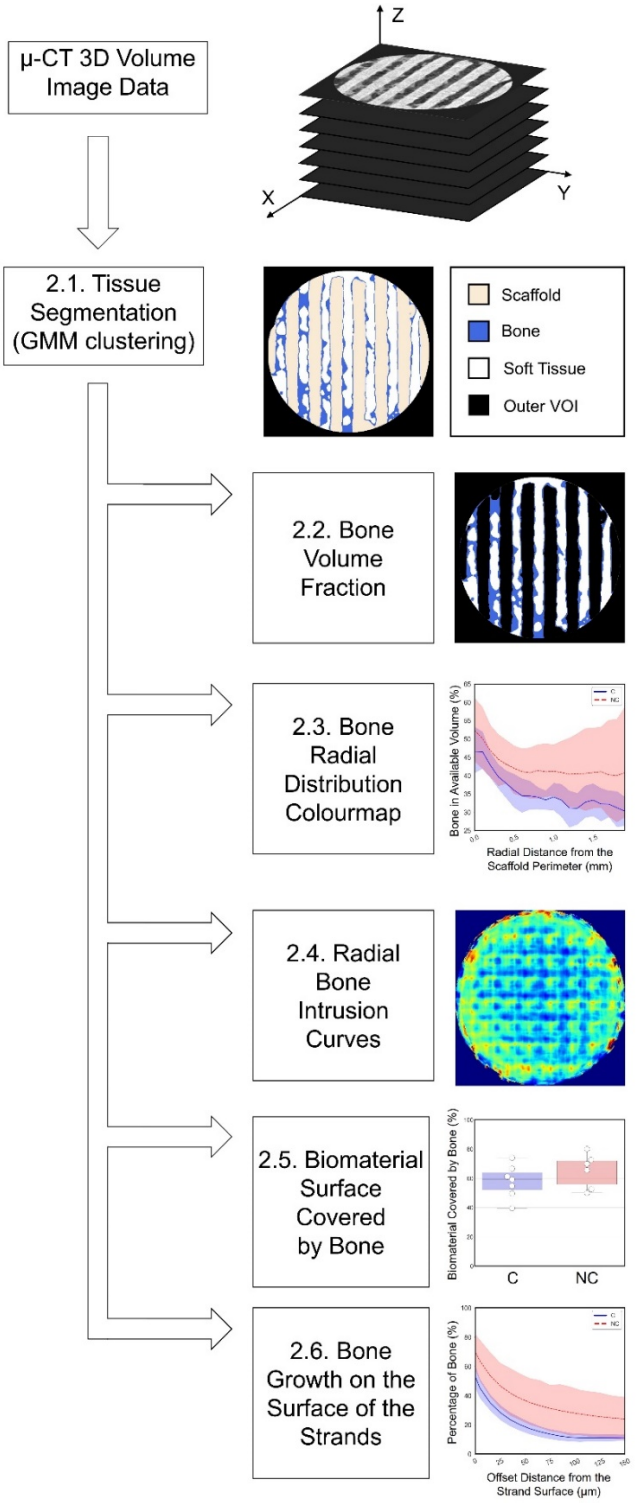

Fig. S6.1. Schema representing the main stages of the image analysis process.

The image analysis processing steps are described in more detail in the following four stages:

Segmentation

a) Load stacks of µ-CT reconstructions (.tiff format).

b) Reshape image as 1D array (flatten).

c) Fit a Gaussian Mixture model (GMM) with 4 components to the grayscale pixel distribution.

d) Assign pixels to the regions background (*i.e.* outside the VOI), void (*i.e.* non-mineralised tissue), bone and scaffold according to the means of the resulting GMM model components in increasing order.

e) Apply a median filter using a disk-shaped structuring element of radius 50 µm (5 pixels).

Quantification of the Bone Volume Percentage

a) Determine volume of bone and void (*i.e.* non-mineralised tissue) regions.

b) Measure bone fraction as relative percentage of bone volume over available volume (100*(bone/(void+bone)).

Quantification of the Radial Bone Intrusion Curves

a) Iterate each z-stack.

b) Apply a thinning algorithm to each stack eroding the external perimeter of the sample in successive bands with a disk-shaped structuring element of radius 100 µm.

c) Calculate bone fraction for each peeling band.

Representation of the Bone Distribution Axial Colormaps

a) Load segmented images.

b) Obtain the 2D z-projection of the volume.

c) Generate a 2D colormap representing the distribution of bone fraction.

Biomaterial Surface Covered by Bone

a) Load segmented images

b) Remove thin-walled possible artefacts on bone tissue applying a 3D morphological opening of the bone volume with a ball-shaped structuring element with radius 20 µm.

c) Calculate the contact region of bone and biomaterial as the intersection of the biomaterial with a dilation of the bone with a ball-shaped structuring element with radius 20 µm.

d) Calculate the fraction of contact pixels over available biomaterial surface pixels

Bone Growth on the Surface of the Strands

a) Load segmented images.

b) Remove thin-walled possible artefacts on bone tissue applying a 3D morphological opening of the bone volume with a ball-shaped structuring element with radius 20 µm.

c) Generate concentric regions of interest with thickness of 10 µm covering the biomaterial surface by combining dilation with a disk-shaped structuring element with radius 10 µm and Boolean operations.

d) In each region of interest determine the percentage of bone (100*(bone volume/region volume)).

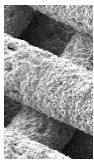

Chapter 7

MimetikOss® 3D Technology Transfer

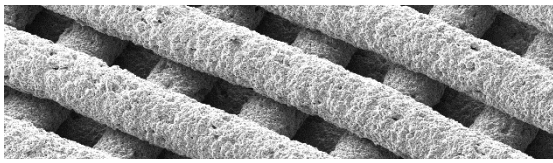

MIMETIKOSS® 3D TECHNOLOGY TRANSFER

7.1. Introduction

The following chapter summarises the work done during the course of this thesis to transform the developed DIW of CaP-ink technology into a commercial product. This work has been done in collaboration with the departments of research and development, manufacturing and quality affairs in Mimetis Biomaterials S.L.

7.2. Steps in the Technology Transfer

Patenting the Technology

The first step before the technology transfer was to patent the developed technology ensuring that all the efforts towards the development of a product concluded in a competitive, original and unique solution [1].

Definition of the Business Model

There are many different ways of commercialising a same concept. For example, in our case, we could have sold the technology to other experienced companies in the 3D printing industry, or we could have chosen to sell 3D printers to hospitals and provide the ink as a consumable product (in a similar way as most inkjet paper printers are commercialised for its use in offices). However, after studying all the pros and cons, we opted to sell a complete solution to the surgeon. The uncertainty and difficulties in the regulatory side with personalised medical devices, and the difficulty to control the quality of a process performed outside the company, almost completely precluded the print-in-hospital way. Moreover, we considered that offering a complete solution to the surgeons would provide an extra added value to the company. Once defined a general idea of the business model, all the sub-steps of this process and the protocol for the interaction with the surgeon for the design of the personalised devices was defined, with the help of trusted collaborative clinicians.

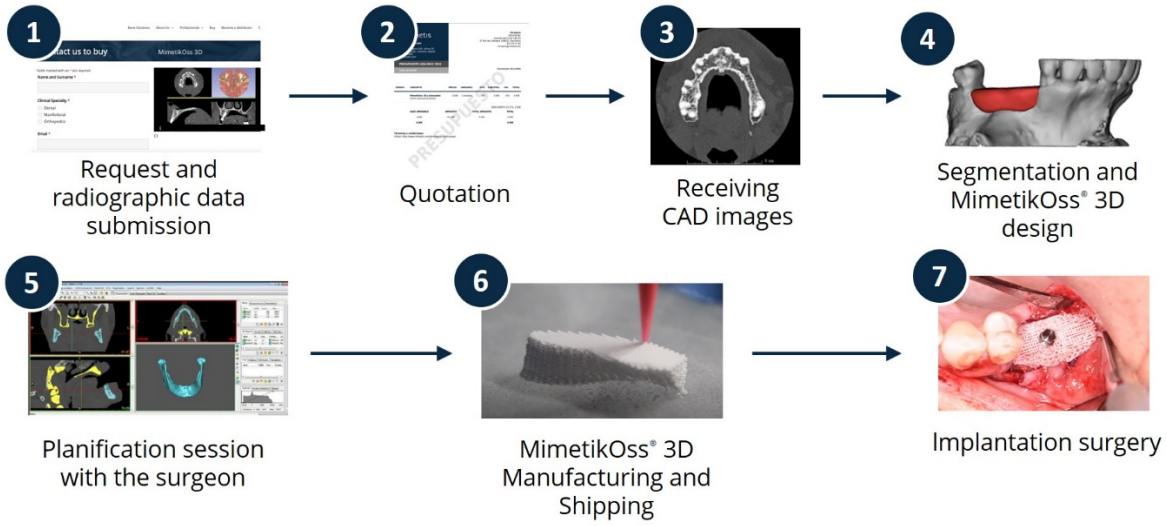

Fig. 7.1. Schema of the main steps in the production workflow of MimetikOss® 3D patient-specific bone grafts.

Definition of Raw Materials

The original protocol used research-intended raw materials. These materials had to be replaced by raw materials compliant with the quality standards of a medical device. A market research was performed to define the medical grade raw materials most suitable for the manufacturing of the product.

Definition of the Process Machines

Following the quality standards of the company's other commercial medical device (*i.e.* MimetikOss Granules) it was decided to manufacture this product inside a clean room as well. Implementing the manufacturing process of the 3D-printed grafts in clean conditions entailed a series of restrictions and limitations. New machines suitable for these conditions had to be purchased for the processing of the product. Additionally, a custom-made 3D printer was developed with an industry-oriented design (less versatile but more user-friendly and robust than the previous one used for R&D purposed), composed only of materials accepted in a clean room (*i.e.* chemically stable, not porous and not of natural origin). Afterwards, the manufacturing process with the new machines and raw materials was optimised. Protocols (*i.e.* standard operating procedures (SOPs) and work instructions (WIs)) were elaborated.

Definition of the Patient-Specific 3D Design Process

Choosing a business model consisting in selling a personalised solution implies that the design process is internalised in the company as part of the manufacturing process. Therefore, this process had to be well defined and optimised in a similar manner to the manufacturing process. First, a research on the market was made to determine which was the best combination of software required for the segmentation and design process and what were the regulatory requisites. Afterwards, WIs for segmentation and design of different reference indications were elaborated. Additionally, SOPs defining the role of each operator in the process were defined, as well as a manufacturing tracking that allows liability for each step according to the responsibilities of the operator. Finally, the design process was validated by simulating the design of personalised bone grafts on CT images of real dental, maxillofacial and orthopaedic cases, manufacturing the scaffolds and fitting them to anatomical models of the bone defects printed in resin.

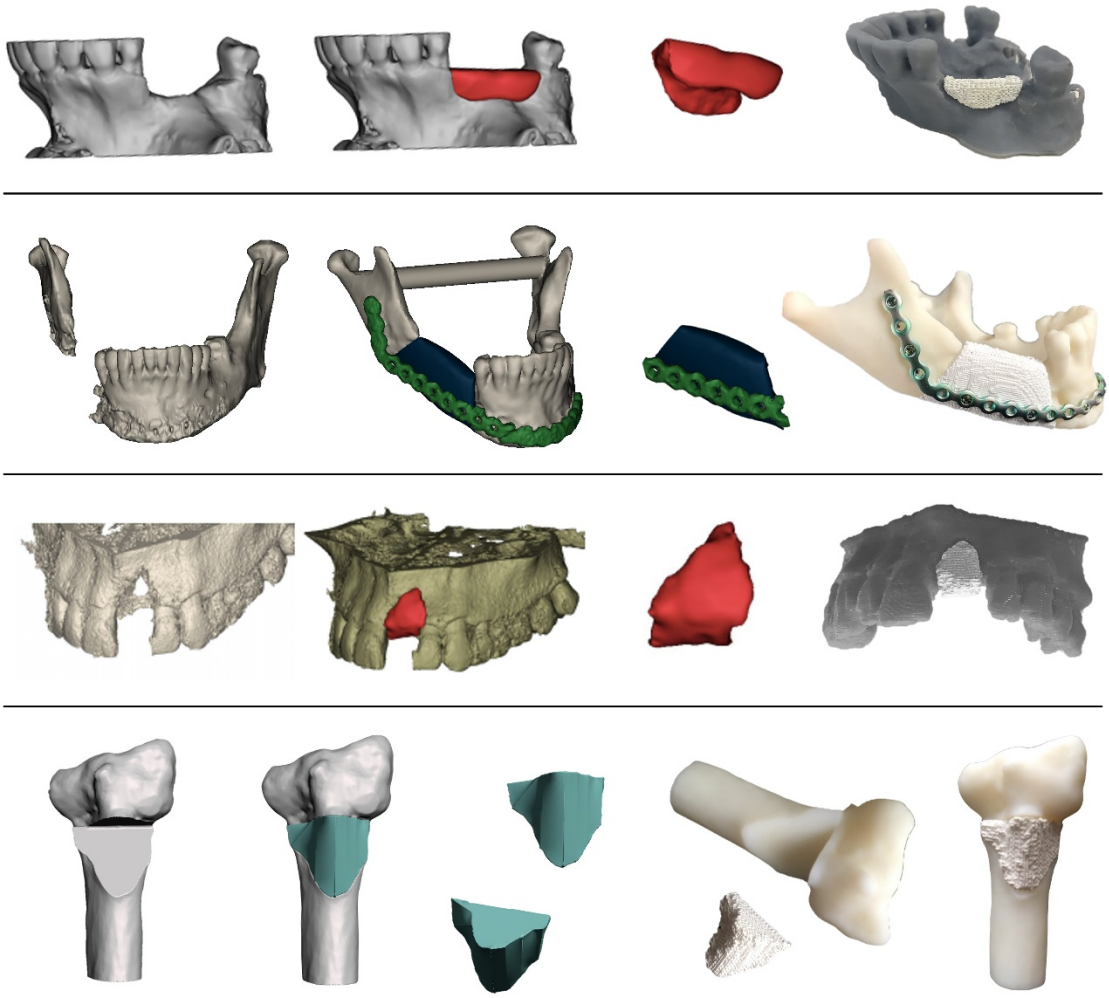

Fig. 7.2. Examples of dental, maxillofacial and orthopaedic bone defects that can be treated with MimetikOss® 3D. From left to right: Anatomical model of the bone defect, anatomical model fitted with the designed patient-specific bone graft, geometry of the bone graft and 3D-printed scaffold fitted into the 3D-printed bone defect anatomical model.

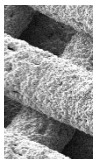

Packaging Definition

Different packaging strategies were studied. The constraints for this process were: (1) reduced process time; (2) double sterile barrier; (3) adjustable dimensions to fit scaffold personalized shapes. It was concluded that heat-sealable pouches sterilised by wet heat were the most suitable solution.

Definition of a Quality Control

Having an exhaustive control of the quality of the final parts is a crucial step in the manufacturing process of a medical device. However, this aspect is usually disregarded in research domains. For this reason, a set of quality control test was defined in order to control the external geometry accuracy, printing deposition accuracy, composition, clean condition of the manufacturing process and sterility of the final product.

Verification of the Product

Tests were performed to guarantee that the final product properties were meeting the initially defined requirements. Additionally, it was verified that the manufacturing process had an acceptable reproducibility and its properties were not altered after an ageing corresponding to the defined product's shelf life.

Validation of the Product

The adequate biological performance of the final product was validated through *in vivo* experiments. The outcome of these studies was focused on assessing the biocompatibility of the product as well as the bone regeneration capabilities (*e.g.* osseointegration, osteoconduction and resorbability).

Documentation of the Design and Development Process

In parallel to the previous steps, all the design and development process was documented and summarised following the ISO 13485:2016 standard [2]. Therefore, the information was compiled and structured following the process stages: design and development planning, inputs, outputs, review, verification, validation, transfer and control changes.

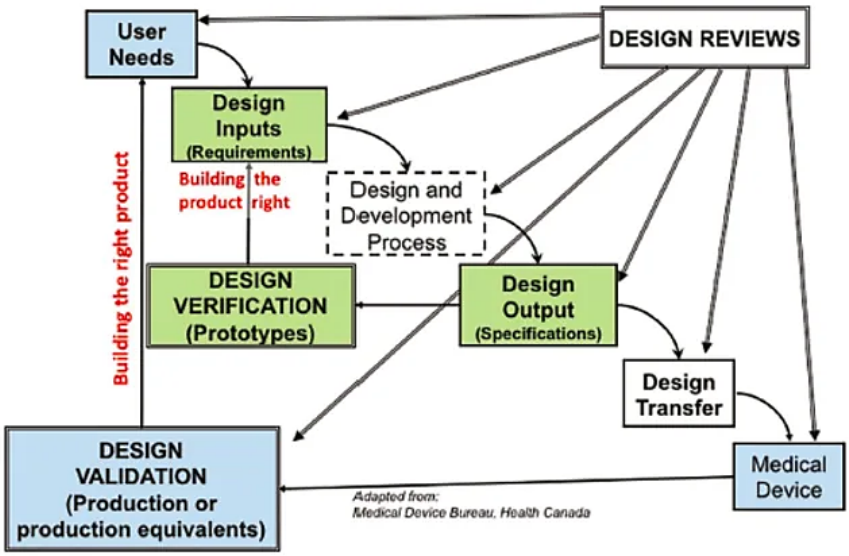

Fig. 7.3. Stages of the design and development process of a medical device according to ISO 13485:2019. Image adapted from [3].

Technical Documentation of the Product

A document containing a detailed description of the product specifications was created. This document included the product's intended use (indications), a risk analysis of the product, a detailed list of the raw materials used (providers and

specifications), an in-depth physicochemical description of the product as well as details of the packaging and labelling, and verification and validation data.

Obtaining of the Legal Permissions

After having all the manufacturing process exhaustively defined, verified, validated and documented, the technical documentation of the product was sent to the corresponding legal authorities in order to process the corresponding personalised medical device manufacturing licence to be able to launch MimetikOss® 3D to the market. With the European Medical Device Regulation (MDR) now in full force, from May 26th 2021 on this will be part of the legal requirements for all patient specific implants.

7.3 Conclusion

In October 23rd 2019 the manufacturers licence was obtained, turning MimetikOss 3D into a regulated medical device. Since then, the Mimetis team is working on personalised clinical cases to provide the clinicians with personalised biomimetic bone grafting solutions, being the first of its kind in the market. In parallel, the product keeps evolving with in a continuous amelioration process to fit the patients' needs, remaining at the forefront of bone regeneration solutions.

7.4 References

[1] Maazouz, Raymond Llorens, Ginebra Molins. *Synthetic Bone Graft*. International Patent WO/2019/211449, filed May 03, 2019, and issued November 07, 2019.

[2] ISO 13485:2016 - Medical devices — Quality management systems — Requirements for regulatory purposes, International Organization for Standardization, 2016.

[3] Medical Design Briefs, (2017). https://www.medicaldesignbriefs.com/component/content/article/mdb/features/articles/26238 (accessed March 8, 2021).

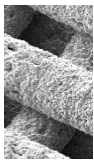

General Conclusions

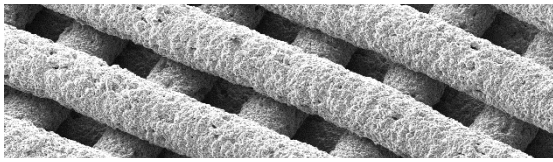

GENERAL CONCLUSIONS

The present thesis was devoted to investigate, develop, validate and transfer to the market innovative bone grafting solutions based on biomimetic calcium deficient hydroxyapatite (CDHA). The efforts were focused on developing novel consolidation strategies and structure geometries and understanding their biological performance *in vivo*. The following conclusions were reached:

- Sphere-shaped granular biomimetic CDHA synthetic grafts exhibit a significantly larger (~20%) preservation of the grafted bone volume when compared to flake-shaped bovine origin xenogenic particulate bone grafts in a three-wall alveolar defect model in minipigs. The morphology of the particles plays a crucial role in the preservation of the grafted volume stability after implantation. (**CHAPTER 2**)

- Hydrothermal consolidation processes of CDHA result in a substantial reduction of the consolidation time compared to the biomimetic reaction treatment (*i.e.* 30 min instead of 7 d), which paves the way for industrial application. The hydrothermal strategies entail changes in the textural properties of the material as a result of the faster reaction kinetics, in addition to giving rise to the formation of a new phase, β-TCP, during the hydrolysis process of α-TCP. The hydrothermal treatment in immersed conditions shows a cell viability and mechanical properties comparable to the biomimetic process. (**CHAPTER 3**)

- The *in vivo* osteogenic properties of 3D-printed CDHA scaffolds hardened with the hydrothermal process were superior to those exhibited by the same materials consolidated by the biomimetic route. Specifically, a significantly higher amount of newly formed bone was found when implanted in rabbit condyle monocortical defects. This was correlated to a higher permeability, demonstrated by a higher protein diffusion in hydrothermally-set samples. These results evidenced the significance of microstructural topography and protein permeability in bone regeneration. (**CHAPTER 4**)

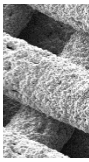

- 3D structures with strand geometries other than cylindrical were successfully printed by direct ink writing using non-circular nozzles. This method was proved effective for increasing both, the specific surface area and the degree of concavity of extrusion-based 3D-printed structures. Using non-circular nozzles introduces additional restrictions in the printing process, since the deposition stability of the strands becomes a critical parameter, the alignment of the nozzle orifice with the printing directions being crucial for a successful printing. Moreover, the phenomenon of strand torsion when changing the printing direction, which normally goes unnoticed due to the rotation-invariant geometry of circular shapes, may results in changes in the architecture of successive layers when using non-circular nozzles. (**CHAPTER 5**)

- 3D-printed CDHA scaffolds composed of star-shaped strands showed similar osteogenic capacity compared to scaffolds composed of the traditional cylindrical strands when tested *in vivo* in a rabbit condyle monocortical defect model. However, when using star-shaped strands bone was distributed more homogeneously in the 3D structure, as the grooves on the strand surfaces helped guiding bone through the core of the scaffold, enhancing the colonisation process. (**CHAPTER 6**).

- The most relevant part of the 3D printing technology developed in the course of this thesis has been patented and transferred to the market under the commercial name MimetikOss® 3D. The product is licensed as a regulated medical device and is currently a reality. (**CHAPTER 7**)

Outcomes Derived from this PhD Thesis

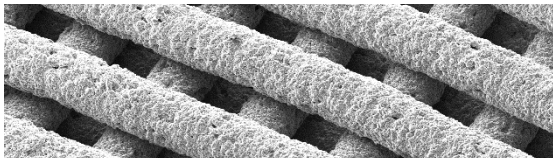

OUTCOMES DERIVED FROM THIS PhD THESIS

Publications

S. Raymond, Y. Maazouz, E.B. Montufar, R.A. Perez, B. González, J. Konka, J. Kaiser, M.-P. Ginebra, “Accelerated hardening of nanotextured 3D-plotted self-setting calcium phosphate inks”, *Acta Biomater.*, 75 (2018) 451–462, doi:10.1016/j.actbio.2018.05.042.

L. Vidal, C. Kampleitner, S. Krissian, M.Á. Brennan, O. Hoffmann, Y. Raymond, Y. Maazouz, M.-P. Ginebra, P. Rosset, P. Layrolle, “Regeneration of segmental defects in metatarsus of sheep with vascularized and customized 3D-printed calcium phosphate scaffolds”, *Sci. Rep.* 10 (2020) 7068. doi:10.1038/s41598-020-63742-w.

Y. Raymond, D. Pastorino, I. Ginebreda, Y. Maazouz, M. Ortiz, M.-C. Manzanares, M.-P. Ginebra, “Computed tomography and histological evaluation of xenogenic and biomimetic bone grafts in three-wall alveolar defects in minipigs”, *Clin. Oral Investig.* (2021). doi:10.1007/s00784-021-03956-y.

Y. Raymond, E. Thorel, M. Liversain, A. Riveiro, J. Pou and M.-P. Ginebra, “3D Printing Non-Cylindrical Strands: Morphological and Structural Implications”*, Addit. Manuf.* (2021). doi:10.1016/j.addma.2021.102129.

Y. Raymond, C. Lehmann, E. Thorel, R. Benítez, J. Franch, M. Espanol, M. Bonany, M.-C. Manzanares, C. Canal, M.-P. Ginebra, “Hydrothermal processing of 3D-printed calcium phosphate scaffolds enhances bone formation in vivo: a comparison with biomimetic treatment”, Under revision in *Acta Biomaterialia*. (May 2021).

Y. Raymond, E. Thorel, C. Lehmann, R. Benitez, A. Riveiro, J. Pou, J. Franch, M.-P. Ginebra, “3D Printing with Star-Shaped Strands: A New Approach to Enhance Bone Regeneration”, Under revision in *Advanced Healthcare Materials*. (June 2021).

Patents

Maazouz, Raymond Llorens, Ginebra Molins. “Synthetic Bone Graft”. International Patent WO/2019/211449, filed May 03, 2019, and issued November 07, 2019.

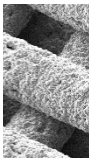

Conference Participation

S. Raymond, Y. Maazouz, M.-P. Ginebra. “Development of patient-specific biomimetic bone grafts”, *10th IBEC symposium*, Barcelona (Spain), May 2017. **Poster communication**

S. Raymond, Y. Maazouz, M.-P. Ginebra. “3D-printed CaP patient-specific bone graft substitutes: Industrial flow chain”, *9th International Workshop on Interfaces: New Frontiers in Biomaterials*, Santiago de Compostela (Spain), April 2018. **Oral communication**

J. Konka, S. Raymond, Y. Maazouz, M.-P. Ginebra. “Direct ink writing with self-setting α-TCP inks: effect of processing parameters”, *9th International Workshop on Interfaces: New Frontiers in Biomaterials*, Santiago de Compostela (Spain), April 2018. **Oral communication**

S. Raymond, M.-P. Ginebra. “2D-3D Printing Technologies for Ceramics and Glass – 3D-printed Patient-specific Bone Graft Substitutes: Industrial Flow Chain”, *V Congreso Hispano-Luso de Cerámica y Vidrio / LVI Congreso Nacional SECV*, Barcelona (Spain), October 2018. **Invited talk tutorial course**

J. Konka, S. Raymond, Y. Maazouz, M.-P. Ginebra. “Development of biomimetic hydroxyapatite bone grafts by 3D direct ink writing”, *V Congreso Hispano-Luso de Cerámica y Vidrio / LVI Congreso Nacional SECV*, Barcelona (Spain), October 2018. **Oral communication**

L. Vidal, S. Krissian, M.A. Brennan, Y. Maazouz, S. Raymond, M.-P. Ginebra, J. De Lima, P. Humbert, C. Kampleitner, P. Rosset, P. Layrolle. “Reconstruction of large bone defect in sheep with customized 3D-printed calcium phosphate scaffolds”, *Termis European Chapter Meeting 2019 (TERMIS-EU)*, Rodes (Greece), May 2019. **Oral communication**

S. Raymond, Y. Maazouz, E. B. Montufar, R. A. Perez, B. González, J. Konka, J. Kaiser, M.-P. Ginebra. “Novel strategies for the hardening of 3D-printed biomimetic bone grafts”, *7th shaping conference (ECerS)*, Aveiro (Portugal), September 2019. **Oral communication**